VALENCE LOSSES AT INTERFACES IN ALUMINIUM ALLOYS

Ewan Douglas William Maclean

Submitted for the degree of Doctor of Philosophy at the Department of Physics and Astronomy and the Department of Chemistry, University of Glasgow.

November, 2002

SUMMARY

The power and potential of electron energy loss spectroscopy (EELS) as an analytical technique in electron microscopy is undisputed. Much of the focus of current research is on the extraction of structural and bonding information from energy loss near-edge structure. However, the valence loss region contains a wealth of information including data on the optical, electronic and physical properties of a material. Despite the fact that the signal intensity is considerably greater in this region, it is often overlooked as considerable data processing is required to extract the information.

In particular, the valence loss EELS spectrum of a material can be used to calculate its complex dielectric function. However, close to an interface between two dielectric media, a peak corresponding to the interface is observed in the EELS spectrum. This peak must be removed before accurate bulk dielectric data can be determined. However, relativistic and non-relativistic equations exist to model the EELS response of two and three-layer systems. This latter case is of particular interest in the investigation of thin intergranular films within ceramic or composite systems. The thickness of such films can have a significant effect on the strength of the ceramic or composite but is relatively insensitive to material composition. Recent models have suggested that the thickness of the intergranular film is correlated with the dispersion forces acting on the interface. These forces can be expressed in terms of the Hamaker constant, which depends on the complex dielectric functions of the components. If the dielectric functions can be determined using valence loss spectroscopy it should be possible to measure the Hamaker constant and thus obtain information on the dispersion forces. However, due to the complexity of the three-layer system it is of interest initially to explore the simpler two-layer case.

The aim of this project was to investigate EELS from two-layer systems and relate the results to the existing theory. Two systems were investigated, magnesium silicide platelets within an aluminium matrix and silicon precipitates within an aluminium matrix. Both systems were prepared through thermal treatment of a 6061 Al alloy.

The majority of the data presented in this thesis was acquired using EELS. However, energy dispersive x-ray spectroscopy (EDX) and electron microscopy were also used. EELS was performed on two different electron microscopes, the VG HB5 STEM and the FEI Tecnai TF20 (S)TEM. The bulk of the results were acquired on the HB5.

To facilitate the comparison of theoretical and experimental results, the data was separated into bulk and interface components. The component amounts were then plotted against distance from the interface. Bessel functions were then fitted to this plot to give characteristic values. These values represented how well the optimal interface position had been chosen, the comparative decay of the interface plasmon on each side of the interface and the relative thickness of the bulk material.

The experimental data from most of the interfaces examined indicated significant variations in the thickness of the sample. Despite this, the experimental results were found to follow the trend suggested by the theoretical equations. Analysis of the characteristic values indicated that the data from the HB5 and Tecnai for an interface showed a strong correlation. However, comparison of the experimental values with the theoretical reference showed a deviation of ~20%.

Though the source of this deviation was not clear, a number of possible causes were investigated. Theoretical models were generated of systems with a variety of thickness profiles. In addition, systems containing steps, wide and narrow bulk plasmons and a thin interfacial layer of a third material were all considered. The deviation between the results from experiment and the simple theoretical model was believed to be consistent with the factors affecting EELS from a real interface. In particular, thickness variations and imperfections at the interface were found to be the most likely cause of the discrepancy between theory and experiment.

Finally, additional work that could be performed to extend the applicability of this thesis to three-layer systems is discussed. In particular, the determination of dielectric functions from thin interfacial phases is considered.

ACKNOWLEDGEMENTS

Initially, I would like to thank my supervisors Prof. Alan Craven and Dr David McComb with whom it was a great pleasure to work. Their enthusiasm, guidance, assistance, tolerance and sarcasm throughout my PhD were invaluable in enabling me to achieve and learn so much.

Thanks to Prof. George Weatherley, for providing a better quality alloy and for a number of helpful discussions. Also to Brian Miller, who performed some of the more menial parts of the sample preparation for many of the later samples and was always a cheery face, willing to help.

Special thanks to Dr. Sam McFadzean who, despite doing far too much, was always willing to give assistance. Thank you also to Jim Gallagher who provided technical support in chemistry and kept the microscopes running (or at very least, not-running in a very purposeful way).

For the Tecnai work, I am indebted to Dr Maureen MacKenzie who operated the microscope and assisted me with the instrumentation section on the Tecnai. Also to David Hamilton who spent time writing plug-in modules and Paul Thomas from Gatan who has been of great help with the *Digital Micrograph* software.

To Frances Docherty for guiding me at the beginning of my PhD, Mhairi Crawford for putting up with me towards the end of my PhD and all my office mates in between: Thank you!

Thank you also to all the members of SSP, past and present, for helpful discussions, helpful actions, guidance, giving up microscope time for me and generally being great.

A big thank you to the Cecilian Society, its members, my flatmate David Crooks and all members of the lunch table for keeping me sane and giving me something other than my PhD to think about when necessary.

Thank you, of course, to my girlfriend Cara Strachan for putting up with so much.

Finally, I'd like to thank my parents who, despite numerous explanations, think that my PhD is "something to do with electrons".

DECLARATION

This thesis is a record of the work carried out by me in the Department of Physics and Astronomy and the Department of Chemistry at the University of Glasgow. The work described herein is my own, apart from the operation of the Tecnai microscope and the mechanical grinding of some of the later samples. These tasks were performed by Dr Maureen MacKenzie and Brian Miller respectively.

Some of the results contained in chapter 6 were presented at EMAG'01 in Dundee. As a result they have also been published in:

Maclean, E. D. W., Craven, A. J. and McComb, D. W., 2001, *Institute of Physics Conference Series*, **168**, 259.

This thesis has not previously been submitted for a higher degree.

CONTENTS

LIST OF TABLES

LIST OF FIGURES

CHAPTER 1

INTRODUCTION

This chapter will discuss the background and possible applications of the work presented in this thesis. The intention of this chapter is to introduce some of the factors governing the performance of advanced materials. In particular, the role of interfacial layers within advanced materials will be discussed. The understanding of these layers is key to understanding many of the properties of the materials. To this end, the application of electron microscopy techniques to the investigation of these interfacial layers could allow a greater understanding of advanced materials.

1.1 Interfacial Layers within Advanced Materials

Ceramic materials have a number of very useful properties. They are known for being very strong and having excellent chemical and temperature resistance. However, ceramics are also brittle and hence are prone to brittle failure. Tailoring of the grain size within the ceramics can result in increased strength and decreased brittleness (Zavattieri and Espinosa, 2001). This has been shown to be related to the formation of intergranular films at grain boundary interfaces (Becher *et al.*, 2000). These films are found to be of relatively constant thickness in a given material, even from different boundaries (Clarke, 1987).

An alternative way of utilising the properties of ceramics is in metal-matrix composites. By combining a high strength phase with a strong ductile phase, it is possible to have a strong material that does not suffer from the brittleness of a ceramic. However, the strength of such materials is not noticeably better than conventional engineering materials. The area in which metal-matrix composites excel, is in strength to weight ratio. Composites are extremely strong for their weight and so are useful structural materials.

Interfacial thin films are also of importance within metal-matrix composites. During the processing or subsequent heat treatment of some metal-matrix composites, it is observed that crystalline products form as a result of a reaction between the alloy and the reinforcing phase. The formation of these products depletes the matrix of some of its alloying

additions, resulting in a poorer quality alloy. However, if a small amount of strontium is added to the same system as an alloying addition, the growth of these crystalline phases is inhibited (McComb *et al*, 2000). Instead, a 2-3nm amorphous film forms at the interface between the reinforcing phase and the matrix. Unlike the crystalline products, the amorphous film leaves the quantity of available alloying elements largely unchanged. In addition, the amorphous film assists in the sintering process. Further to this, links have been made between the presence of an amorphous film and superplasticity within some aluminium alloy composites (Koike *et al*, 1995).

Determining the properties of these interfaces is essential in understanding the properties of the materials themselves. In particular, knowledge of the factors governing the formation and thickness of the interfaces is key in this understanding.

1.2 Intergranular Film Thickness

Clarke (1987) proposed two methods for predicting the equilibrium thickness of an intergranular phase within ceramics. This work has also been applied to interfacial films within metal-matrix composites, an area where it is also believed to be valid (McComb *et al.*, 2000).

The first of these methods utilises the work of Widom (1978) and de Gennes (1981) to determine the free energy at the interface. By applying minimum energy arguments and assuming thermodynamic equilibrium, a stable thickness for the interfacial layer is determined. The other method is based on the argument that for a stable intergranular phase thickness, the net normal force acting on the film must be equal to zero. According to this theory, the forces acting at the interface can be simplified down to two opposing forces, assuming there is no externally applied stress.

The first of these forces is a structural disjoining pressure (Derjaguin and Churaev, 1974) acting to increase the thickness of the intergranular phase. During the preparation of a ceramic, the material is heated to a high temperature. The intergranular phase forms during this process and, because of the temperature, can be considered to be liquid. In a system comprised of two grains in different orientations separated by a thin liquid interface phase, it is proposed that the liquid phase is not randomly oriented. Instead, it develops a short-

range orientational order close to each grain. This order arises from a preferred orientation of the layer of interfacial molecules at the surface of the grain. This extends out into the interfacial region as each layer orders itself slightly to accommodate the previous. If the ordering extends a distance of the order of ξ into the intergranular phase, then ξ is known as the correlation length associated with the orientational fluctuations.

If the width, h, of the intergranular phase is then reduced to $\leq 2\xi$, the orientational order arising from each grain will start to interfere with the other. This is energetically unfavourable and so the system would experience a force to return it to its previous state. It is this force which gives rise to the structural disjoining pressure, Π_{ST}. An approximate form for Π_{ST} is given by eqn 1.1.

$$\Pi_{ST} = -4\phi_0 \exp\left(\frac{-h}{\xi}\right) \qquad \textbf{Equation 1.1}$$

where ϕ_0 is the free energy difference between ordered and disordered states of the interfacial film.

The second force is the van der Waals (or London) dispersion force (Π_{DISP}). This is an attractive force which acts across the interfacial phase to bring the two grains closer together. The force arises from electromagnetic interaction between induced dipoles in each phase (London, 1937). Hamaker (1937) extended this theory to give a measure of the attraction between two bodies. The work of Dzayloshinskii *et al.* (1961) gave direct applicability to the case of two interacting phases separated by a third. This geometry is described by eqn 1.2.

$$\Pi_{DISP} = \frac{\hbar}{8\pi^2 h^3}\int_0^\infty \sum_{n=1}^{\infty} \frac{1}{n^3}\left[\left(\frac{\varepsilon_a(i\zeta)-\varepsilon_b(i\zeta)}{\varepsilon_a(i\zeta)+\varepsilon_b(i\zeta)}\right)\left(\frac{\varepsilon_c(i\zeta)-\varepsilon_b(i\zeta)}{\varepsilon_c(i\zeta)+\varepsilon_b(i\zeta)}\right)\right]^n d\zeta \qquad \textbf{Equation 1.2}$$

Where $\varepsilon_k(i\zeta)$ is the value of the complex dielectric function of material k at imaginary frequency $i\zeta$ (Parsegian and Ninham, 1969). An imaginary frequency is used purely to simplify the mathematics; it has no physical significance. Eqn 1.2 can also be expressed in terms of the Hamaker constant, H_{abc} (sometimes denoted A_{abc}).

$$H_{abc} = \frac{3\hbar}{4\pi}\int_0^\infty \sum_{s=1}^{\infty} \frac{1}{s^3}\left[\left(\frac{\varepsilon_a(i\zeta)-\varepsilon_b(i\zeta)}{\varepsilon_a(i\zeta)+\varepsilon_b(i\zeta)}\right)\left(\frac{\varepsilon_c(i\zeta)-\varepsilon_b(i\zeta)}{\varepsilon_c(i\zeta)+\varepsilon_b(i\zeta)}\right)\right]^s d\zeta \quad \textbf{Equation 1.3}$$

$$\therefore \Pi_{DISP} = \frac{H_{abc}}{6\pi h^3} \quad \textbf{Equation 1.4}$$

Making use of several approximations, it is observed that the results for both the energy and force approach have the same form. The thickness of an interfacial layer, separating two materials is given approximately by eqn 1.5.

$$h \approx \xi \ln\left(\frac{162\pi kT}{H_{abc}}\right). \quad \textbf{Equation 1.5}$$

The value of ξ is often approximated using unit cell lengths. Therefore, with knowledge of the Hamaker constant it is possible to calculate an approximate film thickness. Indeed this has been done by a number of people (*e.g.* Clarke, 1987, Knowles and Turan, 2000). However, calculation of the Hamaker constant is not trivial. In particular, to calculate the dielectric function at imaginary frequencies, a Kramers-Kronig relation (eqn 1.6) must be used (Hough and White, 1980). This requires knowledge of the imaginary part of the dielectric function (ε'') over a large frequency range.

$$\varepsilon(i\zeta) = 1 + \frac{2}{\pi}\int_0^\infty \frac{\omega\varepsilon''(\omega)}{\omega^2+\zeta^2} d\omega \quad \textbf{Equation 1.6}$$

1.3 The Dielectric Function

Discussions involving dielectrics often refer to the dielectric constant. In actuality, the dielectric constant is a function of frequency as well as having a complex component. The static dielectric constant is the value of the dielectric function at very low frequencies. At optical frequencies (10^{14}-10^{15} Hz) for transparent materials, the dielectric function is equal to the square of the refractive index for that material. As with the dielectric function, the refractive index is a function of frequency (hence the splitting of white light by prisms). This relationship works in reverse and the dielectric function is often calculated from experimental refractive index and absorption data from a material.

In order to evaluate eqn 1.6, it is necessary to know the imaginary part of the dielectric function over a full range of frequencies. Conventional optical spectroscopy techniques (*e.g.* Dagastine *et al*, 2000) generally do not cover the entire range of frequencies. For many systems the requisite data are not available and so many workers use theoretical models to generate dielectric functions for a material. These functions are then used in the calculation of Hamaker constants (*e.g.* Bergström, 1997, Fernández-Varea and Garcia-Molina, 2000). However, as the theoretical techniques introduce a number of approximations, the resulting dielectric functions, and hence Hamaker constants, are unreliable (French *et al.*, 1995). It is therefore preferable, where possible, to use experimentally determined dielectric functions. In order to acquire the necessary data, an experimental technique which offers not only a large frequency range with good frequency resolution, but also offers the spatial resolution necessary to obtain information from a 2-3nm intergranular film is required. Electron Energy Loss Spectroscopy (EELS) is such a technique.

1.4 Electron Energy Loss Spectroscopy

EELS is a technique usually performed within an electron microscope. When a beam of electrons passes through a sample, many of the electrons interact with the sample and lose a small amount of energy. The nature of the interaction determines the amount of energy lost. The incident electron causes an oscillatory electric field. This field interacts with the electronic structure of the material, losing energy in the process (Egerton, 1996). In particular, the electric field causes a localised polarisation within the material. The polarisation of a material is closely linked with its dielectric constant (eqn 1.7).

$$\underline{P} = \varepsilon_0(\varepsilon - 1)\underline{E_0} \qquad \textbf{Equation 1.7}$$

Where $\underline{P}$ is the polarisation, ε_0 is the permittivity of free space, ε is the dielectric function and $\underline{E_0}$ is an externally applied electric field. It is through this link that it is possible to probe the dielectric function of a material using EELS (Ritchie, 1957).

The study of EELS has two main areas, the study of core losses and the study of low losses. Core loss spectroscopy deals with the excitation of electrons from the core electronic states of a material to a higher level. One of the most common uses of core loss spectroscopy is in determining elemental composition (*e.g.* Egerton, 1982). However, core

loss spectroscopy has found applicability to a number of different areas including the determination of coordination number and symmetry (*e.g.* Garvie *et al.*, 1994), probing dislocations (*e.g.* Batson, 1999) and investigating local bonding (*e.g.* Batson *et al.*, 1987).

Low loss EELS covers the interaction of a fast electron with the valence or conduction band of a material. In particular the incident electron can cause a bulk oscillation in the valence band. This is known as a bulk plasmon and appears as a peak in the low loss spectrum. The low loss area of the spectrum has been used variously in identifying the composition of biological specimens (*e.g.* Hainfeld and Isaacson, 1978), determining the composition of alloys (*e.g.* Williams and Edington, 1976), ascertaining specimen thickness (*e.g.* Egerton and Cheng, 1987), analysing bulk material properties (Oleshko *et. al.*, 2002) and of course determination of electronic structure and dielectric functions (*e.g.* Daniels, 1970; Batson *et al.*, 1986).

1.5 EELS from an Interface

In many systems the spatial resolution of EELS is better than 1nm. Therefore the determination of the dielectric function from an intergranular film should be straightforward. However, when an electron beam passes close to an interface between two materials of different dielectric functions, an additional peak is observed in the energy loss spectrum. This peak arises as a result of the interface itself and is known as an interface plasmon peak (*e.g.* Garcia-Molina *et al.*, 1985). One particular case of the interface plasmon is when one of the materials is vacuum. In this case, it is known as a surface plasmon (Howie and Milne, 1984). The interface plasmon is dependent on the dielectric functions of the two materials on either side of the interface. It is therefore not possible to obtain the dielectric function of an interfacial layer without first compensating for the effect of the interface on the EELS spectrum. Fortunately, EELS of an interface has been well discussed in literature, not only for the case of a simple planar interface (Walls, 1987), but also for cylindrical interfaces (Walsh, 1991), small particles (*e.g.* Wang, 1996) and more complex structures (Howie *et al.*, 1999). The situation becomes more complex for a three-layer case (two materials separated by a third), though once again equations describing this situation are given in literature (Howie and Milne, 1985).

The vast majority of literature covering EELS of two and three layer systems is theoretical. There are very few papers comparing the theoretical equations with actual experimental data. Those that do, generally do not perform an in-depth comparison. The closest work to that presented in this thesis, performed by Moreau *et al.* (1997) gives an extensive comparison between theory and experiment. However, the work only covers the energy and shape of peaks at various distances and does not examine trends in decay and growth of plasmons. Conversely, Scheinfein *et al.* (1985) examined the decay of the aluminium plasmon and the movement of the surface plasmon in a Al-AlF_3 system. However, the study of the aluminium decay appears to use the decay of intensity at 15eV. As both the interface and the bulk AlF_3 plasmons will contribute intensity at 15eV, this is not the most accurate gauge. In addition, the necessary use of a carbon film in the sample adds further complications. Without a full experimental comparison, attempts to extract the dielectric function from a material close to an interface are likely to produce artefacts.

1.6 Aims of this Work

In this thesis the results of EELS performed over interfaces in an aluminium/magnesium silicide and an aluminium/silicon system will be examined. These will then be compared with the theoretical results as given in the literature. This work is performed with a view to giving a greater experimental understanding of energy losses from interfaces. It is hoped that this will prompt future work in this area, eventually leading to the accurate determination of dielectric functions and hence intermolecular forces within three-phase systems of the type discussed in section 1.2.

Clearly, investigations performed on a three-layer system would have direct applicability to the analysis of the interfacial films described above. However, the theoretical treatments make certain assumptions, most noticeably that the interface is sharp, planar and parallel to the electron beam. This alone is not trivial to achieve in a two-layer experiment. Attempting to achieve this with a three-layer system would be exceptionally time-consuming and a likely source of error. As a result, it was advantageous to analyse a simpler system and hence produce firm foundations for the extension of the work to more complex systems.

1.7 Structure of the Thesis

In the following chapter the theory discussed above will be expanded. In addition, related theory will be introduced. In chapter 3, the instrumentation and related theory will be described. The basic experimental techniques used in operating these instruments will also be dealt with in this chapter. Chapter 4 contains a general discussion of the materials systems used, before describing the method for preparing suitable samples for analysis. Some new analytical techniques are introduced in chapter 5 along with tests performed to ensure their validity. The use of these techniques and others in the analysis of data is then covered in the latter part of the chapter. Chapters 6 and 7 present the results from this work along with a comparison to the corresponding theory. Finally, chapter 8 consists of overall conclusions and suggestions for further work.

CHAPTER 2

THEORY

In this chapter, the background theory necessary to aid understanding of the work covered in this thesis will be discussed. Initially electron energy loss spectroscopy (EELS) will be introduced, with particular emphasis on valence loss EELS. The effect of a single and double interface on the valence loss spectrum will then be considered. Finally, a detailed discussion of the complex dielectric function will be presented.

2.1 Electron Energy Loss Spectroscopy

The interaction of electrons with a material is the source of a number of analytical techniques, many of which are regularly used in electron microscopy. One such technique is electron energy loss spectroscopy (EELS). In EELS, electrons that have passed through the sample are collected. Many of these electrons have lost small amounts of energy, ΔE, through inelastic scattering within the sample, where ΔE depends on the exact interactions involved. An intensity proportional to the number of electrons which have lost a specific amount of energy is recorded and this is used to create an EELS spectrum.

An EELS spectrum is effectively a probability distribution giving the probability that an incident electron will lose a certain amount of energy. Indeed, the energy loss function is often expressed as a probability with respect to distance in the direction of electron motion and loss frequency, $\left(\frac{d^2P}{dzd\omega}\right)$. The loss frequency is the frequency corresponding to the amount of energy lost. It can be shown (Ritchie, 1957) that the loss function is proportional to $Im[-1/\varepsilon(\omega)]$ where ε is the complex dielectric function of the material. The applications of this and the dielectric function will be discussed in detail in section 2.4. Figure 2.1 shows an EELS spectrum highlighting the various features.

The largest feature in the spectrum is the zero loss peak which results from electrons which have passed through the sample without losing energy. This peak has a finite width, which is due to imperfect monochromaticity in the electron beam. The finite resolution of the

system (~0.5eV) means that electrons which have lost only a small amount of energy (*e.g.* those giving rise to phonon excitations) are also included in the zero loss peak. The region up to about 30-40eV corresponds to incident electrons which have lost some of their energy to electrons in the material causing them to undergo inter and intra band transitions. Also in this range are the electrons which have caused plasmon excitation (section 2.1.2). Higher energy losses result from electrons which have lost large amounts of energy to inner-shell electrons in an atom, promoting them to a higher level. As can be seen by the scale factor in Fig. 2.1 this area of the spectrum is of much lower intensity than the low loss region and so requires longer in which to acquire the spectrum to provide a suitable signal to noise ratio.

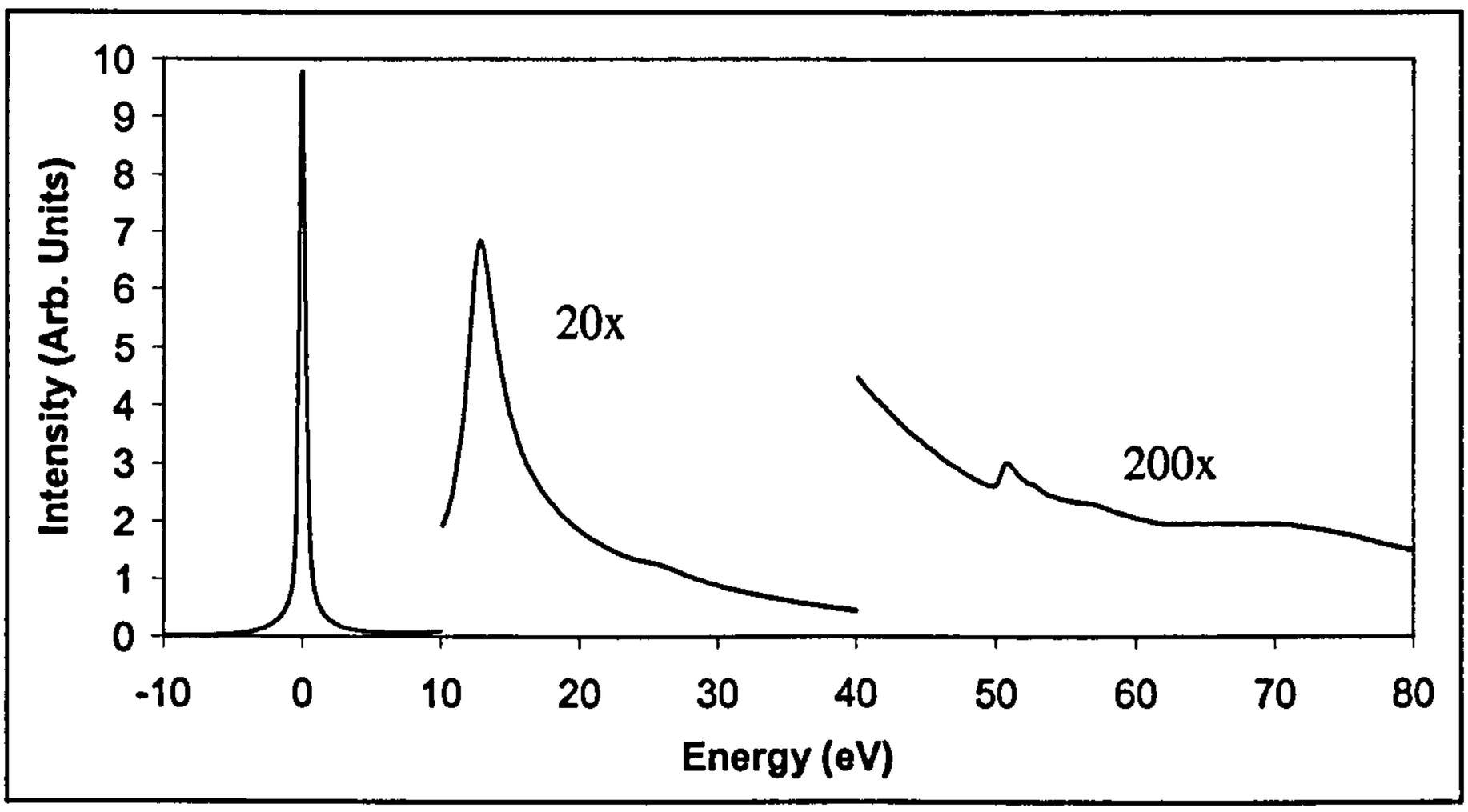

Figure 2.1 EELS spectrum of Mg_2Si showing the zero loss peak, plasmon peak (~13eV) and the Mg edge (50eV)

The angle through which an electron is scattered is also of interest and is often expressed in terms of the scattering vector q. This is given approximately by eqn 2.1 (Egerton, 1996).

$$q^2 = k_0^2\left(\theta^2 + \overline{\theta}_E^2\right) \qquad \textbf{Equation 2.1}$$

Here, the magnitude of the wave vector for the incident electron $k_0 = 2\pi/\lambda$, θ is the angle through which the electron is scattered and $\overline{\theta_E} = \overline{E}/\left(\gamma m_0 \mathrm{v}^2\right)$ is a characteristic angle corresponding to a mean energy loss $\overline{E}$ (Egerton, 1996).

2.1.1 Core loss EELS

The majority of current work done with EELS, deals with the core loss spectrum. In core loss spectroscopy, the incident fast electron interacts with a core electron in the sample atom, promoting the core electron to a higher level and causing the incident electron to lose an amount of energy equivalent to the difference in energies between the two states in the atom. Clearly the final state must be unoccupied and so the core electron is promoted to an empty state above the Fermi energy and in some cases ionised out of the atom. The energy lost by the incident electron is dependent on the element concerned and the initial energy state of the core electron. A core electron promoted from a 1s shell results in a K edge, a 2s shell results in an L_1 edge and so on with a similar naming scheme to x-ray spectroscopy.

In general, core loss spectroscopy is used primarily to determine the quantities of different elements present in a system. However, more complex analysis, particularly of the fine structure near the edges, can give information on phases, structures and in some cases symmetry of the local atomic environment (Keast *et al.*, 2001). This technique is known as energy loss near edge structure (ELNES).

2.1.2 Valence Loss EELS

Whereas core loss spectroscopy deals with single electron excitations, valence loss (also known as low loss) EELS can be a single or a multiple electron excitation. A single electron can be excited from the valence band to an empty state above the Fermi level. The effect of single-electron excitation is discussed later in this section. However, much of the interest in valence loss EELS deals with the simultaneous excitation of a number of electrons in the valence band. This excitation is known as a bulk (or volume) plasmon.

Valence loss can be modelled by approximating the electronic structure of the solid to that of a free-electron gas. The effect of the ion lattice is assumed to be relatively minor and is incorporated as an effective mass, m^*, for the electrons and the use of a damping constant Γ. When the incident electron enters the solid, the electrons within the solid are repelled, 'compressing' the electron gas. The electrons within the gas are free to repel one another and so, once the incident electron has moved out of the solid, the electrons begin to move to a lower energy configuration. This causes an oscillation to be set up with a characteristic

frequency known as the plasmon frequency. On emerging from the solid, the incident electron has lost energy. This energy is required to establish the oscillation. The incident electron can be approximated to an oscillatory electric field ($E_0 e^{i\omega t}$) . Using this, and by considering the forces in the system, the following equation modelling the motion of a 'quasi-free' electron within the solid can be obtained.

$$m^* \underline{\ddot{x}} + m^* \Gamma \underline{\dot{x}} = -e\underline{E_0} e^{i\omega t} \qquad \textbf{Equation 2.2}$$

The vector displacement of the electron is then given by:

$$\underline{x} = \frac{e\underline{E_0}}{m^*\left(\omega^2 + i\Gamma\omega\right)} \qquad \textbf{Equation 2.3}$$

This electron displacement gives rise to a polarisation within the solid

$$\underline{P} = -en\underline{x} = \varepsilon_0 \chi \underline{E_0} \qquad \textbf{Equation 2.4}$$

where n is the number of free electrons per unit volume. This equation can be rearranged in order to obtain the electronic susceptibility (χ) which, using the definition of the dielectric function ($\varepsilon(\omega) = 1 + \chi$), gives

$$\varepsilon(\omega) = \varepsilon' + i\varepsilon'' = 1 - \frac{\omega_p^2}{\omega^2 + \Gamma^2} + \frac{i\Gamma\omega_p^2}{\omega\left(\omega^2 + \Gamma^2\right)} \qquad \textbf{Equation 2.5}$$

ω_p is the plasmon frequency where

$$\omega_p = \sqrt{ne^2/\varepsilon_0 m^*}\,. \qquad \textbf{Equation 2.6}$$

However, as previously stated, the data collected within the microscope is related to the energy loss function ($Im[-1/\varepsilon]$).

$$\mathrm{Im}\left(-\frac{1}{\varepsilon(\omega)}\right) = \frac{\varepsilon''}{\varepsilon'^2 + \varepsilon''^2} = \frac{\omega\Gamma\omega_p^2}{\left(\omega^2 - \omega_p^2\right)^2 + \left(\omega\Gamma\right)^2} \qquad \textbf{Equation 2.7}$$

This model, known as the Drude model, enables approximate plasmon energies and loss functions to be calculated for most bulk material systems showing simple plasmon behaviour (such as aluminium and silicon). However, a number of factors are ignored, resulting in poor prediction of loss functions for some materials. In particular, single-electron excitations are largely ignored by this theory. These excitations can have a variety of effects on the loss spectrum.

The most obvious effect is that single-electron transitions will result in additional counts in the loss spectrum. The Drude model predicts that these transitions will occur only at high q. However, momentum can be transferred from the lattice to the atomic electrons, allowing transitions to occur at much lower values of q. In materials with a significant single-electron component (*e.g.* transition metals) fine structure will be observed in the low loss region (Daniels *et al.*, 1970). As the effect of the lattice is reflected in the band structure of the material, for an insulator the fine structure reflects the joint density of states between the valence and conduction bands. (Egerton, 1996).

Single-electron transitions also have additional, more complex, effects on the loss-spectrum. One effect is that the plasmon peak energy is often shifted from that predicted by free electron theory. This can be explained in simplistic terms by considering bound electrons. In semiconductors and insulators not all the electrons are free to take part in plasmon excitation. Many of the electrons are bound in a lower energy state. To make these electrons free to participate in plasmon oscillations they require energy to promote them into the conduction band. The amount of energy required can be approximated to the band gap energy E_g and a modified expression for the plasmon energy results (eqn 2.8).

$$\left(E_p^i\right)^2 \cong E_p^2 + E_g^2 \qquad \textbf{Equation 2.8}$$

Here $E_p=\hbar\omega_p$, using the expression for ω_p given in eqn 2.6.

If the energy loss function is integrated over all energies, the total probability that the incident electron will be inelastically scattered within the sample is obtained. Clearly, once an electron has been scattered once within a sample it is possible that it may be scattered again. For a small number of successive collisions this is known as plural scattering. If the scattering events are assumed to be independent then the scattering probability should follow Poisson statistics. The probability that an electron will undergo a series of n successive collisions is therefore:

$$P_n = \frac{\left(\frac{t}{\lambda}\right)^n e^{-\frac{t}{\lambda}}}{n!} \qquad \textbf{Equation 2.9}$$

Where t/λ is the ratio of the sample thickness to the mean distance between collisions, known as the mean free path. t/λ is equivalent to the mean number of collisions in the

sample. Using the free-electron approximation it is possible to get an expression for the mean free path (Egerton, 1996):

$$\lambda = \frac{2a_0 m_0 v^2}{E_p \ln\left(1 + \beta^2 / \theta_E^2\right)} \qquad \textbf{Equation 2.10}$$

Where a_0 is the Bohr radius, m_0 is the rest mass of an electron and β is a limiting angle. However, this expression tends to overestimate values for many materials. A better approximation can be obtained using scattering theory (Egerton, 1996). An approximate value of λ can be calculated using eqn 2.11.

$$\lambda \approx \frac{106F\left(E_0 / E_m\right)}{\ln\left(2\beta E_0 / E_m\right)} \qquad \textbf{Equation 2.11}$$

In this equation λ is given in nm, β in mrad, the incident energy, E_0, in keV and the mean energy loss, E_m, in eV. F is a relativistic factor defined by eqn 2.12.

$$F = \frac{1 + E_0/1022}{\left(1 + E_0/511\right)^2} \qquad \textbf{Equation 2.12}$$

For an incident energy of 100keV, F=0.768.

The mean energy loss, E_m, can be calculated from an energy loss spectrum of a specimen of known thickness. However, where this is not practical, it can be obtained using an approximate formula (eqn 2.13), assuming the atomic number, Z, is known.

$$E_m \approx 7.6 Z^{0.36} \qquad \textbf{Equation 2.13}$$

For compounds, an effective atomic number must be used (eqn 2.14). This depends on the atomic fraction, f_i, of each element of atomic number Z_i.

$$Z_{eff} = \frac{\sum_i f_i Z_i^{1.3}}{\sum_i f_i Z_i^{0.3}} \qquad \textbf{Equation 2.14}$$

Equation 2.11 is only valid up to a collection angle of ~15mrad at E_0=100keV. However, in the region of validity this equation gives λ values that agree with experimental data to within 15%, over a range of atomic numbers (Crozier, 1990).

With knowledge of λ it becomes possible to determine the thickness of a sample. The sum of all the P_n must be 1 and so we can relate the probabilities to the incident beam intensity,

I, so that $P_n = I_n / I$. If the expressions for the first two P_n are calculated, the following is obtained:

$$P_0 = \frac{I_0}{I} = e^{-\frac{t}{\lambda}} \qquad \textbf{Equation 2.15a}$$

$$P_1 = \frac{I_1}{I} = \frac{t}{\lambda} e^{-\frac{t}{\lambda}} \qquad \textbf{Equation 2.15b}$$

Where I_0 corresponds to the total intensity of the zero loss peak and I_1 corresponds to the intensity (excluding the zero loss peak) of a spectrum where the collected electron have undergone only one scattering event (often referred to as a single-scattered spectrum).

From equations 2.15a & 2.15b, two equations can be formed to give t / λ:

$$\frac{t}{\lambda} = \ln\left(\frac{I}{I_0}\right) \qquad \textbf{Equation 2.16a}$$

$$\frac{t}{\lambda} = \frac{I_1}{I_0} \qquad \textbf{Equation 2.16b}$$

This allows the thickness of sample to be calculated from a full or single-scattered spectrum.

Plural scattering within the sample is often undesirable as it can make analysis of the spectrum more difficult. In particular, calculation of the dielectric function (section 2.4.2) requires a single-scattered spectrum. In order to avoid (or at least reduce) plural scattering it is necessary to use a very thin sample. This in itself poses problems, as the signal from the bulk reduces so that the normally negligible surface effects start to become significant. However, it is possible to deconvolute an experimental spectrum to give a single-scattered spectrum.

The experimentally observed zero loss peak $Z(E)$ can be represented thus:

$$Z(E) = I_0 R(E) \qquad \textbf{Equation 2.17}$$

Where $R(E)$ is the instrument response function which allows for the finite resolution of the experimental spectrum. A single-scattered spectrum $S(E)$ has the relation:

$$\int S(E)dE = I_1 = I\left(t/\lambda\right)e^{-t/\lambda} = I_0\left(t/\lambda\right) \qquad \textbf{Equation 2.18}$$

and the corresponding experimental spectrum is represented as:

$$J_1(E) = R(E) * S(E) \qquad \textbf{Equation 2.19}$$

Where * represents a convolution over energy loss. It can be seen that a double-scattered spectrum is given by

$$D(E) = \frac{S(E) * S(E)}{2! I_0} \qquad \textbf{Equation 2.20}$$

The denominator arises from eqn 2.9. As observed experimentally, the double-scattering is

$$J_2(E) = R(E) * D(E) = \frac{R(E) * S(E) * S(E)}{2! I_0} \qquad \textbf{Equation 2.21}$$

This argument can be continued for triple-scattering and so on. Eventually the observed spectrum, as recorded, can be seen to take the following form:

$$\begin{aligned} J(E) &= Z(E) + J_1(E) + J_2(E) + J_3(E) + \ldots \\ &= R(E) * [I_0 \delta(E) + S(E) + D(E) + \ldots] \\ &= Z(E) * \left[\delta(E) + \frac{S(E)}{I_0} + \frac{S(E) * S(E)}{2! I_0^{\,2}} + \ldots \right] \end{aligned} \qquad \textbf{Equation 2.22}$$

where $\delta(E)$ is a unit area delta function. The fourier transform can then be taken to change the convolutions to products. This yields

$$j(\nu) = z(\nu) \left[1 + \frac{s(\nu)}{I_0} + \frac{[s(\nu)]^2}{2! I_0^{\,2}} + \cdots \right] \qquad \textbf{Equation 2.23}$$

where the lowercase character indicates the fourier transform of its uppercase counterpart. Eqn 2.23 is equivalent to the Taylor series expansion for $exp[s(\nu)/I_0]$. Taking logarithms of both sides and rearranging gives:

$$s(\nu) = I_0 \ln \left[\frac{j(\nu)}{z(\nu)} \right] \qquad \textbf{Equation 2.24}$$

Hence from the experimentally measured spectrum and zero loss it is possible to determine the single-scattered spectrum. This technique is known as fourier-log deconvolution.

The single-scattering distribution can be related to the dielectric constant as:

$$S(E) = \frac{I_0 t}{\pi a_0 m_0 v^2} \mathrm{Im} \left[\frac{-1}{\varepsilon(E)} \right] \ln \left[1 + \left(\frac{\beta}{\theta_E} \right)^2 \right] \qquad \textbf{Equation 2.25}$$

2.2 Energy Loss at a Single Interface

The derivation of the loss probability has been presented elsewhere by other workers (*e.g.* Garcia-Molina *et al.* 1985; Wang, 1996; Bolton and Chen, 1995). However, it is included for completeness and the derivation is of use in the understanding of later chapters. The initial theory is relativistic, though a simpler non-relativistic expression is given in section 2.2.1, which is sufficient for this work.

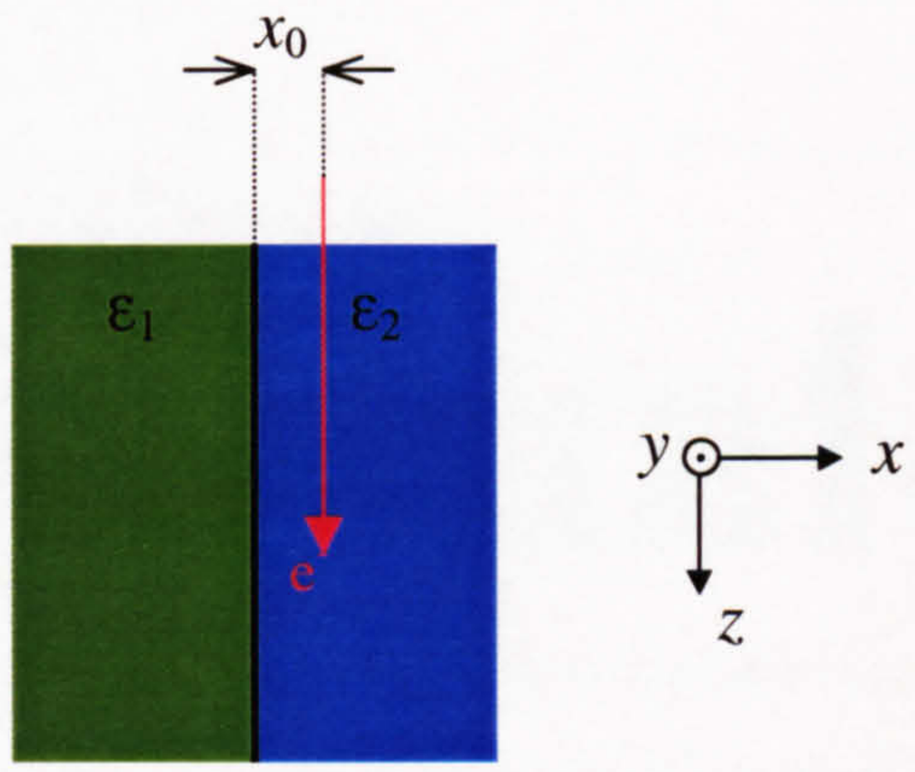

Figure 2.2 Geometry of electron beam with respect to the interface

The derivation will be presented here in terms of the Hertz vector $\Pi(r,t)$ (Walls, 1987). This is related to the standard electromagnetic potentials ϕ and $\boldsymbol{A}$ by

$$\phi = -\nabla.\Pi \qquad \mathbf{A} = \left(\frac{\mu\varepsilon}{c^2}\right)\frac{\partial \mathbf{\Pi}}{\partial t}$$

Where μ is the relative permeability, which will be taken as 1. The electric and magnetic fields are then given by

$$E = \nabla(\nabla.\Pi) - \left(\frac{\mu\varepsilon}{c^2}\right)\frac{\partial^2\Pi}{\partial t^2} \qquad E = -\nabla\phi - \frac{\partial A}{\partial t}$$

c.f.

$$H = \left(\frac{\varepsilon}{c^2}\right)\nabla\times\frac{\partial\Pi}{\partial t} \qquad H = \left(\frac{1}{\mu}\right)\nabla\times A$$

The Hertz vector may be Fourier transformed with respect to time:

$$\Pi(r,\omega) = \left(1/2\pi\right)\int e^{i\omega t}\Pi(r,t)dt$$

If the case of an electron moving, with velocity v, parallel to an interface between two materials (Fig. 2.2) is considered, the current density J can be written:

$$J(r,t) = ev\delta(z - vt)\delta(y)\delta(x - x_0)$$

$$\Rightarrow J(r,\omega) = ev\delta(y)\delta(x - x_0)\exp\left(\frac{i\omega z}{v}\right) \qquad \textbf{Equation 2.26}$$

Where z is the direction of motion, x is the direction perpendicular to the interface and x_0 is the perpendicular distance of the electron from the interface.

It can be seen from symmetry that the position in the yz plane is immaterial. Hence we can define $\rho = (0,y,z)$ and $K=(0,k_y,k_z)$. If Π and J are further transformed, the following are obtained:

$$\Pi(K,\omega,x) = \iint e^{-iK\cdot\rho}\Pi(r,\omega)dydz \qquad \textbf{Equation 2.27}$$

$$J(K,\omega,x) = \iint e^{-iK\cdot\rho}J(r,\omega)dydz = \iint e^{-iK\cdot\rho}ev\delta(y)\delta(x - x_0)e^{\frac{iwz}{v}}dydz$$

$$\Rightarrow J(K,\omega,x) = 2\pi ev\delta(x - x_0)\delta(\omega - k_z v) \qquad \textbf{Equation 2.28}$$

It can be shown from symmetry that the Hertz vector can have no y component, hence $\Pi = (\Pi_x,0,\Pi_z)$. From equations 2.27, 2.28 and the wave equation for Π (eqn 2.29):

$$\left(\nabla^2 + \varepsilon\omega^2/c^2\right)\Pi = \left(1/i\omega\varepsilon\varepsilon_0\right)J \qquad \textbf{Equation 2.29}$$

the following is obtained:

Medium 1

$$\left(\frac{d^2}{dx^2} - \alpha_1^2\right)\Pi_z = 0$$

$$\left(\frac{d^2}{dx^2} - \alpha_1\right)\Pi_x = 0$$

(no current in medium 1)

Medium 2

$$\left(\frac{d^2}{dx^2} - \alpha_2^2\right)\Pi_z = \frac{2\pi ev}{iw\varepsilon_2\varepsilon_0}\delta(\omega - k_z v)\delta(x - x_0)$$

$$\left(\frac{d^2}{dx^2} - \alpha_2^2\right)\Pi_x = 0$$

(current parallel to electron motion)

Where $\alpha_i^2 = K^2 - \varepsilon_i\omega^2/c^2$.

The non-diverging solutions are:

Medium 1

$$\Pi_z = Ce^{\alpha_1 x}$$

$$\Pi_x = De^{\alpha_1 x}$$

Medium 2

$$\Pi_z = \left[\frac{-2\pi e\mathrm{v}}{i\omega\varepsilon_2\varepsilon_0\alpha_2}\delta(\omega - k_z\mathrm{v})e^{-\alpha_2 x_0}\right]e^{\alpha_2(x_0 - |x - x_0|)} + Ae^{-\alpha_2 x}$$

$$\Pi_x = Be^{-\alpha_2 x}$$

Both α_1 and α_2 have a positive real part causing the above equations to be bounded at large x. The constants in the above equations are calculated by using the standard boundary conditions of E and H at the interface (*i.e.* at x=0). This yields:

$$A = \Lambda\frac{\alpha_2 - \alpha_1}{\alpha_1 + \alpha_2}$$

$$B = \frac{2ik_z\alpha_2\Lambda(\varepsilon_1 - \varepsilon_2)}{(\alpha_1 + \alpha_2)(\alpha_1\varepsilon_2 + \alpha_2\varepsilon_1)}$$

The values of C and D are not required for the following calculations and so are not given.

In the above equations the value of Λ is given by:

$$\Lambda = \frac{-2\pi e\mathrm{v}}{i\omega\varepsilon_2\varepsilon_0\alpha_2}\delta(\omega - k_z\mathrm{v})e^{-\alpha_2 x_0}$$

The loss probability can be expressed in terms of a retarding force acting on the incident electron (eqn 2.30).

$$\frac{d^2P}{dzd\omega} = \frac{1}{\hbar\omega}\frac{dF}{d\omega} \qquad \textbf{Equation 2.30}$$

Where F is the force on the electron, which is given by the standard expression for the retarding force on an electron in an electric field (eqn 2.31).

$$F = -eE_z(x_0, 0, \mathrm{v}t, t) = \frac{-e}{(2\pi)^3}\iiint e^{i(k_z\mathrm{v}-\omega)t}E_z(K, \omega, x_0)dk_y dk_z d\omega \qquad \textbf{Equation 2.31}$$

The electric field can be obtained from the expression relating the electric field to the Hertz vector. Hence, after some further calculation, the following form for the loss probability is obtained:

$$\frac{d^2P}{dzd\omega} = \frac{e^2}{2\pi^2\varepsilon_0\hbar v^2}\int_0^{k_y^m} \mathrm{Im}\left[G - \frac{1-\varepsilon_1\left(\frac{v}{c}\right)^2}{\alpha_1\varepsilon_1}\right]dk_y \qquad \textbf{Equation 2.32}$$

Where k_y^m is the upper limit of k_y and is normally determined by the collection aperture. Here:

$$G = \left[\frac{2\alpha_1{}^2(\varepsilon_2-\varepsilon_1)}{\varepsilon_1\alpha_2+\varepsilon_2\alpha_1} + (\alpha_2-\alpha_1)\left(1-\varepsilon_1\left(\frac{v}{c}\right)^2\right)\right]\frac{e^{-2\alpha_1|x_0|}}{\varepsilon_1\alpha_1(\alpha_1+\alpha_2)}$$

This integral can only be calculated numerically and does not simplify further without making use of assumptions. However, this calculation can be greatly simplified by ignoring relativistic effects.

2.2.1 Non-relativistic Expression

If a classical approximation is taken, $v/c \rightarrow 0$, then eqn 2.32 simplifies to give the result for an electron travelling in medium 2 (Howie and Milne , 1985; Walls, 1987):

$$\frac{d^2P}{dzd\omega} = \frac{e^2}{2\pi^2\varepsilon_0\hbar v^2}\left\{\mathrm{Im}\left(\frac{-1}{\varepsilon_2}\right)\left[\ln\frac{k_y^m v}{\omega} - K_0\left(\frac{2\omega x_0}{v}\right)\right] + \mathrm{Im}\left(\frac{-2}{\varepsilon_1+\varepsilon_2}\right)K_0\left(\frac{2\omega x_0}{v}\right)\right\}$$

Equation 2.33

where $K_0(y)$ is the zeroth order Bessel function, which is discussed in Appendix 1. For the case of an electron travelling in medium 1, ε_1 and ε_2 are interchanged.

Eqn 2.33 has two main terms, the bulk plasmon term ($\mathrm{Im}[-1/\varepsilon]$) and the interface plasmon term ($\mathrm{Im}[-2/(\varepsilon_1+\varepsilon_2)]$). The equation shows that the bulk term will increase with distance from the interface whilst the interface term will decrease. In the limit of large x_0 the loss function tends to the bulk plasmon term as would be expected.

As x_0 tends to zero, it would be expected that the bulk term would reduce to zero. For this to be the case the Bessel function would require a limiting value equal to the logarithmic term for small x_0. Using the approximation for small z ($K_0(z) \approx \ln(z)$) it can be see that the two terms are equal for the case where:

$$k_y^m = \frac{1}{2x_0}$$

For x_0 approaching zero, this cannot be true as k_y^m is finite. Further analysis reveals that for a set value of k_y^m the logarithmic and Bessel terms are equal for a small, non-zero value of x_0. This is clearly non-physical and so it can be assumed that there are some problems with the non-relativistic approximation close to the interface. However, for non-zero values the correction is small and so the approximation is of value.

Another useful check on the equation is the case where the electron beam is passing through vacuum close to an interface. In this situation ε_2=1 and so the equation reduces to:

$$\frac{d^2P}{dzd\omega} = \frac{e^2}{2\pi^2\varepsilon_0\hbar v^2}\left\{\mathrm{Im}\left(\frac{-2}{\varepsilon_1+1}\right)K_0\left(\frac{2\omega x_0}{v}\right)\right\} = \frac{e^2}{2\pi^2\varepsilon_0\hbar v^2}\left\{\mathrm{Im}\left(\frac{\varepsilon_1-1}{\varepsilon_1+1}\right)K_0\left(\frac{2\omega x_0}{v}\right)\right\}$$

Which is the expression given in Howie and Milne (1984) for a beam travelling in a vacuum external to a semi-infinite solid. This equation models the behaviour of a 'surface plasmon'.

2.2.2 Comparison of Relativistic and Non-relativistic Expressions

Both relativistic and non-relativistic equations were available for calculating loss functions. Unlike the relativistic equation, the non-relativistic approximation did not require the use of numerical integration. This considerably simplified the calculation of loss functions. However, it was necessary to compare the results from the two equations to examine any deviations between the non-relativistic and the relativistic equations.

The relativistic and non-relativistic expressions were used within *Matlab* (Appendix 3) to generate simulated energy loss data for different distances from the interface in an Al/Mg_2Si system at 100kV(Fig 2.3a-c) and using a k_y^m of $10^{10}m^{-1}$. Examination of the ratio of relativistic/non-relativistic indicates that the correction for 100kV is small. The most significant difference at all distances is at very low energy loss (<4eV). This is due to imperfect removal of the zero loss peak from the original data. As these graphs were calculated from experimental dielectric data, such artefacts were not easily avoided. This occurs at much lower energy than the area of interest and so can be ignored.

x_0=-10nm

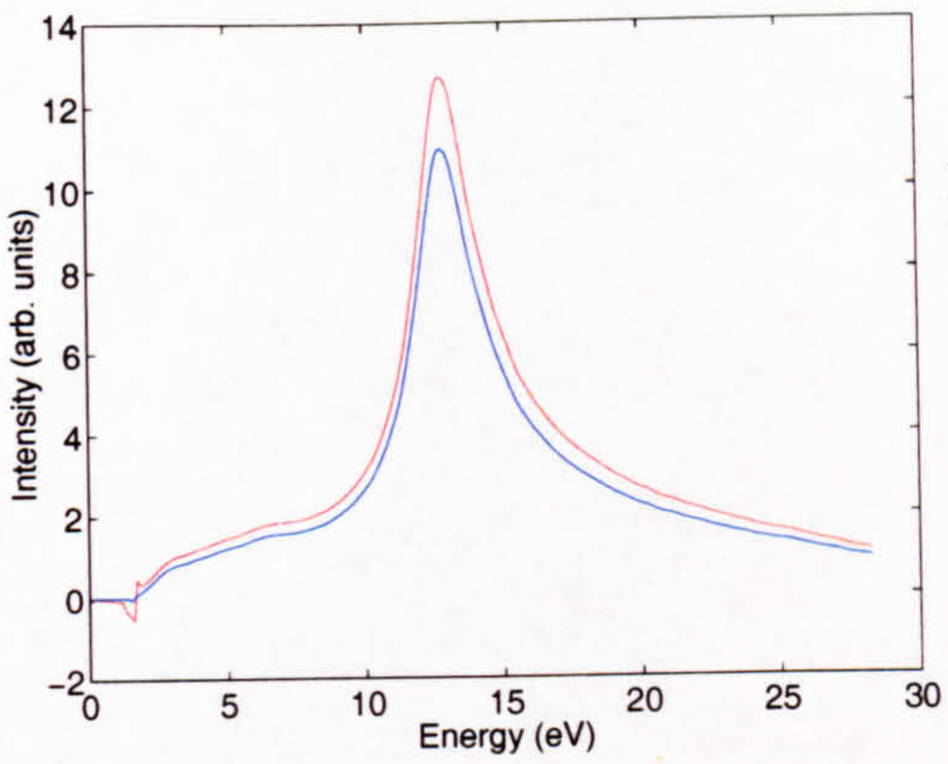

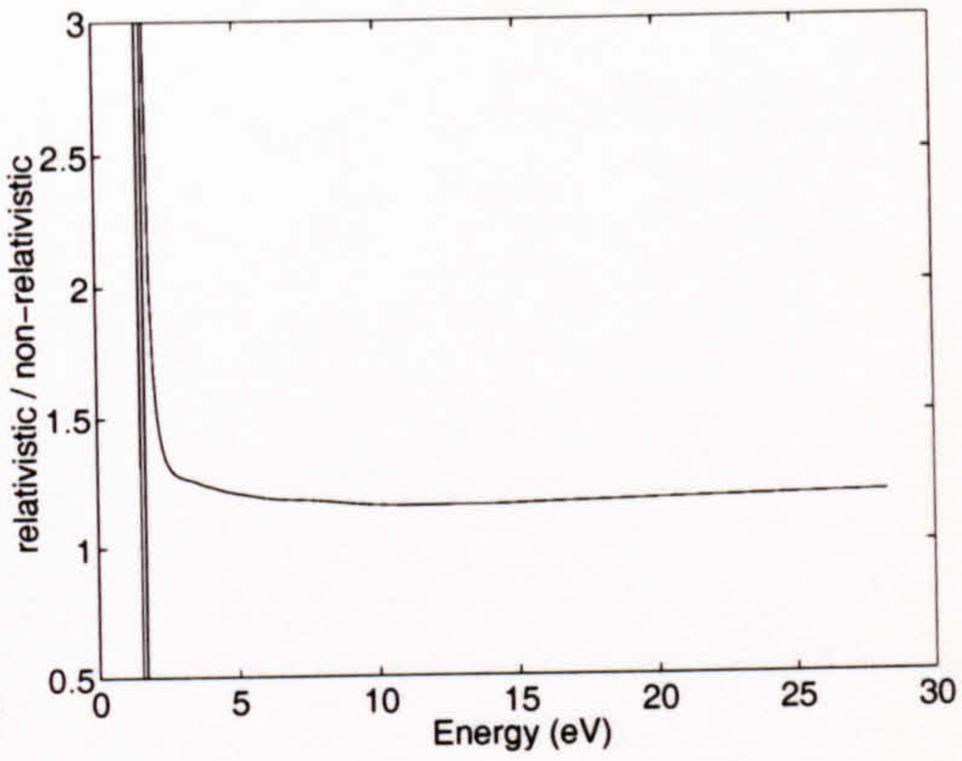

x_0=-2nm

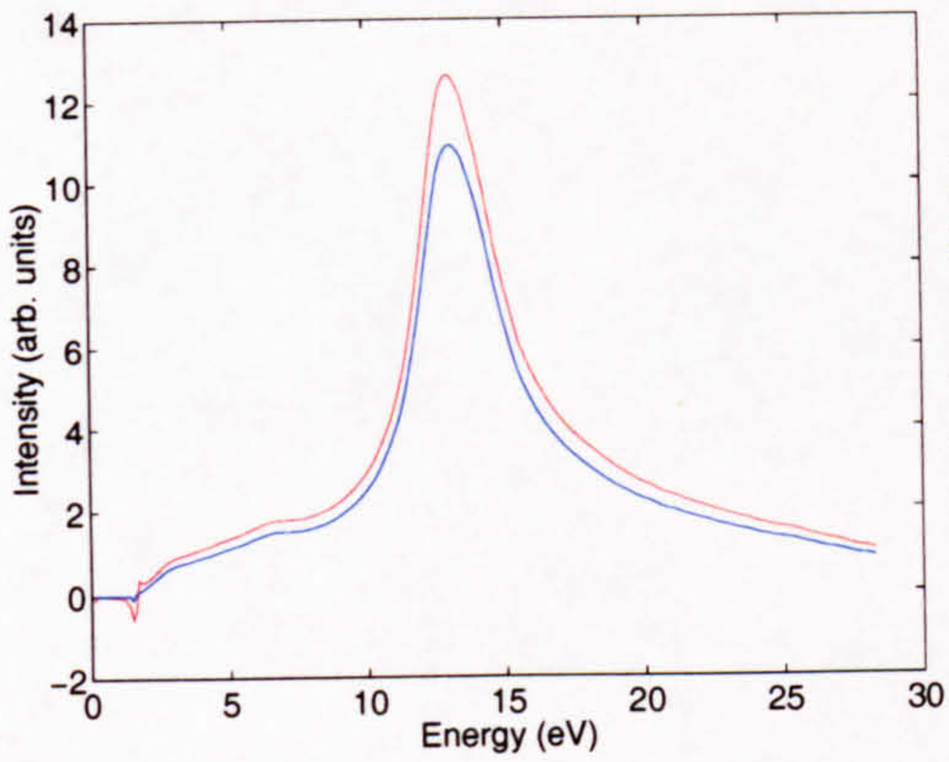

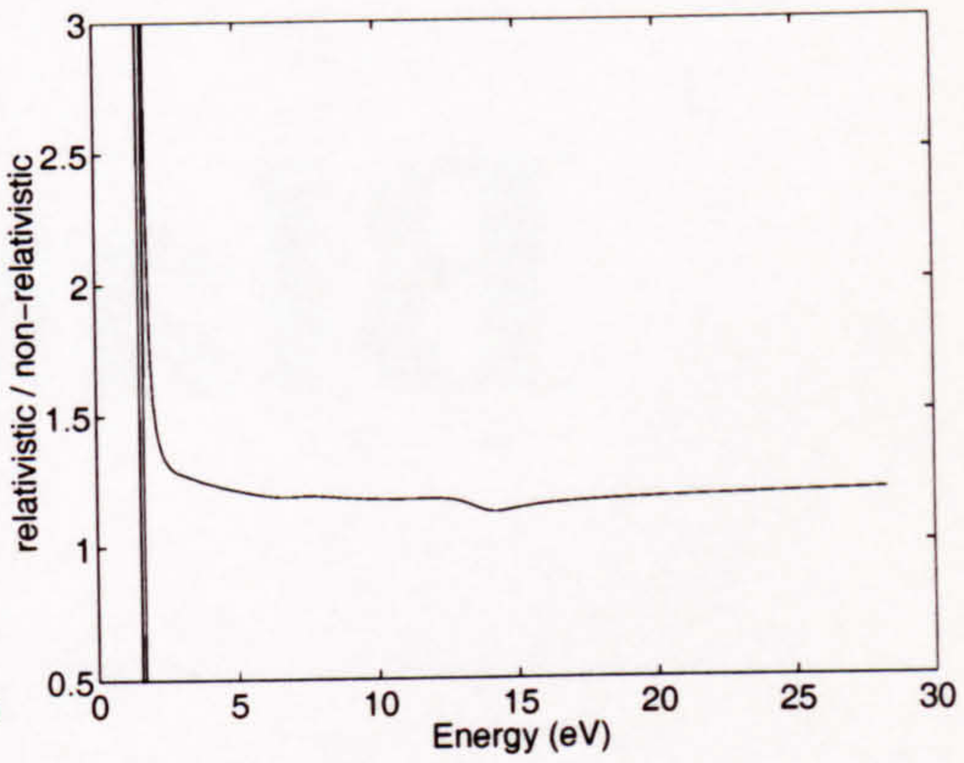

x_0=-0.5nm

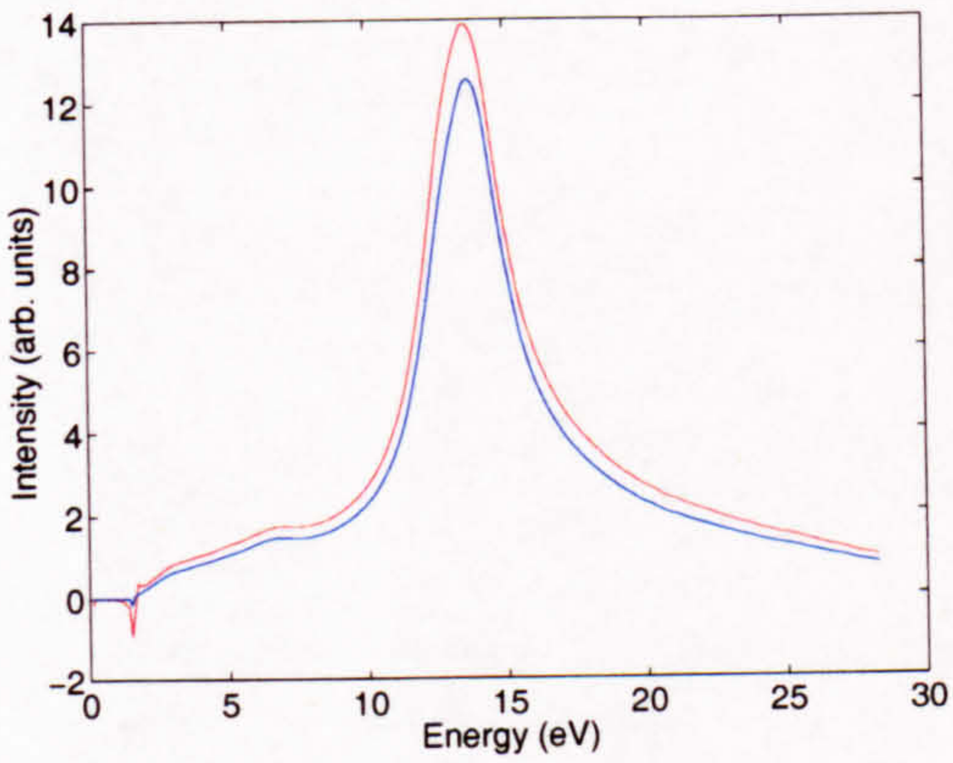

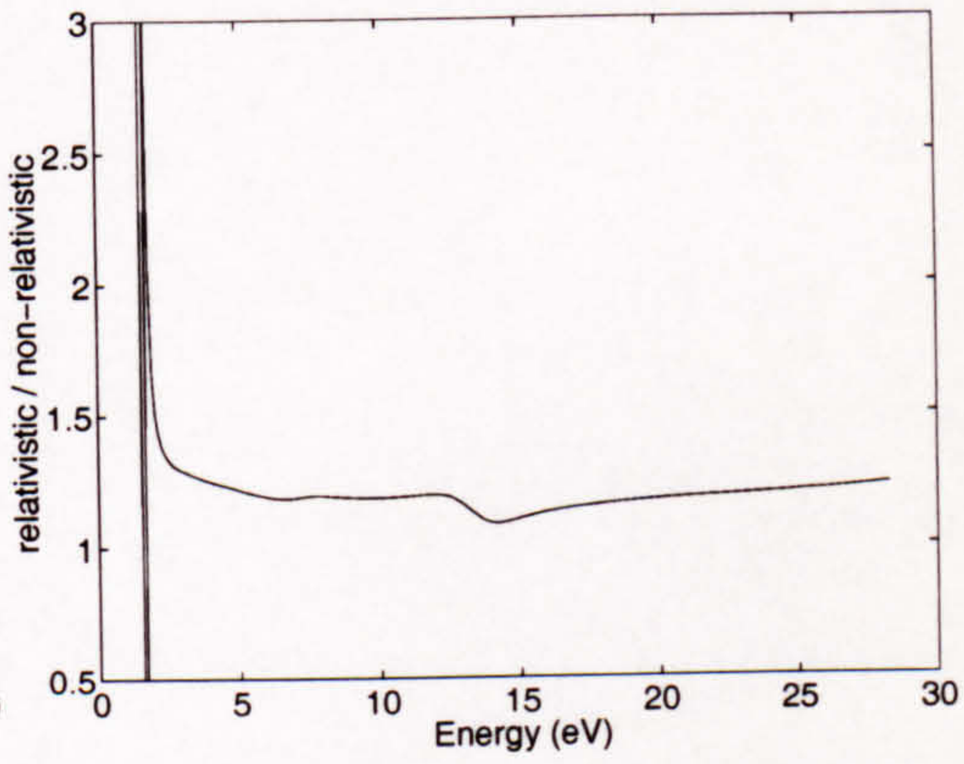

Figure 2.3a: Graphs showing calculated energy loss spectra for an Al/Mg_2Si interface using relativistic (red line) and non-relativistic (blue line) equations (*left*). Included is the ratio of relativistic/non-relativistic loss spectra (*right*). Corresponding x_0 values are given on the far left.

x_0=-0.05nm

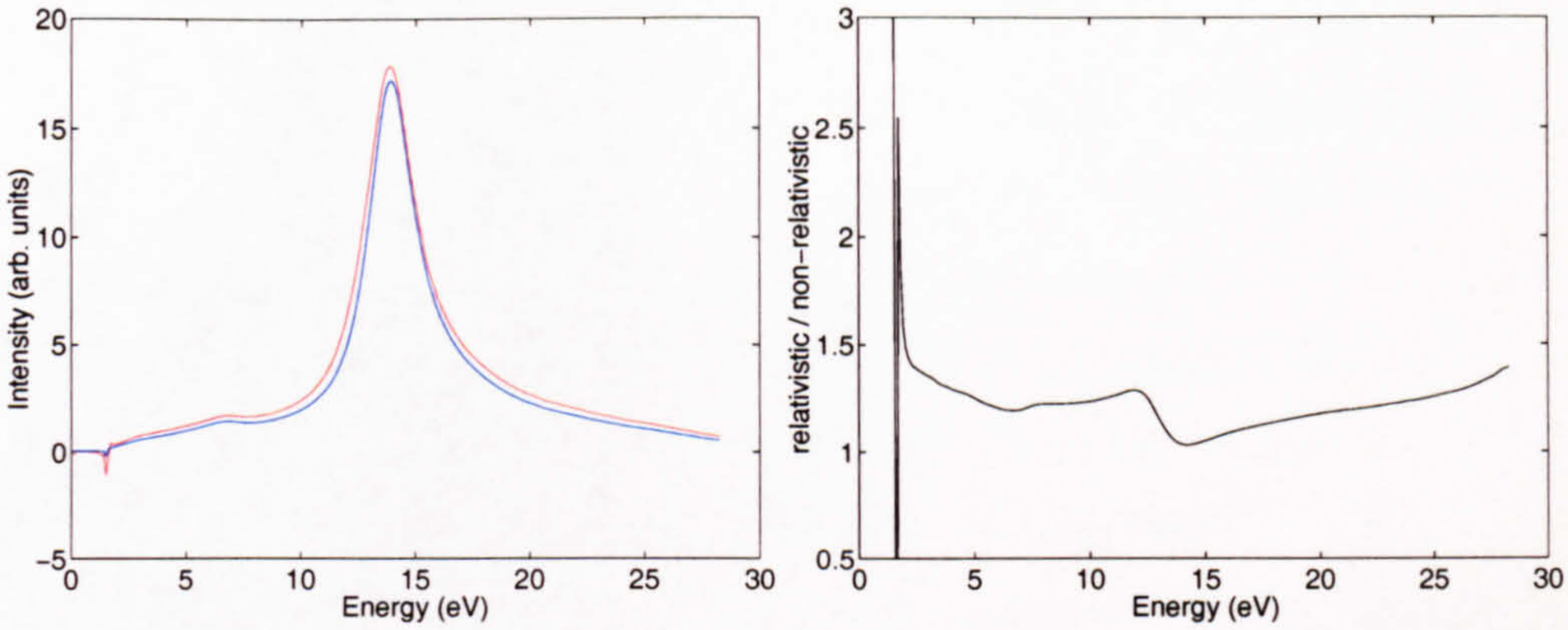

x_0=0nm

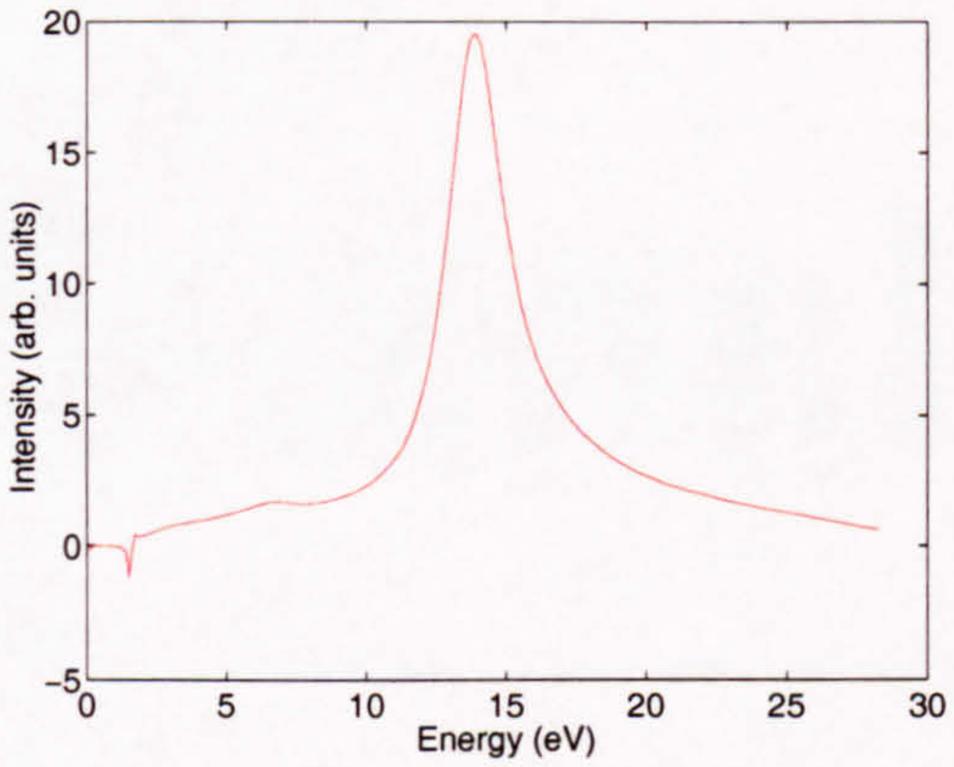

x_0=0.05nm

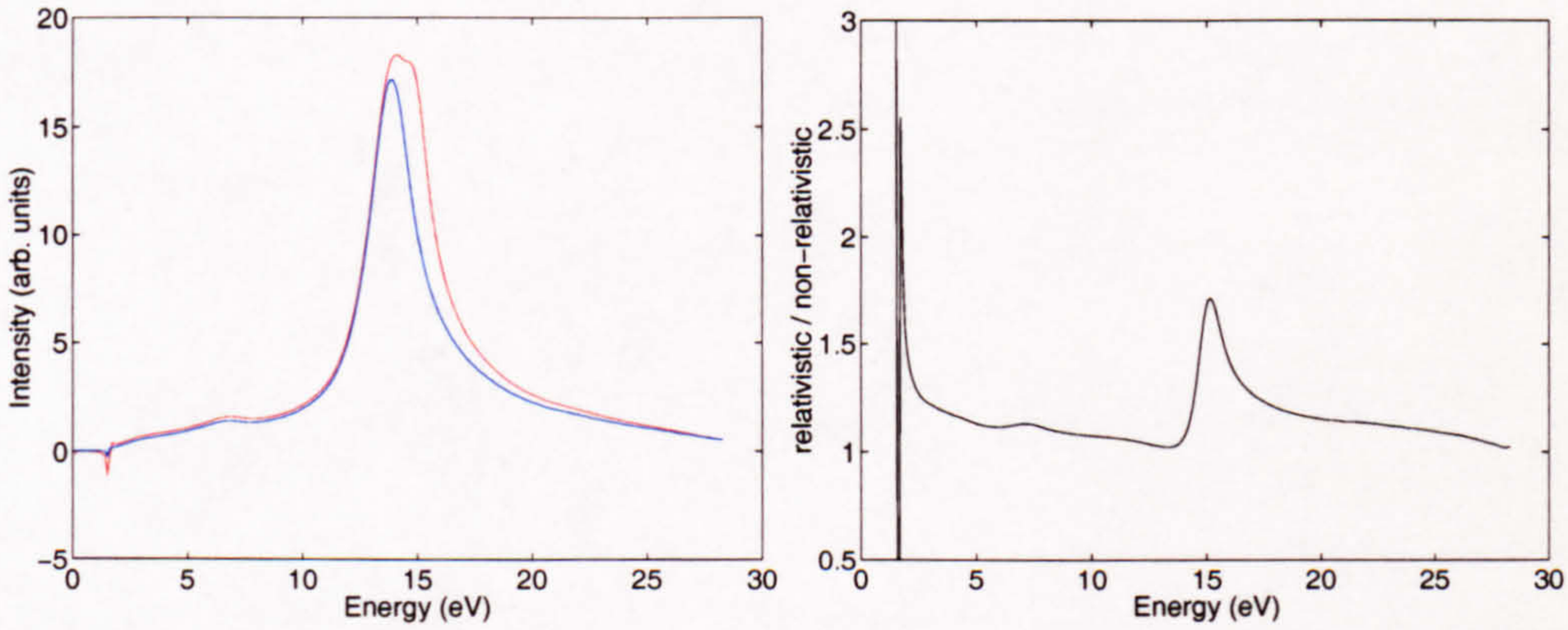

Figure 2.3b: Graphs showing calculated energy loss spectra for an Al/Mg_2Si interface using relativistic (red line) and non-relativistic (blue line) equations (*left*). Included is the ratio of relativistic/non-relativistic loss spectra (*right*). Corresponding x_0 values are given on the far left. Centre graph corresponds to x_0=0 for which the non-relativistic function is undefined.

x_0=0.5nm

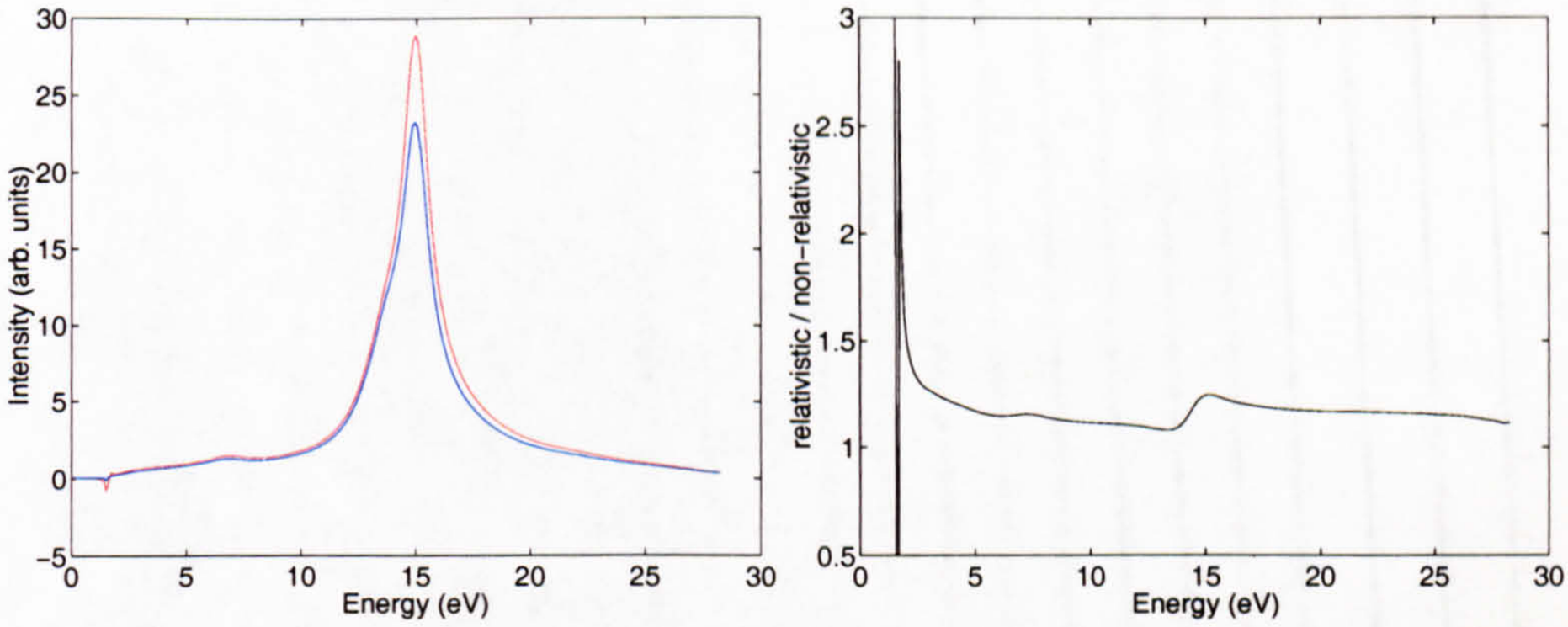

x_0=2nm

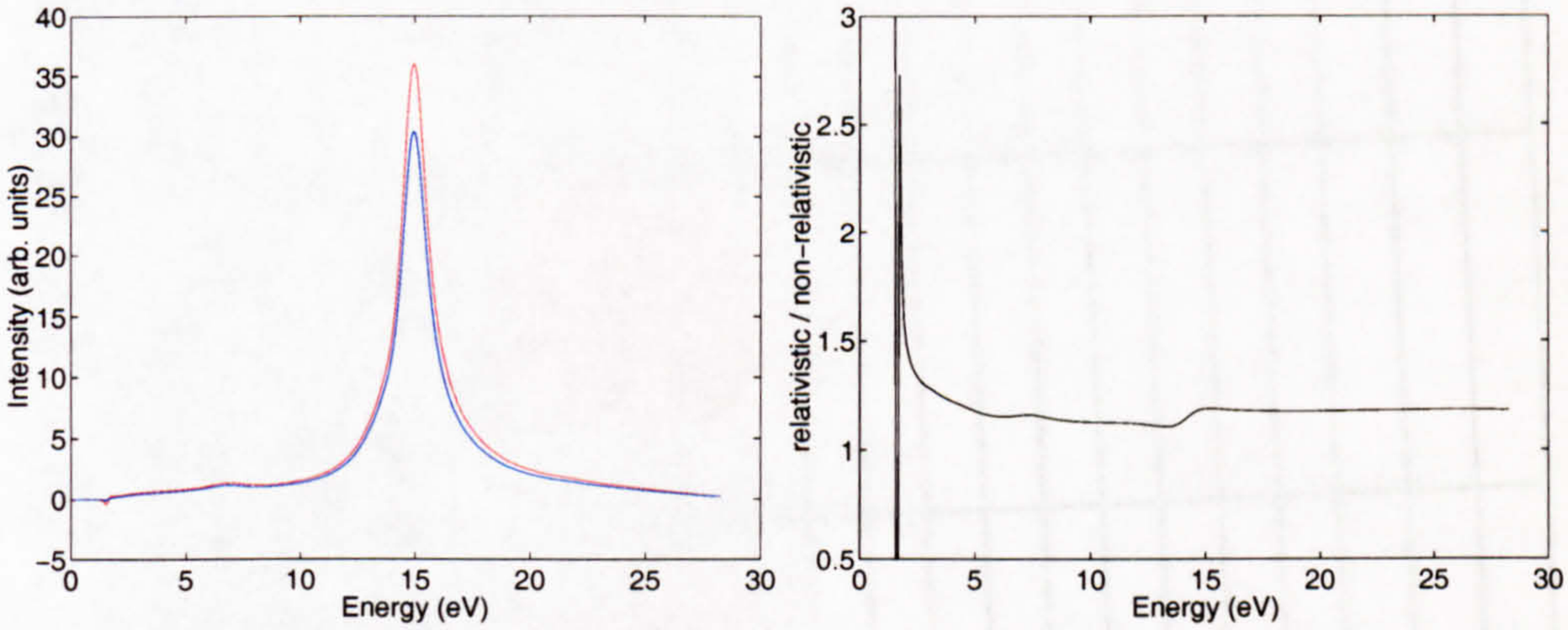

x_0=10nm

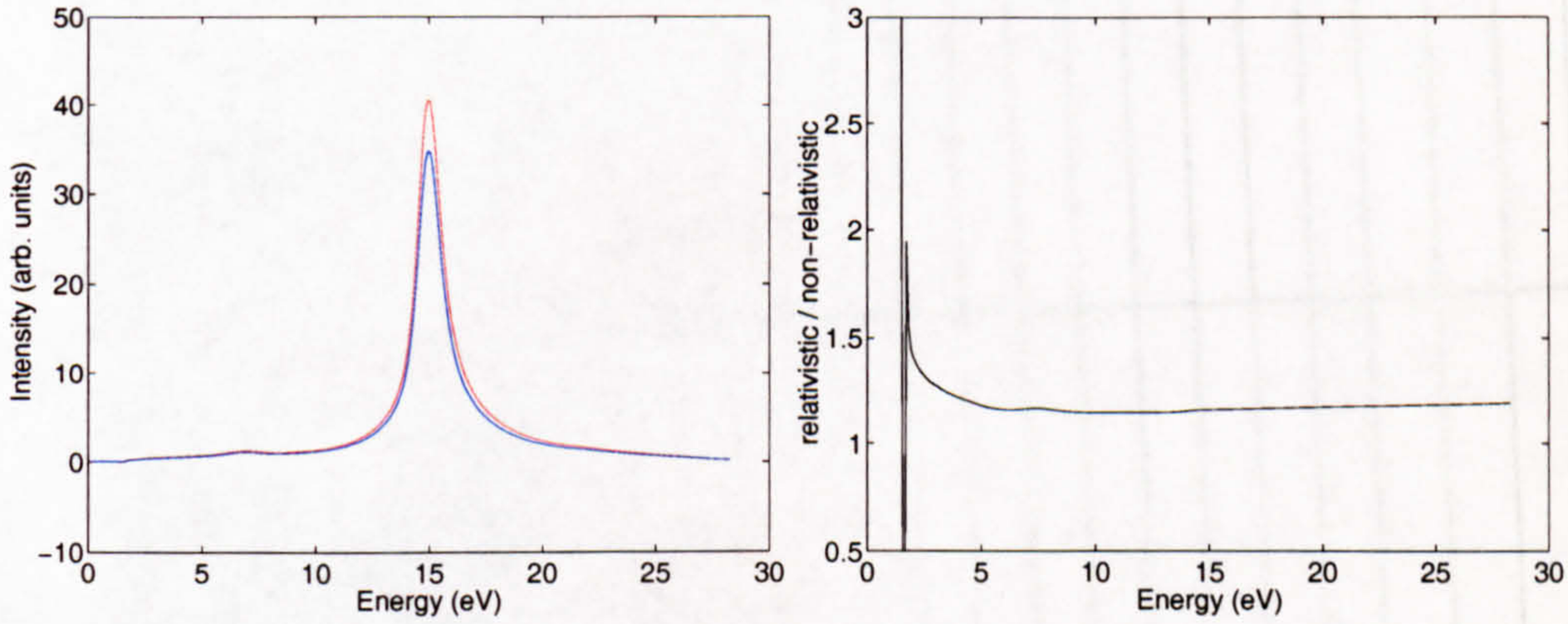

Figure 2.3c: Graphs showing calculated energy loss spectra for an Al/Mg_2Si interface using relativistic (red line) and non-relativistic (blue line) equations (*left*). Included is the ratio of relativistic/non-relativistic loss spectra (*right*). Corresponding x_0 values are given on the far left.

Closer to the interface, the two forms differ more significantly, most noticeably around the energy of the plasmon peak. The graphs in Fig. 2.3b demonstrate the problem with the Bessel function. For the chosen k_y^m a distance of 0.05nm causes the Bessel function to cancel with the log term, effectively removing any bulk contribution. This is shown by the non-relativistic data being identical at 0.05nm on either side of the interface. However, it is not possible to move the electron probe a distance of 0.5Å accurately. In addition, 0.5Å is an order of magnitude smaller than the probe size. Therefore this problem with the non-relativistic term close to the interface is not significant. Further away from the interface the difference is, to a good approximation, just a constant factor. The pre-factors were not included in the calculations as these were not dependent on frequency. It was therefore expected that the relativistic and non-relativistic equations would differ by a constant factor.

Clearly, as the incident beam energy is increased, relativistic effects will become more significant. As some of the data was acquired on the FEI Tecnai microscope, which operates at 200kV, it was of interest to investigate the difference between the relativistic and non-relativistic equations for an accelerating voltage of 200kV. Fig 2.4 gives the simulated ratios for small distances away from an Al/Mg_2Si interface. The value of k_y^m used was $10^{10}m^{-1}$. Once again the ratio of relativistic to non-relativistic is fairly constant, with the largest deviations not noticeably increased from the 100kV case. A much greater difference is apparent at lower energies, up to 10eV, compared with 100kV. However, these differences are still comparatively small and are below the energy of interest. These results indicate that the non-relativistic equation is still valid at 200kV.

The equations were also used to calculate energy loss spectra at various distances from an Al/Si interface (Fig. 2.5a-c). From these spectra the corresponding relativistic/non-relativistic ratio was determined. As with the Al/Mg_2Si system the ratio was effectively constant at larger distances from the interface with greater deviation occurring as the interface was approached. At very small distance from the interface, the deviation was larger than for the same distance in the Al/Mg_2Si system. Despite this, the difference was not large enough to make the non-relativistic approximation invalid.

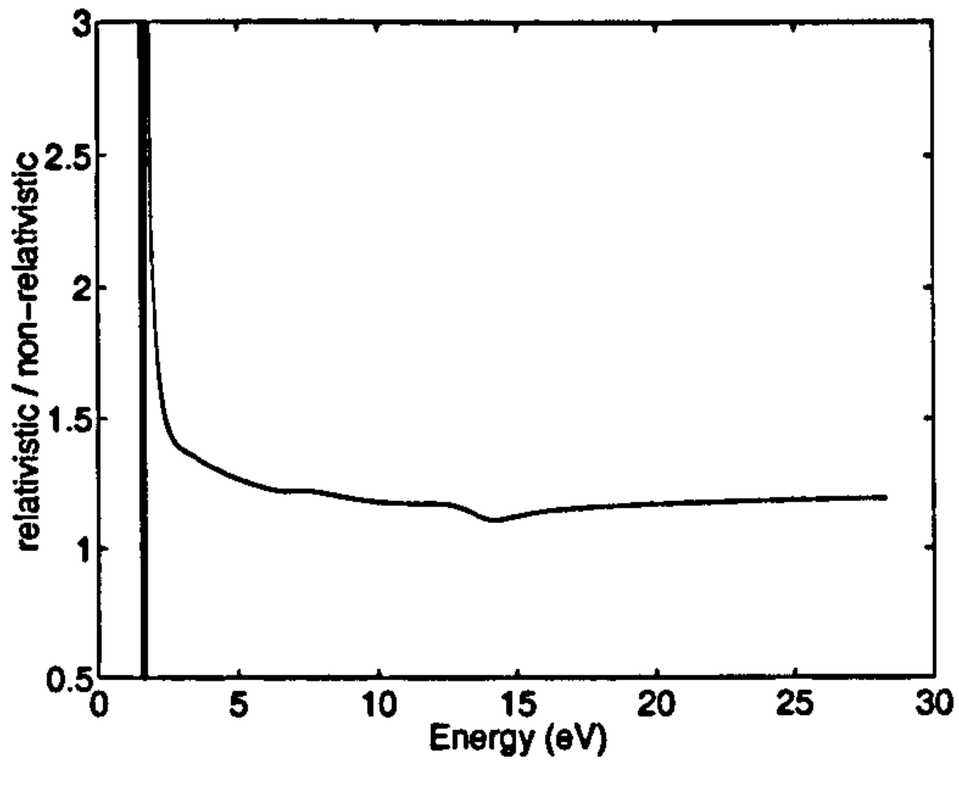

x_0=-2nm

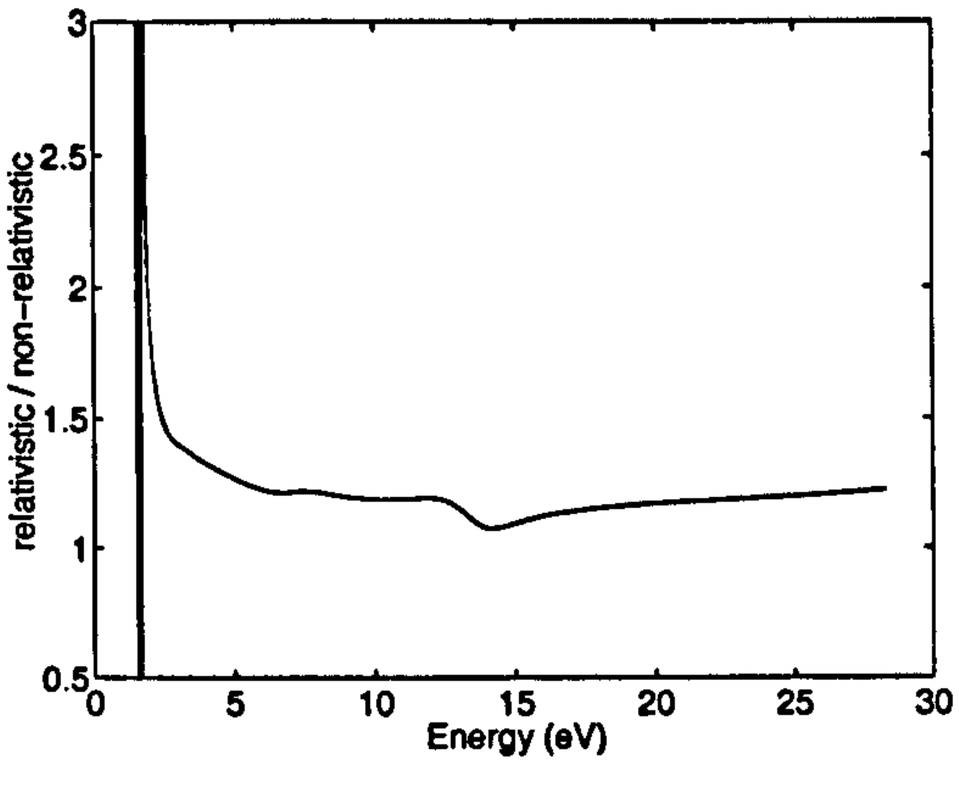

x_0=-0.5nm

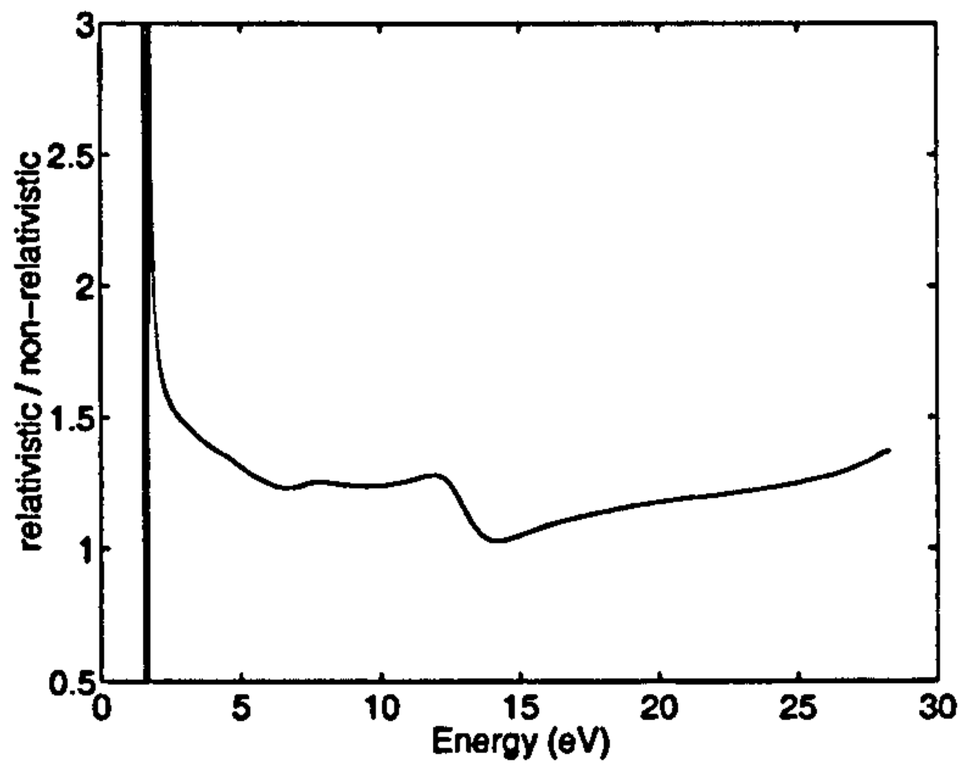

x_0=-0.05nm

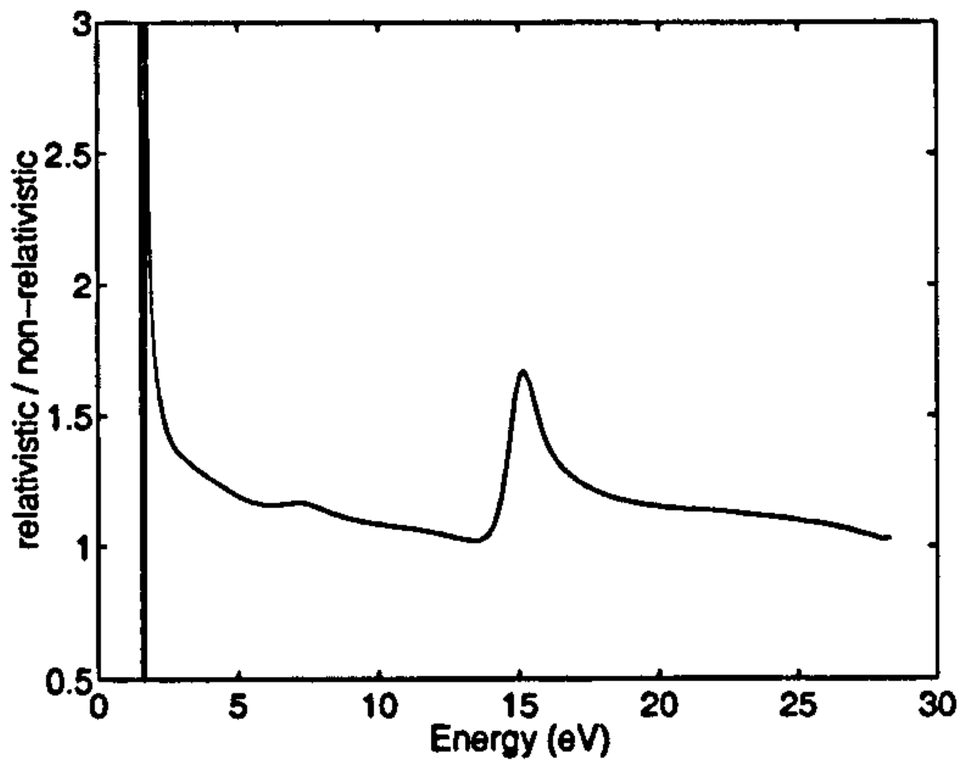

x_0=0.05nm

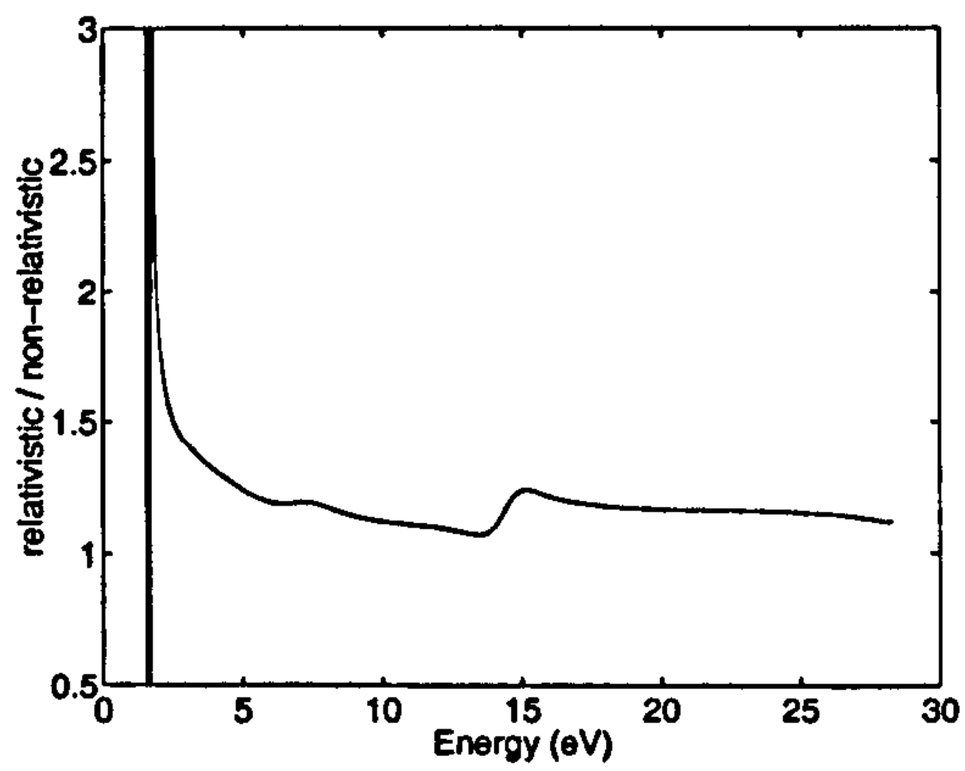

x_0=0.5nm

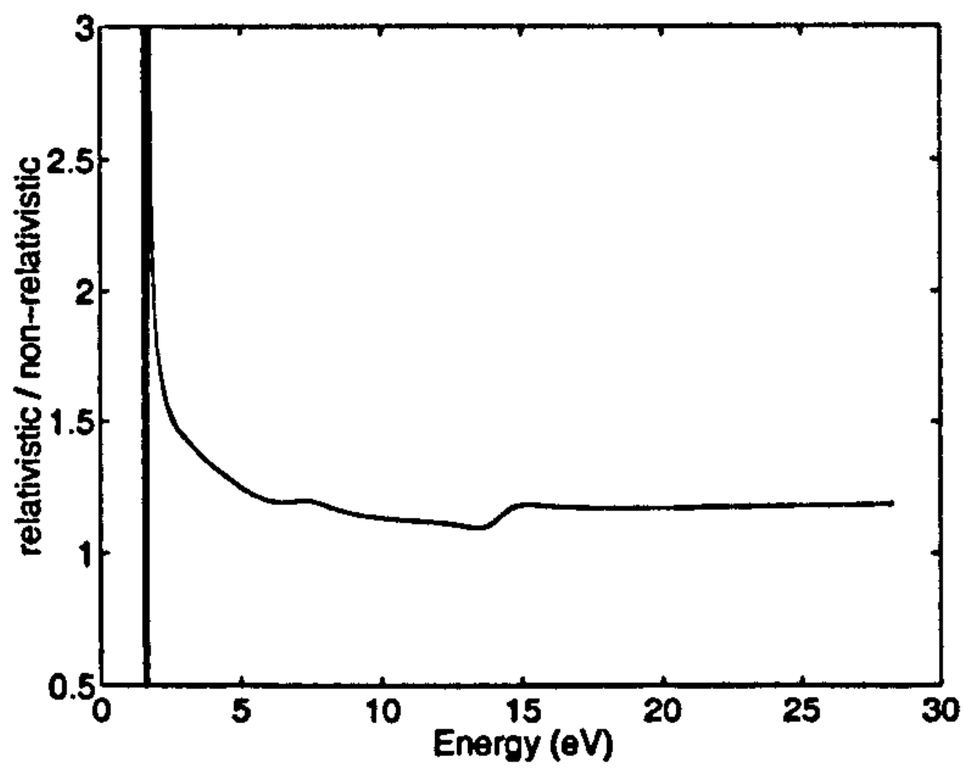

x_0=2nm

Figure 2.4: Graphs showing ratio of relativistic / non-relativistic loss spectra for an accelerating voltage of 200kV. Corresponding x_0 values are given beneath each graph.

x_0=-10nm

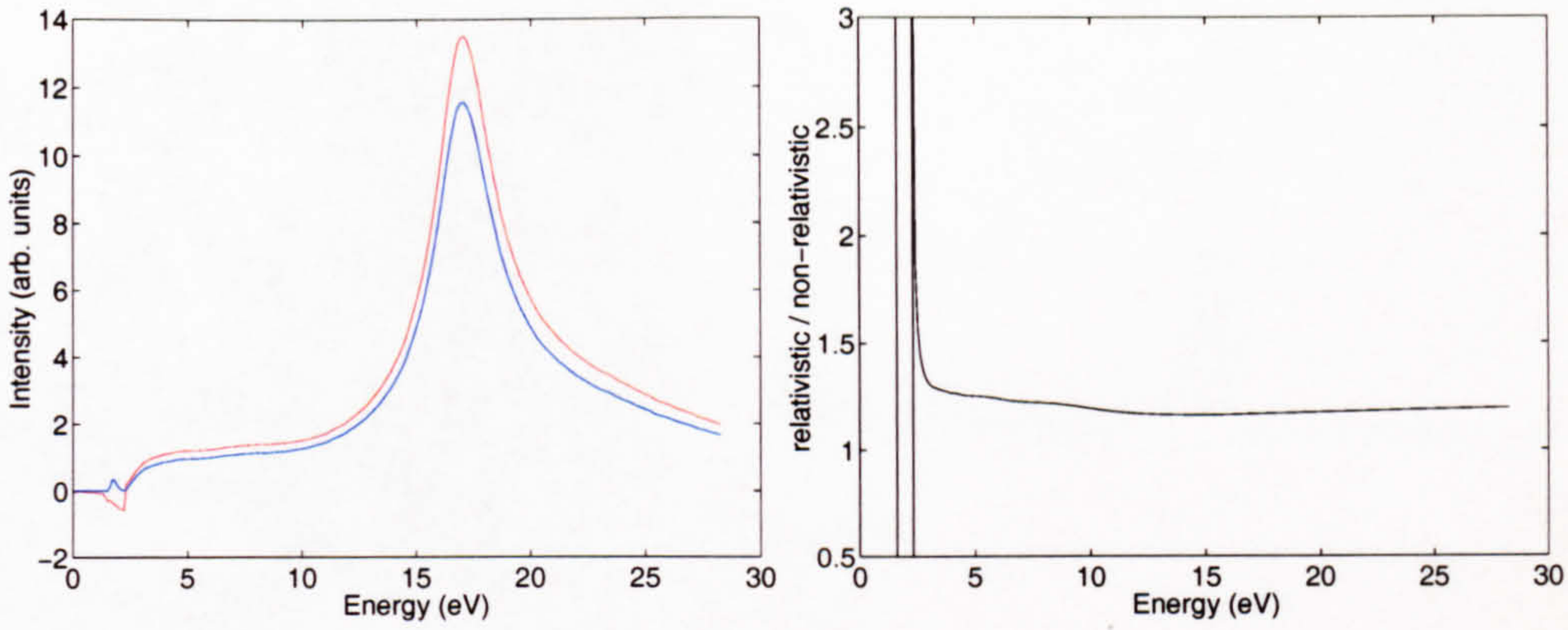

x_0=-2nm

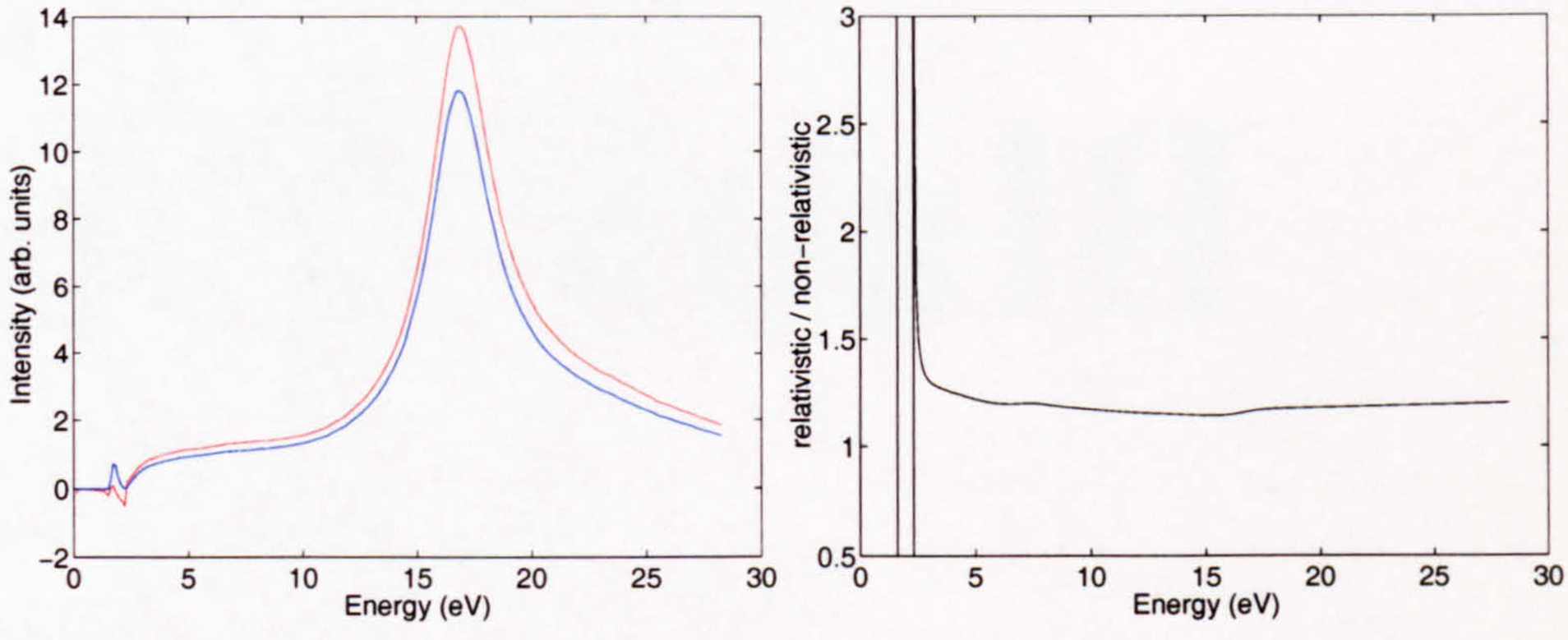

x_0=-0.5nm

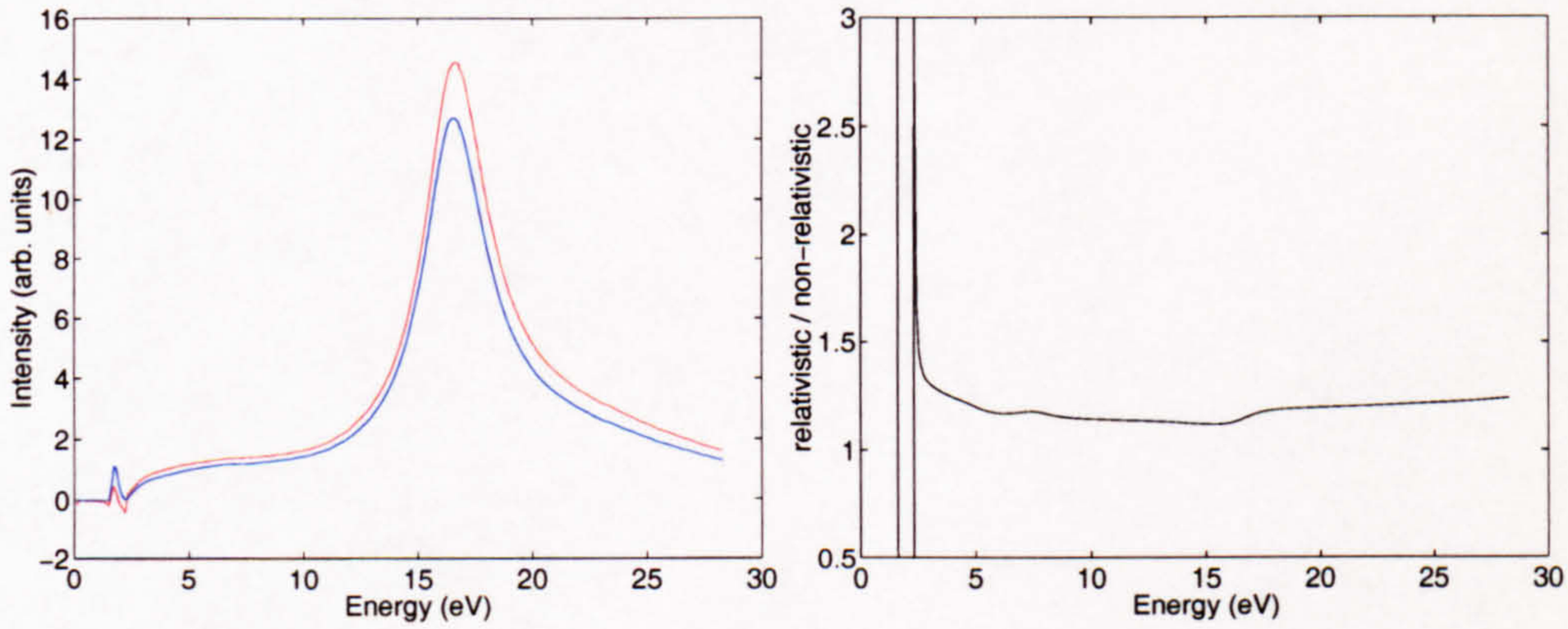

Figure 2.5a: Graphs showing calculated energy loss spectra for an Al/Si interface using relativistic (red line) and non-relativistic (blue line) equations (*left*). Included is the ratio of relativistic/non-relativistic loss spectra (*right*). Corresponding x_0 values are given on the far left.

x_0=-0.05nm

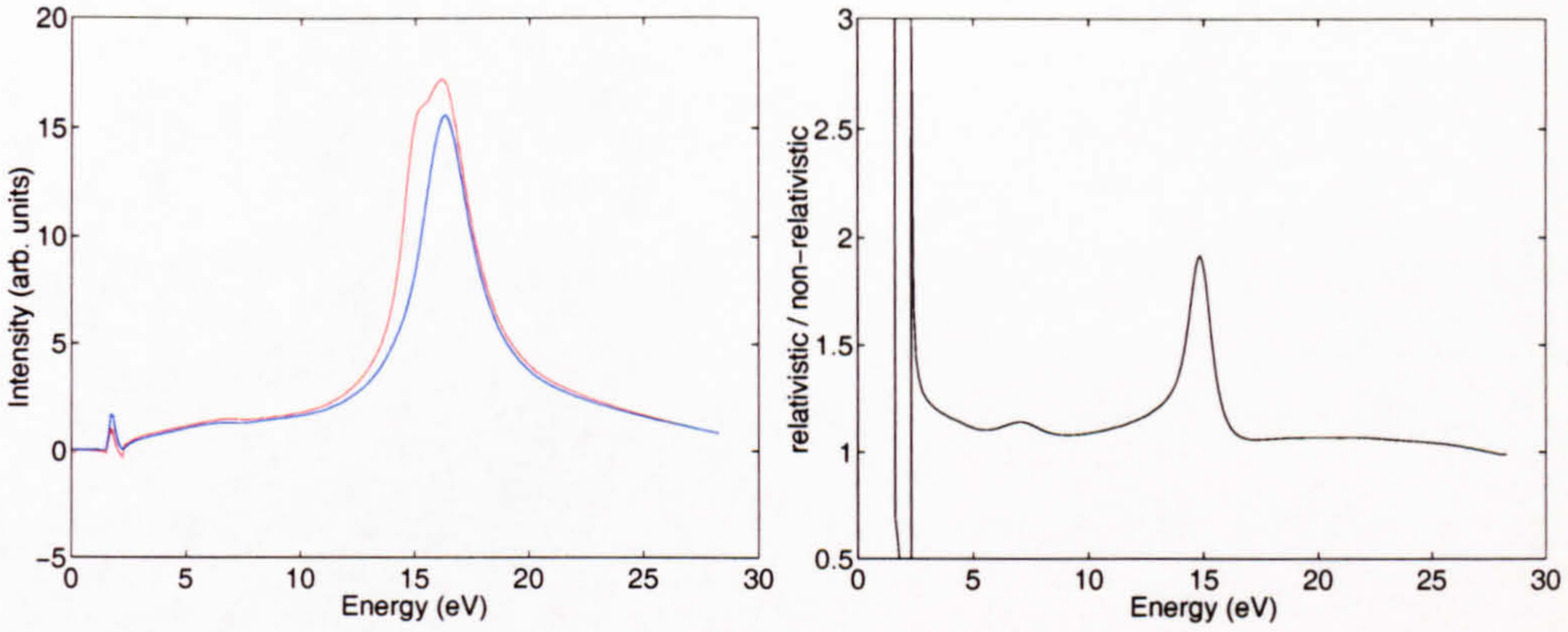

x_0=0nm

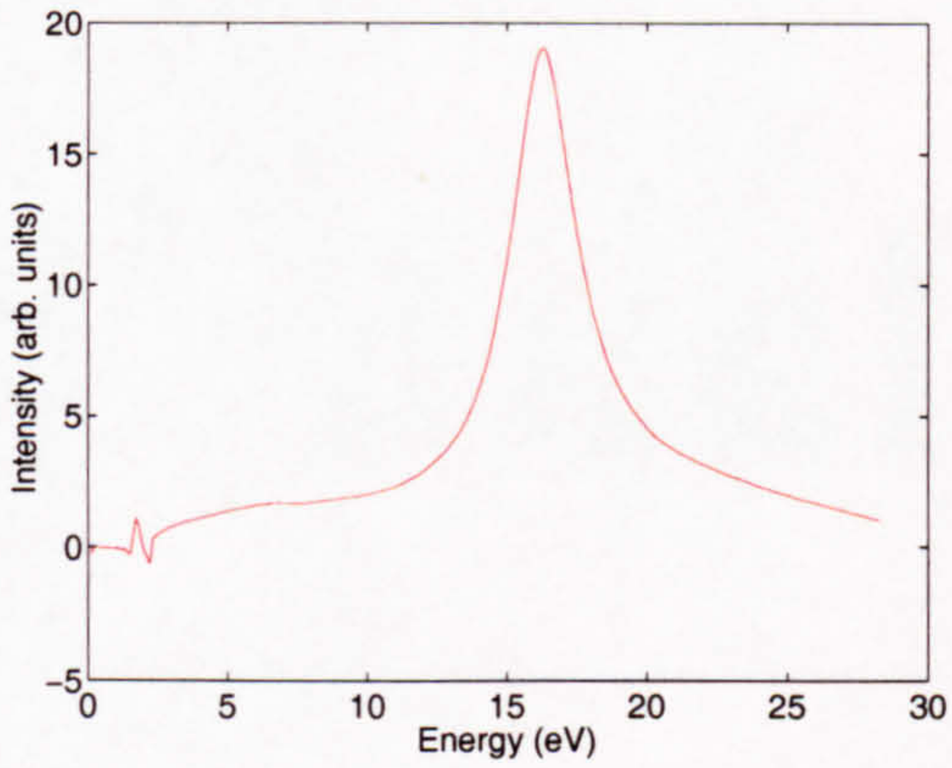

x_0=0.05nm

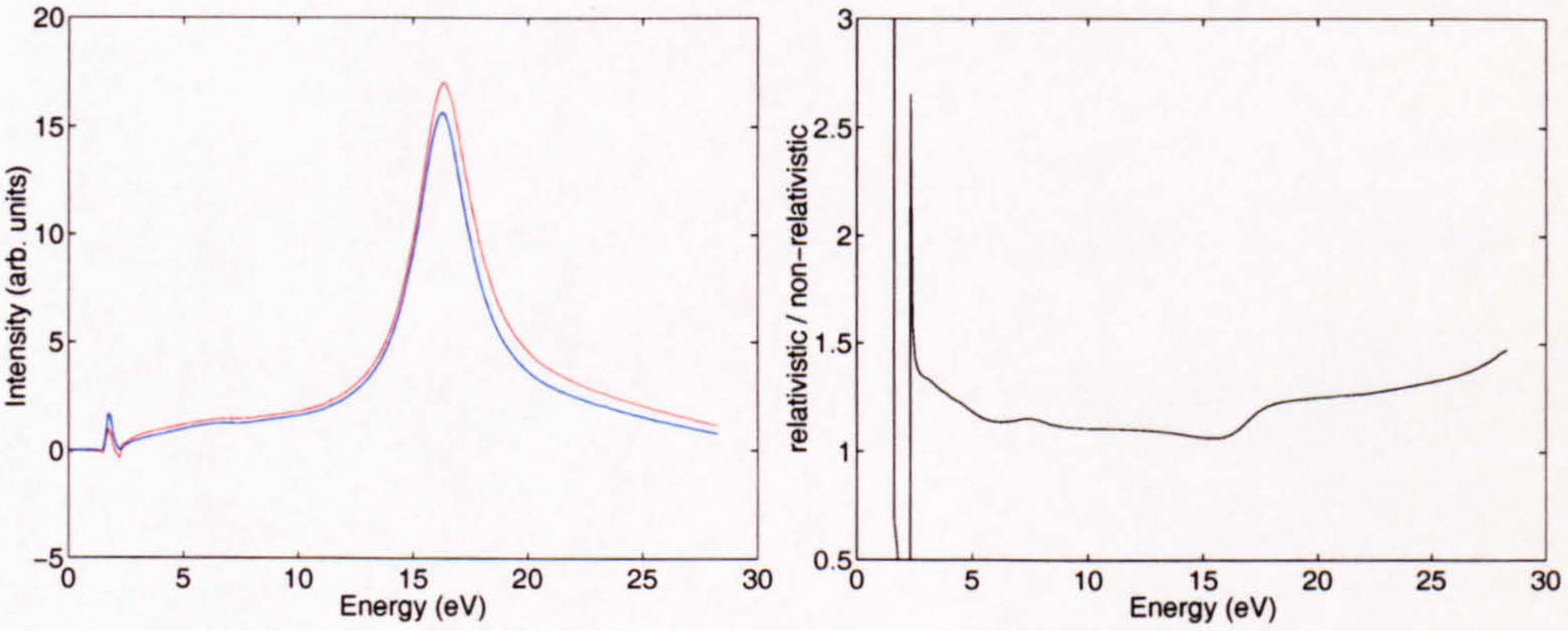

Figure 2.5b: Graphs showing calculated energy loss spectra for an Al/Si interface using relativistic (red line) and non-relativistic (blue line) equations (*left*). The ratio of relativistic/non-relativistic loss spectra (*right*) is also shown. Corresponding x_0 values are given on the far left. Centre graph corresponds to x_0=0 for which the non-relativistic function is undefined.

x_0=0.5nm

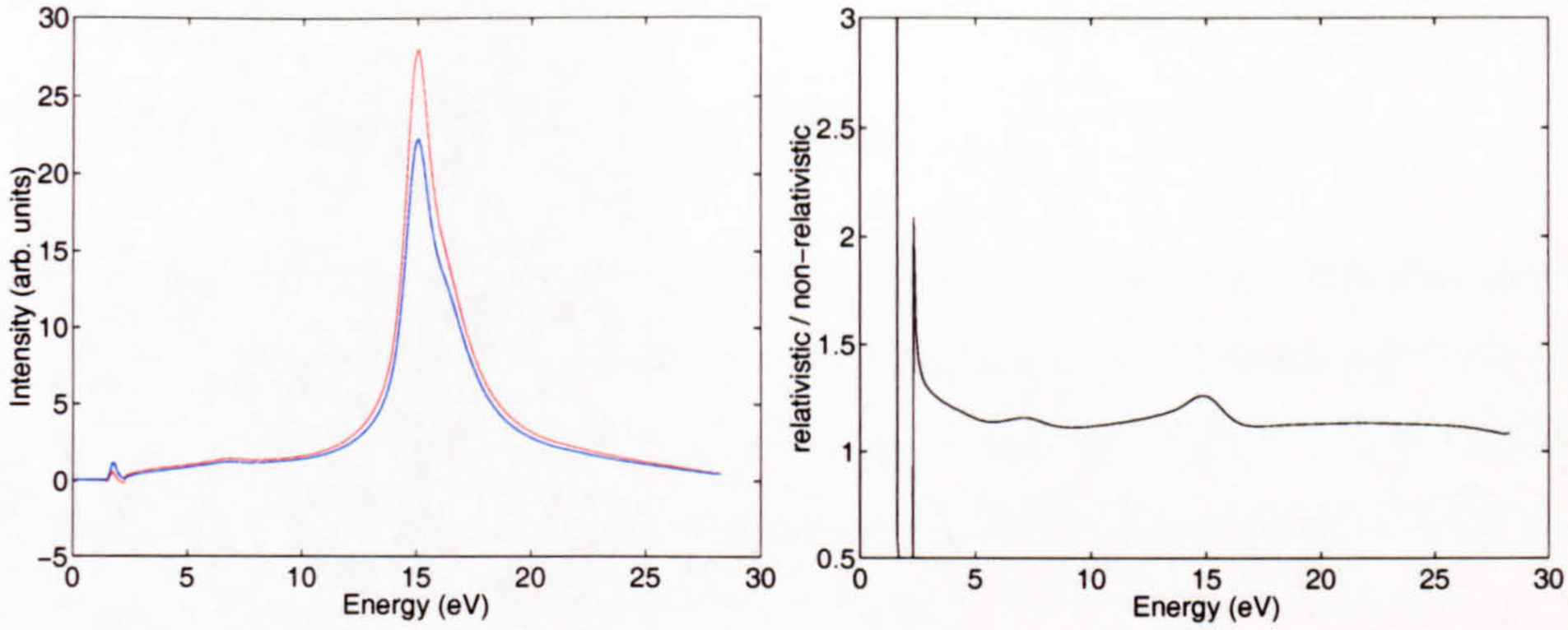

x_0=2nm

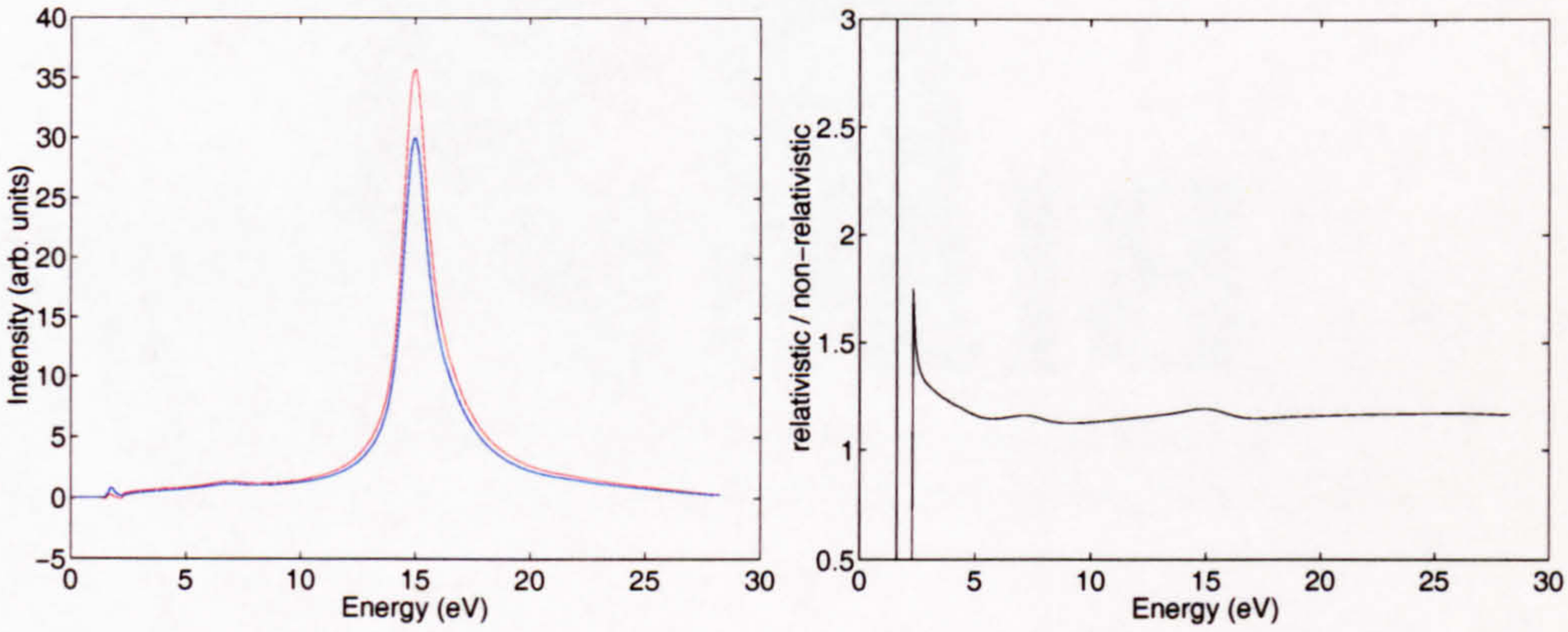

x_0=10nm

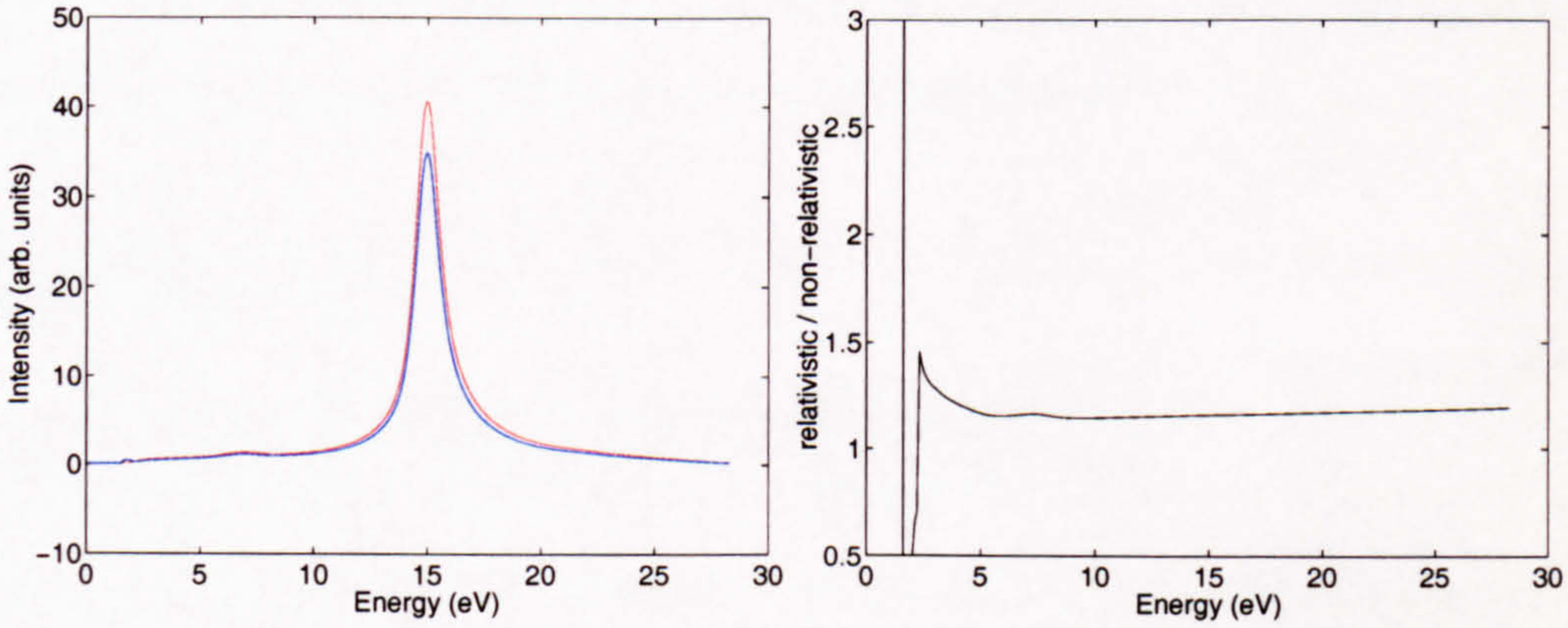

Figure 2.5c: Graphs showing calculated energy loss spectra for an Al/Si interface using relativistic (red line) and non-relativistic (blue line) equations (*left*). The ratio of relativistic/non-relativistic loss spectra is also shown (*right*). Corresponding x_0 values are given on the far left.

2.3 Energy Loss at a Double Interface

The natural extension to the single interface case is the double interface. This has more practical use than the single layer as it enables information to be determined from an interface where a thin interfacial phase, of the type described in chapter 1, has formed between the bulk materials. Fig 2.6 shows the geometry of such an interface with the electron beam travelling externally to the interfacial phase.

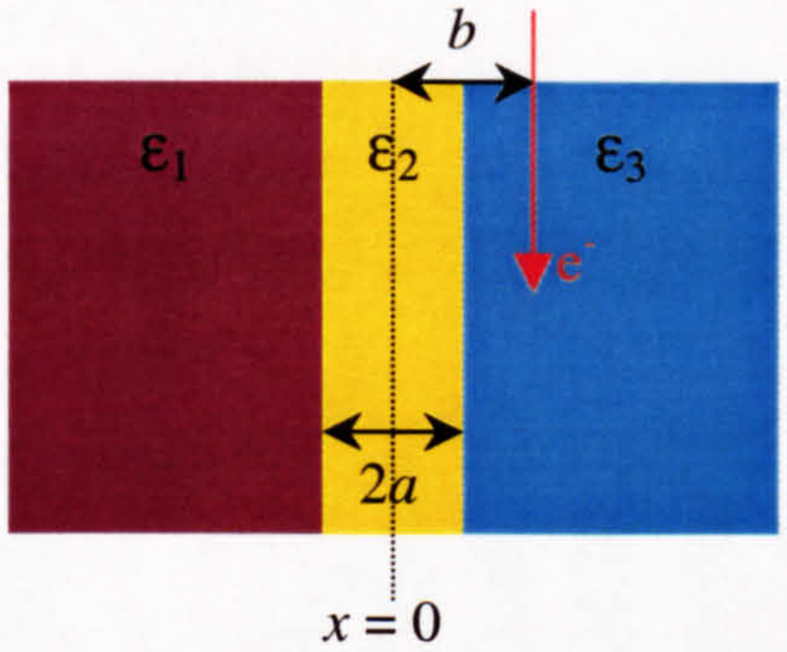

Figure 2.6: Geometry of three-layer system with parallel electron beam. Beam is shown moving externally to the interfacial phase.

The equation modelling the non-relativistic movement of an electron in this setup has been discussed in literature (Howie and Milne, 1985) and is given below.

$$\frac{d^2P}{dqd\hbar\omega} = \frac{e^2}{2\pi^2\varepsilon_0\hbar^2v^2K}\left\{\mathrm{Im}\left(-\frac{1}{\varepsilon_3}\right) + F(\varepsilon_1,\varepsilon_2,\varepsilon_3,K,a)e^{-2K(b-a)}\right\}$$

$$F = \mathrm{Im}\left\{\frac{1}{\varepsilon_3}\frac{(\varepsilon_2+\varepsilon_1)(\varepsilon_2-\varepsilon_3)e^{2Ka}-(\varepsilon_2-\varepsilon_1)(\varepsilon_2+\varepsilon_3)e^{-2Ka}}{(\varepsilon_2+\varepsilon_1)(\varepsilon_2+\varepsilon_3)e^{2Ka}-(\varepsilon_2-\varepsilon_1)(\varepsilon_2-\varepsilon_3)e^{-2Ka}}\right\} \quad \textbf{Equation 2.34a}$$

In addition to this, Walls (1987) gives an equation for the same three-layer system but with the electron beam travelling internal to the interface phase. The equation is stated below.

$$\frac{d^2P}{dzd\omega} = \frac{e^2}{2\pi^2\varepsilon_0\hbar v^2}\int_0^{k_y^m}\frac{1}{K}F'dk_y$$

$$F' = \mathrm{Im}\left\{\frac{-1}{\varepsilon_2}\frac{\xi_1^+\xi_3^+e^{2Ka}+\xi_1^-\xi_3^-e^{-2Ka}+\xi_1^+\xi_3^-e^{-2Kb}+\xi_1^-\xi_3^+e^{-2Kb}}{\xi_1^+\xi_3^+e^{2Ka}-\xi_1^-\xi_3^-e^{-2Ka}}\right\} \quad \textbf{Equation 2.34b}$$

Here $\xi_i^{\pm} = (\varepsilon_2 \pm \varepsilon_i)$. By interchanging subscripts 1 and 3 in eqn 2.34a, the equation becomes applicable for an electron travelling through medium 1.

2.4 Dielectric Function and Kramers-Kronig

2.4.1 The Complex Dielectric Function

Among the most useful data that can be obtained from the low loss EELS spectrum is the complex dielectric function of the sample. The dielectric function gives a wealth of information on the physical and particularly the electronic properties of the material. Most directly it can be related to the optical properties of the material as:

$$\varepsilon(\omega) = N^2 = (n + ik)^2$$

Where n is the refractive index and k is the extinction coefficient.

In theory, optical experiments will probe the dielectric response to a transverse field whereas EELS will give the longitudinal response. In practice, the differences between the spectra obtained are generally small (Daniels *et al.*, 1970) and so the two can be compared. However, care must be taken to note that there are still differences (Walls and Howie, 1989). Palik (1985) is an excellent reference for optical measurements which can easily be converted to give dielectric functions and loss functions for comparison. The data acquired by optical methods is generally of considerably higher resolution than that obtained using EELS. However, the range of frequencies accessible through EELS is far superior.

The parts of the dielectric function yield different information. The real part probes the low energy structure. In particular, the plasmon peaks generally occur at an energy close to a zero with a positive slope in the real part of the dielectric function. The imaginary part offers information on the band structure of the material. The energy at which it becomes non-zero represents the band gap of the material, whilst the behaviour above this energy can be linked to the joint density of states.

2.4.2 Kramers-Kronig Analysis

As shown in eqn 2.7, the loss function is a function of both the real and imaginary parts of the dielectric function. If both the real and imaginary parts of $1/\varepsilon$ are known, it is possible to calculate the dielectric function. Kramers-Kronig analysis allows the calculation of

Re*[1/ε]* from the corresponding loss function. The Kramers-Kronig transformation takes the following form.

$$\mathrm{Re}\left[\frac{1}{\varepsilon(E)}\right]=1-\frac{2}{\pi}P\int_0^\infty \mathrm{Im}\left[\frac{-1}{\varepsilon(E')}\frac{E'}{E'^2-E^2}\right]dE' \qquad \textbf{Equation 2.35}$$

For this, the assumption has been made that $\varepsilon(-E) = -\varepsilon^*(E)$, where ε^* denotes the complex conjugate of ε. P refers to the Cauchy principal part of the integral and allows calculation of the integral despite the function being undefined for $E=E'$. For evaluation of this integral there are a number of points to observe. The loss function used must not contain any multiple scattering. In practice, deconvolution can be performed to calculate the required single-scattered spectrum (provided a zero loss peak is present within the spectrum)(section 2.1.2).

Further to this, for accurate results, the spectrum should be corrected for the effect of the limited angular range reaching the spectrometer. In theory, electrons can be scattered through very large angles. The presence of the collection aperture limits the angular range to a half-angle of 12.5 mrad. This is indicated by the logarithmic term in eqn 2.25. For small angular divergences (α), division by the logarithmic term is normally sufficient.

A standard low loss energy spectrum will cover the range 0-100eV. In contrast with this, Kramers-Kronig analysis requires integration over all positive energies. Despite the loss function tending to zero at high frequencies, its value is still not negligible at 100eV. It is however reasonable to extrapolate the function to higher energies using a power law fit of the form AE^{-r} as this is the form predicted by the Drude Model (section 2.1.2). The values of A and r can be chosen to fit the experimental data.

Finally, the result from the Kramers-Kronig transformation lacks an absolute scale as ordinarily the sample thickness necessary for the prefactor in eqn 2.25 is unknown. To correct for this, the Kramers-Kronig sum rule is used. This is obtained by setting E=0 within eqn 2.35.

$$1-\mathrm{Re}\left(\frac{1}{\varepsilon(0)}\right)=\frac{2}{\pi}\int_0^\infty \mathrm{Im}\left[\frac{-1}{\varepsilon(E')}\right]\frac{1}{E'}dE' \qquad \textbf{Equation 2.36}$$

For a metal, *Re[1/ε(0)]* becomes large as E tends to 0, so the left hand side of eqn 2.36 becomes effectively unity. For an insulator, the imaginary part of the dielectric function is

small at low E and so $Re[1/\varepsilon(0)]$ tends to $1/n^2$ where n is the refractive index for visible light. It may initially appear that the static dielectric constant would be a more appropriate value for $\varepsilon(0)$. However, since the EELS spectrum does not provide accurate data below about 0.5-1eV due to the limited energy resolution, the dielectric constant at visible light frequencies is more suitable.

2.5 Summary

This chapter outlined the theory required in understanding the techniques used in this thesis. To understand all aspects of this thesis it is also necessary to discuss the experimental instrumentation and related theory relevant to this work. Chapter 3 gives a detailed discussion of the instrumentation used along with associated theory and experimental techniques.

CHAPTER 3

INSTRUMENTATION AND EXPERIMENTAL TECHNIQUES

3.1 Introduction

The main instrumentation used to collect the data along with the general analytical electron microscopy techniques used are described in this chapter. The more specific techniques employed will be discussed in detail in subsequent chapters

Each sample was examined in a conventional transmission electron microscope (CTEM) to ensure that it had thin areas suitable for analysis using EELS and that it contained the desired precipitates. Electron diffraction was used to ensure that the precipitates and the matrix had the correct orientation relationship and provided a check using crystallography that the correct precipitates were being examined.

In the metal alloys examined, a number of precipitates are possible (section 4.1). Therefore it was important to determine the composition of the precipitates. This was achieved using energy-dispersive x-ray (EDX) spectroscopy within the CTEM.

Having ascertained the composition of the precipitates, the interfaces themselves could then be investigated. This was done using EELS performed in a scanning transmission electron microscope (STEM). EELS was used to investigate the Howie equation (eqn 2.33) as well as providing data for calculating the dielectric functions of the materials of interest.

3.2 CTEM

3.2.1 CTEM Bright and Dark Field Imaging

Bright and dark field imaging were used to study the precipitates and their immediate surroundings. Mechanical damage or strain in the vicinity of precipitates can cause defects or dislocations. This will have an effect on the EELS data from that region making it difficult to interpret. Most of the imaging was performed in an Akashi EM002B

microscope operating at 120kV. Some imaging was performed in a JEOL 1200 microscope but this was operated at 100kV. The EM002B has smaller spot sizes and selected area apertures than the 1200; this enabled localised diffraction from smaller precipitates.

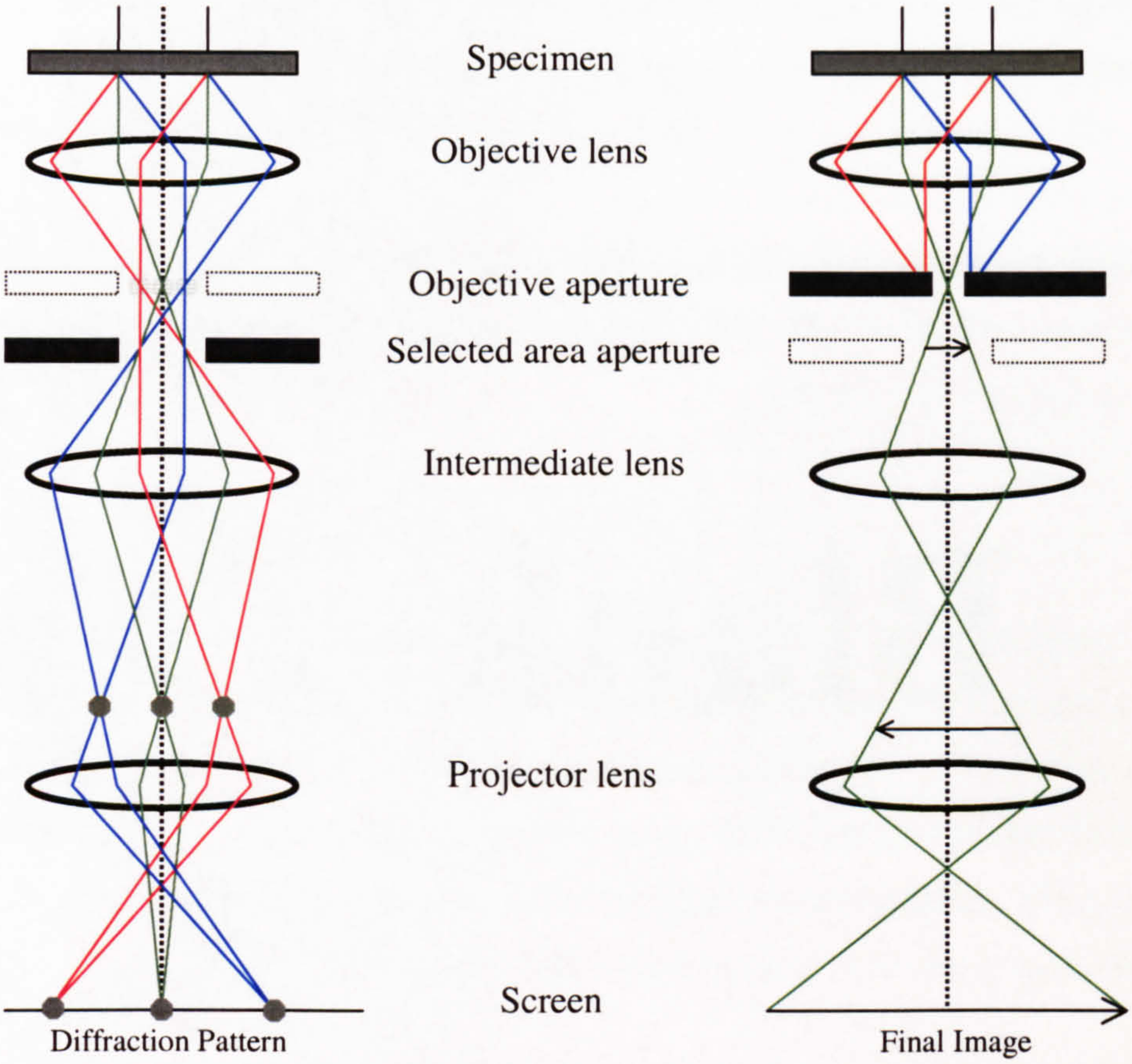

Figure 3.1 Schematic of the lower half of a TEM column in diffraction (left) and imaging (right) modes.

Fig 3.1 shows a TEM column set up in diffraction (*left*) and bright field imaging modes (*right*). Standard bright field imaging was performed with a small objective aperture positioned on the optic axis of the microscope to allow the undiffracted beam to pass through the aperture whilst blocking the majority of the scattered electrons. This gave contrast in the image and, in particular, made the precipitates more visible against the matrix when appropriate diffraction conditions were set up. Dark field imaging was performed by obtaining a two-beam condition. The electron beam was then tilted, resulting in a movement of the selected area diffraction pattern on the screen. The beam was tilted to move the diffraction spot corresponding to the undiffracted beam to the original position of a suitable spot corresponding to a diffracted beam. This, in turn, caused the movement of the reflection from the opposite g-vector onto the optic axis. Placing a small objective

aperture about this reflection gave the required dark field image. This meant that only those specific parts of the image contributing to that reflection would appear bright. By selecting a reflection from the aluminium matrix it was possible to give greater contrast between the matrix and the precipitates. As the orientation relationship links the orientation of the precipitates to that of the matrix, this technique was of use for locating precipitates in a specific orientation.

The magnifications of the microscopes were calibrated using cross-gratings and the camera lengths were calibrated using diffraction patterns from the aluminium matrix of the samples in specific orientations.

3.2.2 CTEM Diffraction Techniques

The precipitates and the orientation relationship between the precipitate and the surrounding matrix were initially identified using diffraction methods. In systems where a number of precipitates were present, the precipitates of interest had diffraction patterns that could be indexed easily when tilted to specific poles. The other precipitates present were generally caused by impurities and had more complex crystallographies. This resulted in considerably more complex diffraction patterns, which could not be easily indexed.

Both condensed beam and selected area diffraction were used. However, the majority of the work was done with selected area diffraction. This was achieved by placing a selected area aperture in a plane conjugate to the specimen. The smallest selected area aperture was of a size that enabled diffraction information to be obtained from a 150nm wide precipitate without including any of the surrounding matrix. However, this is only accurate for diffraction spots close to the optic axis. The presence of spherical aberration in the objective lens causes slightly different areas of specimen to be selected for different spots. As the spherical aberration is dependent on the cube of the angle with the optic axis, the effect is more significant for higher order beams.

Kikuchi lines provide a convenient method to determine and, more importantly, orient exactly a crystal on specific poles. Kikuchi lines arise from a combination of elastic and inelastic scattering. As illustrated schematically in Fig. 3.2, the incoming electron beam is inelastically scattered at P. P is now the origin of a spherical wavelet. The intensity of this

scattered beam decreases with increasing scattering angle (more electrons go along PQ than PR). The rays along PQ and PR are at the Bragg angle for a set of crystal planes and so are elastically scattered. This means that in the extended direction along PQ there is an electron deficiency compared to the surrounding, there are insufficient electrons along PR and hence RR' to compensate for this. Similarly, the reverse is true along QQ' where there is an electron excess compared to the surrounding. When this is extended to 3D this results in pairs of Kikuchi lines, the 'excess' and 'defect' lines, which are locked to the orientation of the crystal. When the crystal is oriented exactly at a diffracting condition Kikuchi lines lie halfway between the zero order beam and associated sets of diffraction spots.

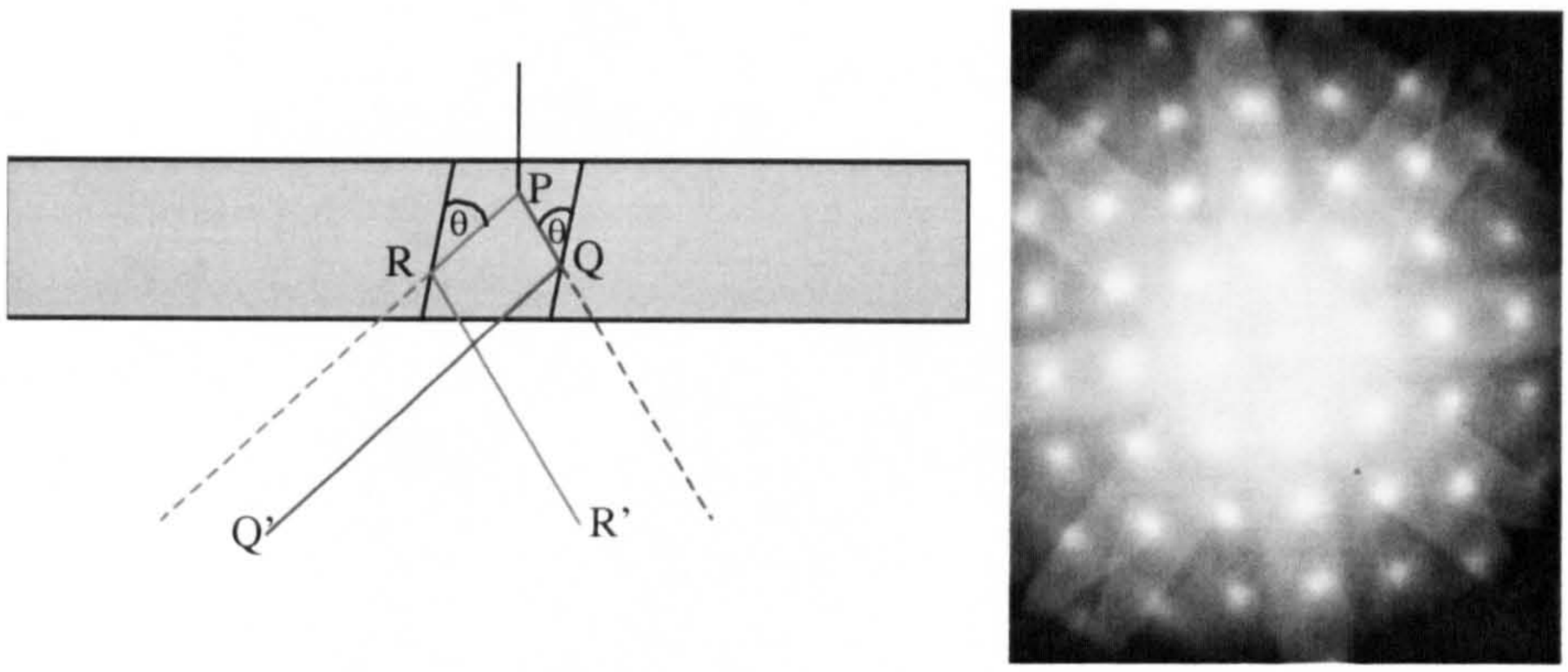

Figure 3.2 Kikuchi diagram and [100] pattern from aluminium.

The treatment above is simplified and the observed patterns are actually more complex. For example, when the beam travels exactly parallel to a set of crystal planes, no Kikuchi lines should be observed. This is because the gains and losses of background intensity will exactly balance. In practice, it is found that a band of higher intensity forms. This band appears between the 'expected' positions of the Kikuchi lines and is known as a Kikuchi band (Fig 3.2 *right*). The origin of Kikuchi bands is complex, but can be explained through dynamical scattering from Bloch waves. This is discussed in *e.g.* Hirsch *et al.* (1965). For this treatment it is sufficient to state that the geometry of Kikuchi lines can be used, treating the edges of the bands as Kikuchi lines.

Tilting of the sample results in movement of the Kikuchi pattern and by tilting in a suitable direction it is possible to 'follow' a specific pair of Kikuchi lines. By doing this it is possible to tilt easily to any pole from another, assuming the microscope rod provides sufficient tilt.

It can be shown from the Howie-Whelan Equations (Williams and Carter, 1996) that in a specimen of thickness t oriented in a two-beam condition, the intensity of the Bragg diffracted beam is given by:

$$I_g = \left|\phi_g\right|^2 = \left(\frac{\pi t}{\xi_g}\right)^2 \frac{\sin^2\left(\pi t s_{eff}\right)}{\left(\pi t s_{eff}\right)} \qquad \textbf{Equation 3.1}$$

$$s_{eff} = \sqrt{s^2 + \frac{1}{\xi_g{}^2}}$$

Where s_{eff} is the effective excitation error corresponding to an excitation error s which is a measure of the deviation from the exact Bragg condition. ξ_g is the extinction distance for the material.

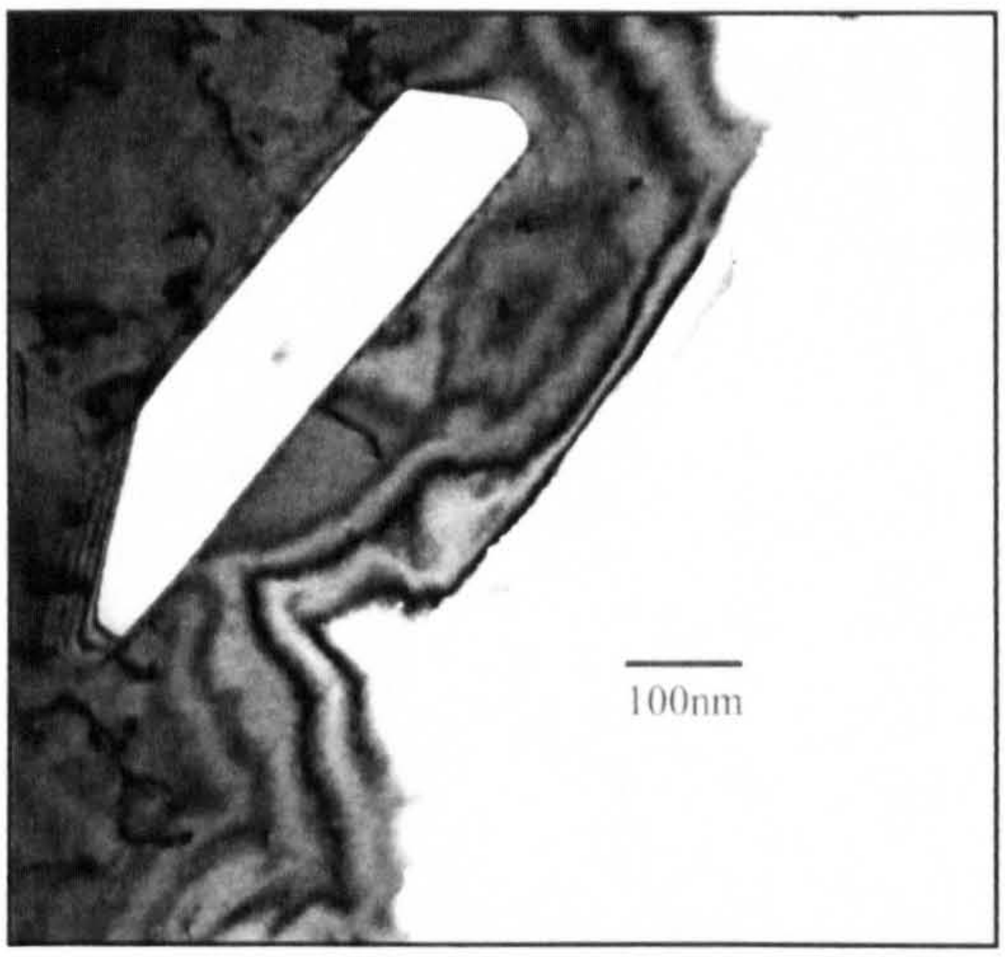

Figure 3.3: Bright field image of an area showing thickness fringes.

In two-beam conditions the intensity of the undiffracted beam I_0 is given by I_0=1-Ig. Examination of eqn 3.1 shows that, for constant s, the intensity of the diffracted beam, and hence the undiffracted beam, varies periodically with thickness t. This results in dark and light areas on the sample indicating variations in thickness. These are known as thickness fringes (Fig. 3.3). The spacing of the thickness fringes can be used to identify the magnitude of the thickness variation. A single 'cycle' (*i.e.* dark-light-dark or vice-versa) indicates a thickness change of ξ_g (Fig. 3.4). Absolute measurements of t require exact orientation to the Bragg angle or knowledge of the value of s. Despite this, information on relative thickness can be easily obtained. Care must be taken if the sample is tilted, as the electron beam is no longer perpendicular to the plane of the sample. In such a situation, the

fringes indicate the thickness in a direction parallel to the beam rather than the conventional sample thickness. Scattering within the sample gradually reduces the visibility of the fringes as the thickness increases. For this reason, thickness fringes cannot be used in particularly thick areas. However, using this technique assessments were made of the degree to which the thickness of a thin area of the sample varied.

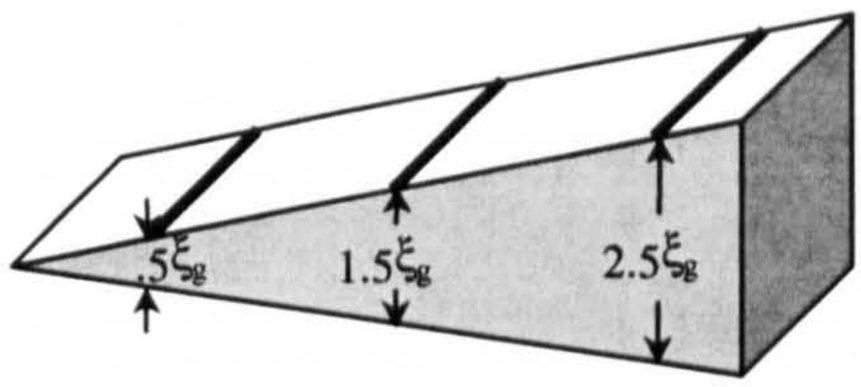

Figure 3.4 Schematic of thickness fringes in a wedge-shaped specimen

Both the 002B and the 1200 microscopes are equipped with double tilt rods which meant the sample could be tilted in two perpendicular directions, though in the 002B this was limited to about $\pm 10^{o}$ in each direction.

3.3 The enhanced VG HB5 STEM

3.3.1 The Microscope

The VG Microscopes HB5 system was used almost solely for microanalysis using EELS. Imaging was used to locate and record precipitates of interest, whilst diffraction was used to align the precipitate/matrix interface for subsequent microanalysis.

The HB5 at the University of Glasgow has been modified by the addition of three post-specimen lenses (PSLs) to aid in imaging and EELS. In addition to this it is fitted with a z-lift stage that enables the specimen to be kept at constant height in the objective lens (Craven & Buggy, 1981). This means that the microscope can be operated with a standard objective lens setting. This, in turn, means that there is a known fixed angular compression of the electrons leaving the lens. Another advantage of this set-up is that minimal adjustment is needed when performing EELS on different areas of the specimen.

Figure 3.5 shows a schematic of the Glasgow HB5 set up for EELS analysis.

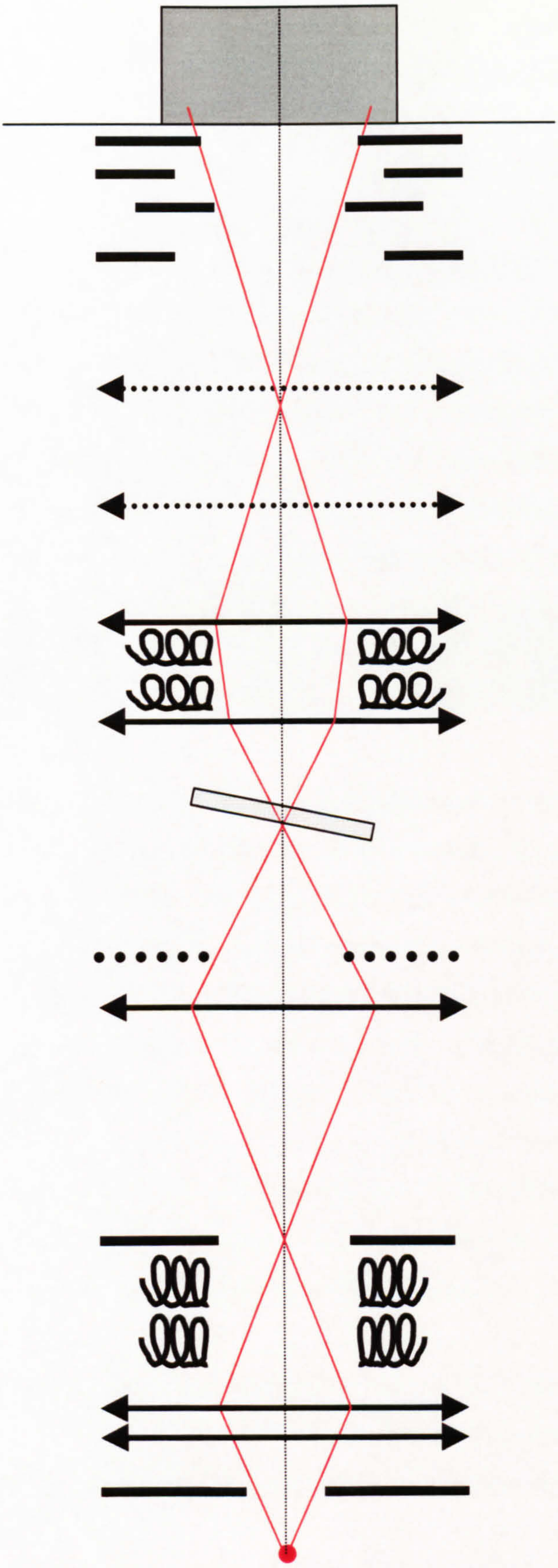

Figure 3.5 Schematic of the VG HB5 electron optics set up for collection of EELS data. (Items shown dotted are not being used)

Electrons in the HB5 are produced by a field emission gun (FEG) source. FEG sources provide high monochromaticity and high electron brightness and are ideal when using a small spot size. The HB5 FEG source is a single crystal of tungsten supported on a tungsten wire. The sharpness of this tip means that the application of a few kV potential to the tip results in a large electric field strength sufficient to narrow the barrier for cold field emission, allowing electron tunnelling. The FEG requires working at high vacuum; the vacuum in the gun chamber is about 10^{-11} mbar. The high vacuum is required to reduce the presence of contaminants. During use, these contaminants in the microscope build up on the tip; this raises the work function of the tungsten and lowers the emission current. More importantly contaminants can become ionised and bombard the tip causing roughening of the surface and locally sharpening it. This can cause undesired changes in the electric field and also electron emission from other parts of the tip. The contaminants can be removed from the tip by 'flashing' it. This involves briefly passing a large current through the support wire of the tip. The microscope column does not require such a high vacuum, so is operated at 10^{-8} mbar and is separated from the gun by a differential pumping aperture.

The physical size and angular convergence of the probe at the specimen is initially defined by the virtual objective aperture (VOA) and further defined by the objective and condenser lenses. Four different diameter VOAs are available; a smaller VOA will result in a smaller convergence angle but the beam will also contain less current as more of it is blocked by the aperture. The HB5 is fitted with two condenser lenses, condenser lens 2 being positioned slightly above condenser lens 1. The two lenses give a greater selection of probe sizes and convergence, though in practice only condenser lens 2 is used as it provides a higher current and hence greater convergence. Normally, the HB5 is operated with a probe diameter of 1nm. The condenser lens is focussed to place the beam crossover in the plane of the selected area aperture. This enables the selected area aperture to remove stray electrons caused by scattering from the VOA.

The image in the microscope is built up by scanning a small electron probe in a raster across the sample. This scanning action is performed by the scan coils. The size of area of specimen being scanned relative to that on the display, defines the magnification of the observed image.

The sample within the HB5 is held in a cartridge, which enters the microscope vacuum. A number of different cartridges are available offering a variety of capabilities. This work was mostly performed using a ±30° tilt x-ray holder. This allowed tilting of up to 30° in two perpendicular directions. The specimen holder within this cartridge is made from beryllium in order to reduce the absorption of x-rays generated by the sample and to prevent the detection of x-ray lines from the holder (section 3.6.1).

The post-specimen lenses allow the HB5 to perform a number of different tasks more effectively. PSL1 is used to maximise the EELS signal. Of the three post-specimen lenses it offers the greatest amount of angular compression and thus allows a greater number of electrons to enter the spectrometer. PSL2 and PSL3 provide different amounts of angular compression, modifying the contrast observed in the image. PSL2 is generally used for standard diffraction contrast images. PSL3 can be used in association with the collector aperture to give a greater level of diffraction contrast, closer to that seen in a TEM. In addition, PSL3 can be used in rocking-beam mode to enhance the visibility of Kikuchi bands, aiding specimen tilting to the correct orientation.

The HB5 has a number of detectors for imaging: one bright field and three annular dark field (ADF) detectors. Three of the detectors are interchangeable. These are the bright field and two of the ADF detectors, which have central holes of different diameters. The third ADF detector, which is a large angle detector, is slightly lower down the column and can be used in conjunction with one of the other detectors, though this is rarely done. Both the bright field and dark field detectors are made up of scintillator material that emits photons on being hit by an electron. These photons are detected by a photomultiplier tube, the signal is amplified and eventually passed to a cathode ray tube. The ADF detector has a central hole that allows electrons which have not undergone elastic scattering or have been scattered through small angles to pass through undetected whilst collecting electrons scattered through larger angles. This provides a dark field image but allows the non-elastically scattered electrons to enter the EELS spectrometer.

The EELS spectrometer is a GATAN 666 parallel electron energy loss spectroscopy (PEELS) spectrometer. This will be discussed in section 3.4.1. The small and large interchangeable ADF detectors provide a collection angle at the detector of 25mrad and 50mrad respectively. Normally a smaller aperture is used to define this collection angle.

There are in fact two apertures in this region of the microscope, the collector and spectrometer apertures. The collector aperture is used as the defining aperture for the spectrometer and is positioned before the interchangeable ADF. The spectrometer aperture is used to remove stray electrons caused by scattering from the edge of the collector aperture and hence minimise spurious signals within the spectrum.

3.3.2 Diffraction in the HB5 STEM

Since the orientation relationship between the precipitate and the matrix was known, the Kikuchi bands from the matrix were used to align the precipitate/matrix interface parallel to the electron beam to high accuracy. Due to the nature of the STEM, diffraction techniques are implemented differently than in a CTEM. However, the principle of reciprocity (Keyse *et al*, 1998) enables comparisons to be made between the CTEM and STEM. The principle of reciprocity effectively states that if the angles of collection in the CTEM and of convergence in the STEM are equivalent (and similarly the angles of convergence in the CTEM and of collection in the STEM), as shown in Fig. 3.6, then the image contrast will be identical. This has implications in diffraction which are discussed below.

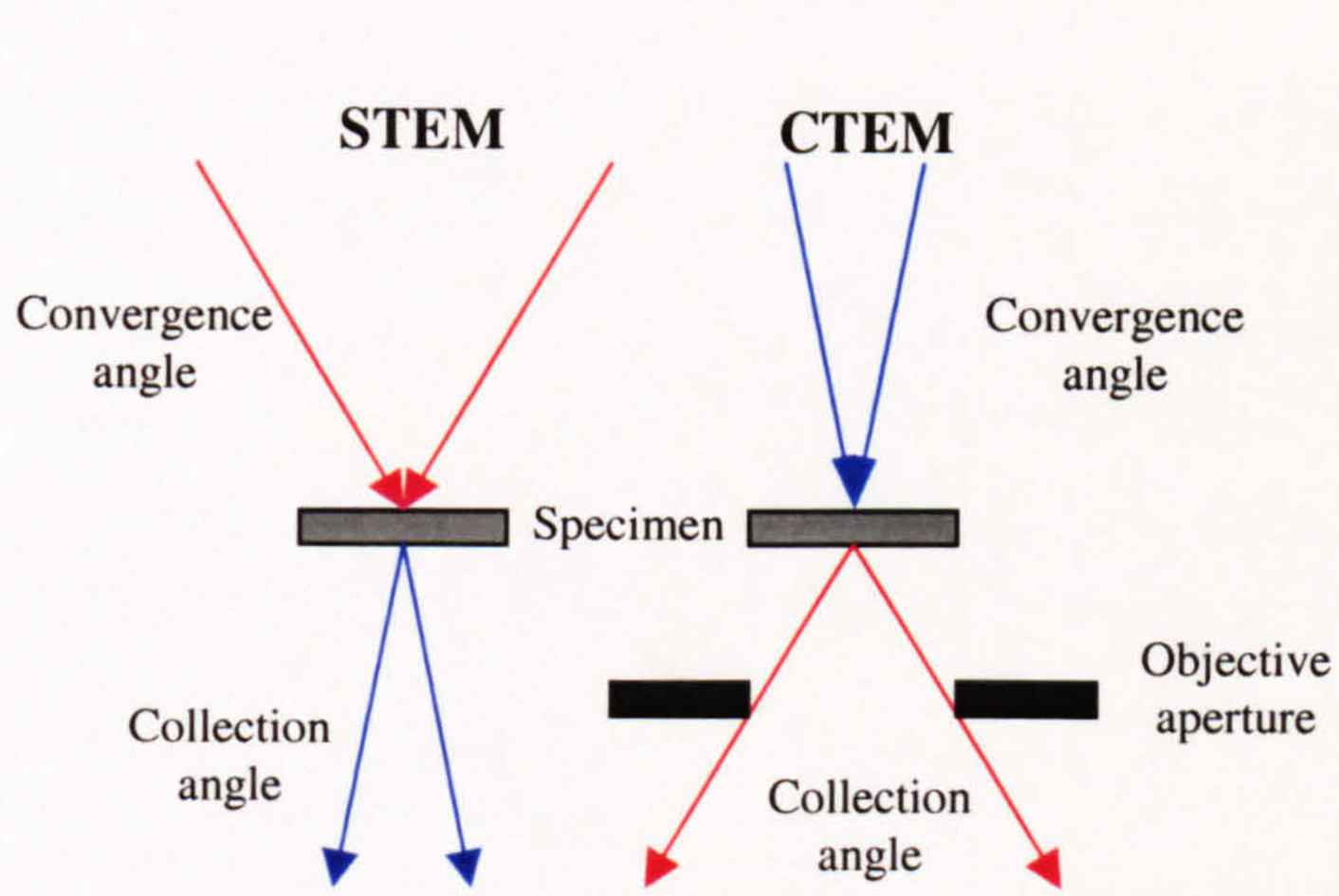

Figure 3.6 Schematic comparing important angles in the STEM with a convergent beam and the CTEM with a parallel beam.

The technique used for performing diffraction was the rocking-beam method. Initially, the condenser lens is weakened to allow approximately parallel illumination to fall on the specimen. The scanning system is then used to rock the beam about the SA aperture. As the SA aperture is conjugate with the specimen this results in the beam falling on the same area of specimen but at different angles of incidence. A simplified schematic of this can be

seen in Fig. 3.7. The beam is rocked in two dimensions and the angle through which the beam is deflected is used to adjust the effective camera length of the system.

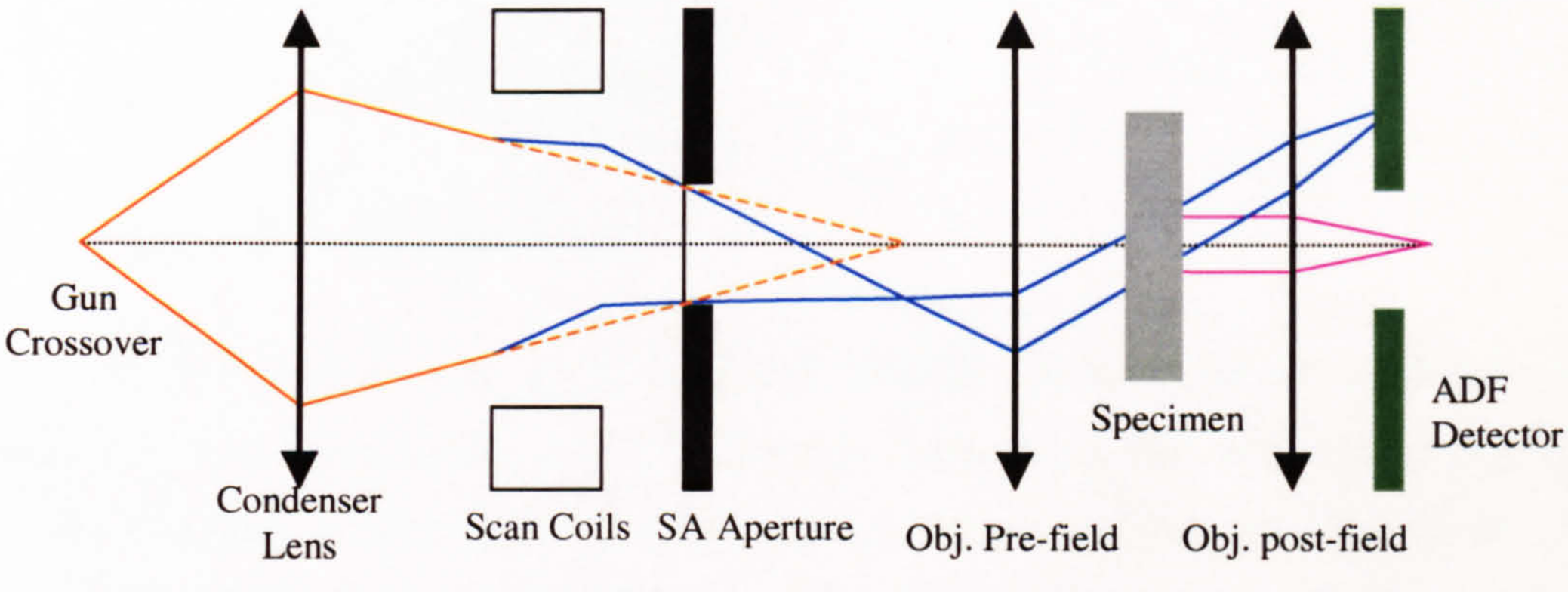

Figure 3.7 – Schematic of STEM in rocking-beam diffraction mode. Only the scanned beam (blue) is shown entering the sample and one diffracted beam (pink) and the undiffracted beam (blue) shown exiting the sample.

If a small axial detector is used, strong intensity is detected from a suitably oriented plane when the incident angle is $2\theta_B$. The use of a small collector aperture allows this diffracted beam to pass, whilst preventing stray electrons falling on the detector. This gives rise to a diffraction pattern that is equivalent to a selected area diffraction pattern in a CTEM.

If instead an ADF detector is used, for a specific Bragg condition the undiffracted beam falls on the ADF detector (assuming the collector aperture has been removed) whilst the diffracted beam passes through the annulus. In a strong diffracting condition, the undiffracted beam loses significant intensity to the diffracted beam. Therefore, when the signal from the ADF detector is converted and displayed on the CRT, a Kikuchi-like map is created, corresponding to the orientation of the area of specimen (Craven, 1977). It is then possible to use the post-specimen lenses to alter the compression of the beam and hence the contrast of the Kikuchi bands.

3.3.3 Diffraction Contrast in the STEM

As discussed in the previous section, the principle of reciprocity makes it possible to obtain diffraction contrast in the STEM similar to that observed in a CTEM. Due to the near-parallel illumination required in a CTEM, a small collection angle is required in a STEM. This can be easily achieved using PSL3. However, a small collection angle results in a smaller amount of signal falling on the detector and hence the image becomes noisy. This

problem can be partially rectified by integrating the signal over a period of time, which can be performed by the attached image acquisition system.

3.4 EELS within the HB5

3.4.1 The EELS Spectrometer

The spectrometer used was a GATAN 666 PEELS spectrometer. A schematic of the spectrometer is shown in Fig. 3.8. The electron beam enters the spectrometer through the entrance aperture. It then passes through two quadrupole and two sextupole lenses which focus the beam in two dimensions and correct second order aberrations respectively. The magnetic prism deflects the beam through 90° and in the process disperses the beam slightly (electrons of different energies will have a different radius of curvature in the magnetic field) and also has a further focussing effect. The four quadrupole lenses then increase this dispersion and project the beam onto a YAG scintillator which is optically coupled to a 1024 channel photodiode array. The result is that electrons of different energies fall on different areas of the photodiode array allowing parallel detection of the energy spectrum. The excitation of the post-prism quadrupoles changes the dispersion and the range of electron energies recorded *e.g.* 0.1eV per channel will give a range of about 100eV. Dispersion settings of between 0.05 and 2eV per channel are available. Here the majority of the work was done with 0.1eV per channel dispersion. By changing the voltage on the electrically isolated drift tube, it is possible to offset the spectrum energy. This allows acquisition of core loss spectra at high dispersions. In addition, this is used to calibrate the energy dispersion and the absolute energy-loss scale.

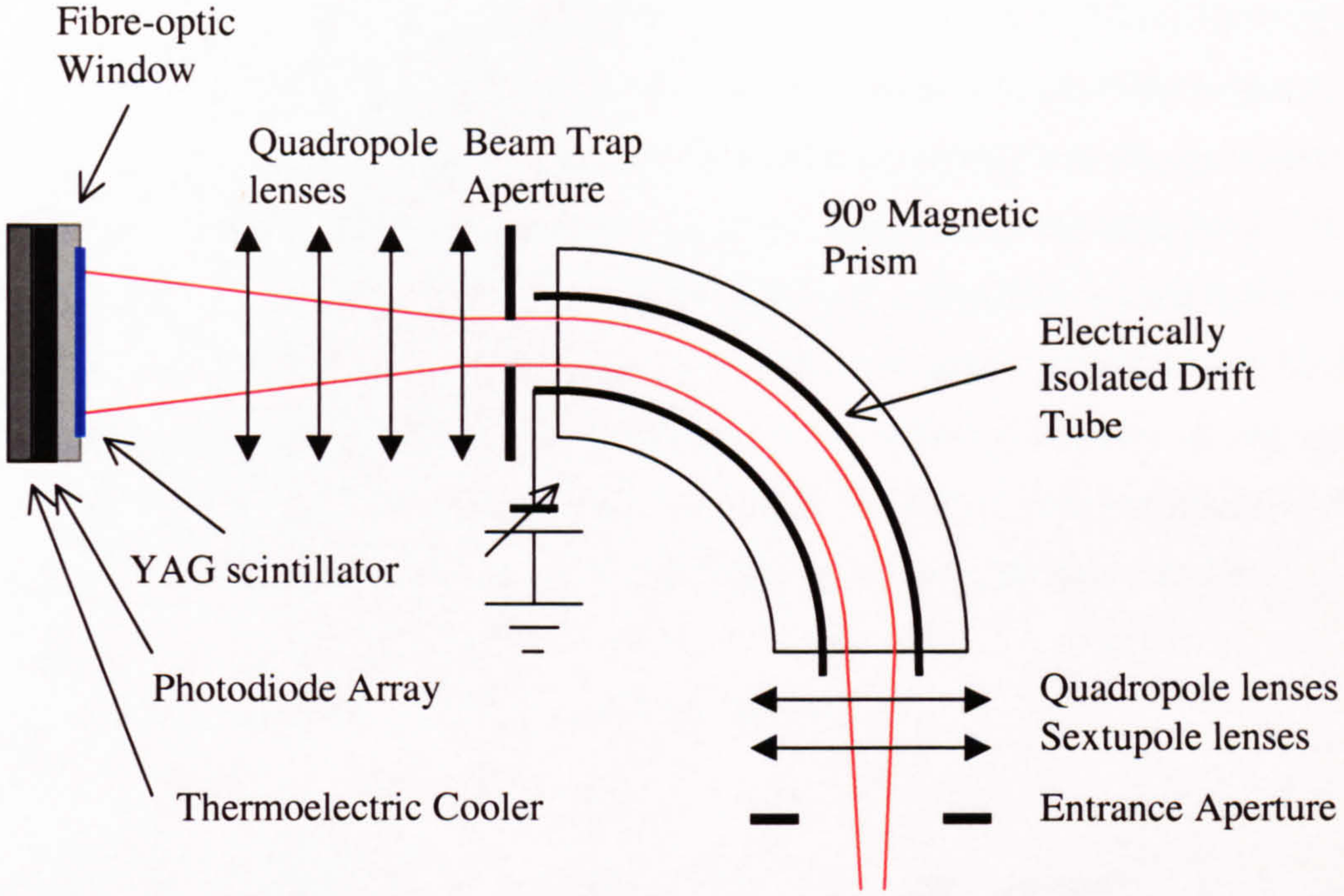

Figure 3.8 Schematic of GATAN 666 PEELS Detector.

3.4.2 Microscope Setup

The schematic diagram in Fig 3.5 shows the microscope as it is set up for collection of EELS data.

To ensure the microscope is properly aligned, the following procedure is used. Once the sample has been inserted, a suitable area is found and the sample focussed with the z-shift. The PSLs are turned off for the main alignment. The selected area aperture is then inserted and used to check the condenser stigmation. A virtual objective aperture (VOA) is then inserted (normally 100μm diameter) and the objective stigmation checked. The objective aperture (ROA) is used to define the optic axis; to do this the VOA is removed and a 70μm or 100μm diameter objective aperture inserted. This aperture is then centred by minimising the image shift when the objective lens current is wobbled. At this point, the objective aperture is centred on the optic axis and its position can be used to align the spectrometer and collector apertures. To do this, the microscope is changed into rocking-beam mode (known as SA mode). In this mode, electrons are scattered from the edge of the objective aperture and recorded by the ADF detector. If there is no sample in the way of the electron beam, the objective aperture appears as a bright ring. The centre of this ring is used as a

visual indication of the optic axis. This position is then marked and the objective aperture removed. By recording the current from the spectrometer aperture as the beam is scanned, the aperture can be imaged. Grigson coils are used to shift the beam on to the spectrometer axis. The collector aperture (which is imaged in the same manner as the objective) is then mechanically aligned to this axis. Each post-specimen lens is mounted in such a way that the entire lens can be mechanically aligned with sufficient accuracy. The PSLs are turned on individually and aligned to re-centre the image of the collector aperture on the optic axis. The effect of this is that if the current to the PSL is altered, then the image of the collector aperture expands and contracts concentrically about the optic axis position.

Once the microscope is aligned EELS data can be recorded.

3.4.3 Collection of EELS data

All EELS data were collected on the HB5 using the GATAN 666 EELS spectrometer. This spectrometer was controlled by GATAN EL/P software, which was also used for the subsequent data processing and analysis. The data for a single low loss spectrum was taken as a series of 100 acquisitions, each acquisition lasting for 40 milliseconds. These acquisitions were summed automatically by the software. This gave a good balance between time for each spectrum and minimising the quantity of noise in the spectrum.

In order to achieve the best data from the photodiode array, it is desirable to maximise the signal to noise ratio. This could be easily achieved by maximising the current falling on the array. However, the photodiode saturates if more than 16000 counts are recorded in a single channel. As discussed in section 2.1, the largest feature in the EELS spectrum is the zero loss peak. This is normally the only feature that has suitable magnitude to cause a problem with detector response. A beam blanking system was used to control the intensity of the spectrum. This device allowed the beam to reach the detector for short, selectable periods during the acquisition. As variations in thickness within the sample will affect the number of counts in the zero loss peak, the beam blanking system was set to ensure that the largest channel within the zero loss peak was between 8000 and 10000 counts. This enabled EELS data to be taken from a limited range of thicknesses without readjustment of the beam blank.

The zero loss peak has long 'tails' which extend into the area of interest in the low loss spectrum. To gain accurate information from this area it is necessary to subtract the effect of the zero loss peak. The EELS software performs this by modelling the lower energy side of the zero loss peak, mirroring it and subtracting it from the spectrum. In order for this to be possible, the energy of the peak was offset to place it at around channel 180 on the diode array. This ensured that there was a suitable number of channels to the left of the zero loss peak for modelling and allowed for energy drift in the detector.

Prior to any data being taken, the detector had to be set up. The first step in this procedure was to flood the diode array with electrons. This was done to equalise the charge distribution in the YAG scintillator, reducing the variation in response for different channels. The flooding was performed by removing all the apertures from the beam, setting the energy dispersion to 0eV and using PSL2. This spread the illumination uniformly over the scintillator. The detector was flooded for about 10 minutes. After this, all the relevant apertures were re-inserted and the desired dispersion selected. The EELS spectrum was then focussed to minimise the width of the zero loss peak. In the Glasgow HB5 it should be possible to minimise the FWHM of the zero loss peak to ~0.5eV. If this was not possible it was an indication that the microscope may need realigned. The majority of the data presented in this thesis was acquired with an energy resolution (zero loss FWHM) of 0.5eV. The energy dispersion of the spectrum was then calibrated using an automated routine present in the EL/P software. This routine varied the voltage applied on the drift tube and using the subsequent change of position of the spectrum, determined the calibration.

In order to reduce the artefacts caused by remaining variations in diode response four spectra were acquired instead of one. Each of the spectra was displaced by 1eV relative to the previous and the spectra were later aligned and summed. In addition to this there was signal always present from the diode array, even when the beam was not entering the detector. To remove this, a spectrum was acquired with the same settings as a standard spectrum but without the beam entering the detector. This resultant spectrum was subtracted from all the spectra before analysis. As this background spectrum did not vary noticeably during a session it was sufficient to acquire one dark current per run.

Energies and approximate widths of the plasmon peaks from several materials are given in table 3.1.

Material	Experimental Plasmon Energy (eV)	Experimental FWHM (eV) @ 0.5eV Resolution
Magnesium Silicide	13.0	3.3
Aluminium	15.0	1.5
Silicon	16.7	4.2
Amorphous Carbon	29.4	19.0

Table 3.1 – Plasmon peaks of interest

The carbon plasmon was of interest as it gave a measure of the extent of carbon contamination present on the sample. Carbon contamination is a major problem in the acquisition of good EELS data. Hydrocarbons diffusing across the specimen surface are polymerised by the electron beam and cause a localised increase in thickness (Schamm and Zanchi, 2001). In addition, the carbon peak is quite broad and so affected the visibility of some of the peaks of interest.

3.4.4 Contamination

One technique used to reduce the amount of contamination observed, was to flood the specimen. This involved removing all the apertures and gradually reducing the area of specimen irradiated. This had the effect of locking the hydrocarbons in place over a wide area of the sample so only a small amount of carbon was seen in any one place. This solution was unfortunately localised to one area of specimen and only lasted a maximum of about 30 minutes. In addition, when applied to thicker areas of sample, the electrons are unable to reach the exit side of the specimen. As a result, only one side of the sample is improved.

The other, more effective, method of reducing the contamination was to use a plasma cleaner. A plasma cleaner uses an oxygen/argon gas mixture to create a plasma within a vacuum. This plasma creates oxygen radicals, which react with C to remove it as CO (Isabell *et al.*, 1999). Normally the process is done for only a few minutes and the entire sample is treated simultaneously. The samples were plasma cleaned immediately prior to

being placed in the microscope and this was done, where possible, in the sample holder that was being used in the microscope session that day.

3.4.5 Specimen Drift

Specimen drift was also a major problem within the microscope. When the sample had been mechanically moved, it continued to drift for a period afterwards. This was due to relaxation of the specimen shift mechanism. As distances of fractions of a nanometre were being investigated, even tiny drifts could significantly change experimental results. The specimen drift was found not to be constant and so could not be easily compensated for. To minimise the effect of the drift, all measurements were taken relative to the interface with the interface position being relocated after each point. The position of the interface could be found with high accuracy, using EELS. The above was done by electrically adjusting the probe position. In addition, after every 4 points the microscope was returned to scanning mode, the magnification reduced and the sample repositioned to its state at the beginning of the run. This was done using the electrical shifts. The electrical shifts cause some misalignment of the objective lens, which can reduce the energy resolution of the low loss EELS spectrum. However, if the electrical shift applied is less than about 150nm, this is not significant. The procedure for acquiring data also provided a check for the extent of drift. As four spectra were recorded from the same point these spectra should be effectively identical. The difference between these spectra indicated the amount that the specimen had drifted during the course of the four acquisitions.

3.5 The FEI Tecnai (S)TEM

The FEI Tecnai TF20 microscope is a state of the art nanoanalytical (S)TEM which has recently been installed at the University of Glasgow. This microscope was operated by Dr Maureen Mackenzie and it was used for only a small number of experiments. As a result, only a limited discussion of this microscope will be given, identifying important features.

The Tecnai is designed as a high-resolution nanoanalytical electron microscope. It is fitted with both a Gatan Enfina PEELS and an EDAX EDX spectrometer and can perform conventional imaging with an information limit of 1.5Å. Electrons are produced by a Schottky field emitter and are accelerated by an operating voltage of 200kV. The column

operates at a vacuum of 10^{-8} mbar, similar to that of the HB5. In addition, it is fitted with a liquid nitrogen cold finger to reduce the mobility of hydrocarbon contamination. The sample stage is computer-controlled and has spatial drift rates of <0.5nm/min. However, the main interest in the Tecnai is in its ability to perform spectrum imaging.

A spectrum image is a digital image where every pixel in the image corresponds to an analytical spectrum. More precisely, spectra are acquired from a 2D array of equally spaced points. Such spectra can be x-ray emission or EELS, though in this thesis only EELS spectrum images are discussed. The spectra are acquired by stepping the focussed STEM probe from one point to the next. As the probe is under computer control the position of the points is determined accurately. The result is a 3D data cube, known as a spectrum image (Fig. 3.9). This cube has two spatial dimensions and an energy dimension, such that the vertical columns are complete energy loss spectra for the energy range acquired. Images can be generated from this cube by slicing in a particular plane. In this way, it is possible to display spatial vs energy images, where the energy loss spectra are shown relative to their corresponding position (similar to a line spectrum image, *e.g.* Fig. 6.9). Alternatively, energy slices can be displayed, where the intensity of each pixel in the image is obtained from the number of counts in a chosen energy window. For example, –2eV→2eV will give an image using the number of counts in the corresponding zero loss peaks of the area analysed, known as a zero loss image.

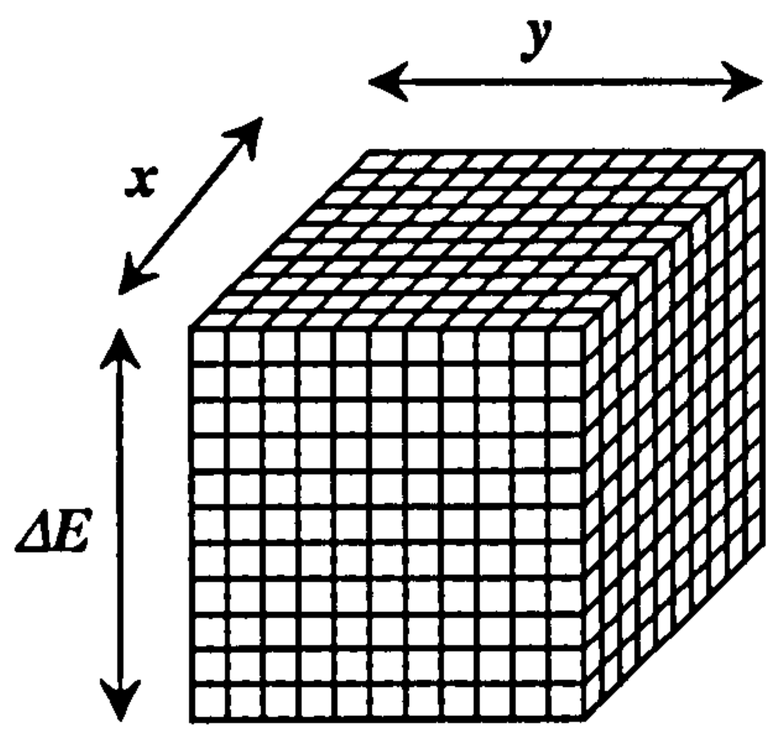

Figure 3.9: The structure of a spectrum image

The size and number of points within a spectrum image can be altered prior to acquisition. However, as each point is acquired individually, large spectrum images take a long time to acquire. One method to reduce this time and still produce high-quality data is to limit the

spectrum image to only one spatial dimension. This is known as a line spectrum image or a line scan. Spectrum imaging is discussed in section 5.6.1.

The Tecnai was operated using a probe size of ~0.5nm and a collection semi-angle of 11mrad. This gave a current in the probe of ~0.02nA and an energy resolution of 0.85eV. The sample was held within a double-tilt rod which offered ±80° α tilt[1] and ±30° β tilt (Fig. 3.10).

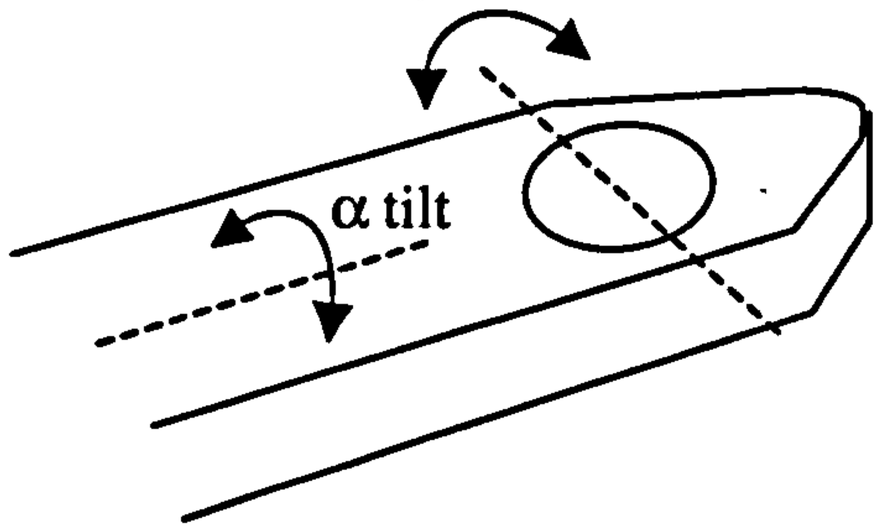

Figure 3.10: Schematic showing the directions of α and β tilt of the Tecnai sample rod.

3.6 EDX

3.6.1 EDX Detector

The X-ray detector fitted to the EM002B is a windowless Oxford Instruments Link lithium-drifted silicon detector with a detector area of 30mm^2. This detector allows the detection of x-rays from elements heavier than boron. The detector is controlled by a QX2000 system. This system has limited compatibility with conventional MSDOS systems but sufficient that a program was written to convert files from a suitable output format to a comma-delimited file suitable for Excel.

The HB5 is also fitted with a Link Si(Li) detector. However, as imaging and tilting are more difficult in the HB5 in addition to the considerably smaller count rate than observed in the EM002B, it was rarely used.

---

[1] 80° of tilt is not practically useful. According to the FEI literature, at only 60° of tilt, 0nm^2 of sample is visible to the electron beam. It is sufficient to say that the tilt is not limited by the stage in the α direction.

3.6.2 Microscope and Detector Setup

For collection of EDX data the EM002B was aligned as standard for imaging. The objective aperture was removed for the duration of the acquisition period, as it could result in undesired x-rays from the aperture itself. The spot size was reduced to obtain x-ray data from a localised region. The spot size was chosen to give information on a precipitate of interest with a minimum of information from elsewhere. However, the count rate is proportional to the current so a balance had to be struck.

Due to the finite response time of the detector, there is a certain amount of 'dead' time when the detector is unable to register x-rays. This dead time increases with the count rate, so it is desirable not to have too many x-rays incident on the detector at one time. The detector software is able to calculate the amount of dead time and hence the corresponding live time. In general, the dead times observed were between 10 and 20 percent of the live time. Data were collected for a live time of 100s using an energy dispersion of 20eV per channel. The detector has 1024 channels and so this gave an energy range of zero to 20keV.

3.6.3 Data Collection

The main peaks of interest were Mg Kα, Al Kα, and Si Kα. Other peaks observed were Fe Kα,β, Cu Kα,β and Cr Kα,β. The peak energies are presented in table 3.2

Element	Peak	Energy (KeV)
Mg	Kα	1.25
Al	Kα	1.49
Si	Kα	1.74
Cr	Kα	5.41
	Kβ	5.95
Fe	Kα	6.40
	Kβ	7.06
Cu	Kα	8.04
	Kβ	8.90

Table 3.2 – EDX peak energies

3.7 Summary

The equipment described in this chapter enabled the characterisation and subsequent data acquisition from the samples of interest. Even before this could be done, the samples had to be prepared and made into a form that could be analysed within the microscope. The following chapter discusses the materials systems used and the procedures involved in their preparation for electron microscopy.

CHAPTER 4

SAMPLE SELECTION AND PREPARATION

Generally, theoretical expressions found in literature for interfacial loss functions consider ideal interfaces, where 'ideal' means sharp, planar interfaces which are exactly parallel to the incoming beam (Fig. 2.2). If experimental results are to be accurately compared with theory, the interfaces chosen must meet these criteria as closely as possible. Therefore it is of interest to select a material system known to contain interfaces of this nature. Further to this, application of additional criteria on the choice of material system can simplify the data acquisition and subsequent analysis. In particular, it is beneficial to choose a system which is well understood, where the component materials have narrow bulk plasmons which are well separated (at least ~1.5-2 eV) and where samples are relatively simple to prepare.

Two systems that met these requirements were selected. The systems were Al/Mg_2Si and Al/Si. For these two systems the sample preparation techniques are very similar and are covered in the following sections.

4.1 Al/Mg_2Si System

The Al/Mg_2Si system refers to a system composed of an aluminium matrix containing small magnesium silicide (Mg_2Si) platelets. One of the simplest ways to create such a system is by heat treatment of an Al/Mg/Si alloy. The specific alloy selected was a 6061 alloy which has a nominal composition of 97.93 wt% Al, 1% Mg, 0.6% Si and the remainder largely comprising Cr and Cu. This alloy is of interest to industry as upon heat treatment it forms small hardening precipitates which trap dislocations. This results in a strong, light material. The alloy is extremely useful as a structural material and has applications for example in the manufacture of bikes and racecar components. These applications arise as a result of its medium strength and low cost compared to other aluminium alloys. It was of interest for this project as with sufficient heat treating it is known to form equilibrium magnesium silicide platelets large enough for the work required.

Magnesium silicide platelets are known to be incoherent with respect to the surrounding aluminium (Eskin *et al*, 1999). However, they do have a known orientation relationship. It is found that (100)Al ‖ (100)Mg_2Si, [100]Al ‖ [110]Mg_2Si (Fig. 4.1) (Jacobs, 1972). This orientation relationship was used within the microscope to align the interface accurately to be parallel to the incident electron beam (section 5.2).

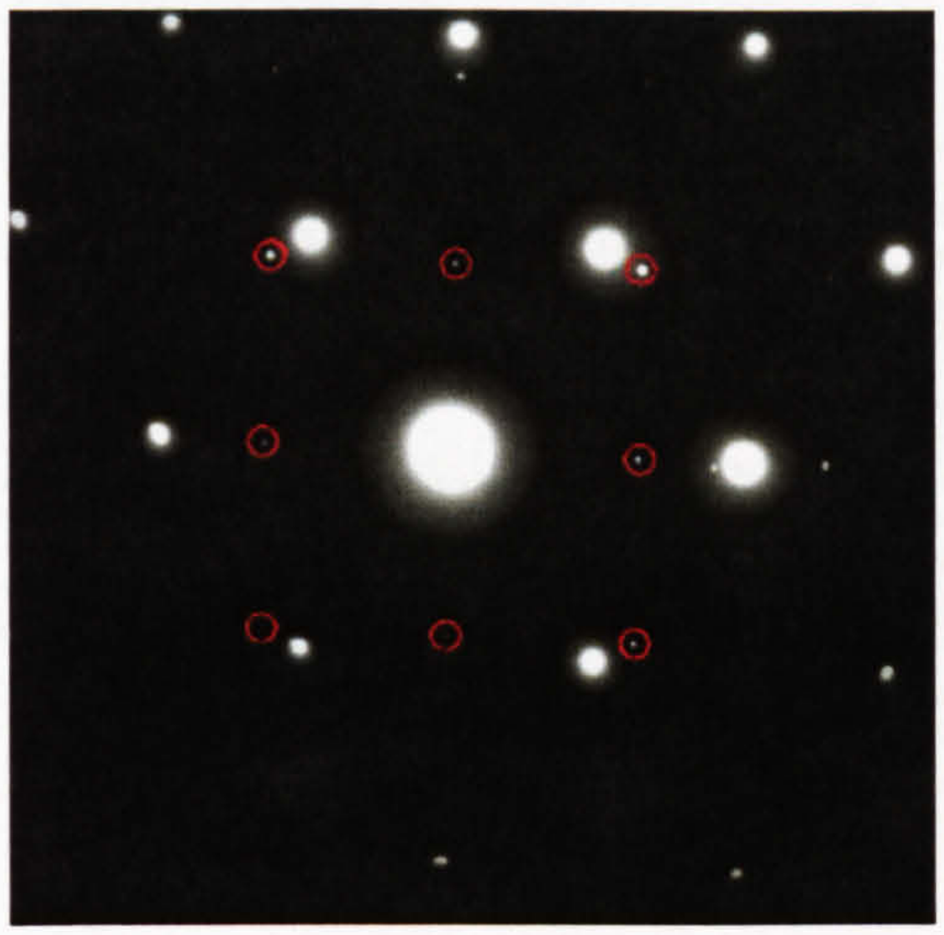

Figure 4.1: [100] Diffraction pattern from the edge of an Mg_2Si precipitate (circled in red) including the [110] diffraction pattern from aluminium.

Mg_2Si is only one of several precipitates that form in Al/Mg/Si alloys (Thomas, 1961; Jain, 1992; Zhen *et al.*, 1997). Each precipitate appears at a different stage of the precipitation process and further heat treating will 'transform' one precipitate into another. The sequence of precipitate formation goes as follows, in order of increasing heat treatment:

- Pre-precipitate clusters
- β" precipitates
- β' precipitates
- β equilibrium Mg_2Si

The β" precipitates are long, thin, needle-like precipitates (Fig. 4.2) and were too narrow to be of use in this project. The crystallography and composition of these precipitates is a matter of continuing discussion in the literature. The β' precipitates are more rod-like than the β" precipitates and they are thicker and tend to be shorter. It can be difficult to differentiate between β' and β" precipitates in isolation. However, when both are seen together, the difference is clear. As with the β", the crystallography and composition is not

agreed upon in literature. There is also a B' precipitate mentioned in literature (Edwards *et al.*, 1998) which has a square cross-section unlike the β' which has a circular cross-section. It was the β-Mg_2Si that was actually of interest. These are cuboidal platelets which 'grow' from the β' precipitates. These cuboidal platelets have the structure of bulk Mg_2Si *i.e.* anti-fluorite structure with a unit cell dimension of 0.639nm (Matsuda *et al.*, 1999).

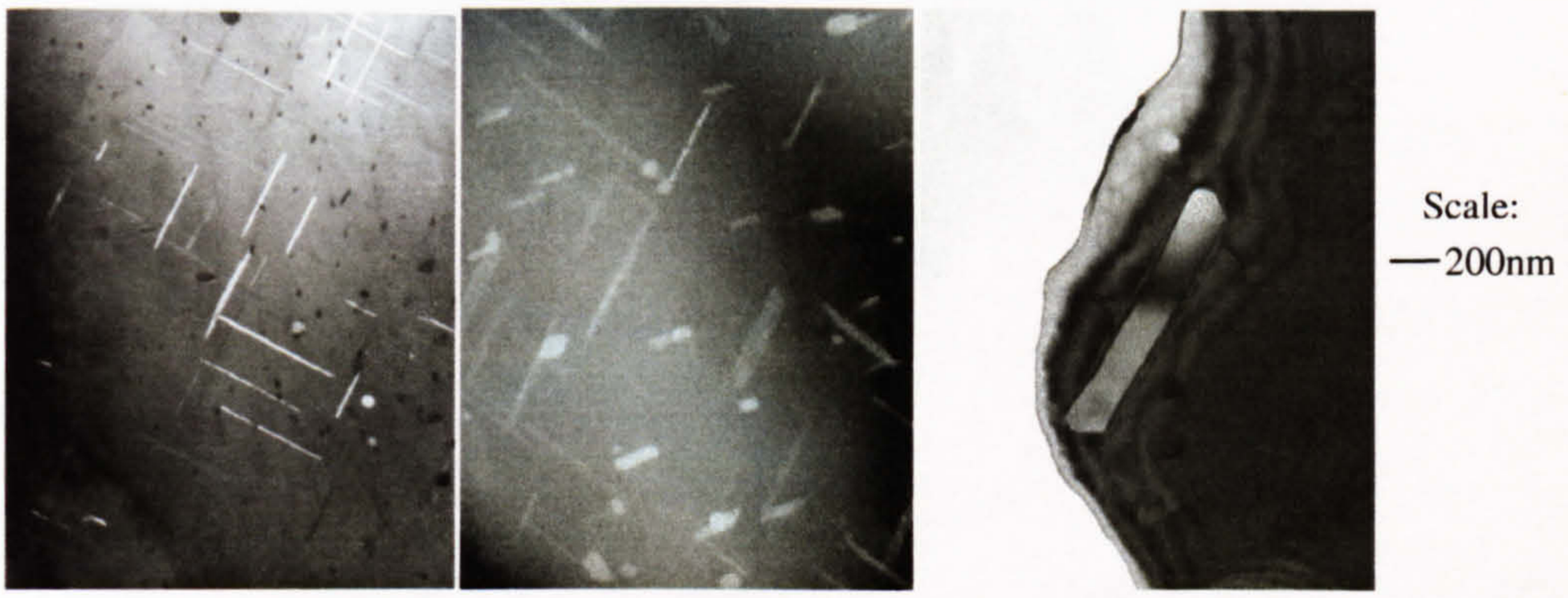

Figure 4.2: TEM images showing three different precipitate types present in 6061 Al alloys. *Left* is predominantly β" rods, *centre* shows the thicker β' rods and *right* shows a β plate precipitate.

The alloy was initially bought in the form of a commercially available rod. Samples made from this rod were found to contain small precipitates of unknown composition. These precipitates were so numerous that they would often encroach on areas of interest making those areas unusable. X-ray spectroscopy of these precipitates indicated the presence of iron (Fig. 4.3). Atomic absorption spectroscopy revealed that iron was present in the alloy as an impurity at a level of approximately 0.5at%. A higher purity alloy was provided by Prof. George Weatherley, which had a similar composition to the commercial alloy but with less Fe present. Samples made from this alloy were found to contain considerably fewer of the impurity precipitates.

Preparation of samples for microscopy involved two main processes: thinning to electron transparency and heat treatment to form the desired precipitates. The bulk of the thinning was performed mechanically, with the remainder done by ion milling. Mechanical thinning puts strain on a sample, causing dislocations. These are undesirable, as dislocations in an area are known to have an effect on the EELS spectra taken from that area (Batson, 1999, Kolodzi *et al.*, 2001). This was potentially problematic, as dislocations moving through the sample would become pinned by the precipitates. Over time the number of dislocations at the interface would build up, with the potential to alter the EELS spectrum. The heat

treatment dissolved existing precipitates allowing the dislocations to move. New precipitates were then formed later in the process. It was decided to perform the heat treatment subsequent to mechanical thinning and prior to dimple grinding or ion milling. By performing the processes in this order, the number of dislocations caused by the mechanical preparation was greatly reduced whilst also avoiding problems caused by heat treatment of a very thin (<50μm) aluminium specimen (section 4.1.2).

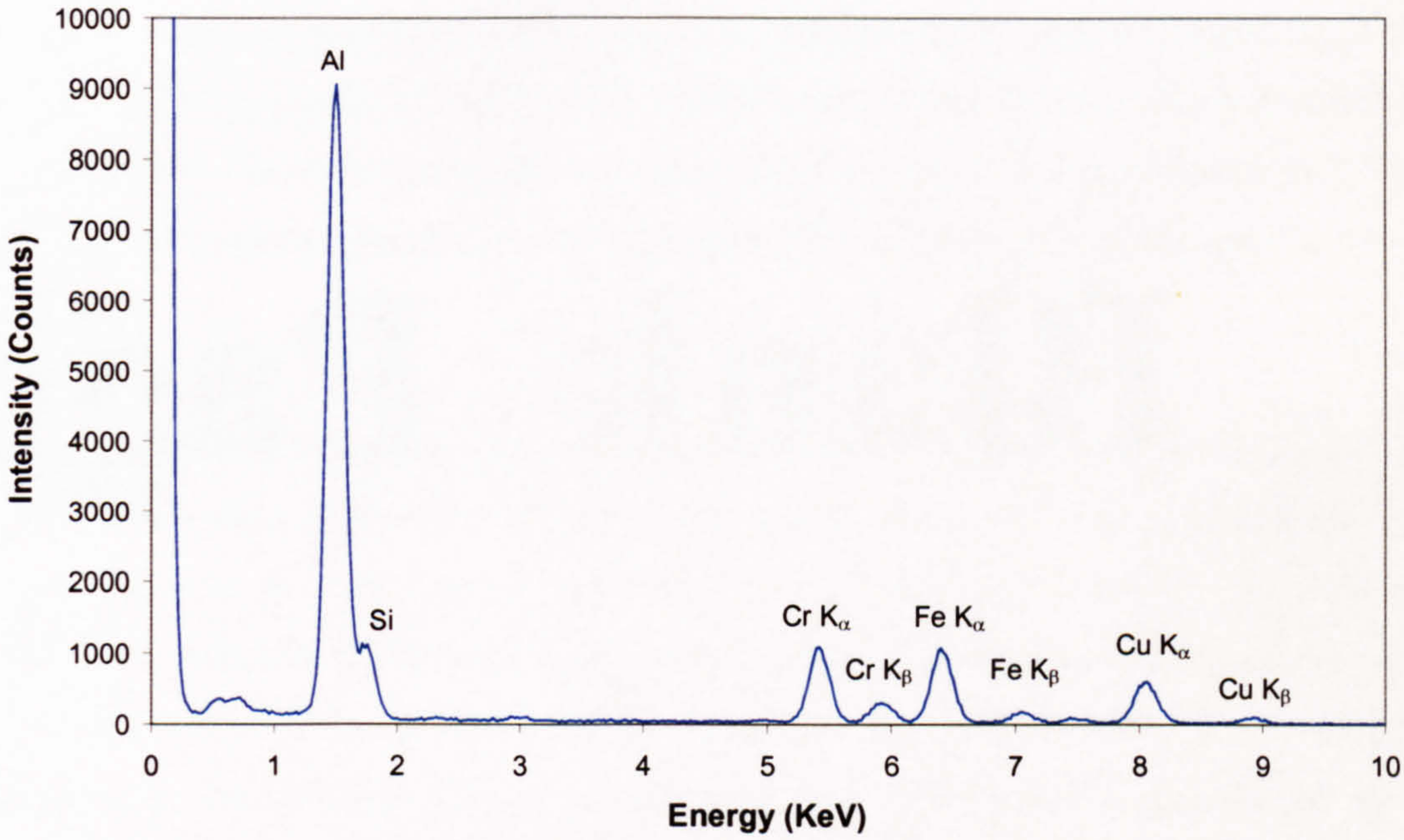

Figure 4.3: X-ray fluorescence spectrum of small impurity precipitates. Main peaks are marked with the element to which they correspond.

4.1.1 Mechanical Grinding

The first step of the sample preparation procedure was the manufacture of the basic disks. Disks of 1-2mm thickness and 3mm diameter were punched out of the bulk alloy using a standard metal punch. A disk was then mounted onto a glass slide using wax as an adhesive. The bulk of the thinning was done by grinding the disks on coarse silicon carbide paper, until the thickness of the disk was close to that desired. The disk was then ground on consecutively finer grades of paper, each grade being used to remove the scratches of the previous one. The disk was then polished on a rotating polishing wheel using 3μm followed by 0.25μm diamond paste. Polishing removed large scratches and any major damage caused by the silicon carbide paper. The samples were polished to a thickness of 200μm and were then ready for the heat treatment process.

4.1.2 Heat Treatment

The purpose of the heat treatment process was to encourage the formation of suitably sized equilibrium magnesium silicide platelets. As has been mentioned previously the magnesium silicide platelets are last in a precipitation series in the alloy. If such an alloy is not heat treated enough, only the precipitates appearing early in the sequence will be formed. Conversely, if the alloy is heat treated for too long at too high a temperature it can result in loss of magnesium from the alloy (Eskin *et al.*, 1999), altering the composition of the precipitates. The heat treatment was made up of two parts: solution treatment, which dissolved the existing precipitates and ageing, which actually caused the growth of the precipitates.

Solution treatment of the alloy was performed first. If the alloy is not solution treated the majority of the alloying elements will be used in a large number of smaller precipitates and so unavailable for the formation of larger precipitates. Solution treatment involves heating a material to dissolve all the precipitates already present. This puts the alloying elements into solid solution allowing them to be dispersed equally about the solid. These alloying elements are then available for the formation of large precipitates during ageing. As a result, solution treated alloys should produce larger, better quality precipitates upon heat treatment. Another effect of solution treatment is the removal of strain and dislocations within the system, particularly dislocations pinned by precipitates during mechanical polishing. Performing a solution treatment effectively 'resets' the alloy, removing the effects of previous ageing treatments. As a solution treatment requires to be at a higher temperature than ageing processes it was this stage that was most likely to result in loss of magnesium.

The solution treatment was performed at 550°C for 15 minutes followed by a quench in brine to room temperature. A quench is a reduction in temperature which occurs over such a short time period that the alloy remains effectively unchanged through the lower temperatures.

The possibility was considered that the increased temperature would result in increased oxidation of the alloy. However, this was believed to be unfounded as the nature of

aluminium oxide is such that it would protect the alloy from further oxidation. Examination of the sample within a TEM supported this, as no evidence of additional oxide growth was observed. Evidence was observed of the loss of magnesium from the sample. However, at such a high temperature this was unavoidable. For this reason the solution and heat treatment were performed prior to dimple grinding. The thickness of the sample prior to dimple grinding was sufficient to limit the magnesium loss to the surface of the sample, leaving the bulk magnesium content largely unchanged. As the surface of the sample was then removed during dimple grinding, the solution treatment was not believed to have any deleterious effects.

The other step in the heat treatment was ageing of the sample. A variety of ageing treatments were investigated. Initially a treatment of 300°C for 1 hour was used. This was found to be insufficient as the majority of precipitates were of the β" type which were not of interest. Some β platelets were evident but they were too few and too small to be of use.

An extended ageing treatment of 6hrs at 350°C was then used. The resultant samples appeared to contain no β" needles, a few β' rods and largely β platelets. It was believed that with additional ageing the number and size of platelets would be increased. To this end, the ageing treatment was extended further.

The final ageing treatment, the one used in the manufacture of all the samples for this thesis, was for 48 hours at 350°C. For this treatment the disks were wrapped loosely in aluminium foil and placed in a silica crucible. The purpose of the aluminium foil was merely to separate the aluminium disks from the silica crucible.

The samples resulting from the ageing treatment were found to contain a number of fairly large Mg_2Si platelets. None of the other Mg/Si precipitates were evident. According to literature, magnesium silicide platelets are cuboidal. The precipitates within the samples rarely displayed regular rectangular shapes (Fig. 4.4). Originally this was believed to result from the ageing treatment being insufficient to allow the Mg_2Si to reach its equilibrium shape. To test this hypothesis, a variety of samples which had been aged for different times were examined. It was found that the shape of the precipitates did not change appreciably between different samples. In addition, X-ray and EELS spectra taken from the precipitates

indicated that they were bulk Mg_2Si. This suggests that the actual reason for the unexpected shapes was that the precipitates were milled by ion milling in planes not parallel to the faces.

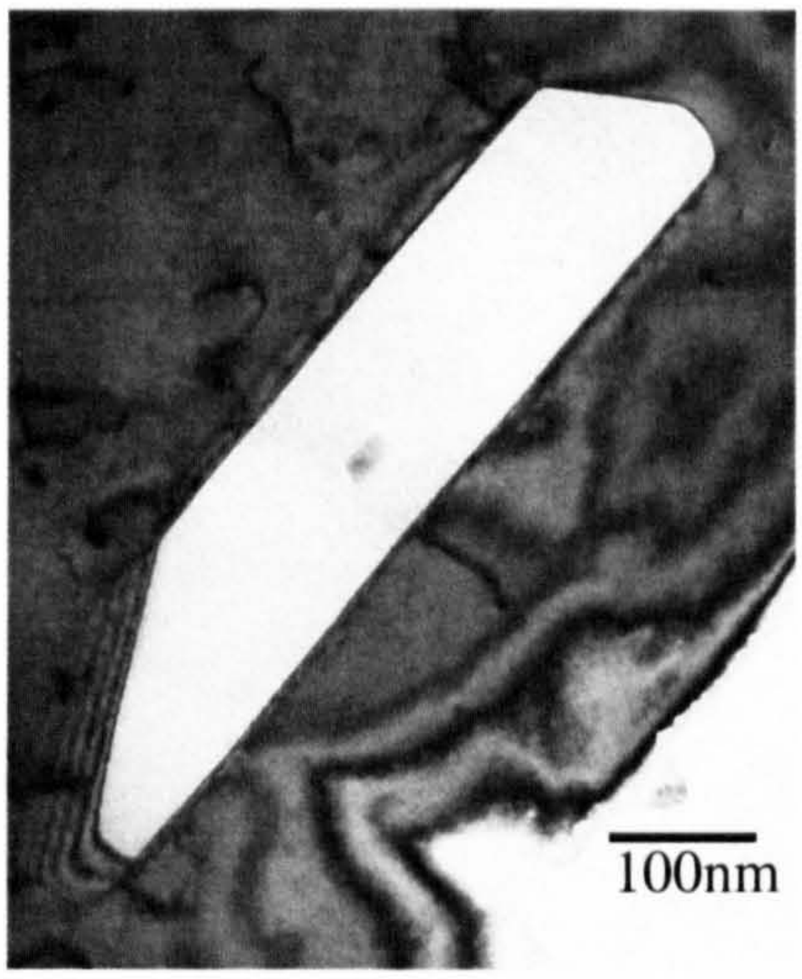

Figure 4.4: An Mg_2Si precipitate.

4.1.3 Dimple Grinding

Following heat treatment, the samples required to be thinned further prior to ion milling. As the samples were entirely self-supporting (many sample thinning techniques involve adhering a thin copper ring to the sample, this provides extra strength to the sample and helps to prevent damage from handling), excessive thinning would make the disks extremely delicate and difficult to handle.

Samples produced by a dimple grinder have only the centre area thinned, leaving a thicker ring of sample around the edge. This thicker ring makes the sample less susceptible to damage caused by manipulation with tweezers. The area in the centre is considerably thinner and is of a thickness suitable for ion milling. By thinning the samples with a dimple grinder it was possible to make a much thinner sample whilst still allowing it to retain sufficient strength.

A dimple grinder works by rotating a small wheel at a variable speed of between about 60 and 500 rpm. The edge of this wheel is covered with a small quantity of abrasive paste and lowered onto the centre of the sample. The rotation of the wheel causes agitation of the abrasive paste, which grinds away the centre area of the sample. The sample itself is

mounted on a rotating table, the speed of which is linked to the speed of the grinding wheel but is considerably slower. The simultaneous rotation of wheel and table results in the grinding of a dimple in the centre of the sample. The dimple grinder is set up in such a way as to allow the user to set the depth of the dimple prior to dimpling (Fig. 4.5). The dimple grinder will then operate until that depth is reached and self-terminate.

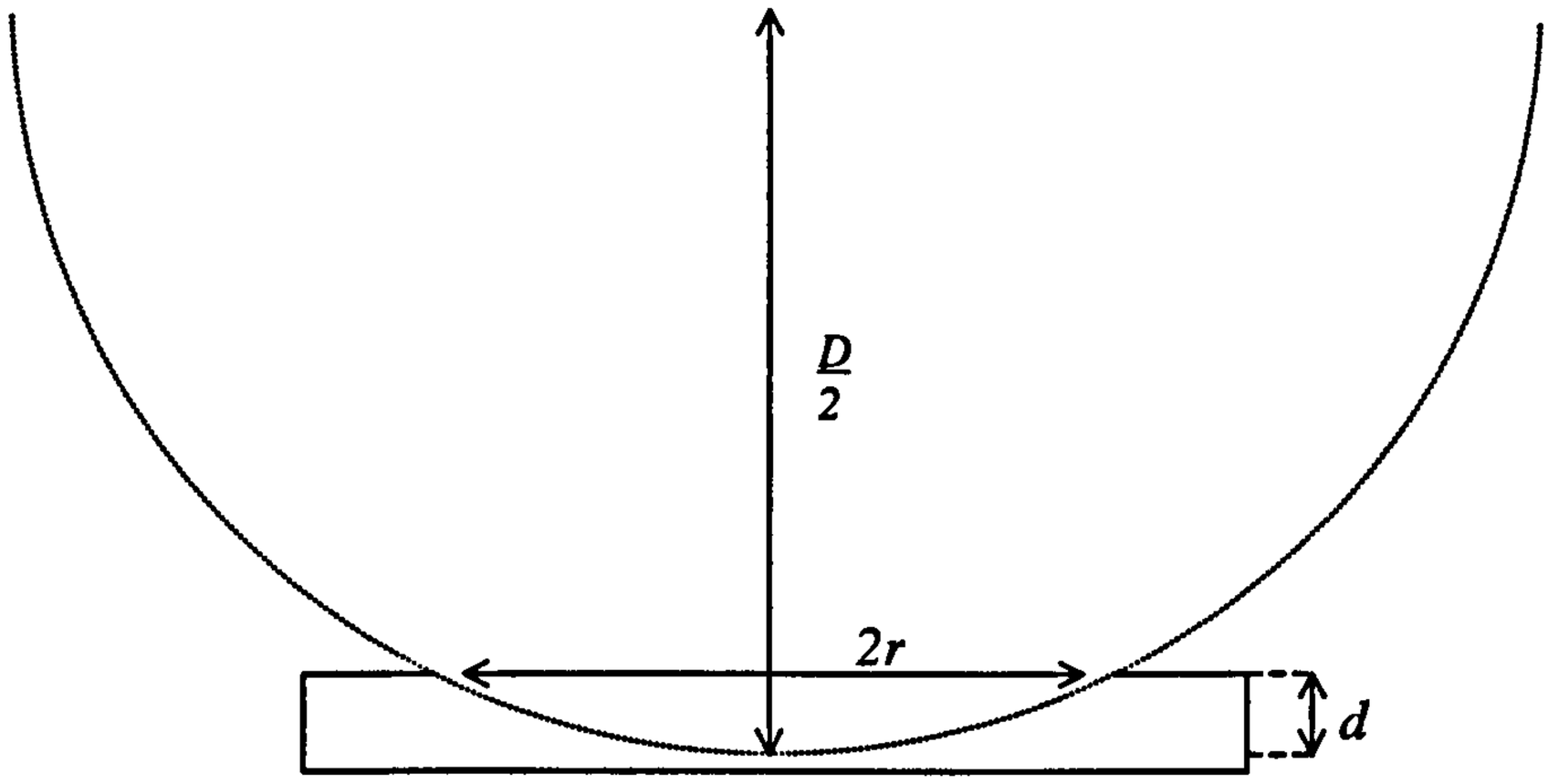

Figure 4.5: Schematic of dimple grinder set-up. *D* is the diameter of the grinding wheel, *2r* is the diameter of the dimple and *d* is the depth of the dimple.

It is known that when dimple grinding a soft material, abrasive from the paste can become embedded in the sample. This results in wearing of the wheel as it moves over the embedded abrasive and a corresponding decrease in the thinning rate of the sample. As aluminium is a soft material, concern was expressed regarding the use of dimple grinding for this project. However, no decrease in thinning rate of the sample or increase in the wear rate of the wheel was evident for aluminium samples compared to samples of harder material.

The samples produced for this thesis were made using a 15mm diameter stainless steel wheel rotating at a speed of between 200 and 300 rpm. The table was rotated at ~6 rpm. In all cases a dimple depth of 180μm was used, leaving a thickness of 20μm at the centre of the sample.

In each case, the bulk of the dimple was ground using 3μm diamond paste. The sample was then cleaned and the remainder done using 0.25μm diamond paste. As with the mechanical grinding, this was done to remove the scratches caused by the previous step.

Finally, the grinding wheel was replaced with a polishing wheel. A polishing wheel has a similar diameter to the grinding wheel except that the area which contacts the sample is made from a soft felt material. The polishing wheel was used with a 0.02μm alumina suspension to remove any remaining scratches and leave the disk as smooth as possible. The use of the polishing wheel meant that the final thickness at the centre of the disk was less than 20μm.

4.1.4 Ion Milling

Once the disk had been dimpled it was necessary to clean it prior to ion milling. The purpose of the cleaning was to remove as many possible contaminants from the surface of the sample as possible. In particular, the presence of hydrocarbon contamination was known to be problematic when taking data in the microscope. Cleaning the sample prior to ion milling meant that a more rigorous cleaning method could be used, with the consequence that more of the hydrocarbon contamination would be removed.

The sample was cleaned using a soxhlet apparatus. Soxhlet apparatus is basically the same as reflux apparatus except that instead of the condensed solvent returning straight to the flask being heated, it is trapped in an upper compartment where the sample is held. This hot solvent dissolves hydrocarbons from the sample and holds them in solution. Once the amount of solvent in the upper compartment increases beyond a certain level, the solvent is exhausted out into the flask, taking the hydrocarbons still held in solution. At this point the process is able to repeat, as the solvent evaporates at a lower temperature that the hydrocarbons. The samples were soxhlet cleaned for approximately 1-2 hours using inhibisol (1,1,1 – trichloroethane with additions to inhibit certain reactions) as the solvent.

Following soxhlet cleaning, the samples were placed in an ion mill and thinned to electron transparency. Ion milling is a slow process, with the time taken dependent on the original thickness of the sample. It was for this reason that it was desirable to make the sample as thin as practical before ion milling in order to reduce the time necessary. For the samples prepared as above, the ion milling process would take of the order of 12 hours continuous milling.

The ion milling was performed using a Gatan DuoMill. Within the DuoMill the sample is held in a chamber at vacuum (nominally $3x10^{-7}$ torr) and is bombarded by argon atoms and ions. These effectively knock out ions from the sample, slowly thinning the sample. Two ion guns, one positioned above and one below the sample, produce and collimate the ion beam at the centre of the sample. This enables the sample to be thinned equally from both sides. As with the dimple grinder, the sample is constantly rotated. This results in the sample thinning more evenly. The rate of thinning is dependent on the angle between the ion beam and the sample, the greater the angle (for angles less than 45°) the faster the thinning is achieved. However, larger angles also increase the depth of damage done by the ion beam so a balance must be struck. All samples were thinned using an angle of 12° and a rotation speed of 2 rpm. The ion guns had an applied voltage of 4kV at a current of 0.5mA.

As mentioned previously, ion milling of a sample is a long process. The DuoMill is fitted with a laser auto-terminator that stops the milling as soon as the laser light transmitted through the sample exceeds a certain level. As the amount of light transmitted is related to the thickness of the sample, the level can be set so the DuoMill terminates once the sample is electron transparent. This allows the machine to be left unattended for long periods. The laser is only capable of being detected once every revolution, which for 2rpm, means every 30 seconds. Since the rate of thinning is so slow, the delay in detection does not present a problem. One possible problem was the redeposition of sputtered material from the sample. Clearly, as material is being knocked out of the sample, that material may be redeposited elsewhere. One of the areas that it was evidently being redeposited was on the viewing window. This window is used not only for viewing the sample but it also allows the laser to pass into the vacuum chamber. As the amount of redeposited material on the window increases, the amount of laser light falling on the sample decreases. If the amount of redeposited material on the window varies, it is likely that the thickness at which the ion mill terminates will vary also. It was observed that the amount of material redeposited on the window did change between samples. This was possibly due to differences in the initial thickness of the sample and also to randomness in where the material was redeposited. As a result it was difficult to set the auto-terminator to create reproducibly thin samples.

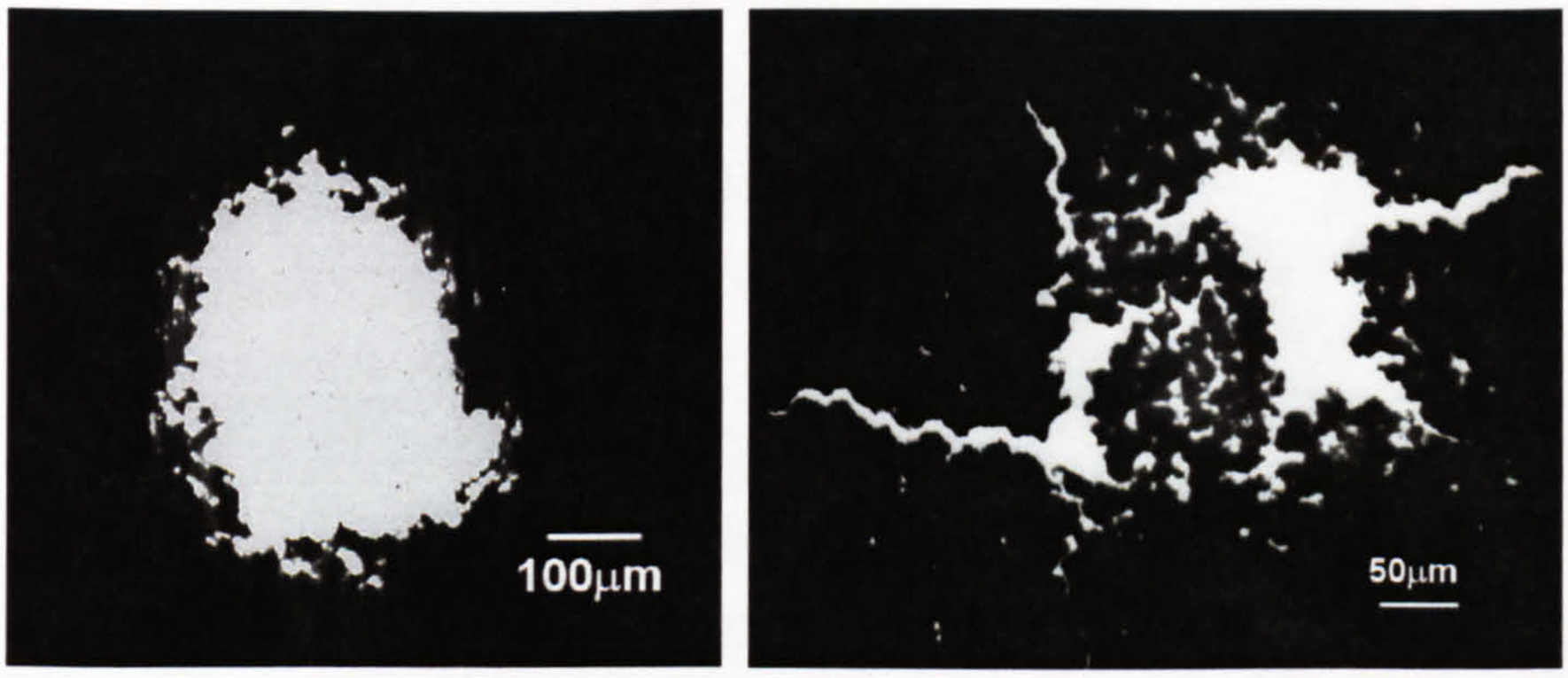

Figure 4.6: TEM images at low magnification of different samples. *Left* shows a large hole compared with *right* where a similar preparation process resulted in a number of smaller holes.

It was believed that the ion mill should make a large area of the sample electron transparent with only a small hole at the centre. In general, this was found not to be the case. In order to have a sufficiently large amount of thin area it was necessary to allow the thinning of a single large hole in the sample. Alternatively, a similar length of time often resulted in the thinning of a number of small holes (Fig. 4.6). If only a single small hole was present, the quantity of thin area was negligible.

4.2 Al/Si System

The Al/Si system was developed from the Al/Mg/Si system using the knowledge that magnesium is lost with excessive heat treatment. Samples that were accidentally solution treated for too long were found to contain solely silicon precipitates and no Mg/Si precipitates. By deliberately using extended solution treatment times, samples containing Si precipitates were made. Following the solution treatment, these samples differed from the previous samples only in the magnesium content. This enabled the remainder of the sample preparation to be performed in the same way as previously, including the ageing treatment.

In fact, silicon precipitates were also present in the samples which had been solution treated for the correct amount of time. It has been suggested that silicon is another of the pre-Mg_2Si phases in the precipitation sequence (Zhen et al, 1997), however this does not appear to be supported in any other studies. One study (Eskin et al, 1999) concludes that silicon precipitates start growing early in the Mg/Si precipitation sequence but do not form

a part of it. Indeed few papers mention the presence of Si precipitates at all, perhaps unsurprising as the number noticed within the Mg_2Si samples for this thesis was very limited. In total, of the order of 2-3 Si precipitates were noticed within a single sample compared to about 30 or 40 Mg_2Si precipitates.

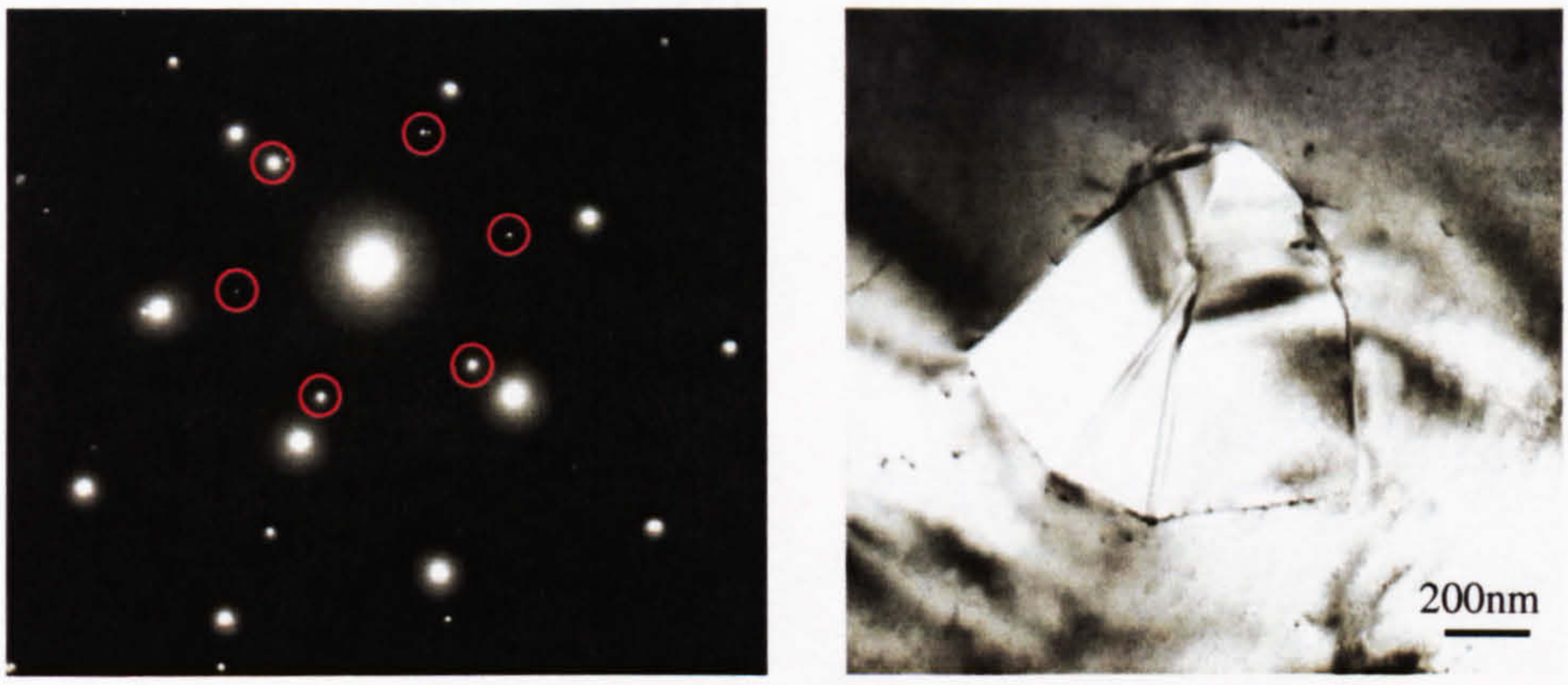

Figure 4.7: Electron diffraction pattern (*left*) showing aluminium and silicon (*circled*) diffraction spots. *Right* shows precipitate from which the diffraction pattern was acquired.

The Al/Si system does not appear to be as well covered in literature as the Al/Mg/Si system, presumably due to the greater number of commercial applications of the latter. However, orientation relationships between aluminium and silicon have been reported (Kobayashi *et al.*, 1976). These relationships are considerably more complex than that for Al/Mg_2Si. The presence of twinning within the silicon precipitates makes determination of orientation relationships complex. Fig 4.7 gives the diffraction pattern recorded from a precipitate within one of the Al/Si samples and the bright field image of the corresponding precipitate. The computer program *Desktop Microscopist* was used to visualise theoretical diffraction patterns and it is believed that the observed diffraction pattern agrees with the theory, allowing for twinning in the precipitate.

4.3 Summary

All the data in this thesis were acquired from samples prepared in the manner described above. The choice of systems was very important in simplifying the process of experimentally proving the theoretical equations describing energy loss from interfaces. The two systems chosen, despite both only providing aluminium/semiconductor interfaces, were sufficiently different to give two separate experimental verifications of eqn 2.33. The techniques used to acquire the data necessary for this are given in the next chapter.

CHAPTER 5

DATA ACQUISITION AND ANALYSIS

In this chapter the various techniques used in the acquisition and processing of the experimental results will be discussed. This includes all the methods used, from initially selecting and aligning an interface of interest, through to analysis of the data. Prior to this, it was necessary to ensure the validity of some of the techniques used. This is discussed in the first section.

5.1 Verifying Analytical Techniques

Many of the methods used in the analysis were standard and well established techniques. However, some more unusual methods were used as they resulted in better quality data. These methods had checks performed on them to ensure that their use was valid. The techniques and validity checks are outlined below.

5.1.1 Linearity of Detector Response

It was generally believed by users of the system, that the response of the photodiode array became non-linear when the number of counts in a single channel increased above 10,000. It was for this reason that it was standard practice to set the beam-blanking unit such that the maximum number of counts in any channel was $<10^4$. It was decided to investigate the number of counts at which the detector response became non-linear. If it transpired that the response was linear up to higher values, it would enable a greater count rate to be used and so provide better signal to noise ratio in the spectra.

To test the detector response, a series of zero loss peaks were obtained from a hole in the specimen. The blanking time was varied between acquisitions so the maximum number of counts in the largest channel varied from about 3000 counts up to 16000 counts. A higher number of counts was not possible as the photodiode array saturates at ~16000 counts. These spectra then had the dark current removed and were aligned (see also section 5.4). A plot of each zero loss peak is given in Fig. 5.1 (*top*). As each spectrum is a sum of 100 acquisitions the total number of counts is much larger. For convenience the zero loss peaks

in Fig. 5.1 have been divided by 10^6. In addition, a ratio was taken of each spectrum with ZL 1, the spectrum containing the highest number of counts (Fig. 5.1 *bottom*). It was observed that the ratio was effectively constant over the range of the zero loss peak for all the different spectra. This indicated that the detector response was linear over the range of counts examined. Perhaps surprisingly, even at high counts little deviation was observed, despite the proximity to saturation. This result validated the use of a greater intensity in the spectrum. In addition, it allowed the development of a further technique.

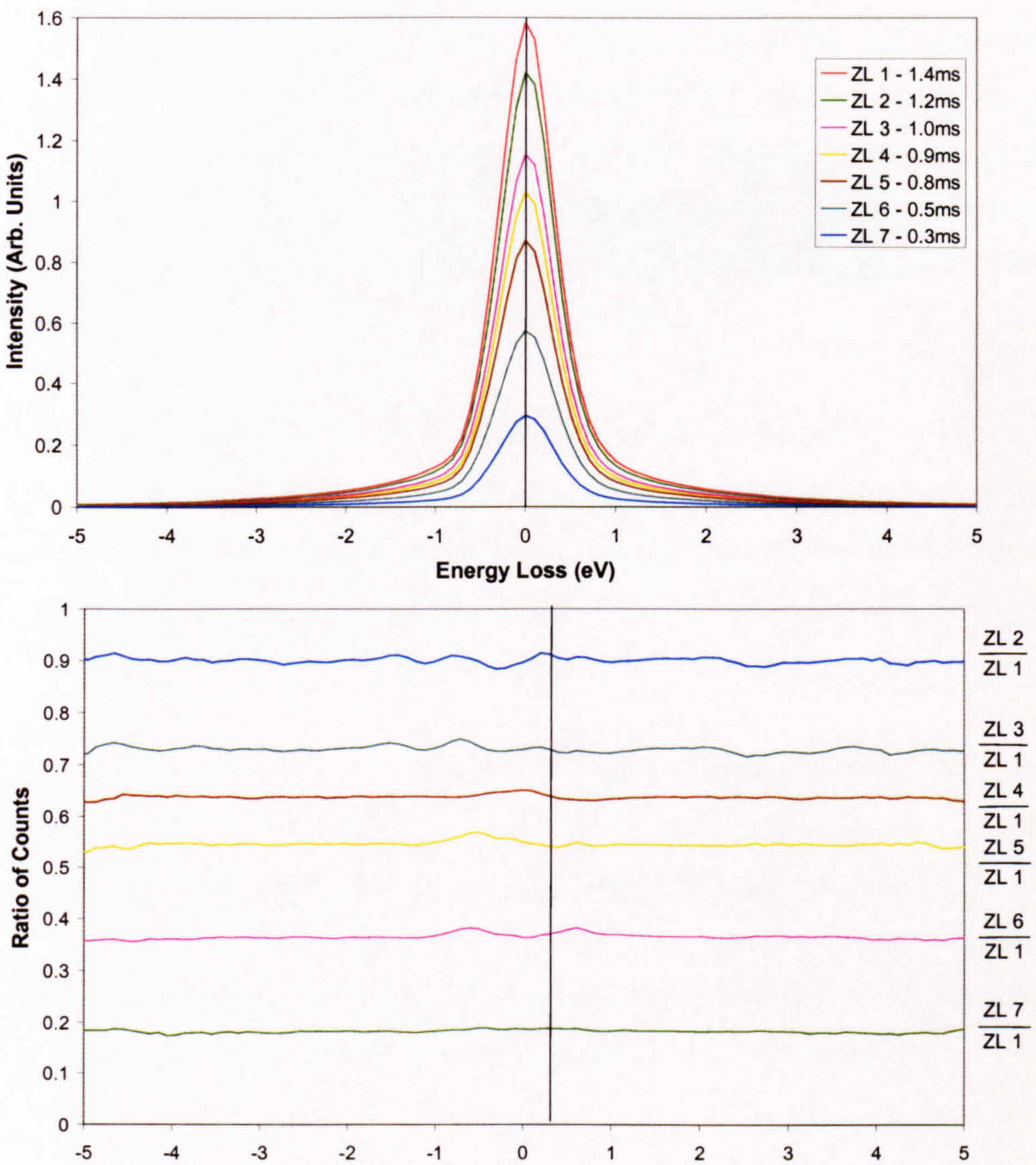

Figure 5.1: Comparison of zero loss peaks acquired with different blanking times (*top*), given is the time during each acquisition that the beam was unblanked. *Bottom* gives the ratio of counts in each zero loss peak.

5.1.2 Substitution of Zero loss Peak into a Saturated Spectrum

Once it had been established that the detector response was linear up to high counts, the possibility of collecting spectra in which the zero loss peak had been allowed to saturate was considered. By allowing the zero loss to saturate, the number of counts in the rest of the spectrum was greatly increased. This resulted in a much larger signal to noise ratio and hence gave better data. As an unsaturated zero loss peak was required for performing a fourier-log deconvolution (section 2.1.2) the presence of a saturated zero loss peak would prevent proper processing of the data. It was therefore necessary to replace the saturated zero loss peak with an equivalent unsaturated peak. This could be done by copying channels from an unsaturated spectrum to a saturated one, assuming the spectra were suitably scaled. Scaling was carried out by altering the intensity of the saturated spectrum to make the magnitude of the lower energy tail of the zero loss peak equal to the same region in the unsaturated spectrum (see also section 5.3.2).

To verify this technique, three types of spectra were recorded. These were a saturated spectrum from the sample, an unsaturated spectrum from the sample and an unsaturated spectrum taken through a hole in the sample. Following acquisition of these spectra, the dark current was removed. The spectra were aligned and scaled so that the number of counts in the region –2.5→-1.5eV was the same.

Figure 5.2 shows a plot of the saturated and unsaturated spectra overlaid. Also shown on this figure is the ratio of the number of counts in the unsaturated spectrum to that in the saturated spectrum. With exception of the area around 0eV, the two spectra showed very strong similarity. This was echoed in the ratio graph, which was effectively constant except for the channels where the zero loss peak has saturated. This result indicated that using a saturated spectrum with a replacement zero loss peak was a valid technique.

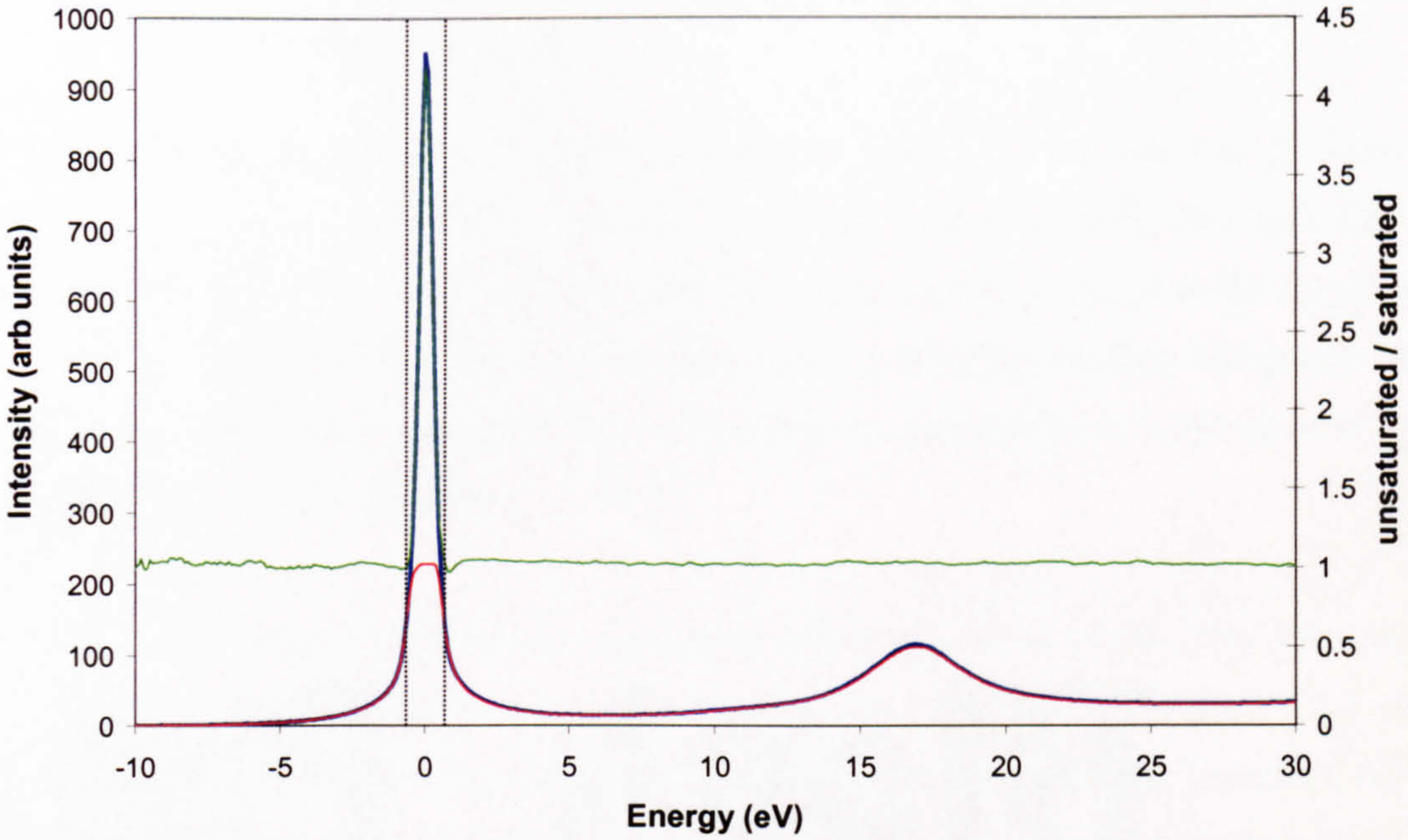

Figure 5.2: Graph comparing scaled saturated (*red line*) and unsaturated (*blue line*) data. Also shown is the ratio of unsaturated to saturated data (*green line* using right-hand axis) indicating the strong similarity in the spectra. The vertical lines indicate the region of replacement.

It was of interest to extend this investigation further to test whether a zero loss peak acquired from a hole would act as a suitable replacement. If it was, then a single unsaturated spectrum taken from a hole could be used, suitably scaled, to replace the zero loss from any saturated spectrum with the same energy resolution and dispersion.

The spectra were compared in the same way as previously and the results indicated that an unsaturated spectrum could be used as a replacement without introducing artefacts. In fact, it is sufficient just to replace the central portion of the zero loss, this area is marked by vertical lines in Fig. 5.2. Beyond this region the original and replacement spectra are identical. By using the saturated data spectra with a single corresponding zero loss peak from a hole, it was possible to obtain an excellent signal to noise ratio whilst not requiring a large number of additional spectra.

5.1.3 Kramers-Kronig Program

As mentioned previously, the Kramers-Kronig transformation on the data was performed by a computer program, *DK*. Before making use of *DK*, it was desirable to check that it produced accurate results. To do this, the output of the program required to be compared with reference dielectric functions. Fortunately there is a large quantity of optical and dielectric data available in the literature which can be converted or used directly for comparison (Palik, 1985; Daniels *et al.*, 1970).

Bulk EELS data were acquired from aluminium and magnesium oxide. The data were collected and processed using the procedure described for bulk data in sections 5.3.1 and 5.3.2. The spectra were then imported into *DK* and a Kramers-Kronig Transformation performed. The dielectric functions generated by *DK* are shown in Fig. 5.3. Included in the same graphs are dielectric functions calculated from optical data (Al - Palik, 1985; MgO – Roessler and Walker, 1967).

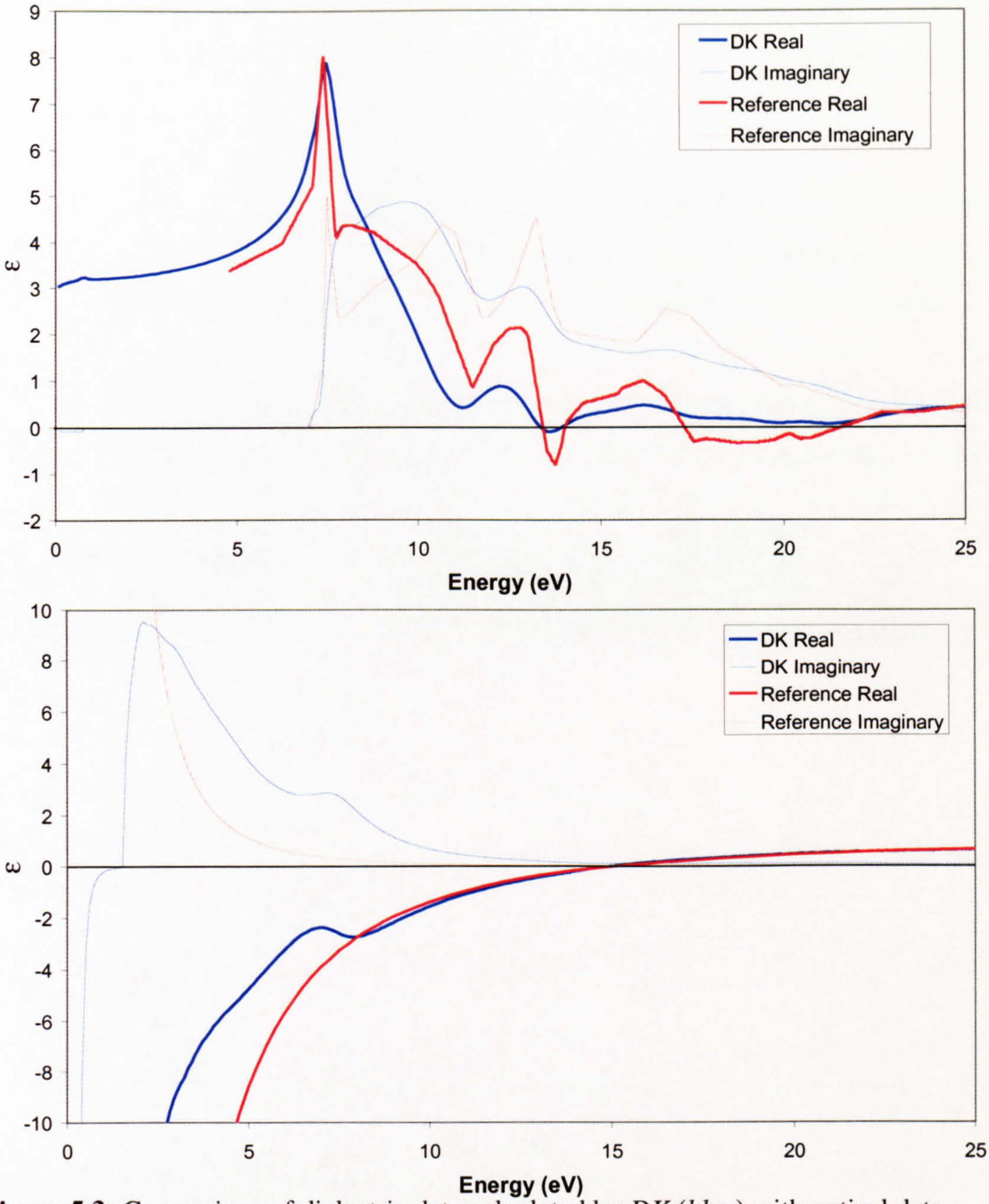

Figure 5.3: Comparison of dielectric data calculated by *DK* (*blue*) with optical data (*red*). *DK* functions are calculated from experimental low loss EELS data acquired from MgO (*top*) and Al (*bottom*).

The dielectric function of MgO appears to deviate quite significantly from the reference function. However, the reference data is taken using reflectance measurements (Roessler and Walker, 1967). This is an optical technique that offers considerably better energy resolution than EELS. The peaks within the *DK* function are not as sharp as those in the reference function. This is likely to be caused by the lower energy resolution of EELS. In

addition, the reference data was taken from a single crystal of MgO, the EELS data was acquired from powdered MgO dispersed on a holey carbon grid. This may also have had an effect on the observed dielectric function. However, a comparison of the peak positions indicates that the *DK* and reference MgO dielectric data are similar.

A greater similarity is observed with the aluminium dielectric function. Above 15eV the two functions are identical. However, deviation is noticed below that energy. It is believed that this is caused by surface effects in the EELS spectrum from the aluminium sample.

In both cases it was believed that the deviation between the dielectric functions was caused by the original EELS data rather than by *DK*. This indicated that the program was working correctly.

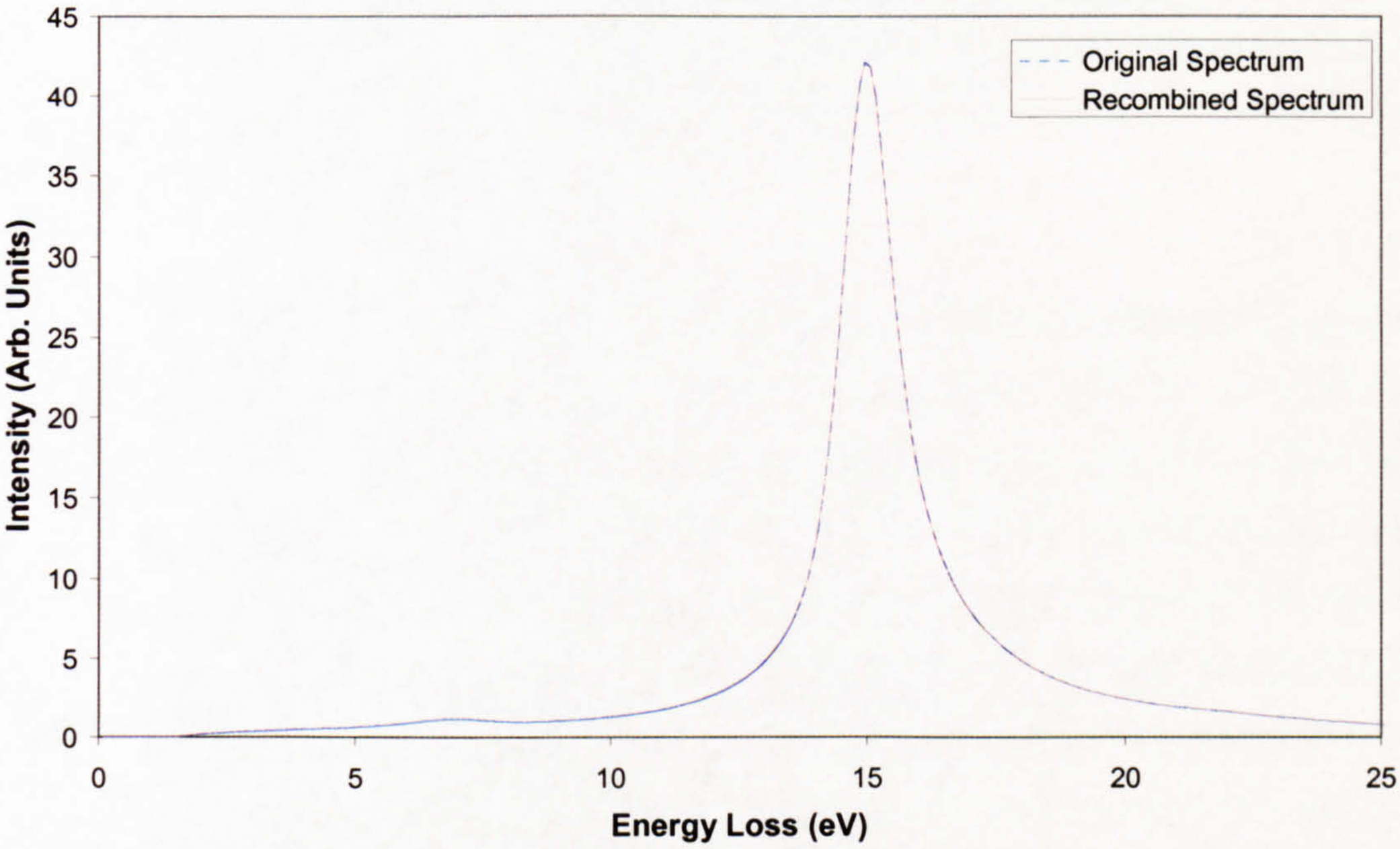

Figure 5.4: Comparison of original energy loss spectrum (*blue*) with spectrum generated by recombined dielectric functions (*red*).

A further test of the program to confirm the results was to recreate a loss function using the dielectric data. The recreated energy loss spectrum should appear identical to the original spectrum used for calculation of the dielectric functions.

Fig 5.4 compares a energy loss spectrum calculated from *DK* dielectric data (Eqn 2.25) with the original experimental energy loss spectrum. The two spectra are identical, as

would be expected. This was further proof that the *DK* program was producing correct results.

5.2 Selecting and Aligning the Interface

Initially it was not felt necessary to select specific interfaces prior to viewing the sample in the STEM as the precipitate interfaces were believed to be sharp and planar. Some selection of interfaces was performed within the STEM. Precipitates that did not go all the way through the sample and so had aluminium covering part of the precipitate could be identified by standard imaging. It was also possible to identify problems with the interface by quickly passing the probe over the interface and viewing the EELS spectrum. If, for example, a spectrum from close to the interface clearly showed two separate plasmon peaks (Fig. 5.5) it was an indication that the interface was tilted. Despite these precautions, early data sets displayed behaviour which deviated from that which would be expected (section 6.1.1). As a result a more rigorous method of interface selection and alignment was employed for the refined technique.

It was decided that the best method of improving the technique was to identify a number of precipitates which were known to have good interfaces and use those for the majority of the data. To identify these precipitates, an extensive study of the specimen was done in the TEM. Each prospective precipitate was examined with the surrounding aluminium tilted to a nearby low-index two-beam condition. If it appeared to have a sharp parallel interface with little thickness variation, suitable images were taken of it for later examination. In addition, a series of images were taken at various decreasing magnifications to provide a map to aid in finding the precipitate at a later point. A diffraction pattern was also taken from the matrix surrounding the precipitate. This procedure was repeated for a number of precipitates.

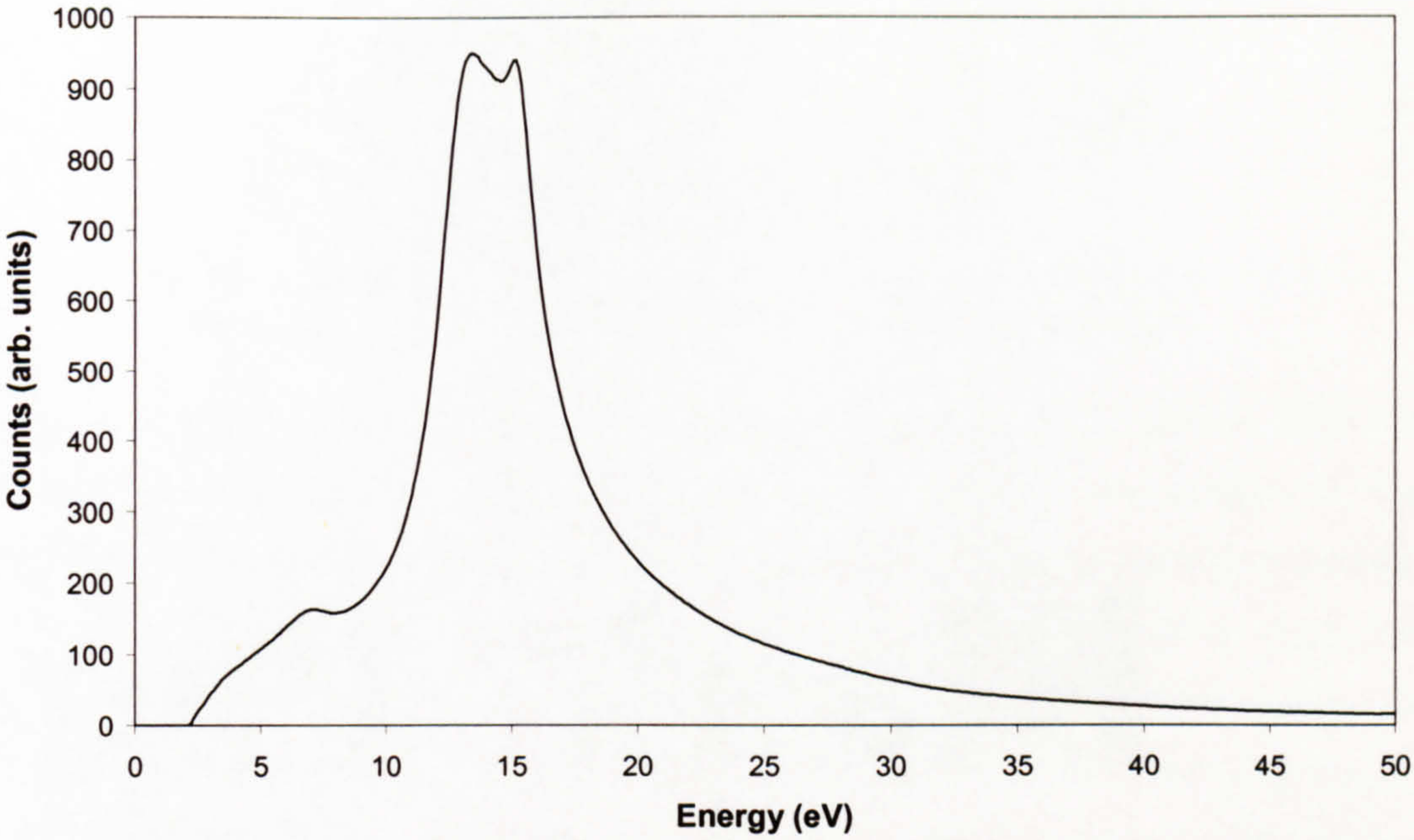

Figure 5.5: Spectrum acquired from a tilted interface. The pronounced double-pronged peak indicates the presence of both aluminium and magnesium silicide bulk plasmons.

Following the microscope session, the images were examined and a number of factors investigated. Firstly, it was important that no thickness fringes were evident in the vicinity of the interface. Thickness fringes at the interface indicated that the interface was tilted slightly with respect to the beam. Thickness fringes in this case were caused by the varying thickness of the aluminium over the precipitate (Fig. 5.6). Secondly, the presence of a large number of dislocations was undesirable, as dislocations are known to affect the low loss spectrum (Brockt and Lakner, 2000) Finally, thickness fringes in the bulk matrix were examined. If the aluminium thickness varied too sharply away from the interface, then it made the comparison between theory and experiment more complex. The 'ideal' case is for no thickness variation at all over the area of interest. Situations close to this were chosen either by selecting interfaces with thickness contours perpendicular to the interface or ones with a large distance between adjacent fringes.

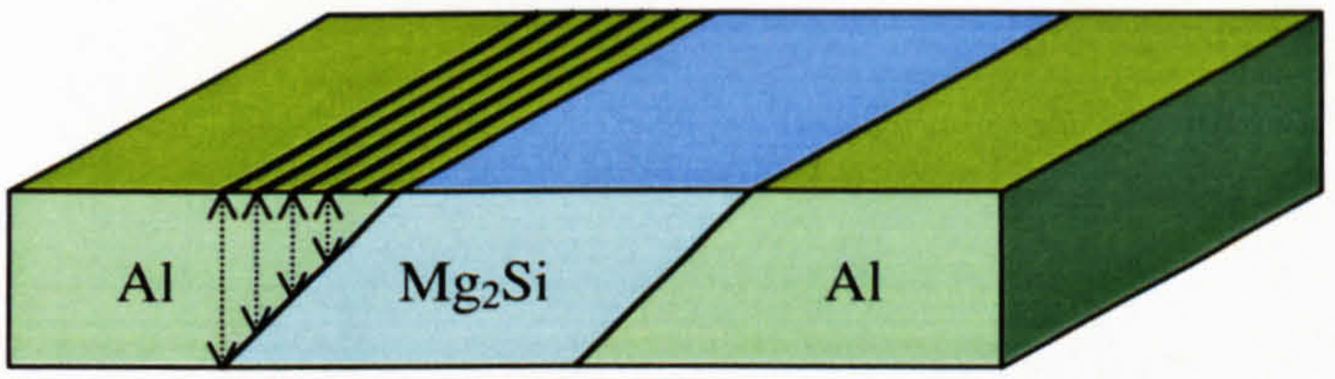

Figure 5.6: Schematic of a tilted interface indicating the varying thickness of aluminium resulting in thickness fringes.

Images of a number of precipitates were examined and diffraction patterns from the surrounding matrix used to assign crystallographic directions to the images. It was observed that the magnesium silicide platelets grew with facets along specific directions. The key facet planes were (using the aluminium coordinate system) {100}, {110} and {111}. Using the known Al/Mg_2Si orientation relationship a transformation matrix was made which enabled directions and planes to be transformed from one coordinate system to another (Kobayashi *et al.*, 1976). The facet planes were transformed into corresponding planes in the Mg_2Si coordinate system. The transformation matrix was:

$$\begin{bmatrix} 1/\sqrt{2} & 1/\sqrt{2} & 0 \\ 1/\sqrt{2} & -1/\sqrt{2} & 0 \\ 0 & 0 & 1 \end{bmatrix}$$

The structure of this matrix meant that, with the exception of (001), no planes or directions with a non-zero 'l' component mapped onto a standard direction within Mg_2Si. For cases where the facet plane in aluminium maps onto a low index plane in the precipitate coordinate system it implies that there may be less of a lattice mismatch between the planes and hence result in a sharper interface. {100} and some {110} facets should therefore provide better interfaces. It was found that tilting to a <110> pole made some {100} and {110} facets parallel to the electron beam. In addition, the texturing of the matrix, resulting from rolling during the manufacture of the alloy, was such that for the majority of precipitates this was the major pole which required the least tilt to bring it parallel to the axis. It was for this reason that a <110> pole was selected. Fig 5.7 gives a bright field image of a precipitate where the surrounding matrix has been oriented to the [011] pole. Two {100} facets parallel to the electron beam are labelled. The other facets of this precipitate are angled to the electron beam, as indicated by the thickness fringes.

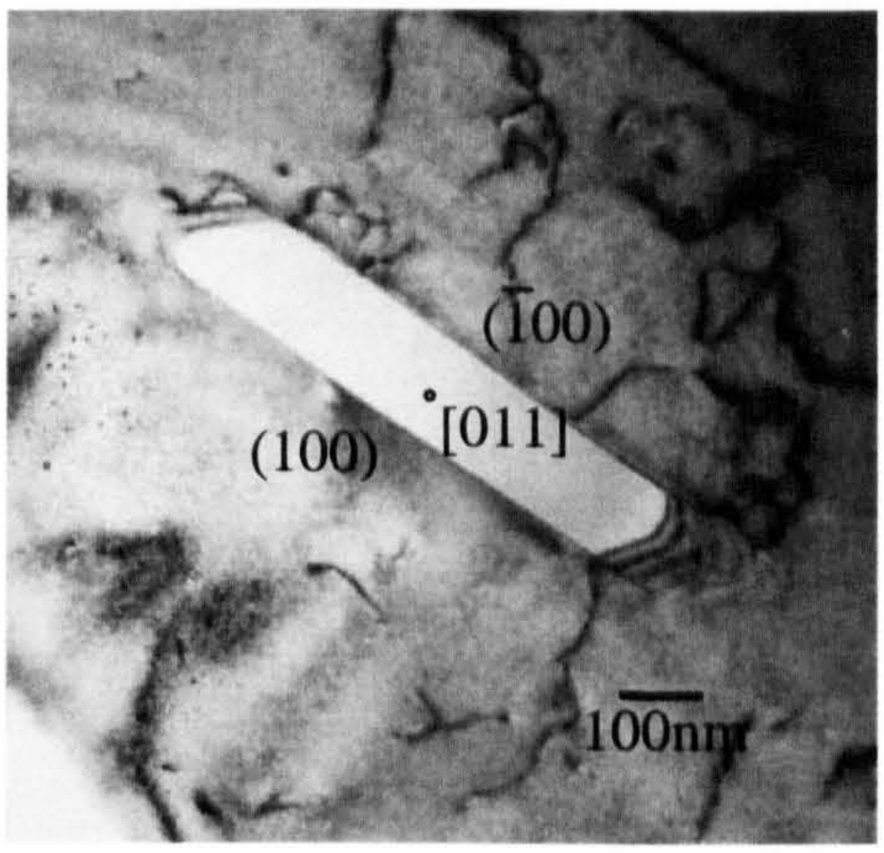

Figure 5.7: Mg_2Si precipitate with matrix oriented to [011] pole. Facet planes parallel to the electron beam are marked.

Once suitable precipitates were identified and characterised, the sample was transferred to the STEM. Following a standard alignment of the STEM (section 3.4.2), a precipitate of interest was located with the assistance of the precipitate map obtained in the TEM. The STEM was then operated in rocking beam mode and the sample tilted to the closest <110> pole using the Kikuchi lines as a guide. The centre of the Kikuchi pattern was aligned to the optic axis using the centre of the aligned objective aperture as a guide. Only one <110> pole was available in the range of the TEM tilt. Therefore, the <110> pole requiring least tilt in the STEM was the one used in the precipitate study in the TEM. When the sample was close to a pole, setting the third post-specimen lens (PSL3) to a high value provided a diffraction contrast image within the STEM. This enabled further examination of the precipitate and comparison with the image obtained in the TEM. Fig 5.8 shows images of the same precipitate taken in the TEM (*left*) and the STEM (*right*). Much of the thickness detail was not evident in STEM, though contrast around the precipitate edges was sufficient to identify facets angled to the electron beam (*e.g.* the lower left precipitate edge in Fig. 5.8.

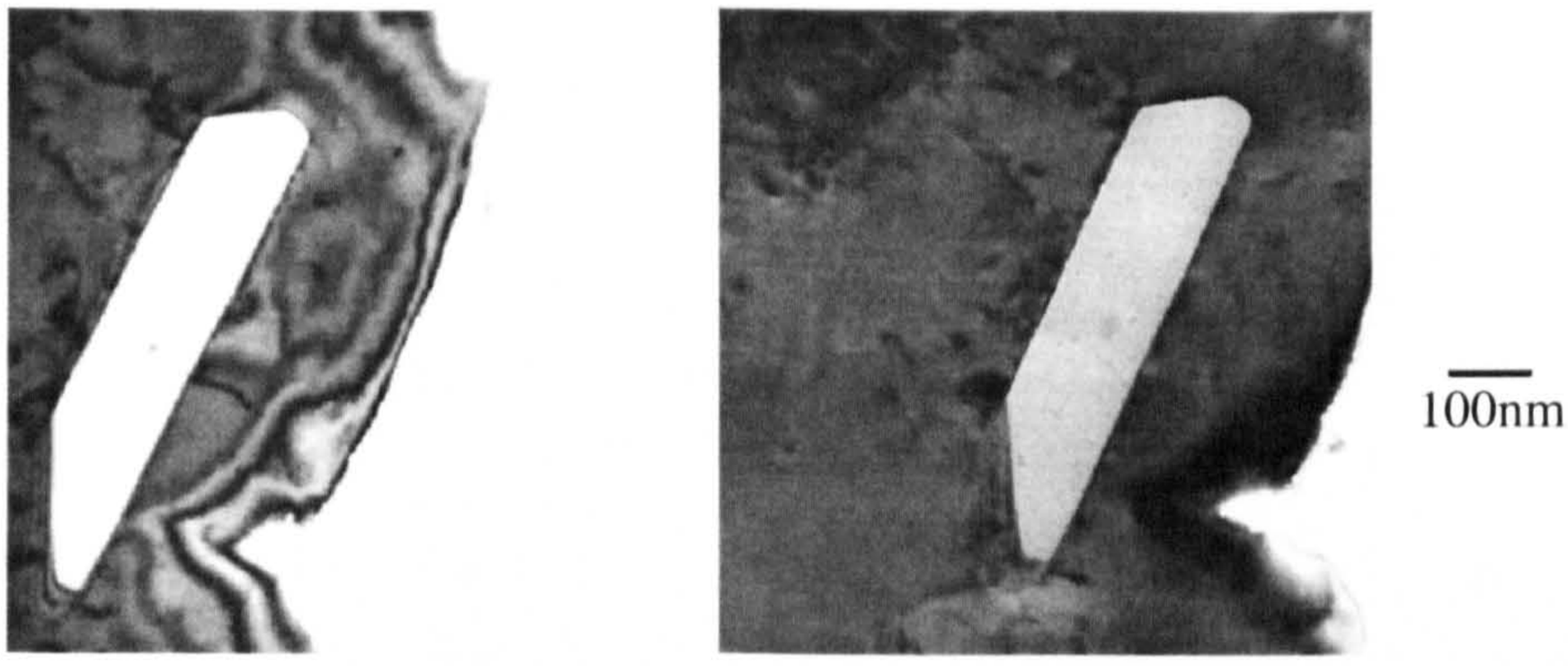

Figure 5.8: Comparison of TEM (*left*) and STEM (*right*) images of the same precipitate.

It was found that data taken shortly after aligning the sample on a pole displayed a large drift. This was found to result from the large change in condensor lens excitation (Delby and Krivanek, 2002) necessary for changing between fixed and rocking beam modes. To minimise this problem, the condensor lens was left to equilibrate for a period of 30-60 minutes prior to data acquisition. Following this period, the diffraction contrast image of the sample was examined again to check for any differences which might suggest a change in the angle of tilt. No difference was observed on any occasion following the equilibration period. This indicated that the tilt angle had not changed noticeably. The interface was then ready for data acquisition.

5.3 Acquisition and Analysis of HB5 Data

5.3.1 Acquisition of Data Across the Interface

The exact method for the acquiring of data, and the data taken, was refined over a number of microscope sessions to solve problems which arose and also to make the process easier. The final technique, which was used in the acquisition of all the data appearing in this thesis, required the collection of 93 distinct spectra per data series. EELS spectra were collected from a set of 12 points 0.4nm apart across the interface. In addition, spectra were taken at 8 points separated by 3.75nm to indicate the trend at greater distance from the interface. Spectra were also taken from points at larger distance from the interface to provide data characteristic of the bulk materials. This data was used for the fitting procedure. To provide a zero loss peak for replacement of the unsaturated peak, spectra with unsaturated zero loss peaks were taken from a point through a hole in the sample. For

each point four spectra were taken, with each spectrum recorded at a different position on the diode array. This was done to reduce the effect of gain variations in the diode array and also give an indication of the extent of spatial drift. Finally, a spectrum was acquired with no electron beam falling on the detector array; this was used to correct for the dark current present in the system.

To acquire the spectra for the data series, the following procedure was used. Initially, once the interface of interest had been located and aligned to the electron beam, the interface was centred on the screen at a magnification of x10M and the scan rotation adjusted so that the interface appeared horizontal. The interface position and any notable features in the vicinity were then noted at a lower magnification, this enabled later repositioning of the interface if it was necessary. The microscope was then put in spot mode at x10M so that the electron probe was no longer scanned across the sample. A continuous EELS acquisition was then taken, giving a new spectrum from the probe position every fraction of a second. The EELS spectrum was observed as the probe position was electrically altered. When the EELS spectrum indicated that the probe was near the interface and at a reproducible point the acquisition was stopped.

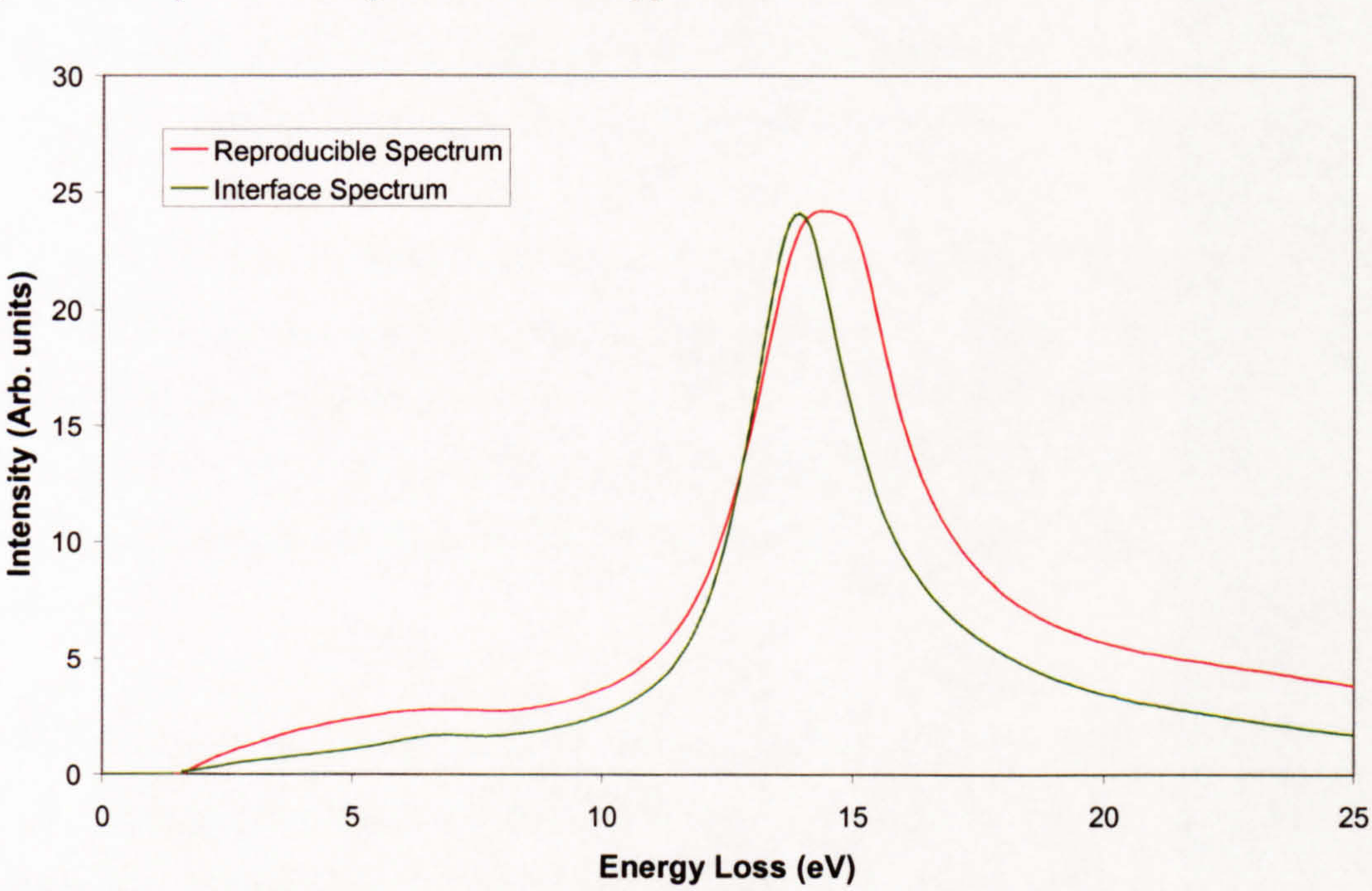

Figure 5.9: Spectrum of reproducible point (see text) and theoretical interface spectrum. Peak in reproducible spectrum appears to be flattened. This is due to the combination of aluminium and interface plasmon peaks.

The reproducible point was one where the spectrum was in a 'recognisable' state. The interface point itself wasn't used as it was difficult to identify without further analysis when the probe was exactly on the interface. This difficulty would have introduced an error of the order of the distance between the points. Normally, there would be a point at which the proportions of the different plasmons were such that the top of the combined peak would be flat or that a second peak would start to 'grow' out of the first. Points such as these were used for the reproducible point, as they were considerably easier to re-identify. In Fig 5.9 one such reproducible point is shown. Included in the same plot is a theoretical interface spectrum for comparison. The reproducible point was clearly not acquired from the interfacial point. It was not important that the central point was not on the interface. If the point was close to the interface the set of points acquired still covered a suitable distance from the interface to obtain all the information required. At the stage of data processing it was apparent where the interfacial point should be and the distances were changed accordingly. This method of re-finding the interface helped to reduce the effect of spatial drift on the data and was considerably more accurate than using the image for realignment.

The disadvantage of re-finding the interface for every point was that it increased the contamination build-up at the interface. To reduce the effect on the data, the spectra closest to the interface were taken first and then data from the further out points were taken. Fig. 5.10 gives a schematic indicating the position and order in which the points were acquired.

Once the reproducible point had been located (or re-located), the probe was moved a set distance away from the interface. The probe was moved electrically, controlled by a 10-turn potentiometer. The potentiometer was rotated an integral number of ¼ turns in the desired direction. A rotation of ¼ turn corresponded to a probe movement of 0.94nm at

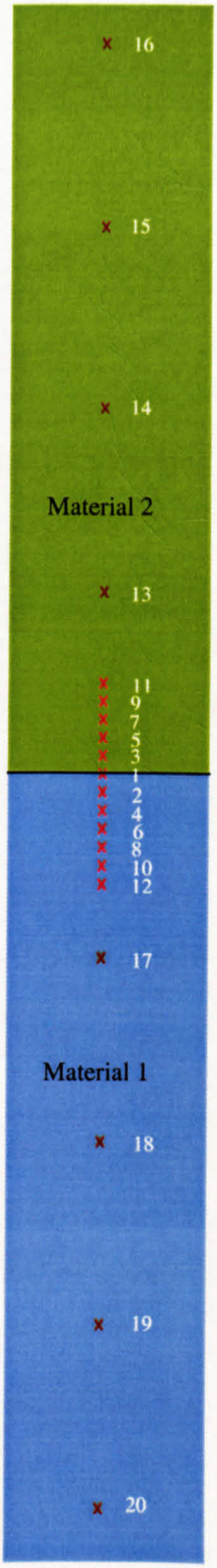

Figure 5.10: Schematic of acquisition procedure. Points are taken at 0.38nm (light red) and 3.75nm (dark red) in the order indicated by the white numbers.

x4M and 0.38nm at x10M. This kind of experiment had normally been done previously by marking set distances on the screen and then moving the probe according to the marks. It was felt that using marks would be more complex and less accurate. Positioning using marks is very dependent on parallax and, as the entire screen height is used, would probably become quite inaccurate at the extremities.

Occasionally, the spectra were observed to be displaced on the diode array by some unknown cause within the microscope. This was known as energy drift. If this occurred during an acquisition, the shape of the spectrum was noticeably altered. As a result the spectrum would be useless for analysis and so that particular spectrum was re-acquired. Fig 5.11 shows a spectrum which has experienced energy drift.

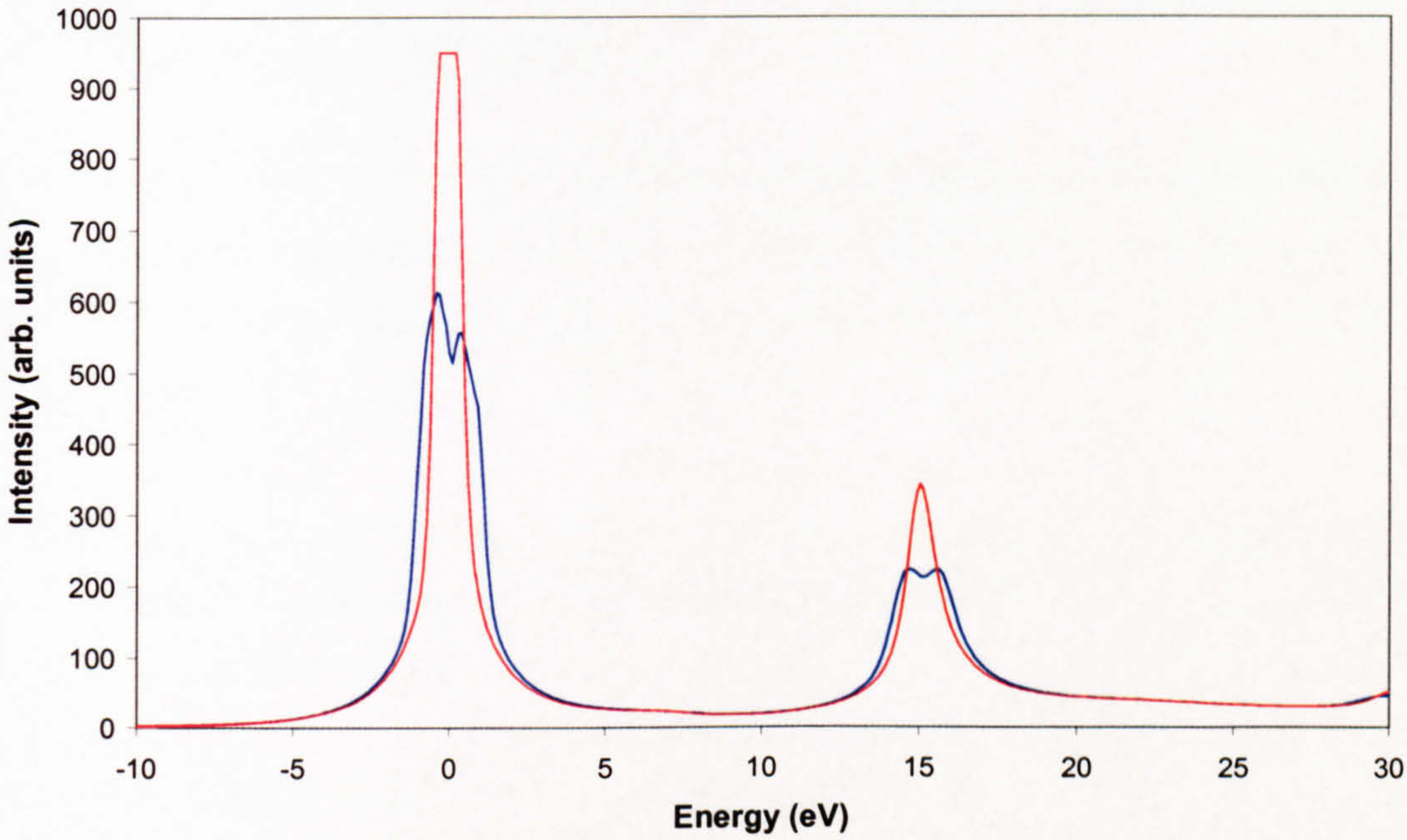

Figure 5.11: Graph of unsaturated data from a point (*red line*) and from the same point when energy drift was experienced (*blue line*). Both spectra have the same scale.

Following the acquisition of the spectra at a point the reproducible point is relocated and the probe moved to a different position. Every four points (*i.e.* every 16 spectra) it was necessary to save the spectra occupying the memory banks of EL/P. During this time the microscope was returned to scanning mode and, if necessary, the interface repositioned. Repositioning of the interface was performed using the electrical shifts. The electrical shifts altered the region of sample scanned by the electron beam. It was therefore possible to examine a nearby area of the specimen without having to move the sample. It was

preferable to use the electric shifts as using the mechanical shifts generally resulted in a lot of spatial drift for a period after use. Following repositioning of the interface, the microscope was returned to spot mode and the sequence continued. Once spectra from the twelve points had been acquired at x10M the magnification was reduced to x4M. At this lower magnification spectra were acquired from 8 different points. The data were acquired in the same way as previously with the exception of the distance between the points. For these points the distance between adjacent points corresponded to one full turn of the potentiometer. This was equivalent to 3.8nm.

All of these spectra together made up a single data series. This series then had to be processed before final analysis could be performed.

5.3.2 Preliminary Data Processing

Before the final fitting and analysis procedures could be performed it was necessary to perform some preliminary processing on the spectra. It was required that the spectra be deconvoluted and, where possible, that the four spectra from a point be consolidated into a single spectrum.

The first step, which had to be done to all the spectra, was that the background current, known as the dark current, must be removed. This made sure that the spectrum was solely the information from the sample and did not contain artefacts from the photodiode array.

Following this, the four spectra from each point were aligned with each other so that the zero loss peak occupied the same channels in each spectrum. Using an interpolation technique, it was possible to align the zero loss peaks to a fraction of a channel so they appeared almost identical. The interpolation technique initially involved aligning the spectra to within one channel. Following this, the spectrum was displaced by one channel and a linear combination of the displaced and the undisplaced spectra performed. This compensated for the slight energy drift that was always present within the system. Fig 5.12 compares the accuracy of aligning unsaturated zero loss peaks using the standard whole-channel and the interpolation techniques. The spectrum aligned using the interpolation technique appears largely identical to the reference spectrum, whereas the whole-channel technique is still displaced. The saturated spectra from a data series were aligned to an

unsaturated hole spectrum. This was done to simplify the replacement of the saturated zero loss peak by the unsaturated peak. By aligning to the unsaturated spectrum at this point it removed the necessity for further alignment. Following alignment, the centre of the zero loss peak was set as 0eV.

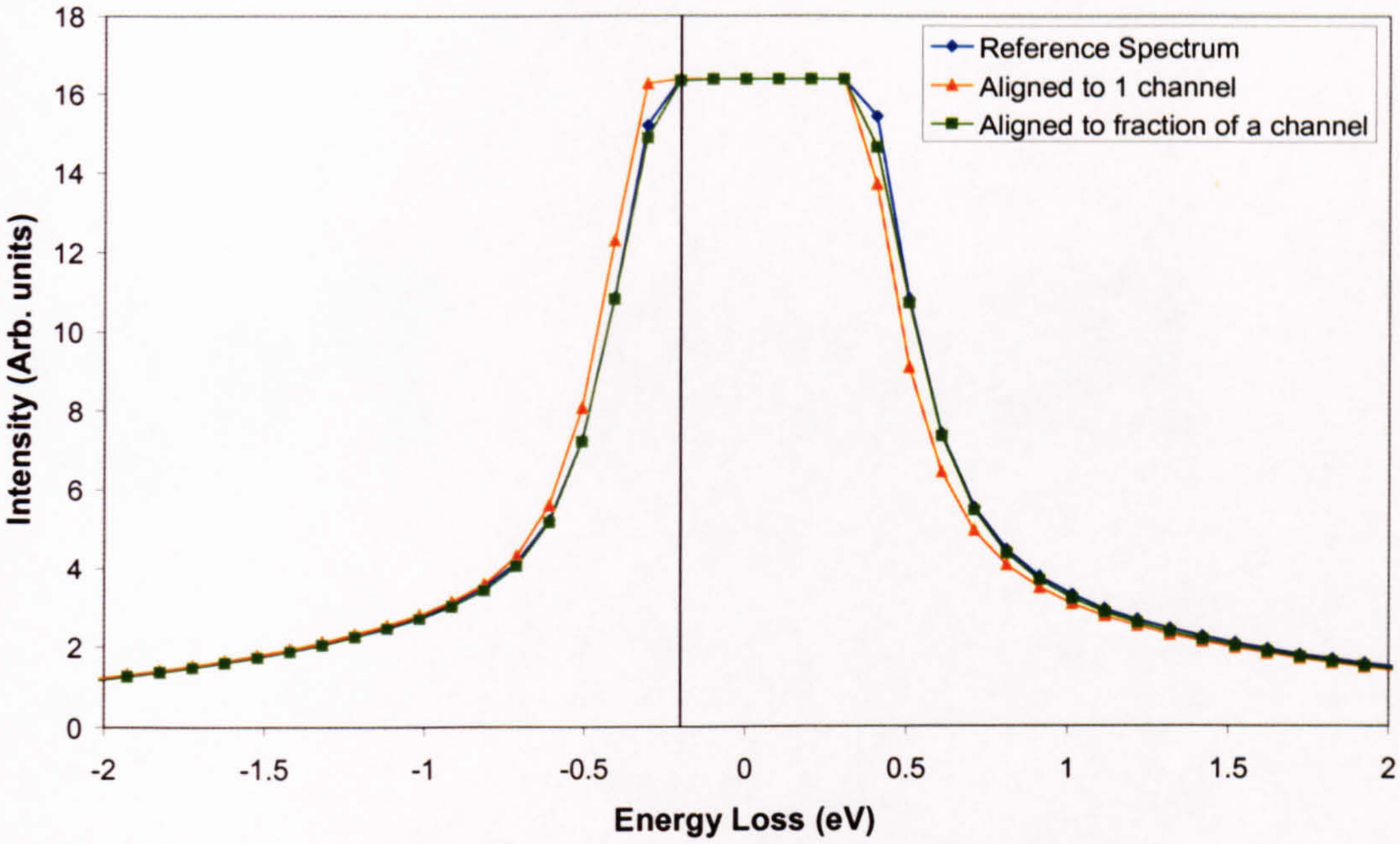

Figure 5.12: Alignment of an unsaturated spectrum to a reference spectrum (*blue*) to an accuracy of one channel (*orange*) and a fraction of a channel (*green*).

The plasmon peaks of the four aligned spectra were then compared. Though the number of counts may vary between spectra, the shape should remain largely the same. If this was observed to be the case, the four spectra were summed. However, if the sample had drifted between or during an acquisition, the plasmon peak would appear different in the different spectra (Fig. 5.13). If the spectra were not the same and had clearly drifted, the spectra were not summed and were processed individually as separate spectra.

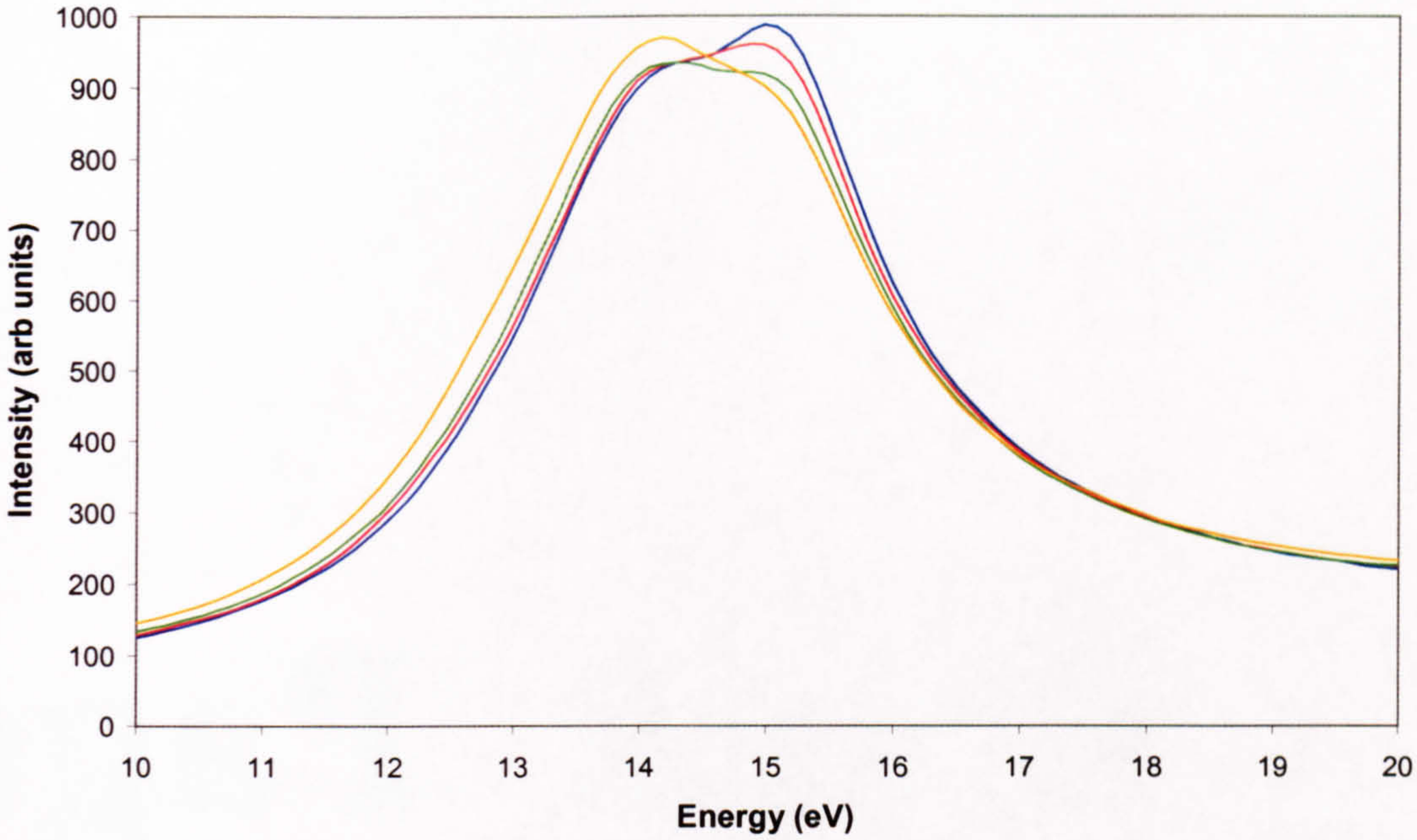

Figure 5.13: Graph of spectra which have drifted spatially between acquisitions. Spectra were acquired in the order *blue*, *red*, *green*, *orange*. Sample was drifting in a direction to cause the electron probe to move from within the Al over the interface into Mg_2Si.

Sample drift for these experiments was caused by a number of different factors. Relaxation of the stage mechanism was the main cause. This occurred after the sample stage had been moved in some way. Normally, the sample would be observed to drift in the direction of movement for some time after the movement. Another cause has been discussed previously, that of significant changes in the condenser lens excitation which results in a movement of the sample. Both of these causes can be minimised by allowing the microscope to settle for a period before acquiring data. The final main cause stemmed from an inadequate air conditioning system. An investigation was performed into the temperature conditions within the microscope room. The temperature was found to fluctuate by 3°C with a cycle time of 10 minutes corresponding to the air conditioning unit switching on and off. The fluctuation in temperature was found to correlate to a spatial drift of around 70nm over a cycle (Fig. 5.14). This drift was reduced to about 40nm when the air conditioner fan was set to full speed. Whilst this still appears to be a large drift, the timescale for the acquisition of the four spectra from a single point is less than 30 seconds. The drift resulting from the fluctuation in temperature is significantly smaller over this time period.

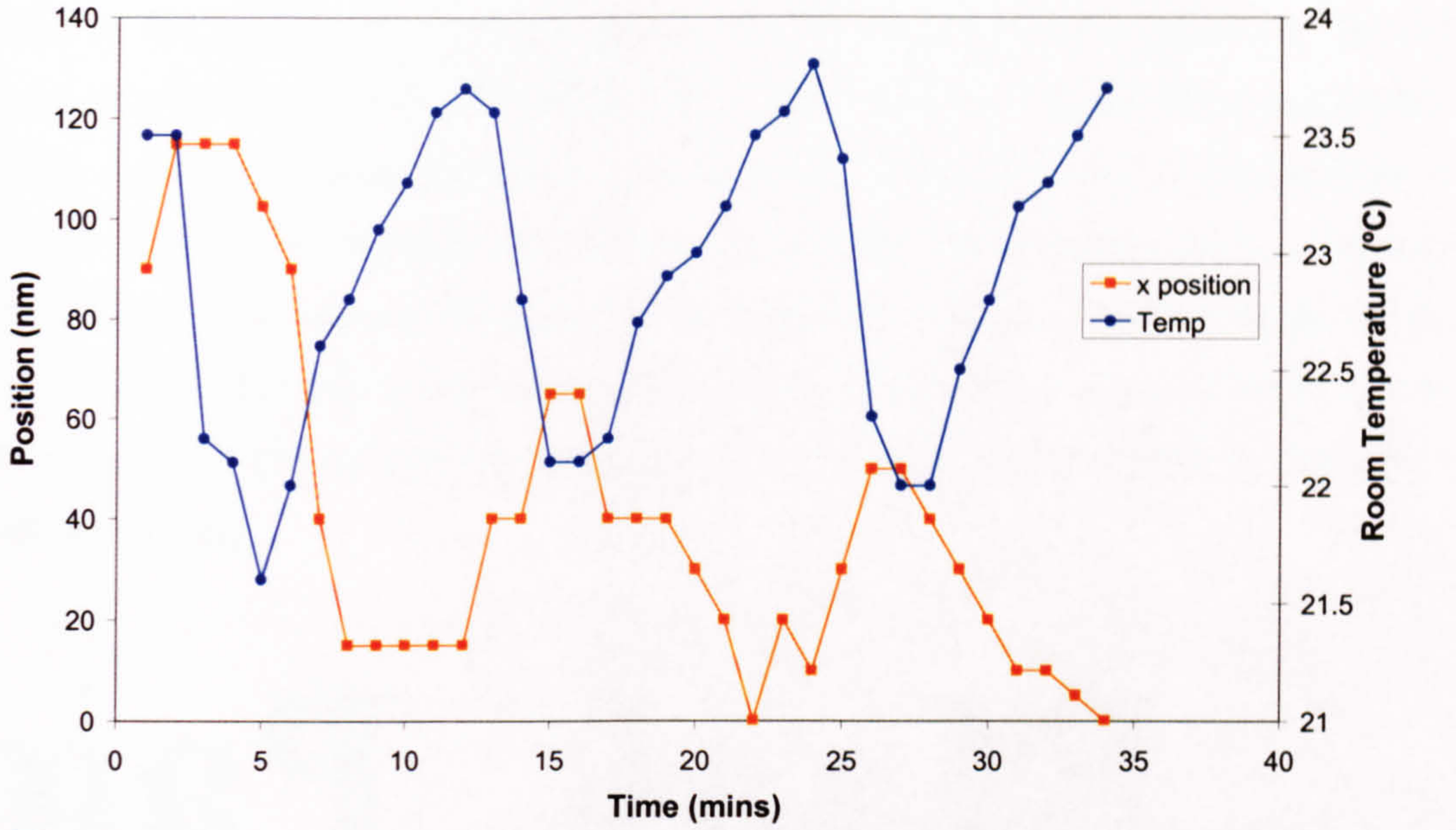

Figure 5.14: Correlation of temperature and sample position within the STEM.

Once all the spectra have been summed, or the decision has been made to process them individually, the unsaturated zero loss peak was added in using the technique discussed in section 5.1.2. This resulted in a full low loss spectrum with an unsaturated zero loss peak (Fig. 5.15). This spectrum was then fourier-log deconvoluted by a procedure within EL/P[1].

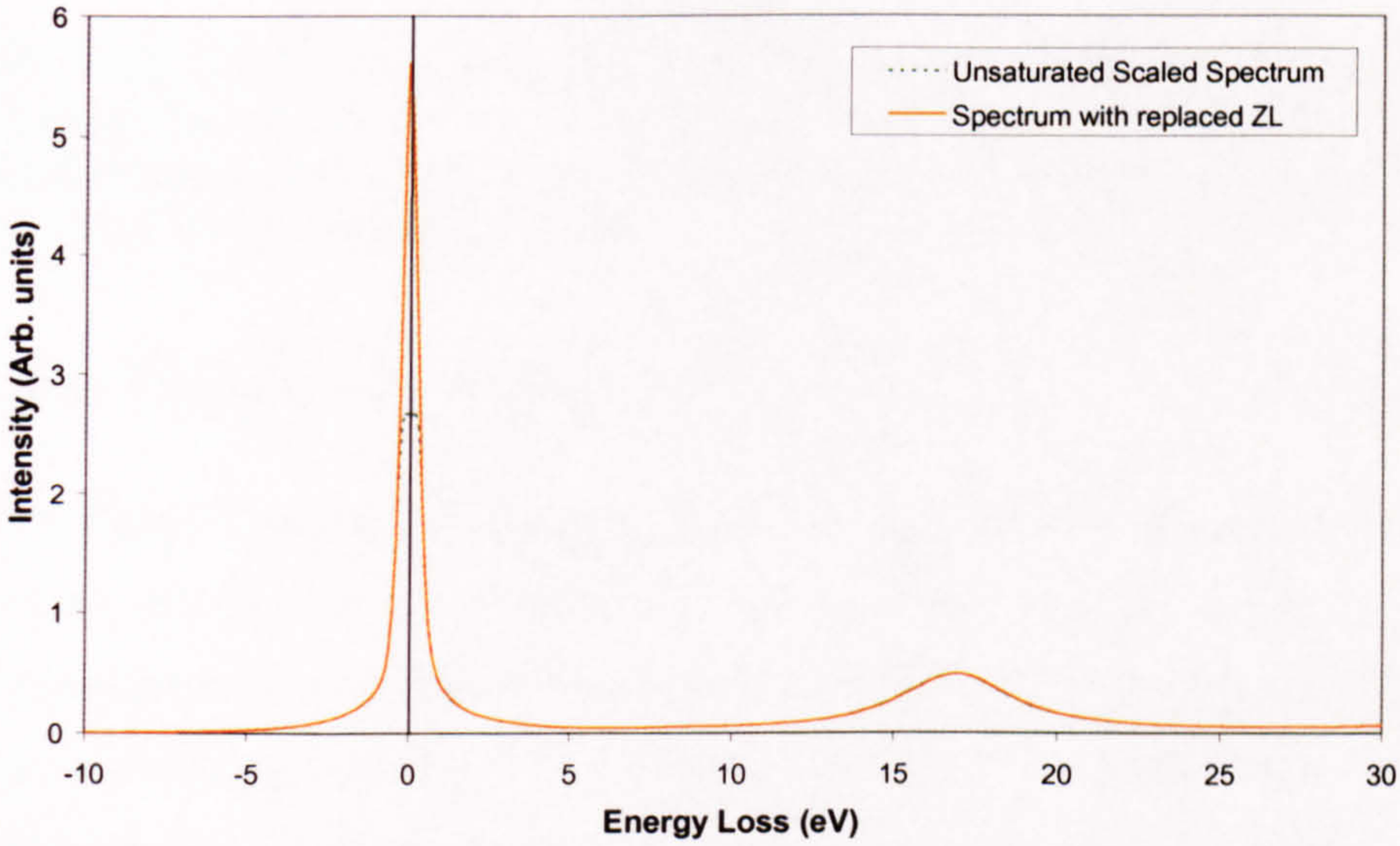

Figure 5.15: Plot showing the result of replacing an unsaturated zero loss peak.

[1] As part of the deconvolution procedure EL/P performed checks on the data to ensure that no background counts were remaining. If the program identified that there were residual background counts, a constant number of counts were subtracted from every channel in the spectrum. The number of counts subtracted was always <0.5% of the plasmon peak height.

It was often observed in deconvoluted spectra, that the second and third plasmons had not been correctly deconvoluted (Fig. 5.16). This was believed to result from incomplete angular collection into the spectrometer, resulting in an imperfect Poisson distribution of the counts. A brief investigation into this was performed. The collection semi-angle was varied between 12.5mrad and 40mrad but no significant difference in the height of the second plasmon following deconvolution was observed. However, as the second plasmon occurs at twice the energy of the first plasmon its magnitude does not significantly affect the data processing.

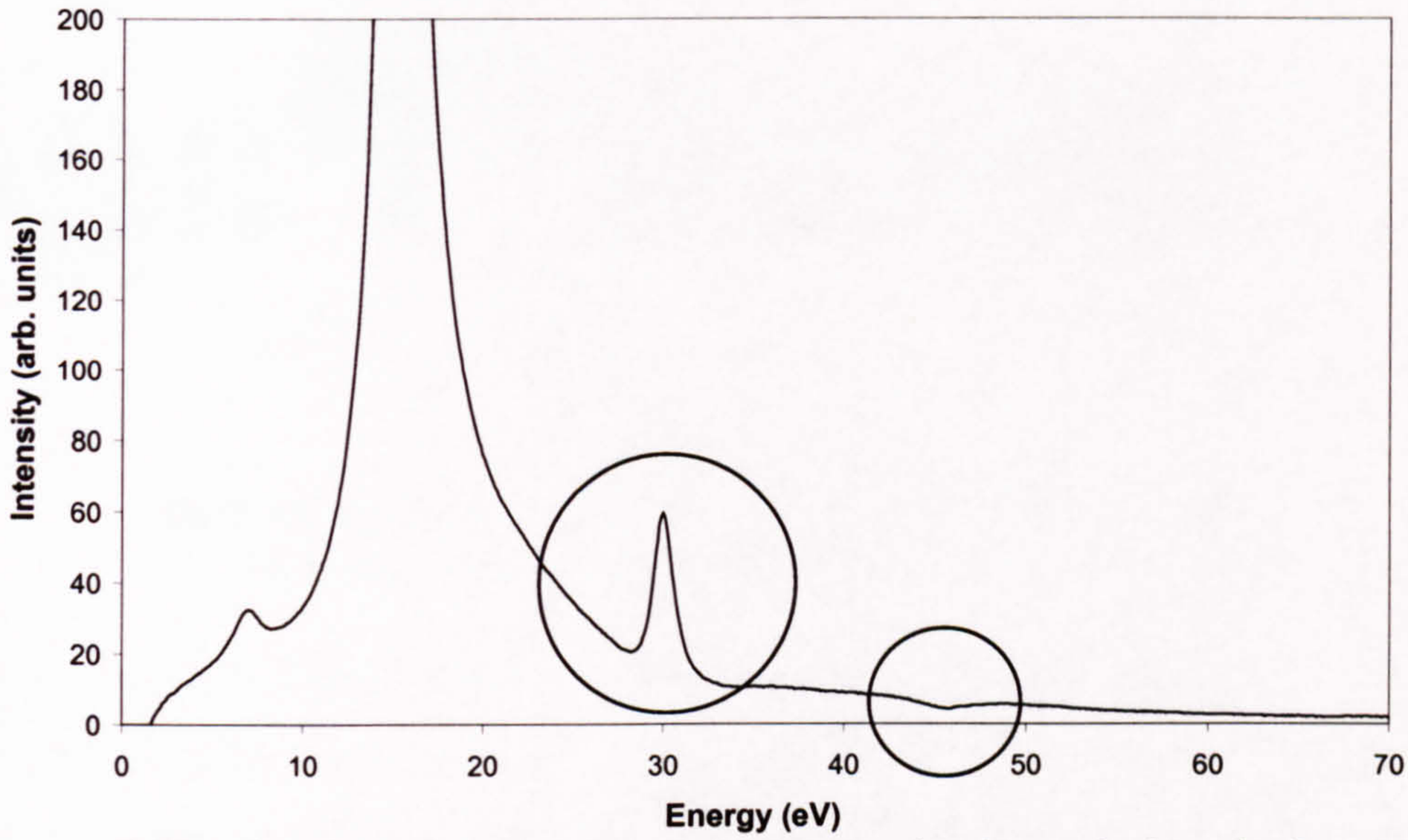

Figure 5.16: Graph indicating the incorrect evaluation of the single-scattering distribution. The area of the second plasmon shows an excess of counts and the area of the third plasmon shows a deficit of counts (both circled). The scale is chosen so the maximum of the first plasmon is 1000.

5.3.3 Data Fitting and Analysis

In the final stage of the data analysis, the effective proportion of each component in the experimental spectra was determined. The four reference spectra (2 bulk spectra, an interface spectrum and a carbon spectrum) were fitted using a least-squares fit technique to each experimental spectrum. Fig 5.17 gives an experimental spectrum with the component spectra fitted to it.

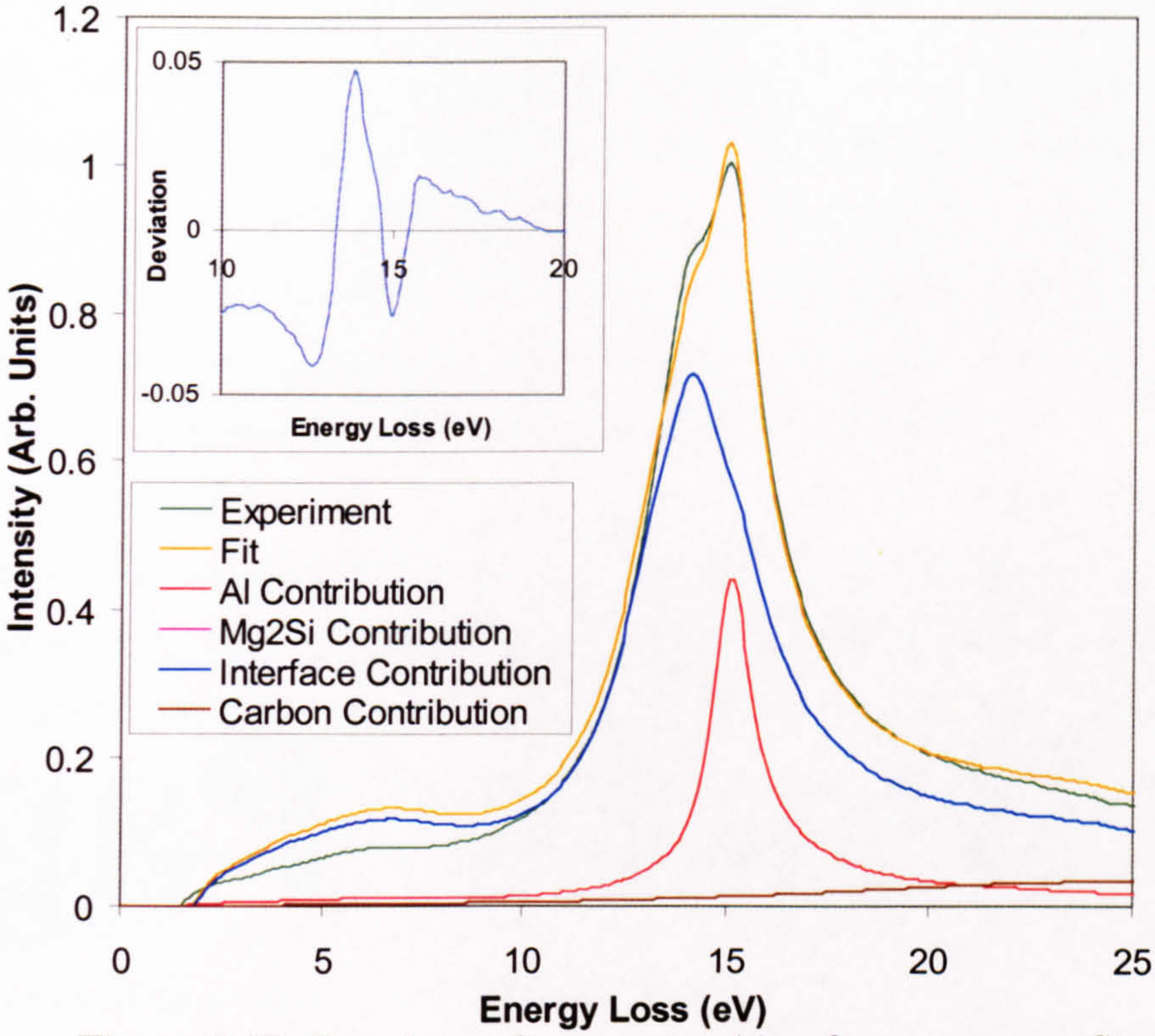

Figure 5.17: Experimental spectrum with reference spectra fitted to it. *Inset* the deviation between the fit and the original data.

All spectra within a series were fitted using the same component spectra. Four component spectra were used. In the case of the Al/Mg_2Si interface, the spectra were aluminium, magnesium silicide, interface and carbon. For an Al/Si interface, the Mg_2Si spectrum was replaced by Si. All spectra used were single-scattered low loss spectra. The aluminium, magnesium silicide and silicon component spectra were acquired along with the rest of the data in the series. This meant that the bulk component spectra were all specific to the series. Fig 5.17 does not show an Mg_2Si component in the fit. This is as the experimental spectrum was acquired from within the aluminium and so no Mg_2Si component would be expected. Despite this, Mg_2Si was included in the fit, it merely has a zero value.

Initially, the interface spectrum used was an experimental spectrum acquired in the same way as the rest of the data (section 6.1). However, the majority of the results presented in this thesis were calculated using a theoretical interface spectrum. The theoretical interface spectrum was generated using dielectric functions obtained from experimental data using a Kramers-Kronig transformation. The non-relativistic equation (eqn 2.33) was used for calculation of the spectrum.

The carbon spectrum used, was one acquired in a sample that was contaminating badly. By moving the probe slowly off the edge of the sample into a hole, a self-supporting 'trail' of carbon was created. The probe was moved sufficiently far away from the edge to make any interfacial effects negligible and allowed to linger for a period. A spectrum was then acquired, this was an amorphous carbon spectra. By utilising this method it is believed that a carbon spectrum most accurately modelling that seen as contamination was obtained. This spectrum was processed in the standard way and used for fitting.

A spectrum was generated for comparison to each processed spectrum using a linear combination of the four component spectra. A least-squares fit was performed over the range 10-28eV using the in-built *solver* function within Excel. The magnitude of each reference spectrum was varied to provide the best fit to the data. It was expected that only one of the bulk spectra would be present within a specific spectrum. Despite this, all four relevant component spectra were fitted to each processed spectrum. The result was the relative proportions of each component in the individual spectra.

The fitting range was deliberately chosen to extend beyond the scope of the bulk and interface plasmons, though excluded the second plasmon of aluminium. This range included energies at which the tail of the carbon plasmon would be present. This was to provide more accurate fitting to the carbon plasmon and hence improve the correction for contamination.

Further processing was necessary to extract useful information from points which displayed spatial drift. Such a points had four different spectra corresponding to a specific single value of x_0. As the sample is likely to have drifted between re-locating the reference point and acquiring the first spectrum, it can be assumed that none of these four spectra actually correspond to that value of x_0.

However, if it is assumed that the sample drifted at a constant rate, the data can be extrapolated back to zero time. The time at which each acquisition finished was recorded with the relevant spectrum. In addition, the duration of each acquisition was also known (4 seconds). An average duration for the time between re-locating the reference point and the end of the first acquisition in a series was measured. It was found to be 8 seconds. A plot was then made of the effective proportion of the four components for each acquisition

against the time for that acquisition. A quadratic trend-line was then fitted to this plot (Fig. 5.18). Though the drift was linear, the relationship between distance and t/λ is not. For this reason a quadratic trend-line was used. Using the intercept of the trend-line, an extrapolation was made to zero time for each component. This value of a component at zero time corresponded to the true value for that component at the measured x_0 value.

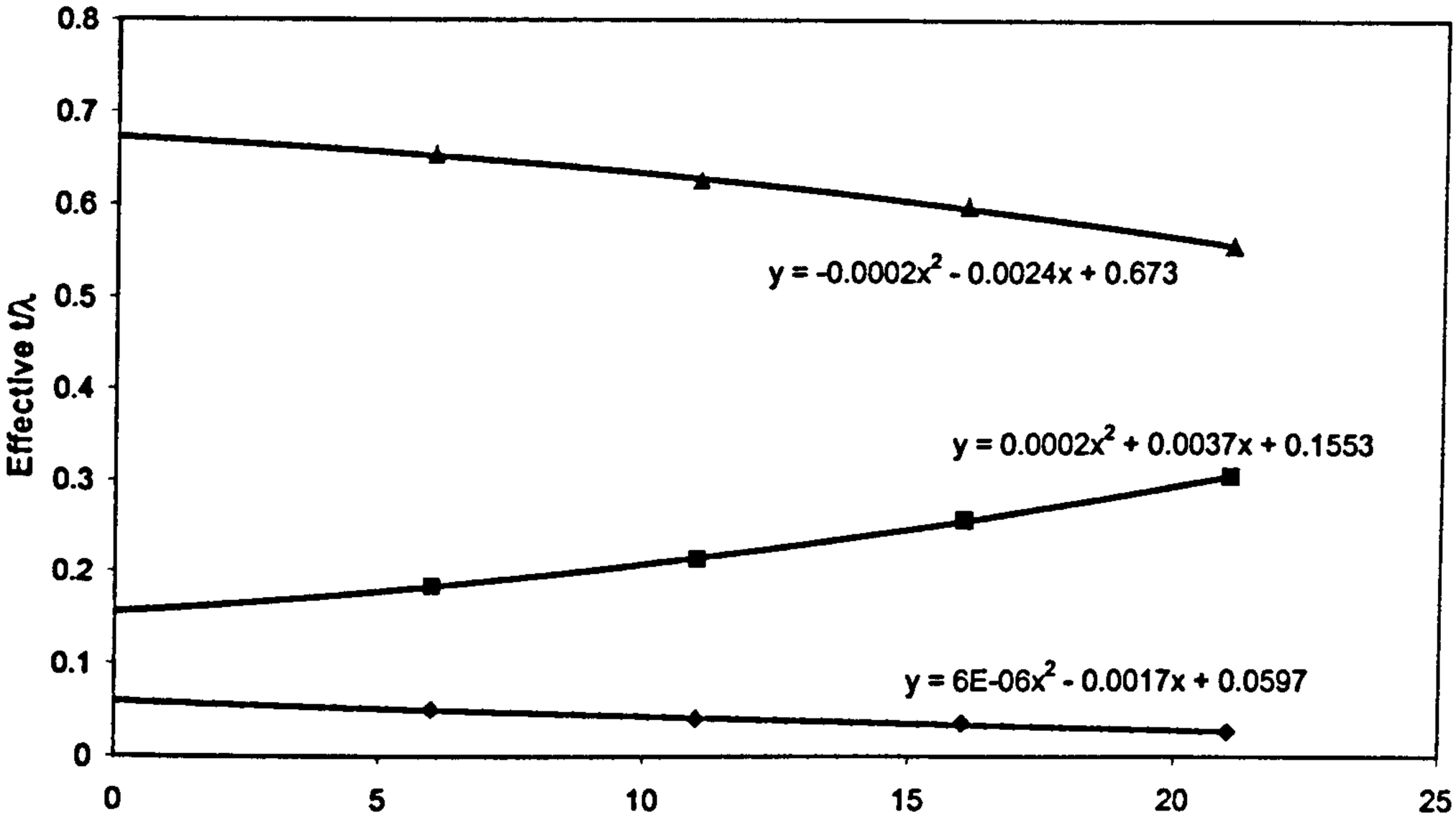

Figure 5.18: Graph for correction of specimen drift. The component values for the four spectra in the series are plotted at the corresponding time value. A best-fit quadratic is then fitted to the data and used to extrapolate back to zero time. Shown are the interface (*green*), Mg_2Si (*blue*) and aluminium (*red*) components. Best-fit lines and equations are included.

The relative proportions of each component of a spectrum were combined with the number of counts in the corresponding component spectrum. This gave the number of counts attributable to each component. It was possible to convert this into an effective t/λ value by dividing by the number of counts in the experimental zero loss peak. The effective t/λ values for each spectrum were subsequently plotted with their corresponding distance from the interface.

As outlined in chapter 2 the Howie equation takes the form of:

$$Loss\ Fn = Bulk \times \left(\ln\left(\frac{k_m^y v}{\omega}\right) - K_0\left(\frac{2\omega|x_0|}{v}\right)\right) + Interface \times K_0\left(\frac{2\omega|x_0|}{v}\right)$$

Therefore, to compare theory with experiment, a Bessel function was fitted to the decay of the interface (eqn 5.1b) and a form of the same Bessel function was fitted to the growth of the bulk plasmon (eqn 5.1a).

$$Interface\ decay\ fit = A_i\left[\ln\left(\frac{1}{B_i}\right) - K_0\left(C_i|x_0|\right)\right] \qquad \textbf{Equation 5.1a}$$

$$Bulk\ decay\ fit = A_i K_0\left(C_i|x_0|\right) \qquad \textbf{Equation 5.1b}$$

Each side of the interface was fitted separately. Eqn 5.1a was fitted to bulk component *i* whilst simultaneously fitting eqn 5.1b to the corresponding interface component. This was performed using a least-squares technique, varying A_i, B_i and C_i to provide the best fit. Fitting of the Bessel function is problematic at small distances from the interface. As the function is asymptotic to the y-axis, the gradient close to x=0 is very steep. This results in weighting of the fit at low x. In order to avoid this, the points at a distance of less than 0.75nm from the interface were excluded from the fit.

x_0=0 corresponds to the interface position. The use of a reproducible point (section 5.3.1) meant that the experimental x_0 values were not correctly aligned. An alignment was performed by extrapolating the interface component on each side of the interface until the components intersected (Fig. 5.19). The point at which the extrapolated interface components intersected was taken to be the interface point and the x_0 values adjusted accordingly. The extrapolation was performed by extending the fit from the $\pm$0.375nm point using the gradient of the fit at that point. The Bessel function is asymptotic to the y-axis and so the interface components should never actually meet if extrapolated correctly.

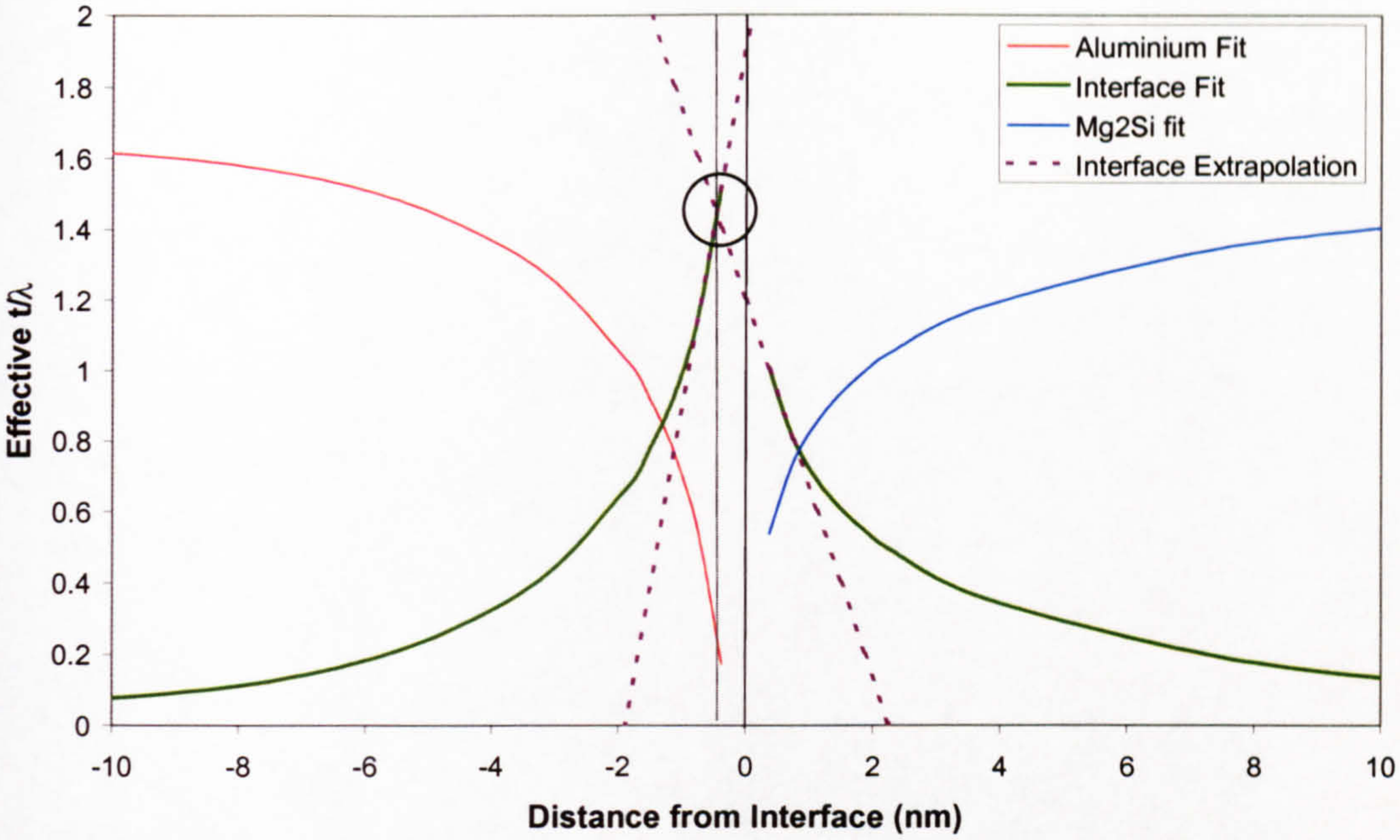

Figure 5.19: Method of calibrating x_0 values. Interface component fits (*green*) are extrapolated (*broken purple line*) to an intersection point (*circled*). This intersection gives the actual interface point (*black broken line*). Extrapolation is performed using the gradient of the Bessel function at the $\pm$0.375nm point.

Following the calibration of the distance from the interface, the Bessel function fit was recalculated to provide corrected values of A_i, B_i and C_i.

5.4 Interpretation of the data

The form of the best-fit lines was chosen to reflect the theoretical equation. Therefore, if a good fit resulted, it was indicative of the experimental data adhering to the theory. However, further comparisons can be made. The variables A_i, B_i and C_i can be related to eqn 2.33 and expected values determined.

The t/λ value will vary with thickness. To compensate for this, A_i acts as a scaling value and allows for areas of different thickness to be analysed in a comparable way. As a result, it would be expected that the values of A_i would vary for data taken from different interfaces. However, the thickness across a single interface is assumed to be constant. Therefore A_1 should be equal to A_2, or equivalently $A_1/A_2=1$. Deviations from this expected value are likely to be caused by incorrect selection of the interface position

Within eqn 2.33, ω corresponds to a full range of frequencies. However, the Bessel function term will have the most pronounced effect on frequencies corresponding to a large number of counts. The largest number of counts within a deconvoluted spectrum is observed at the plasmon frequency. Therefore, a comparison of the plasmon frequencies or energies, will give an approximation to the relative distances over which the interface plasmon decays in each medium. The value of C_i gives the rate of decay of the interface plasmon (and hence the growth of the bulk plasmon) with distance. Comparison of eqns 5.1a and 5.1b with eqn 2.33 gives $C_i=2\omega/v$. Since the effect of Bessel function is most significant on a large number of counts it is reasonable to take ω as ω_p. Therefore the following assumption can be made:

$$\frac{C_1}{C_2}=\frac{\omega_p(1)}{\omega_p(2)}=\frac{E_p(1)}{E_p(2)}$$

It has been discussed in section 2.2.1 that the effective t/λ of each bulk component will reach a plateau value. If it is assumed that the thickness of the sample is constant across the interface then the relative heights of the plateaus will be dependent only on the mean free path *i.e.*

$$\frac{P_1}{P_2}=\frac{(t/\lambda)_1}{(t/\lambda)_2}=\frac{\lambda_2}{\lambda_1}.$$

Here P_1 and P_2 are the plateau values of effective t/λ for bulk materials 1 and 2 respectively. The mean free paths (λ_i) for materials 1 and 2 can be determined using eqn 2.11. The plateau values are very dependent on thickness fluctuations. To minimise the effect of such fluctuations, the plateau values were taken as the values at large $|x|$ of the function fitted to the bulk component.

5.5 Kramers-Kronig Transformation

Not all data was processed in the manner described above. Some data was necessary for generating theoretical spectra. For this, dielectric functions of the materials of interest were required. Standard experimental spectra were acquired from the bulk in the materials of interest. Care was taken to select an area that had a t/λ of between 0.2 and 1. If the area were excessively thick, a large number of counts would be present in the second and possibly third plasmons within the spectrum. This is known to cause problems with

fourier-log deconvolution, resulting in either too many or too few counts in the area of the second and third plasmons. This is not directly problematic for obtaining dielectric data in the energy range of interest. However, the Kramers-Kronig transformation makes use of the entire spectrum in calculating each point. Therefore, there may have been some small effect if the spectrum had deviated significantly from a true single-scattering distribution. It was necessary to avoid particularly thin areas as any surface effects would no longer be insignificant and would, in turn, show up in the dielectric function.

Once a spectrum had been acquired and deconvoluted it was then exported in a text format before being converted for input into DK (Appendix 2). Prior to performing the Kramers-Kronig transformation, the spectrum was truncated at 60eV to remove the core loss edges which feature above that region.

The Kramers-Kronig program requires input of the electron beam energy, the collection semi-angle, the t/λ value for the spectrum and the refractive index of the material. The first three values are all known. The refractive index of the majority of bulk materials is also known. This does not appear to be the case for magnesium silicide. A search of the literature suggests that nobody has experimentally determined the refractive index for Mg_2Si. A number of techniques were considered for determining the refractive index ourselves. Unfortunately, as bulk Mg_2Si crystals are moisture sensitive many of the conventional techniques become impractical. The remaining techniques considered were particularly expensive to perform on materials with a refractive index greater than 3. It has been postulated (Mahan *et al.*, 1996) that the refractive index of Mg_2Si is 3.67. The refractive index is used for scaling of the results from the Kramers-Kronig transformation. It does not have a significant effect on the shape of the resulting dielectric function. In the absence of a suitable alternative, the estimated value of refractive index was used.

The dielectric functions generated were used with the relativistic and non-relativistic equations to calculate theoretical spectra. Fig 5.20 gives the experimentally determined dielectric functions for aluminium, magnesium silicide and silicon.

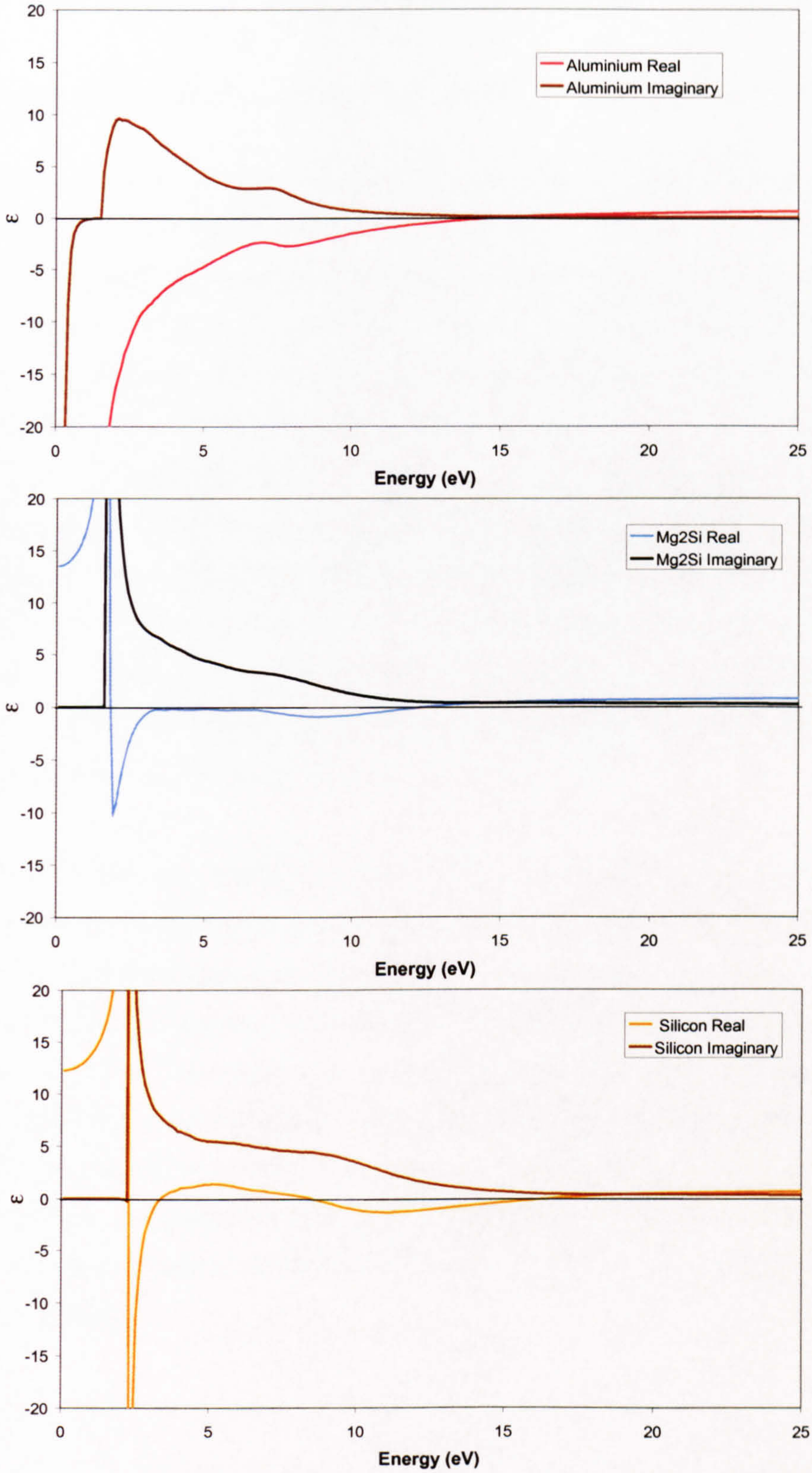

Figure 5.20: Dielectric functions for aluminium (*top*), magnesium silicide (*middle*) and silicon (*bottom*).

5.6 Acquisition and Analysis of Tecnai Data

5.6.1 Acquisition of Data Across the Interface

The acquisition of data was considerably simplified with the Tecnai. Routines within the software for the Tecnai allowed data to be taken from a number of points over a line, known as a line spectrum image[1], or a 2D area, known as a spectrum image[1]. In each case, the dimensions of the line/area, number of points, acquisitions per point and time per acquisition could be altered to provide the best data. However, a balance was required between quality of data and the time taken for the dataset.

The advantage of having the acquisition automated, was that considerably less time was required for the acquisition of the same amount of data. As a result, more data could be taken within a time period equivalent to that for an HB5 dataset. In addition, the drift with the Tecnai was considerably lower than that in the HB5. This, combined with the increased accuracy with which the position of points could be determined (section 3.5), allowed for extremely reliable data.

The different times per acquisition were chosen to balance data quality and total acquisition time. In addition, the acquisition times have to be sufficiently short to prevent the zero loss peak saturating, a necessity as the Tecnai was not fitted with a beam-blank unit. A high number of acquisitions per point was essential to obtain a good signal to noise ratio within the data. The length over which line-traces were taken was also varied but chosen in each case to be in excess of 30nm. This provided a similar spatial range to the HB5 data. The number of points in the line was kept constant at 200. However, as the length of the line was altered for each dataset, the inter-point distance varied between 0.2 and 0.4nm, similar to that for the HB5 data. With these settings, a line spectrum image was acquired in <3 minutes.

---

[1] Though a line-trace covers only one spatial dimension, each point corresponds to a complete low loss EELS spectrum. This means that intensity is measured over two dimensions, those of x and energy loss. Similarly, a spectrum image has x and y in addition to energy loss.

A spectrum image generally provides more data than its line counterpart. As a result the time taken is often considerably longer. Areas were chosen to extend at least 5nm on either side of the interface and 10nm parallel to the interface. The number of acquisitions per point and the number of points were selected to give a good signal to noise ratio whilst keeping the time for a spectrum image below 40 minutes. Fig 5.21 shows the typical dimensions over which spectrum images were acquired.

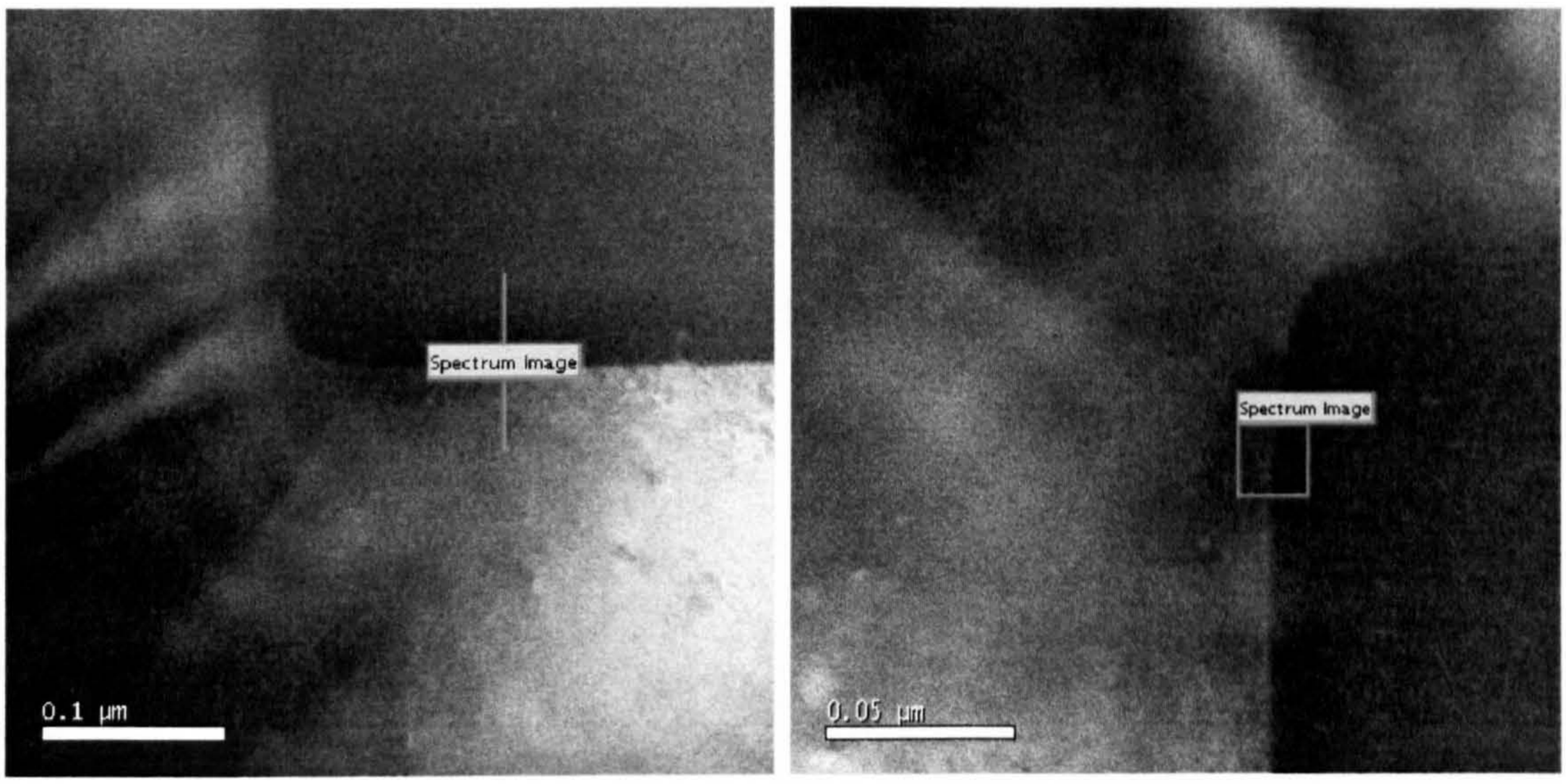

Figure 5.21: Tecnai images indicating setup for acquisition of spectrum images. Data is acquired over the area indicated by the green line for a line spectrum image (*left*) and within the green box for a spectrum image (*right*). Scale markers read 0.1µm and 0.05µm for *left* and *right* images respectively.

5.6.2 Data Processing and Analysis

The initial processing of the data from the Tecnai was quite different to that for the HB5 data. As the amount of data in each dataset was considerably larger for the Tecnai, it was not practical to deal with each spectrum individually. Instead, the Tecnai software had the capability to process entire datasets simultaneously, reducing the time required (Thomas, 2002; Hamilton, 2002).

The number of stages of processing was also reduced from the HB5. It was not necessary to correct for dark counts as this was done automatically by the system. As only a single unsaturated spectrum resulted from each point, it was also not required to sum the spectra or replace the zero loss peak. However, it was necessary to align and calibrate the zero loss peaks, this was done using a plug-in to the software. Following the zero loss alignment,

each spectrum was fourier-log deconvoluted. Fig 5.22 shows the effect of aligning the zero loss peaks. In the 'before' image (Fig. 5.22 *top*) the channels over which the zero loss peaks were observed varied (indicated by the fluctuations in the vertical line). This is corrected in the 'after' image (Fig. 5.22 *bottom*). In addition, the energy offset was calibrated so that the 0eV point corresponded to the centre of the zero loss peak[1].

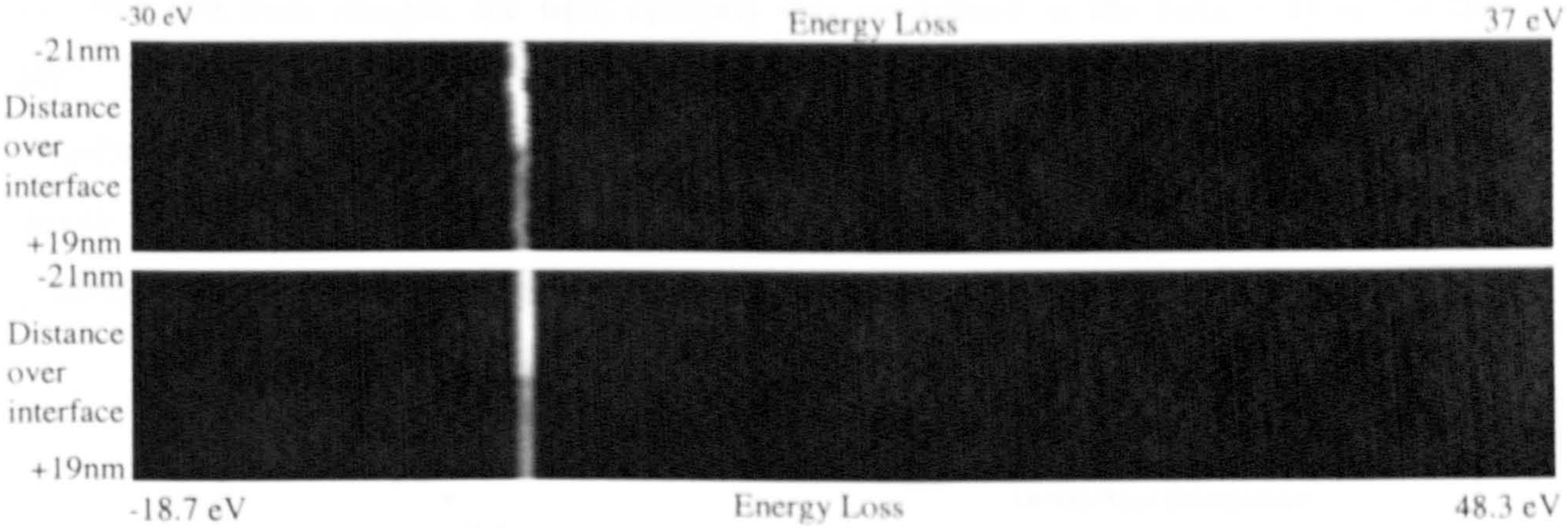

Figure 5.22: Line spectrum image before (*top*) and after (*bottom*) aligning of the zero loss peaks. In each case the vertical dimension indicates distance over the interface and the horizontal dimension gives energy loss. The brightness of each pixel corresponds to the number of counts in that channel. The magnitude of the zero loss peaks is such that no detail is observed anywhere else in the spectra within these images.

The relative components were determined by least-squares fitting using bulk, interface and carbon reference spectra, as before. However, the general procedure was slightly different. Bulk spectra were generated by summing spectra from four adjacent points in the spectrum image. The points were selected to be at least 5nm from the interface on either side. Dielectric functions were calculated from these bulk spectra using a Kramers-Kronig transformation. An interface spectrum was then produced using the non-relativistic equation (eqn 2.33). In this way, two bulk and one interface spectra were obtained for each spectrum image. These, with the bulk carbon spectrum used for HB5 analysis, were used to perform a linear least-squares fit to each spectrum within a spectrum image. Unfortunately, the procedure used for least-squares fitting did not prevent the magnitude of the components becoming negative. This is dealt with more fully in section 7.4.2.

---

[1] It is worth stating at this point, the difference between channel number and energy. The horizontal scale in Fig. 5.22 strictly corresponds to channel number. This has been calibrated to give 0.05eV per channel and so can be related to energy loss. Identical spectra with different energy offsets (*i.e.* energy of the first channel) will appear displaced with respect to each other if plotted by channel, but will be identical if plotted by energy. Fig 5.22 *bottom* has been calibrated such that the zero loss peak is at 0eV.

The results from the least-squares fit were scaled using the number of counts in the zero loss peak from each spectrum in the spectrum image. This was then combined with the number of counts in each of the reference spectra to calculate effective t/λ values.

For line spectrum images, the final analysis was performed in the same way as for the HB5. Data was exported from *Digital Micrograph* into Excel and t/λ plots generated. The interfacial position was determined roughly using the estimated centre of the interface decay (Fig. 5.23). Eqns 5.1a and 5.1b were then fitted as before. Finally the interface position was determined more accurately using the procedure outlined in section 5.3.3.

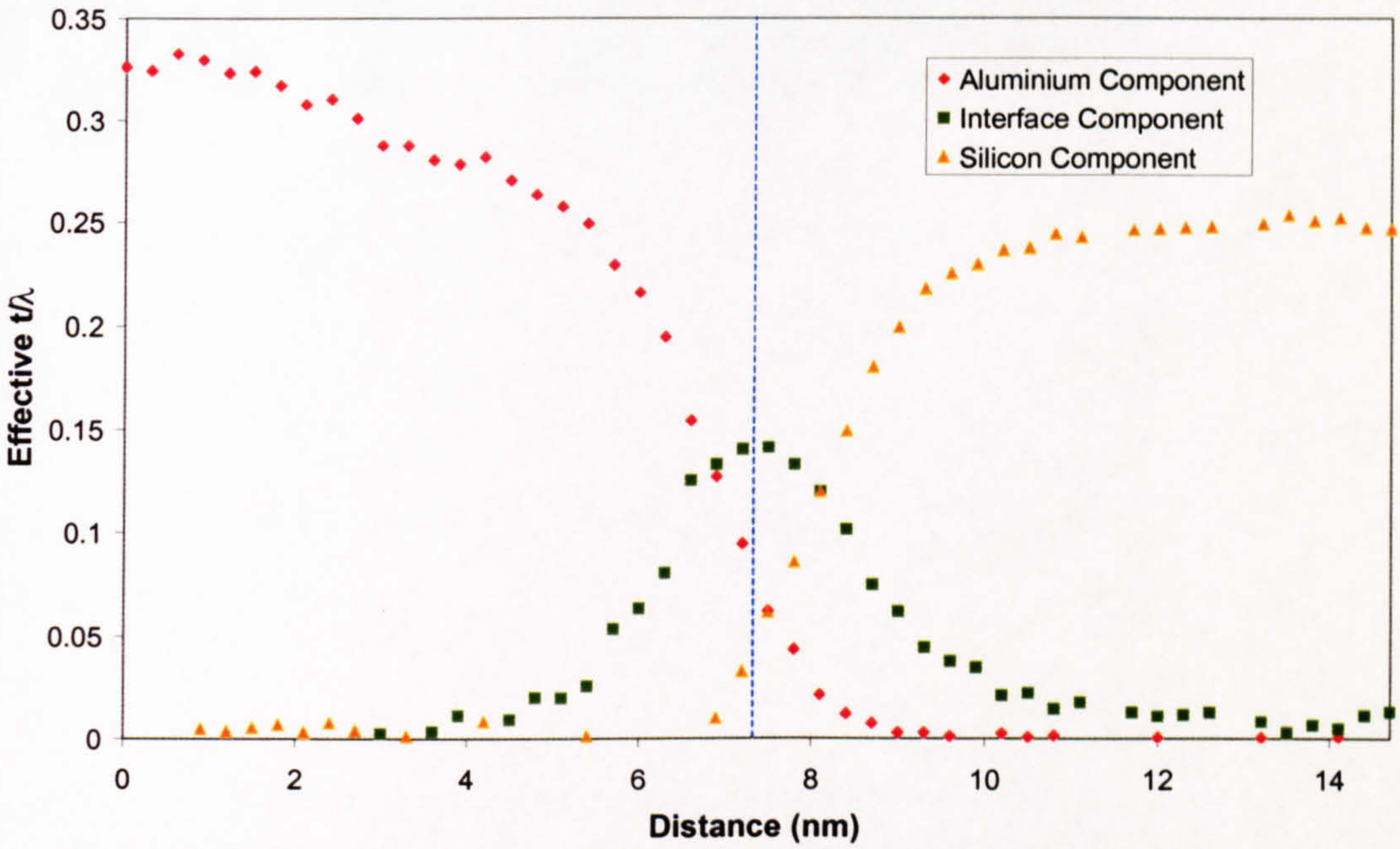

Figure 5.23: Plot of t/λ vs distance. Distance is as acquired from the Tecnai. The new approximate zero position is marked (*broken blue line*). This point was determined using the centre of the peak in the interface component graph.

For spectrum images another step was required. Each spectrum image is equivalent to a number of line spectrum images. As the number of these line spectrum images is often substantial (30 or more) it is not practical to process them all. At least ten lines across the interface were selected from the spectrum image. These were then processed individually as for the final stage of the line spectrum images. Due to the time involved in acquiring a spectrum image, drift was quite noticeable (Fig. 6.11). However, the orientation of the interface was chosen to be vertical on the screen. This caused the spectrum image to be

acquired in lines across the interface[1]. By processing lines individually, the interface point was chosen independently for each one and hence the effect of drift is substantially reduced.

5.7 Summary

The procedures described in this chapter were used for the calculation of the experimental results used for comparison with the theoretical expressions. The results and the comparisons made are outlined in the following two chapters. Chapter 6 discusses the results obtained from the Al/Mg_2Si system and conclusions that can be drawn from them. Chapter 7 covers the same areas for the Al/Si system.

[1] A spectrum image is acquired point by point. The points are acquired sequentially left to right in rows. The rows are acquired top to bottom. These directions are relative to the image as acquired.

CHAPTER 6

RESULTS: Mg_2Si SYSTEM

In this chapter, the results obtained from the Al/Mg_2Si system will be presented. The chapter is split into three main sections. The first discusses the results obtained on the HB5 using the early experimental techniques. This is followed by the results from the refined technique. Finally, data acquired on the Tecnai microscope is presented.

6.1 Experimental Results

6.1.1 Early Experiments

This section gives the results from early experiments performed on the Al/Mg_2Si system. These results were obtained before the techniques involved were refined. The precipitates used were selected at random from an area of the sample. Prior to data collection only limited checks on interface quality were performed. However, the sample was tilted to align the interface to be parallel to the electron beam. This was judged using Kikuchi bands from the matrix, viewed in diffraction mode. When a Kikuchi band running parallel to the interface of interest was centred on the optic axis, the interface was judged to be aligned.

Initially, it was of interest to compare theoretical and experimental interface plasmons. Whilst many of the datasets did not contain a spectrum corresponding to the interface itself, the spatial step-size used normally resulted in the acquisition of at least one spectrum from very close to the interface. Fig 6.1 compares the theoretically calculated interface plasmon with two experimentally observed plasmon shapes taken from different datasets. The experimental spectra were selected as being those acquired from closest to the interface from their respective datasets. The experimental spectra are very similar, though not identical, to the theoretical spectrum. The shape and energy of the interface plasmon is well predicted by non-relativistic theory as seen from Fig 6.1. To examine further the correlation between theory and experiment, the behaviour as the probe was moved away from the interface was investigated.

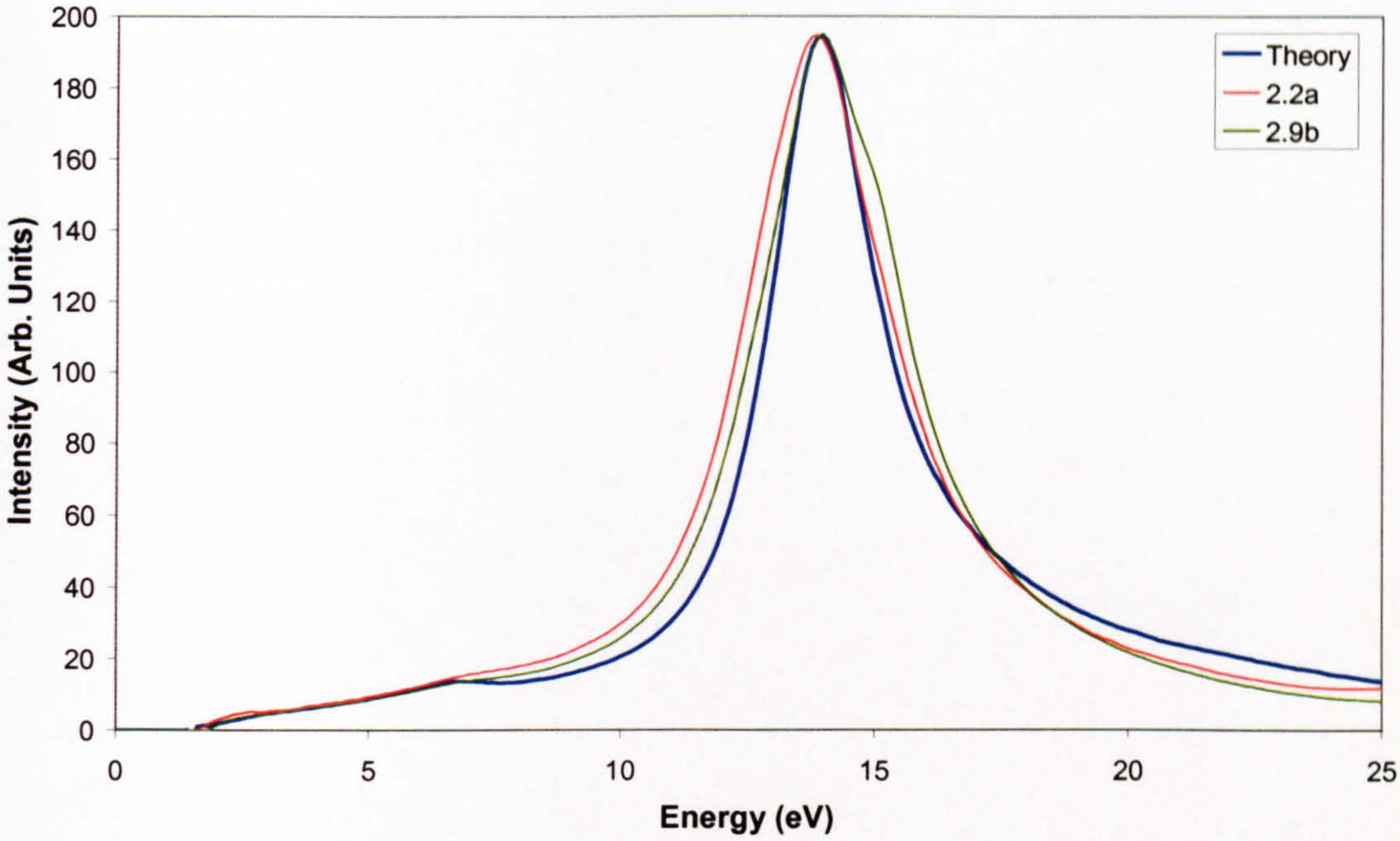

Figure 6.1: Comparison of theoretically calculated (*blue*) and experimentally recorded (*red* & *green*) interface spectra designated 2.2a and 2.9b.

Spectra were acquired at different distances from the interface as outlined in section 5.3.1. These spectra were then processed and analysed using the procedure given in sections 5.3.2 and 5.3.3. The same bulk and interface spectra were used in the fitting procedure for all the datasets. Good bulk spectra showing low contamination were acquired from aluminium and magnesium silicide. The interface spectrum was selected by comparing experimental spectra from different datasets with the theoretical interface spectrum. The experimental spectrum showing greatest similarity to the theoretical spectrum was chosen.

Figure 6.2 gives a plot of t/λ for each component versus distance for an Al/Mg_2Si interface. This plot indicates that the non-relativistic theory, as represented by equation 2.33, predicts the experiment well. In order to compare further the experimental results with theory, a curve was fitted to the bulk and interfacial components on each side of the interface. As can be see from eqn 2.33, the interfacial component should decay according to $K_0\left(\frac{2\omega x_0}{v}\right)$. In order to avoid the asymptotic nature of the Bessel function at x_0=0, an exponential function was used for fitting to the t/λ data. As the fit was purely to indicate qualitatively the trend, this choice of function was valid (Appendix 1). Curves were fitted

in the form Ae^{-Bx_0} to the interface component and $A\left(1-e^{-Bx_0}\right)$ to the bulk component. A and B were varied to provide the best least-squares fit for both curves simultaneously. These curves are also included in Fig. 6.2.

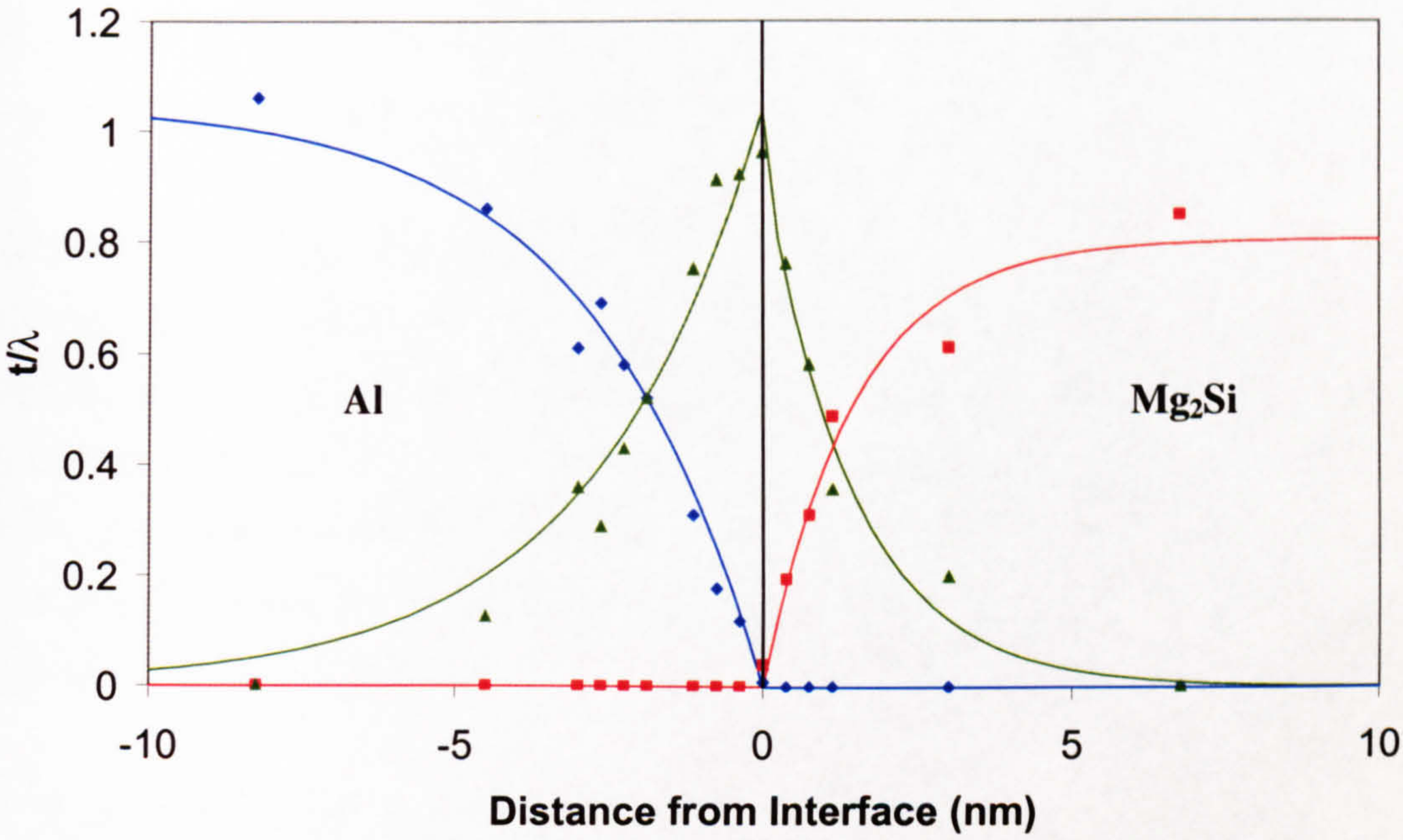

Figure 6.2: Plot of effective t/λ vs distance for the Al (*blue*), Mg_2Si (*red*) and interface (*green*) components from experimental data. Best-fit exponential lines have been fitted to the points on each side of the interface.

The exponential displayed a reasonable fit to the experimental data, providing further agreement with the theory. Further to this, according to free electron theory $\lambda_{Al} = 0.99\lambda_{Mg_2Si}$ (eqn 2.11). Therefore, if the sample had constant thickness over the area of interest, it follows that

$$\frac{t}{\lambda_{Al}} = 1.01\frac{t}{\lambda_{Mg_2Si}}.$$

The ratio of t/λ values from Fig. 6.2 yields 1.22. This indicated that the data was not consistent with the assumption of constant thickness. The data at large x_0 value indicated that the bulk plasmon had not reached a uniform value, particularly on the aluminium side. This could be a result of thickness variations, which would support the incorrect plateau ratio value.

The plasmon energies in aluminium and magnesium silicide differ by around 2eV. Therefore, an asymmetry in the decay lengths would be expected (section 5.4). As the

plasmon energy is higher for aluminium than for magnesium silicide, it would be expected that the decay length of the interface plasmon would be shorter on the aluminium side. Though an asymmetry in decay lengths is observed, it is opposite to that expected. The interface plasmon on the magnesium silicide side of the interface is observed to decay considerably more steeply than the corresponding aluminium.

The early experiments had highlighted a number of problems. In particular, it was necessary to prove whether the asymmetry was opposite to that expected or whether this resulted from an error in the experiment. In addition, it was desirable to increase the distance over which data was taken, in order to determine whether a plateau was reached. This would determine whether there was a variation in thickness as believed. To address these problems and increase the likelihood of acquiring a useable dataset, the experimental technique required improvement.

6.1.2 Experimental Improvements

The improvements in experimental technique are outlined in detail in chapter 5. However, as a summary, the basic improvements made were:

- Selection of better interfaces
- Checks made to ensure limited variation in thickness in the vicinity of the precipitate
- Careful alignment of the matrix surrounding the precipitate to a suitable pole
- Additional data taken at greater distance from the interface to give an indication of bulk behaviour
- Extra care taken to reduce drift
- Use of bulk spectra specific to a precipitate during the fitting procedure

For the early experiments, the interfacial spectrum used for fitting was an experimental spectrum. It was felt that an experimental spectrum would provide a better and more accurate fit than a theoretical one. However, it was observed that experimentally obtained interface spectra appeared to contain a small amount of bulk component. An investigation was performed to examine the quality of fit achieved using a selection of experimental interface spectra; this was then correlated to the quantity of bulk component present in each one. In addition to the experimental spectra, a theoretical spectrum generated using dielectric functions calculated from bulk experimental data was included for comparison.

The experimental interface spectra were all selected from different datasets. Within their respective sets, the spectrum chosen was the one closest to the interface point (section 5.3.3). Two additional spectra were selected as target spectra for performing the fitting. The first of these was acquired at a small distance from the interface on the aluminium side (hereafter referred to as '$Target_{Al}$') and the second from an equivalent distance into the magnesium silicide ('$Target_{Mg}$'). In both cases there was a significant interfacial component in addition to a notable amount of bulk contribution. These spectra were selected as it was anticipated that the experimental interfacial spectra were likely to have a small amount of bulk component present. It was expected that a fitting spectrum with a small amount of aluminium present would fit better to a spectrum containing aluminium, than to one containing only interface and magnesium silicide components. Equivalently, a fitting spectrum containing magnesium silicide would fit better to a spectrum with a magnesium silicide component. The fits were performed using a least-squares fit over the range 10-28eV. The quality of fit value was given by the weighted least squares value $S = \sum_i \left(\frac{N_i^{fit} - N_i^{data}}{N_i^{data}} \right)$ (Lyons, 1991) for the range 12-17eV, where N_i is the intensity of channel i for the fit or the experimental data depending on the superscript. This gave an accurate impression of the quality of fit in the region of the plasmons of interest. The results of this investigation were arranged in order of quality of fit to $Target_{Mg}$, from best to worst. They are presented in Fig. 6.3.

With the exception of the first and last spectra, a general trend was seen in the results. As the fit to $Target_{Mg}$ became worse, the fit to $Target_{Al}$ improved. This was in keeping with the expected result. The two spectra that deviated from this trend were *original* and *theory*. *Original* provided the worst fit to $Target_{Mg}$ and one of the worst fits to $Target_{Al}$. It was this spectrum that was used for a lot of the early fitting, including for Fig. 6.2. This spectrum fitted so poorly largely because the fit range used covers part of the carbon plasmon. For the *original* spectrum the amount of carbon was quite high and the fitting procedure did not allow for the subtraction of carbon. Therefore, when this spectrum was fitted to data that had a negligible amount of carbon present, the resulting fit was poor. The *theory* spectrum was generated using the relativistic theoretical equation (eqn 2.3.2). It

demonstrated the best fit to both $Target_{Al}$ and $Target_{Mg}$ compared with the other spectra. This result was unsurprising as *theory* contains no bulk component.

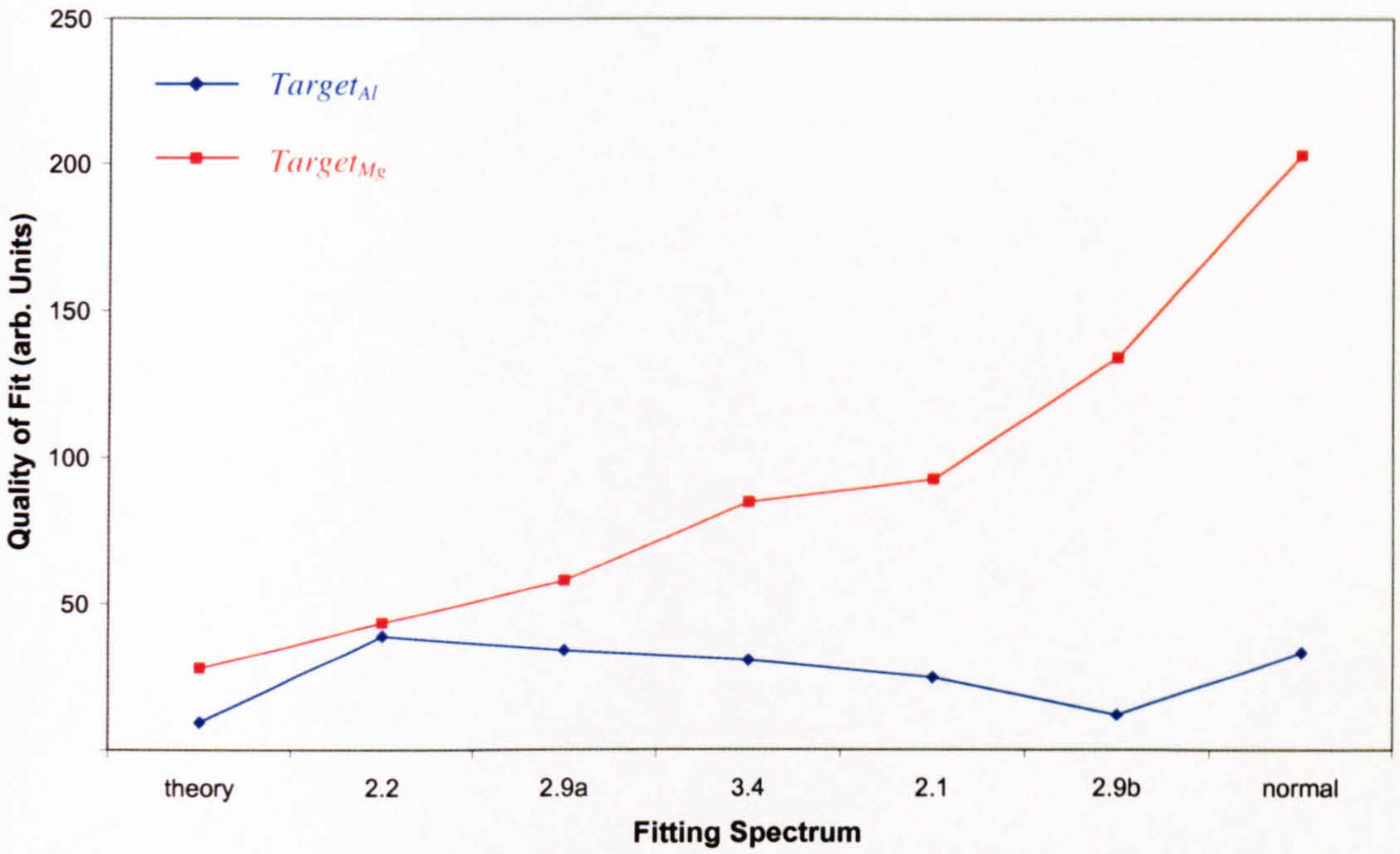

Figure 6.3: Graph indicating quality of fit using different interface spectra. Fit was performed on experimental data taken from a small distance away from the interface into aluminium (*blue*) and Mg_2Si (*red*). Increasing fit value indicates a worse fit.

It was then of interest to correlate the above results to the amount of bulk component present in each of the experimental spectra. To do this, a least squares fit was performed on each spectrum over the range 10-28eV. The fitting spectra used were the theoretical interface spectrum and two experimental bulk spectra. The results from this analysis are presented in Fig. 6.4 in the same order as previously.

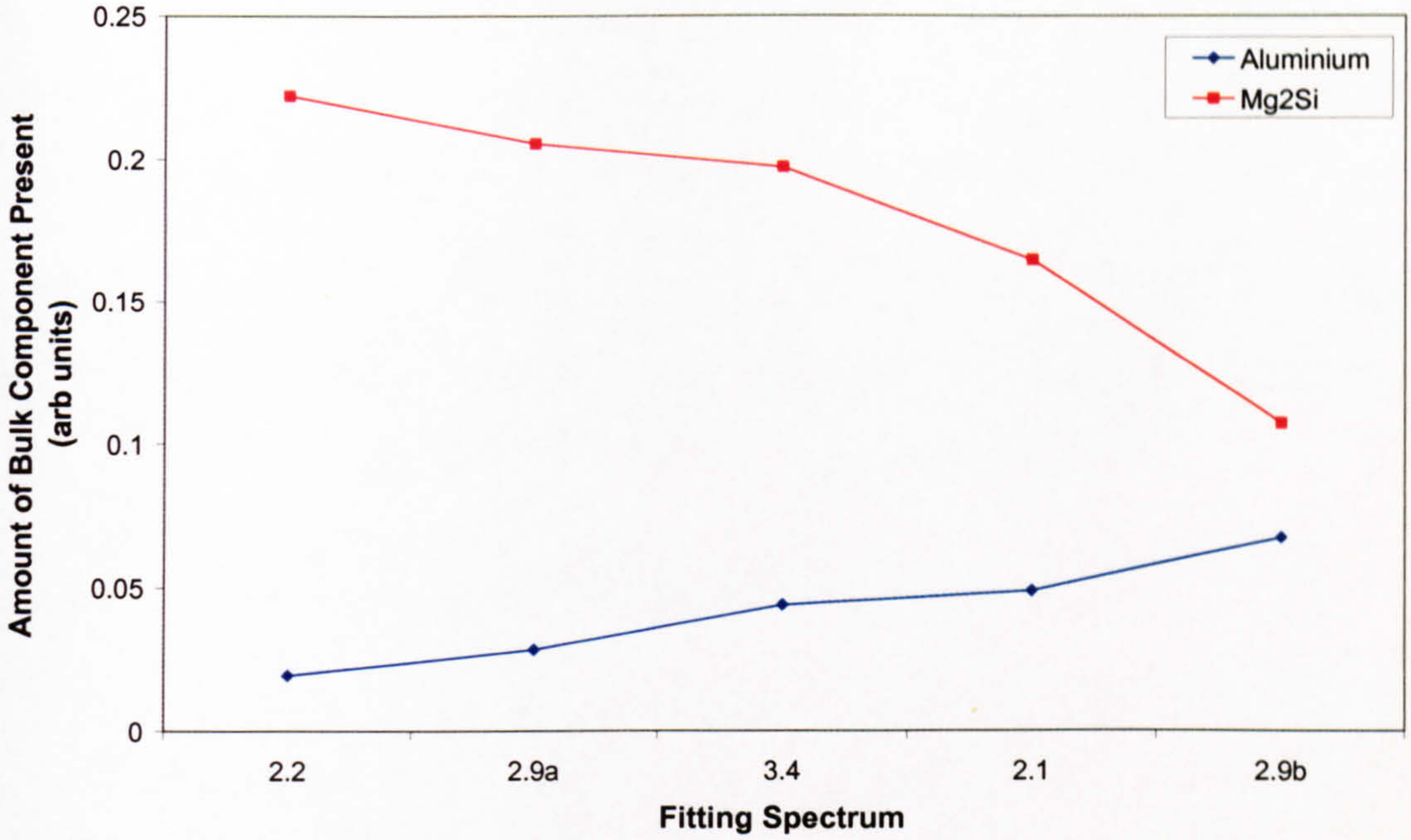

Figure 6.4: Amount of bulk component present in experimental interface spectra. Results are scaled to give an interface component amount of 1 in each case.

Once again a trend was observed in the results. As the amount of aluminium component increased, the amount of magnesium silicide decreased. Perhaps surprisingly, all spectra selected were found to contain both aluminium and magnesium silicide components. This could have resulted from the size of the electron probe. As the probe was approximately 1nm in size, when positioned exactly on the interface it would have extended out to the order of 0.5nm on either side of the interface. This would have caused the excitation of bulk plasmons in addition to the interface plasmon resulting in corresponding peaks in the loss spectrum (see section 8.3).

When the results from figs 6.3 and 6.4 were compared, it was observed that there was a strong correlation between the two. An improvement in the fit to $Target_{Al}$ corresponded to an increased aluminium component (and hence a decreased Mg_2Si component) in the experimental interface spectrum. Similarly, a better fit to $Target_{Mg}$ corresponded to a larger Mg_2Si component (and a smaller aluminium component) in the interface spectrum. This can be seen clearly in the case of spectrum 2.2, which provides the best fit to $Target_{Mg}$ and the worst fit to $Target_{Al}$. This corresponds to having the highest amount of Mg_2Si and the lowest amount of aluminium in the spectra examined.

This investigation demonstrated that experimental interface spectra always contained a bulk component. This bulk component had a significant effect on the quality of the fit and as such, a better fit was provided by a theoretically generated interface spectrum.

Following this investigation all fits were performed with a theoretically calculated interface spectrum using dielectric data from experimental spectra. For convenience, the same interface spectrum was used for fitting to all Al/Mg_2Si data sets.

6.1.3 Experiments Based on Refined Technique

In this section, the results obtained using the improved technique will be presented. As it is neither practical nor useful to present all the data obtained, a representative cross-section will be given. Conclusions specific to this data will also be given in this section, with overall conclusions given in chapter 8.

Both spatial drift and carbon contamination were known to be problematic in the acquisition of data from an interface. To obtain the most accurate results, the data acquired was rated according to its carbon content and the amount of spatial drift apparent. Six data sets showing low contamination and low drift were selected and processed. The data sets were taken from four different interfaces, each with different t/λ values. Fig 6.5 gives a t/λ plot for one such interface. Also shown on the plot is the best-fit line to the different components. For the refined technique, Bessel functions were used for fitting to provide a more accurate comparison with theory. The fits were performed using the procedure given in section 5.3.3.

In general, the fit was observed to be better than that observed for the earlier data, though it starts to deviate at larger negative values. However, this deviation is attributable to the thickness of the aluminium increasing with distance from the interface.

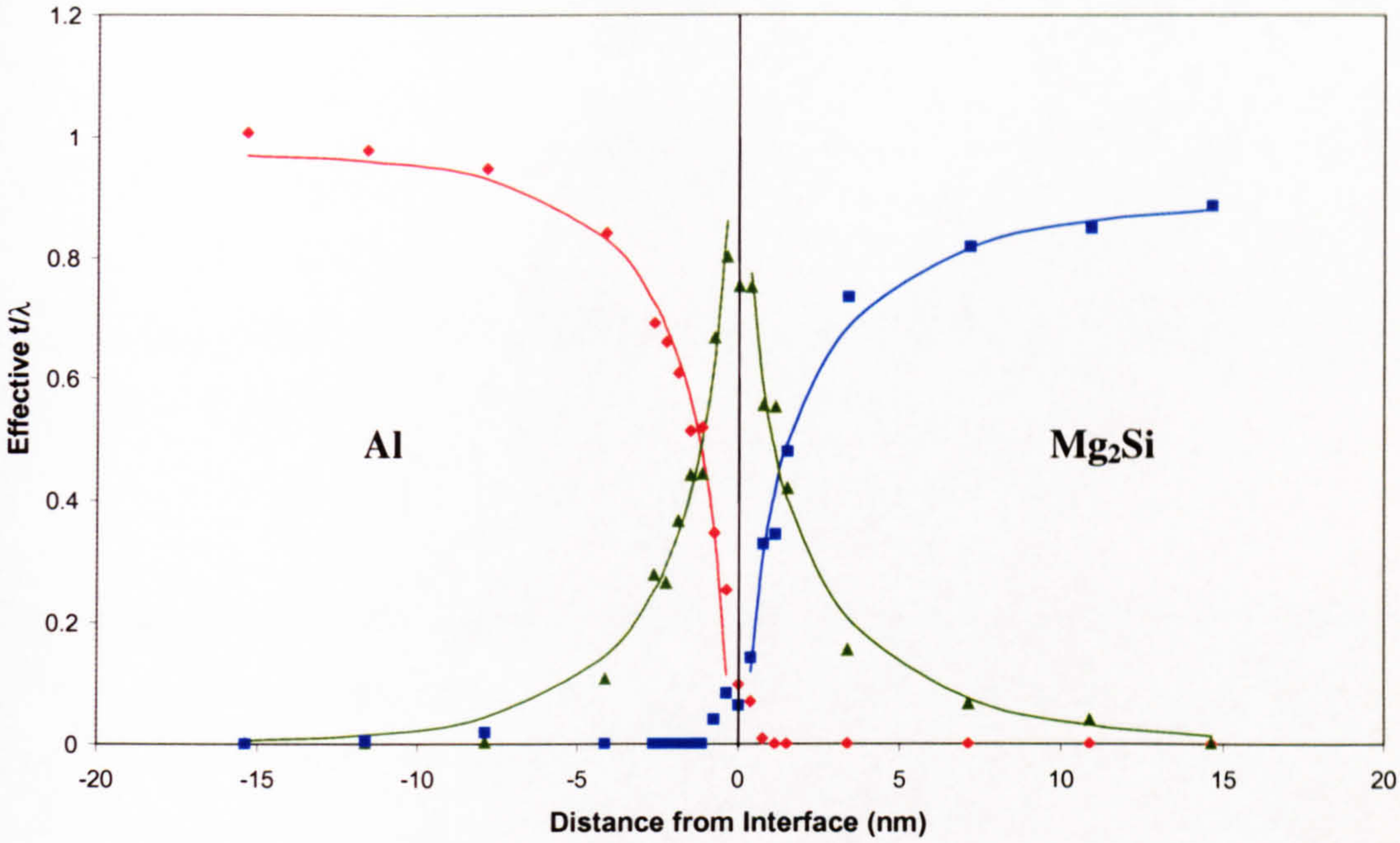

Figure 6.5: Plot of t/λ vs distance for an Al/Mg_2Si interface. Graph indicates the relative proportions of aluminium (*red*), magnesium silicide (*blue*) and interface (*green*) with distance from the interface. Also shown is the function fitted to each component.

One of the most notable features in this data set was the apparent presence of Mg_2Si on the aluminium side of the interface and vice versa. Only one bulk component should be observed on each side of the interface in an ideal system. The bulk components extend to approximately 0.75nm on the opposite side of the interface. It is likely that this results from the spatial extent of the electron probe (section 8.3), which has a diameter of approximately 1nm in the HB5. This overlap of the bulk components was not evident in the earlier experiments. However, the use of an experimental interface spectrum for the fitting procedure prevented it being observed. As the experimental interface spectrum contained components of both Al and Mg_2Si, the effective t/λ of the bulk components appeared to drop to zero at the interface. This is supported by the results in section 6.1.2. The reappearance of a small proportion of Mg_2Si component at larger distance from the interface is not believed to be representative of the true behaviour of the system. The presence of such a small component is likely to be an artefact from the fitting procedure. In particular, the addition of a small amount of Mg_2Si into a fit will compensate for a slight excess of counts on the low energy side of the aluminium. Such an excess of counts can be caused by the presence of a small amount of surface plasmon.

Using eqn 5.2 and taking material 1 to be aluminium and material 2 to be Mg_2Si it is found that

$$\frac{C_{Al}}{C_{Mg_2Si}} = \frac{15}{13} = 1.15$$

As disucussed previously, the expected value for the A_i ratio is 1 and for P_i is 1.01. For the results given in Fig. 6.5 the values obtained were as follows.

$$\frac{P_{Al}}{P_{Mg\,2Si}} = 1.10 \quad \frac{A_{Al}}{A_{Mg\,2Si}} = 1.21 \quad \frac{C_{Al}}{C_{Mg\,2Si}} = 1.30$$

This set shows reasonable agreement with theory. The ratio of A_i values indicates that the optimal interface position was not chosen accurately. This will affect the values of P_i and C_i, possibly accounting for some of the deviation from theory. A comparison of these results with other results obtained from the Al/Mg_2Si system is given in section 6.1.5.

6.1.4 Fitting to Theoretical Data

A number of assumptions had been made in the analysis of the data. The largest of these assumptions was that each spectrum could be decomposed into component parts. In order to justify that this assumption was valid, an analysis was performed on theoretical data. The theoretical data was generated using the relativistic equation (eqn 2.3.2) from experimentally determined dielectric functions (section 5.5). Data was generated for points at different distances from the interface, resulting in a complete theoretical dataset. This theoretical dataset was then analysed in the same manner as an experimental dataset (section 5.3.3) and the results compared with the expected values.

The results for this theoretical system are given in Fig. 6.6. The y-axis of the plot is not strictly t/λ as the theoretically generated spectra have no zero loss peak with which to calculate t/λ values. This is not problematic however as the effective proportion is equivalent to t/λ multiplied by a constant factor.

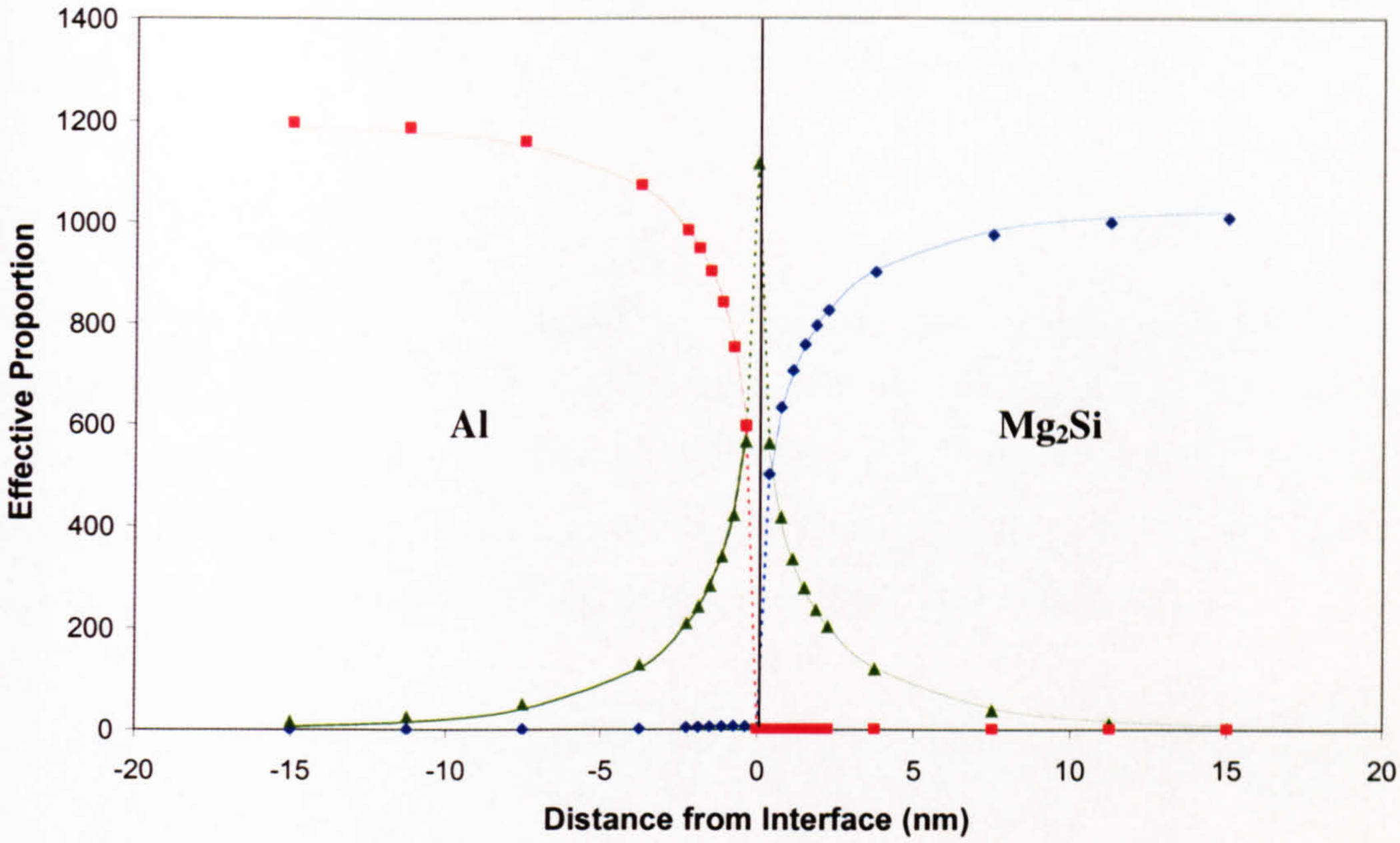

Figure 6.6: Plot of proportion of each component with distance from an interface. Data used was generated using the relativistic equation. Plot shows Al (*red*), Mg_2Si (*blue*) and interface (*green*) components with their respective fits (*solid lines*). Fits are extrapolated to the data point at 0nm (*broken lines*).

The Bessel function provided an extremely good fit to the data, with the interface plasmon declining more sharply on the Mg_2Si side than on the aluminium side, as expected. This result proved that the approach taken in data analysis was valid. In particular, that both the decomposition of spectra into components and the fitting of a Bessel function to a t/λ vs distance plot were justified.

It was of interest to determine the A_i, P_i and C_i ratios for this data. As the expected values rely on a number of assumptions, this theoretical system provided arguably more accurate results.

$$\frac{P_{Al}}{P_{Mg\,2Si}} = 1.18 \quad \frac{A_{Al}}{A_{Mg\,2Si}} = 1.10 \quad \frac{C_{Al}}{C_{Mg\,2Si}} = 1.09$$

The values obtained for the theoretical system were close, but not identical, to the expected values. Most unexpected is the ratio of the A_i values. As there is no uncertainty in the position of the interface, it would be expected that $A_{Al}/A_{Mg2Si}=1$. The similarity between the A_i and C_i ratios suggests that there may be a link between the two. As the Bessel function is undefined for $x_0=0$, the functions on either side of the interface never meet. It is therefore plausible that the inherent asymmetry in the system results in a further asymmetry in the A_i

ratio. The values for the other two ratios show great similarity to those proposed as expected values. This indicates that the assumptions made were valid.

6.1.5 Overall Results for the System

Table 6.1 gives the ratios of interest for six datasets collected and processed using the refined method. In addition, the plateau values on the aluminium side of the interface are included to indicate relative thicknesses in the region of the interface. In order to compare different results from the same interface, sets 3a & 3b were acquired from the same interface, as were sets 4a & 4b. These results represent 4 interfaces in total.

Dataset	Al Plateau	P_{Al}/P_{Mg2Si}	A_{Al}/A_{Mg2Si}	C_{Al}/C_{Mg2Si}
Set 1	1.00	1.14	1.21	1.30
Set 2	1.30	1.20	1.06	1.35
Set 3a	1.83	1.20	1.02	1.25
Set 3b	1.92	1.24	1.01	1.00
Set 4a	0.76	1.30	1.17	1.35
Set 4b	0.71	1.40	1.13	1.24
Average		1.23	1.10	1.25
Standard Error		0.04	0.03	0.05
Theoretical Value		1.18	1.10	1.09
Expected Value		1.01	1.00	1.15

Table 6.1: Table of results for Al/Mg_2Si system.

These results indicate extremely good agreement between the experiment and the theoretical equations. The average value for the plateau ratio differs from both the expected and theoretical values by less that 5%. The ratio of the scaling factor, A_i, shows exceptional agreement with the theoretical case, though deviates more significantly from the expected value. The worst agreement is seen for C_{Al}/C_{Mg2Si} where a deviation of 7.5% and 12.5% is seen for the expected and theoretical results respectively. In all cases the standard error is quite low (<5%) indicating good agreement between the experimental results.

The results from sets 3a and 3b and from sets 4a and 4b do not show marked similarity. This is believed to be due to the variation in carbon contamination present. For sets 3a and 3b the average t/λ contribution from carbon was 0.54 and 0.22 respectively. Sets 4a and 4b had an average carbon t/λ of 0.23 and 0.05 respectively. Whilst the analysis technique allowed for the presence of carbon, it was not possible to isolate totally its effect. As a result, variations in the amount of carbon were likely to have affected the results.

Due to the numerous sources of error throughout the whole experimental and analytical procedure, it was difficult to determine a single quantitative error. Instead, the sources of error will be given, with a discussion of their significance to the final result.

6.1.6 Sources of Error

The errors in the final results arose either from the experiment itself or from the subsequent analysis. Some of these errors have been discussed briefly in previous sections but a more in depth treatment will be presented here.

Much of this work relies on sub-nanometre spatial resolution. The smaller step-size used in data acquisition was 0.38nm. However, it has also been discussed that the electron probe had a spatial size at the sample of 1nm. The most notable effect of this was that the interface contribution did not reach a maximum at the interface. Instead, the interface contribution was observed effectively to plateau in the vicinity of the interface. This was not believed to have an effect on the A_i and C_i ratios, as the fit range starts at greater distance from the interface. However, there may have be a less noticeable effect from the probe size. For example, the probe size may have resulted in convolution with the decay shape to result in a shallower or steeper decay.

Spatial drift of the specimen is another likely source of error. However, the extent of the effect is difficult to quantify. If the sample were drifting at a uniform rate throughout the acquisition then, on a basic level, the results would just be displaced with respect to the interface, an effect which would be corrected during the analysis. In actuality, it would be more complex than this. As the plasmon decay follows a Bessel function, the drift rate has a more significant effect close to the interface than it does further out. This made the drift correction procedure (section 5.3.3) more accurate for some points than others. In addition

to this, it was observed that the drift was not uniform, it varied from point to point in the dataset. These two effects combined, were likely to have caused some alteration in the observed decay of the plasmons.

Contamination was a significant issue for many of the datasets. Though the datasets in Table 6.1 were specifically selected to have a low carbon component, they still had some carbon present. As the carbon plasmon peak is extremely broad, it adds a significant number of counts within the fit range. The inclusion of a carbon spectrum in the fitting procedure compensated for a significant proportion of this. However, the assumption was made that the carbon forming on the sample was purely amorphous carbon. It was noted that fitting using the carbon spectrum was inaccurate when the experimental spectrum contained a small or very large carbon component. In addition, spectra with a greater carbon content also displayed increased counts in the 0-10eV range. This arose from a plasmon peak associated with the carbon π orbital. The higher energy tail of this peak extended into the region of the Mg_2Si plasmon. The fitting procedure will have attempted to compensate for the effect of these two factors in order to obtain the best fit. This would have resulted in an alteration of the proportions of the bulk and interface plasmons, giving spurious values.

Another consideration was that of the range over which the fitting was performed. Ideally, all fits would have been performed over the full energy range of the spectra. In practice, this would have had a severely detrimental effect on the results. Above 28eV a number of factors have an effect on the EELS spectrum. Incorrect removal of plural scattering by deconvolution in an aluminium spectrum results in a notable peak at 30eV, usually accompanied by a deficit of counts at 45eV (Fig. 5.16). At higher energy, core loss edges have a significant effect on the counts. Below 10eV peaks resulting from surface loss or from carbon π orbitals (see above) appear. Attempting to fit to include these regions resulted in bad fits and meaningless results. Conversely, if the fit range did not cover a high enough energy the carbon plasmon did not fit correctly. This generally took the form of massive over-estimation of the carbon contribution to provide a good fit using the lower energy tail of the carbon plasmon. Outside the fit range, the size of the carbon plasmon resulted in significant deviation from the experimental spectrum. It is believed that the fit range chosen provided the most accurate fit possible using this technique. Though

restricting the fit-range is likely to have introduced an error in the fit, this is believed to be small compared with the other errors discussed in this section.

Connected with the discussion above is that of plasmon shapes. The Mg_2Si plasmon is considerably broader than that of aluminium. As a result, small changes in the aluminium plasmon are considerably more noticeable than corresponding changes in the Mg_2Si plasmon. Equally, a small amount of Mg_2Si plasmon was often observed in fits where none would be expected. This was attributed to the broadness of the Mg_2Si compensating for small deficits in counts between the experimental and the combined fit spectra (section 6.1.3) and not believed to be indicative of the presence of Mg_2Si. As a result it is believed that the fit to the aluminium is more accurate than that to Mg_2Si. Once again this error is believed to be small compared with the other errors discussed in this section.

6.1 Tecnai Results

The FEI Tecnai microscope was able to provide a huge amount of data in a short time. This data gave a great deal of information on the interfaces examined. The presentation of such a large amount of data is not easy. However, as with previous sections, a representative cross-section of the various types of data obtained will be presented.

6.2.1 High-Resolution Imaging

Using high-resolution imaging, it was possible to determine the quality of the interface. In particular, the sharpness and the extent to which the interface was parallel to the electron beam were examined. Fig 6.7 shows an image obtained from the Tecnai, with the aluminium tilted to a [100] pole.

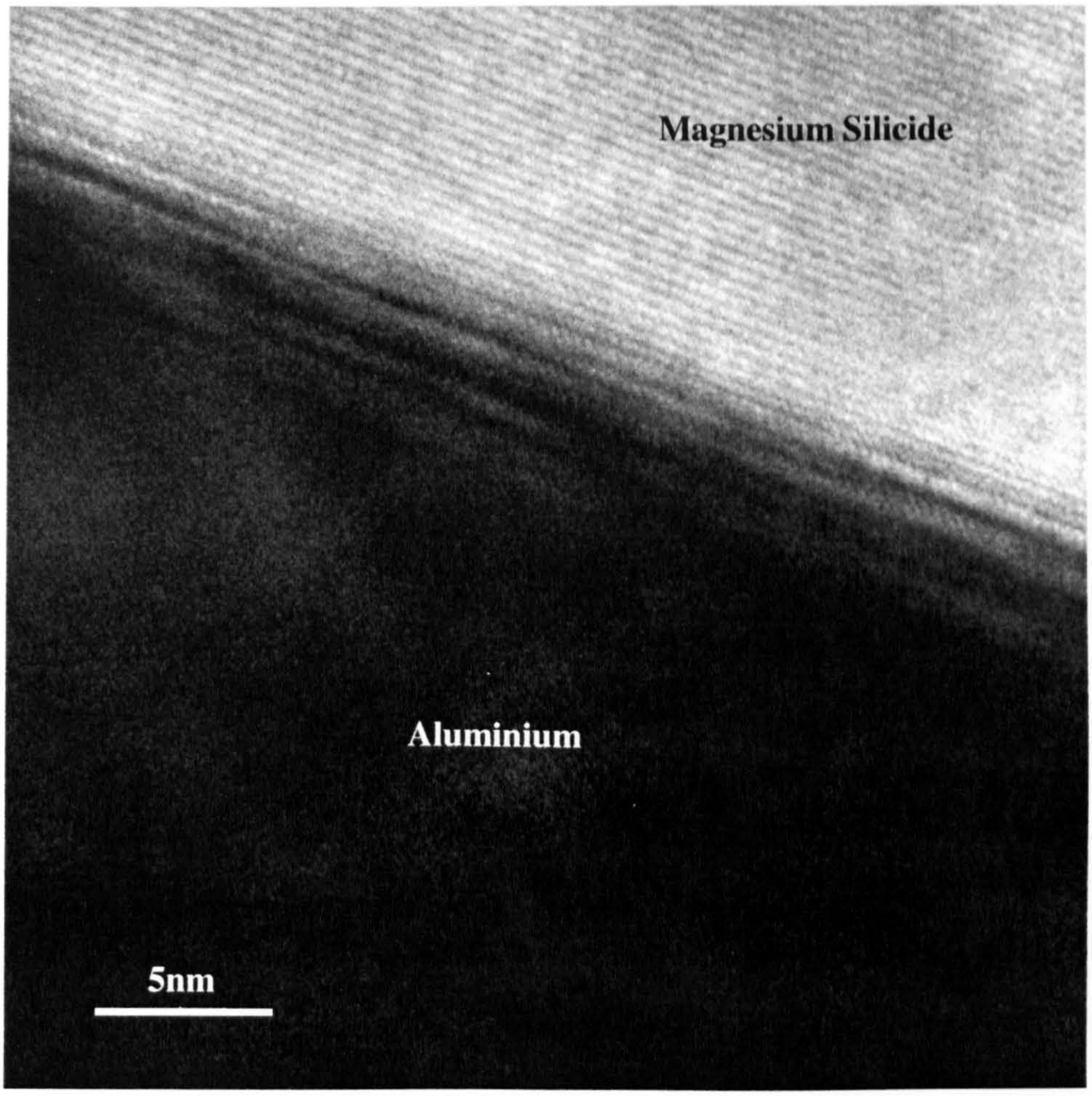

Figure 6.7: High-resolution image of an aluminium/magnesium silicide interface unsuitable for data collection. Aluminium was aligned to a [110] pole.

Within this image, the interface is not abrupt, but instead appears to extend over 5nm. The fading in intensity from the Mg_2Si to the Al suggests that this interface is tilted with respect to the electron beam. As such, it was not a suitable interface from which to acquire data. Unfortunately, due to problems with contamination, this sample had not been fully investigated in the TEM prior to analysis in the Tecnai. As a result, it is difficult to know whether the tilting observed for this interface would have been noted during the TEM investigation. Fig 6.8 shows a high-resolution image of an Al/Mg_2Si interface which is parallel to the electron beam.

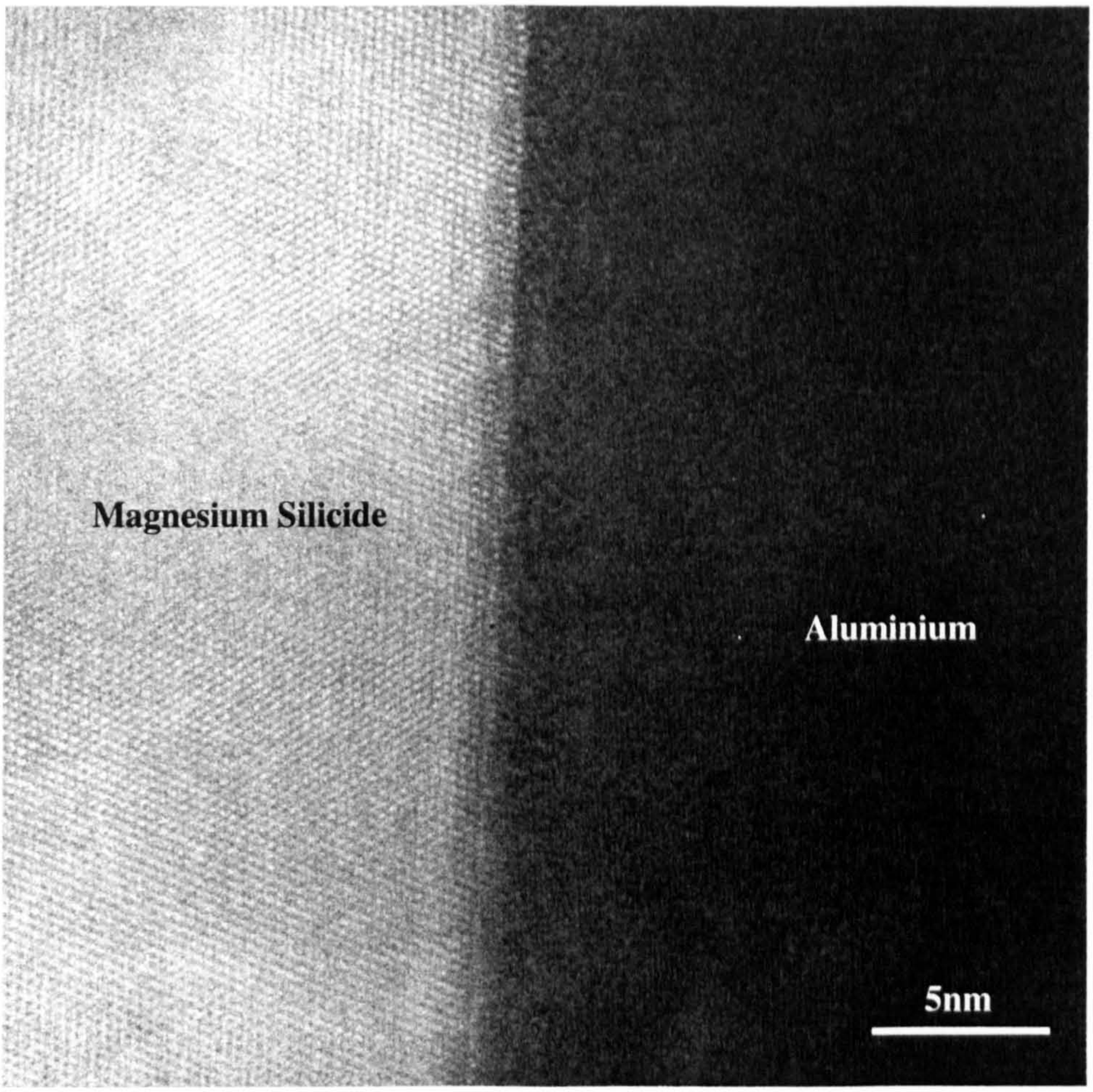

Figure 6.8: High-resolution image of an aluminium/magnesium silicide interface. Aluminium was aligned to a [100] pole.

The lattice planes within the Mg_2Si appear to be approximately parallel to the interface. As a result, steps are not required at this interface to compensate for mismatch between the lattice and interface directions (section 7.4.1). The interface does not appear to be atomically sharp, instead a ~1nm band is apparent at the interface. The nature of this band is not clear. It may contain both aluminium and magnesium silicide. If this were the case, the results would be significantly affected and a broadening of the t/λ plot would be observed. Alternatively, this region could arise through strain between the aluminium and magnesium silicide lattices. This would be expected, as the Al/Mg_2Si interface is incoherent. The effect of this on the data is more difficult to determine. It may not have any effect at all. On examination of the interface, no dislocations are immediately evident. However, it would be expected that the dislocations would occur in the aluminium, as the softer material. Unfortunately, due to the lack of contrast within the aluminium it is not

possible to determine whether dislocations are present. All data acquired from an Al/Mg_2Si interface using the Tecnai were taken over this interface.

6.2.2 Line Spectrum Imaging

The main interest in the Tecnai for this thesis was in its ability to perform spectrum imaging. Line spectrum imaging enables data with a good signal to noise ratio to be taken from an interface in a relatively short period of time.

Data were acquired from a single interface using acquisition times of between 5 and 500ms per acquisition. The number of acquisitions per point was varied between 1 and 10. In addition, spectrum images were taken with 0.2, 0.3 and 0.4nm between points. The data were processed and analysed using the techniques outline in section 5.6.

Fig 6.9 gives a line spectrum image. It is effectively a plot giving processed energy-loss spectra at different distances across an interface. The *y* dimension corresponds to the distance across the interface in steps of 0.35nm and the *x* dimension represents the energy loss in eV. The magnitude of the intensity is represented by the brightness of the point.

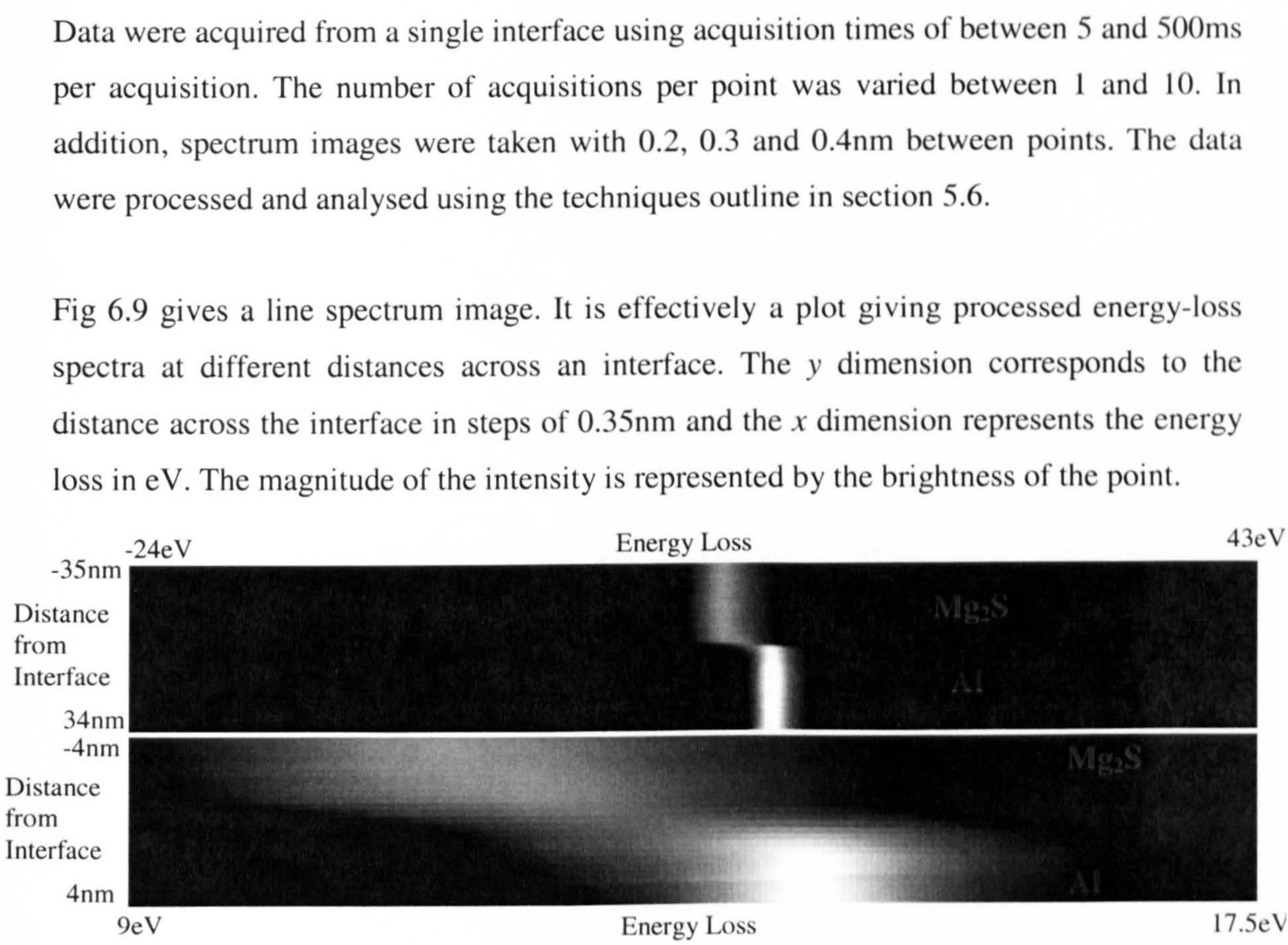

Figure 6.9: Line spectrum image of an Al/Mg_2Si interface (*top*). The intensity of each pixel indicates the intensity of that channel in the EELS spectrum. *Bottom* shows detail of a portion of this image.

Fig 6.9 *top* highlights how sharp the transition in the EELS spectrum is across the interface. The change from the broad Mg_2Si plasmon peak on the upper half of the figure to the much narrower aluminium plasmon peak on the lower half of the figure is very

abrupt. The image requires to be magnified before the interface plasmon peak is evident (Fig 6.9 *bottom*). It was for this reason that a good spatial resolution was a necessity.

The t/λ plot corresponding to this data is given in Fig. 6.10. This data shows the t/λ behaviour over a much larger distance than the data from the HB5. It is evident that the thickness remains fairly constant over the interface. Whilst neither the aluminium nor the magnesium silicide flatten out completely at large distance, only a very slight gradient is observed, particularly with the aluminium component. The data from this interface should therefore be largely unaffected by the problems associated with thickness variations (section 8.1).

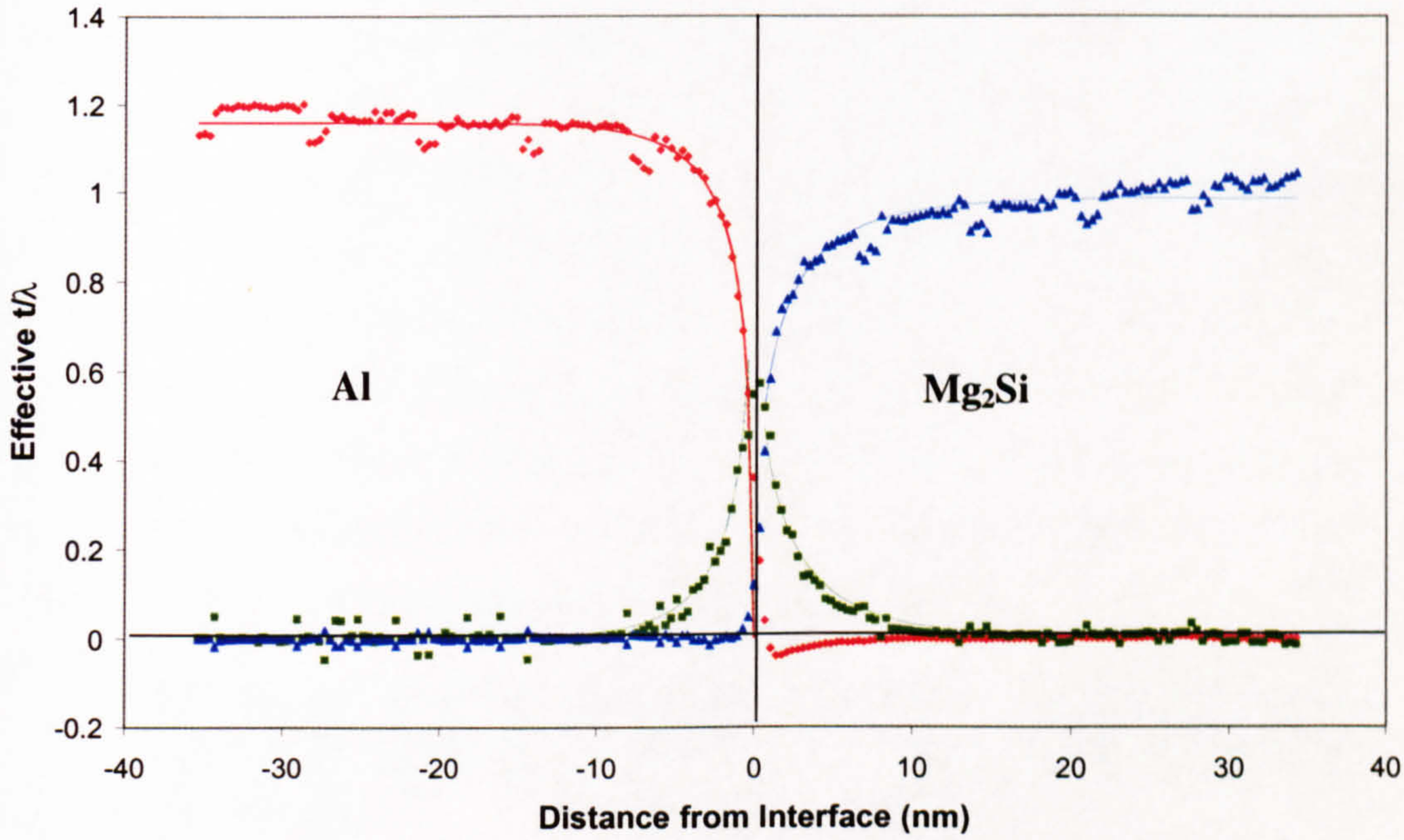

Figure 6.10: Plot of t/λ vs distance for data acquired using the FEI Tecnai. Shown are aluminium (*red*), interface (*green*) and Mg_2Si (*blue*) components with their respective fits.

One problem is apparent with the data shown in Fig. 6.10. Every 7nm, a group of points show a deviation from the general trend of the results. This problem arose from an unresolved issue with the automatic dark current correction. At regularly spaced intervals with some acquisitions, the dark current was not subtracted correctly. As a result, there was a constant background number of counts to some of the spectra and not to others. As the number of points that were affected in the above data series was small compared to the total number of points it is not believed to have affected the fit.

The results obtained for the above series are given below.

$$\frac{P_{Al}}{P_{Mg2Si}} = 1.17 \qquad \frac{A_{Al}}{A_{Mg2Si}} = 1.16 \qquad \frac{C_{Al}}{C_{Mg2Si}} = 1.44$$

As the thickness variation is small, the ratio of the plateau values compares well with the theoretical value of 1.18. The ratio of the actual values of the components at 35nm from the interface is lower, at 1.14. This does not give a true indicator of the thickness variation as both the aluminium and magnesium silicide components show an increase in thickness with distance from the interface. As a result, the plateau values for both components will be high, having a cancelling effect when a ratio is taken.

As with the data from the HB5, the ratio of C_i values is high compared with the theoretical value. However, as mentioned previously, the data on the Mg_2Si side of the interface shows slight thickness variation. As the fitting to bulk and interface components is linked, the thickness variations will have an effect on the fitting to both the bulk and the corresponding interface components. The best-fit line to the interface component on the Mg_2Si side is consistently high beyond a distance of 3nm. This indicates that the decay length on the Mg_2Si side is too long *i.e.* C_{Mg2Si} is too small. If the value of C_{Mg2Si} were increased, the ratio would decrease, bringing it closer to the theoretical value. Therefore, if the thickness were constant within the Mg_2Si the resulting C_i ratio would better reflect the theoretical value.

6.2.3 Spectrum Imaging

The problems posed by representing a large quantity of data are more acute for a spectrum image. A spectrum image measures intensity in 3 dimensions, those of distance parallel to the interface (y), distance perpendicular to the interface (x) and energy loss. Fig 6.11 gives a zero loss image of part of the interface examined in figs 6.8, 6.9 and 6.10. The brightness indicates the magnitude of the zero loss peak in the corresponding EELS spectrum.

It was instantly noticeable that the interface did not appear to be straight. Instead, the interface showed a periodic variation. This variation was believed to result from drift within the microscope. In particular, variations in temperature in the microscope room or of the cooling water are known to cause drift and were likely to be the source. However,

this was not especially problematic as lines perpendicular to the interface were taken (section 5.6.2). Each line had its interfacial point determined independently. Therefore, assuming the drift was minimal during the acquisition of a line, the results were likely to be unaffected.

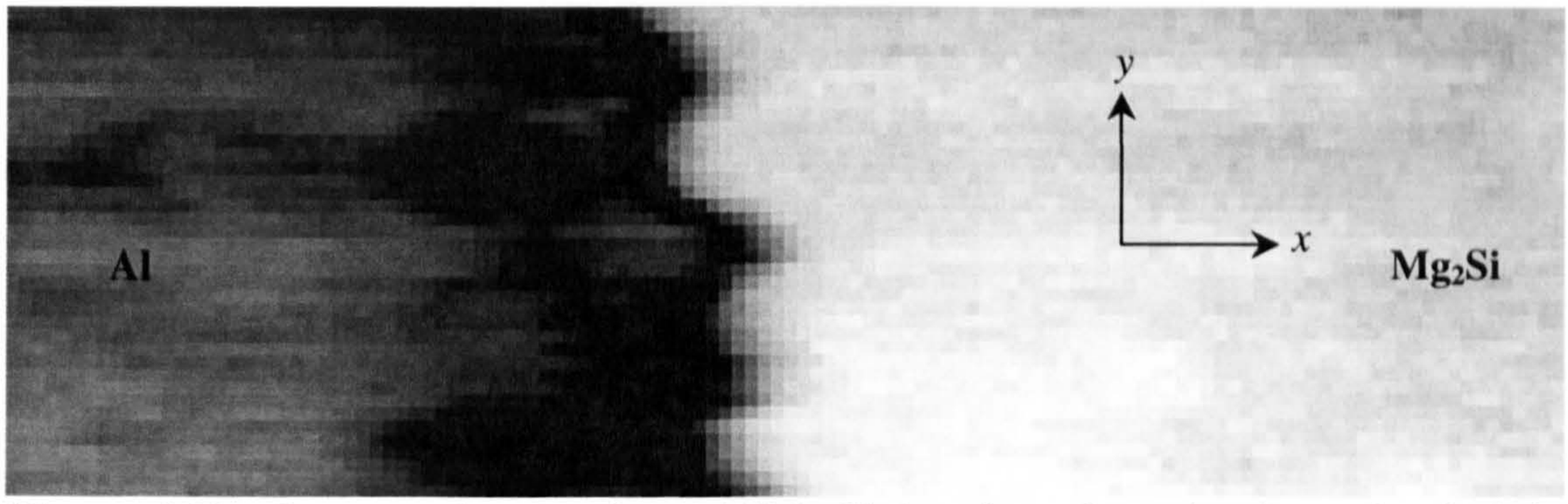

Figure 6.11: Spectrum image of an Al/Mg_2Si interface. Intensity in each pixel is calculated using the number of counts in the corresponding zero loss peak for that pixel. This spectrum image corresponds to an area of dimensions 34nm x 11nm.

Once the spectrum image had been split into components, it was considerably easier to represent. Fig 6.12 gives a 3D surface plot of the effective t/λ of the bulk and interface components vs position. The interface component is presented as a 3D plan view. In each case a darker colour indicates a larger value of t/λ.

Examination of the interface plot indicated that there was not a significant variation in the shape of the interface plasmon decay. Along the length of the interface examined, the decay length appeared to remain largely constant, though the position moved significantly.

In general, the thickness did not vary significantly along the interface length, y, examined. However, the plot indicated that the Mg_2Si was slightly thicker towards the centre of the y range. Similarly, the thickness of the Al was found to be thicker beyond y=10nm. In both cases, the thickness variation is very small and so fairly consistent results would be expected along the length, y, of the interface.

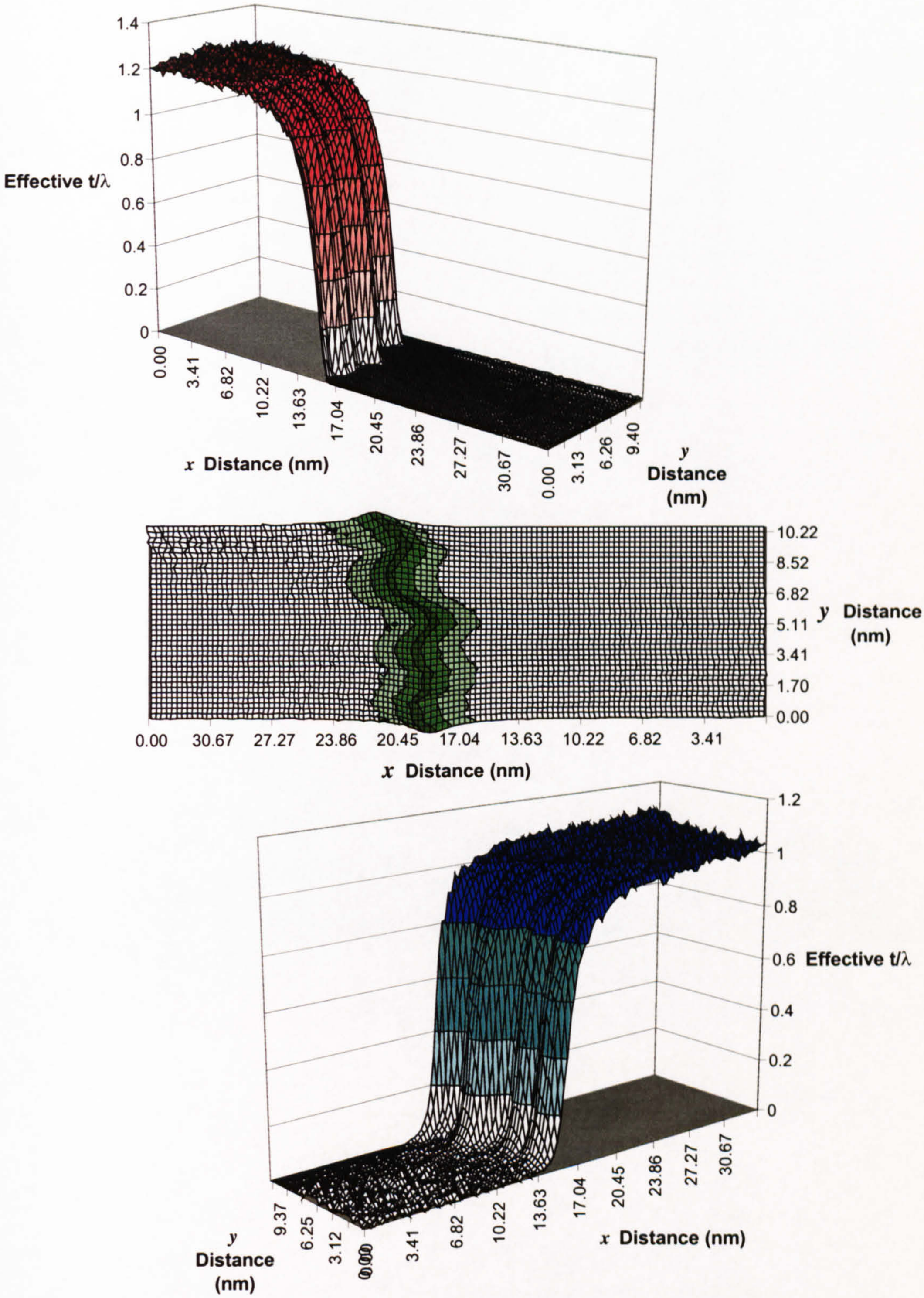

Figure 6.12: 3D surface plots indicating effective t/λ for aluminium (*top*), interface (*centre*) and magnesium silicide (*bottom*) components with respect to distance. Each contour indicates a variation of 0.2 in t/λ.

The 3D data consists of a number of 2D slices (38 in the case of Fig. 6.12) combined. Each 2D slice was a plot of t/λ vs distance from the interface. It was impractical using the techniques available to fit Bessel functions to all the slices. Instead, 9 slices were selected and processed as 2D t/λ plots. One such plot is given in Fig. 6.13.

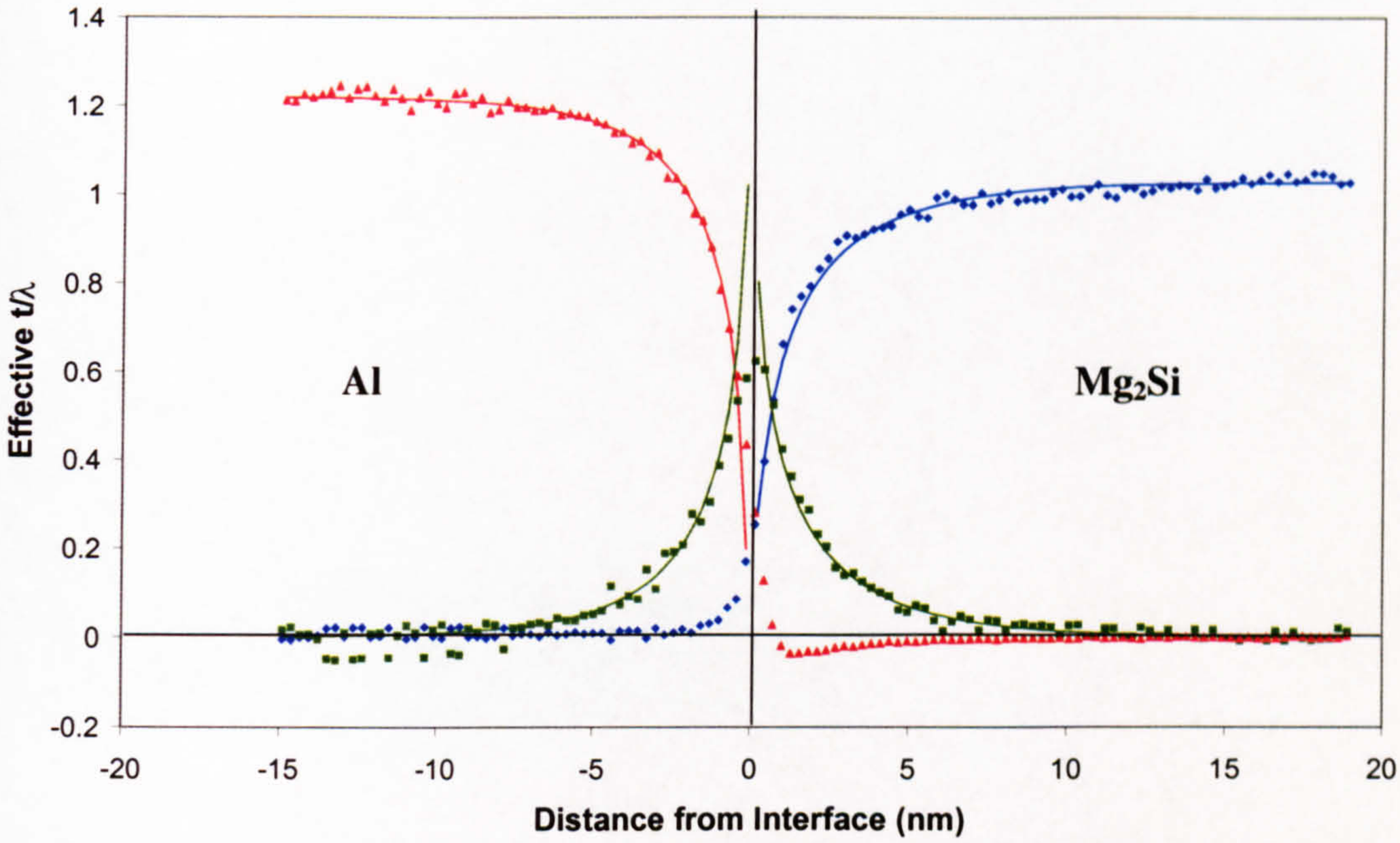

Figure 6.13: Slice of 3D t/λ plot. Proportion of aluminium (*red*), interface (*green*) and magnesium silicide (*blue*) are shown with corresponding best-fit lines. Each point is 0.28nm apart.

The results from this plot are given in table 6.2 along with the other results from this spectrum image. The slice given in Fig. 6.13 was taken from a y distance of 3.55nm.

y Distance (nm)	Al Plateau	Mg_2Si Plateau	P_{Al}/P_{Mg2Si}	A_{Al}/A_{Mg2Si}	C_{Al}/C_{Mg2Si}
0	1.20	1.02	1.18	1.00	1.34
1.18	1.20	1.02	1.18	0.94	1.44
2.37	1.21	1.02	1.19	1.13	1.27
3.55	1.22	1.03	1.19	1.15	1.20
4.74	1.23	1.03	1.20	0.98	1.30
5.92	1.23	1.03	1.20	1.11	1.20
7.10	1.22	1.03	1.19	1.07	1.03
8.29	1.22	1.03	1.18	1.05	0.87
9.47	1.23	1.05	1.17	0.98	0.60
Average	1.22	1.03	1.19	1.05	1.14
Standard Error	0.004	0.003	0.003	0.03	0.09
Theoretical Value			1.18	1.10	1.09
Expected Value			1.01	1.00	1.15

Table 6.2: Table of results for a spectrum image.

As expected, the ratio of P_i values did not vary notably over the area examined and was extremely close to the theoretical value. However, the ratio of A_i values varied by ~15%. This reflected the uncertainty in choosing the interfacial point. Despite this uncertainty, the average value was close to the theoretical value, indicating that the method of selecting the interfacial point is effective.

The ratio of C_i values were not consistent over the range of y distance. Even though the A_i and P_i ratios remained largely the same, the C_i ratios showed a considerably spread. However, comparison of the data and the t/λ plots suggests a cause for this spread. The most significant variation in values is noted for y distances of 7.10, 8.29 and 9.47 nanometres. These correspond to the interface component plateauing at an increasingly positive value on the aluminium side and an increasingly negative value on the magnesium silicide side. This is believed to result from problems with the least-squares fitting of the best-fit lines for the Tecnai data. This is discussed more fully in section 7.4.2. Fig 6.14 shows the data from a y distance of 9.47nm, indicating the problems with the interfacial component.

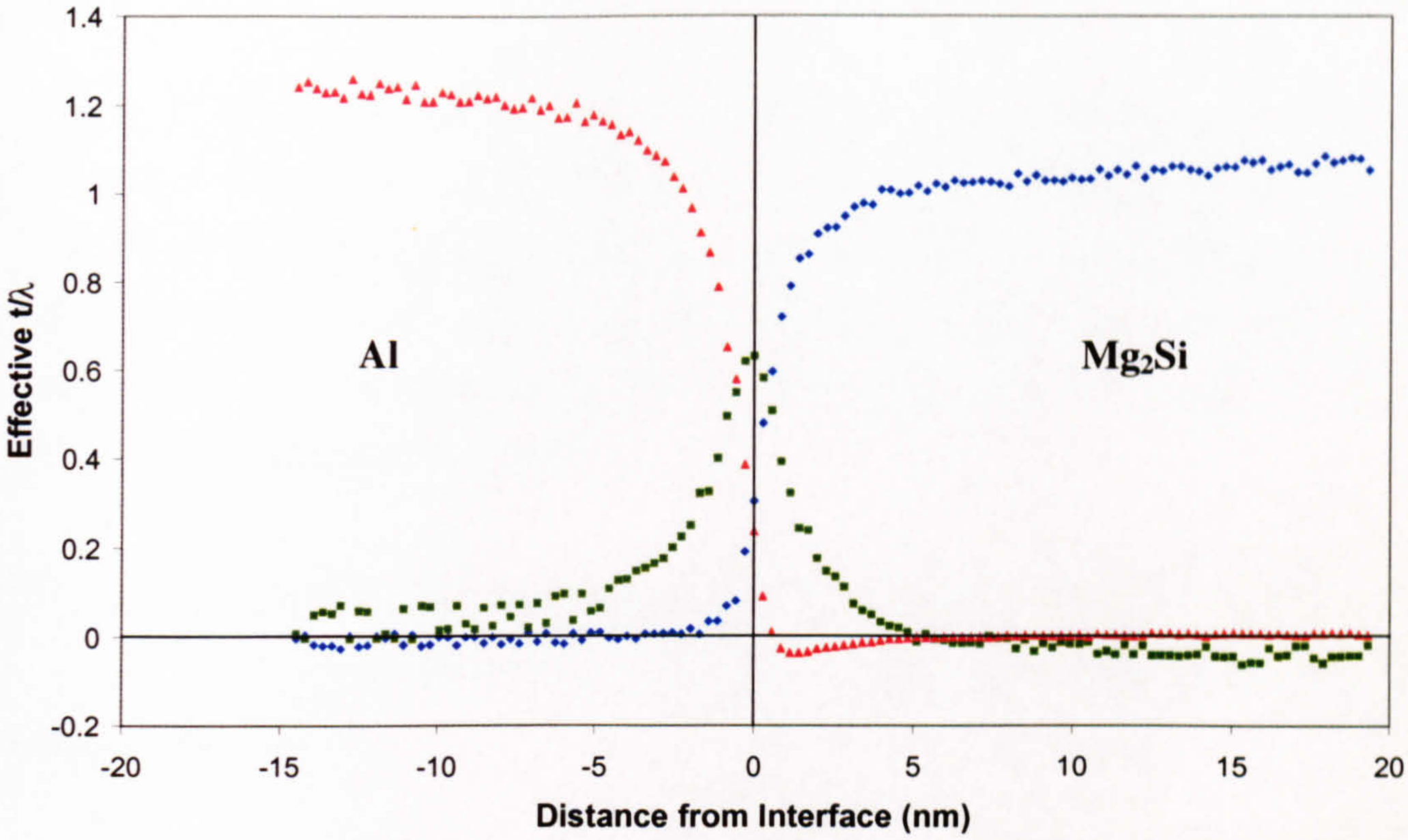

Figure 6.14: Plot of t/λ vs distance from the interface. Interfacial component (*green*) does not fall to zero on Al side and has a negative plateau value on the Mg_2Si side. Also shown are the Al (*red*) and Mg_2Si (*blue*) components.

As the problems have a notable effect on the results from these distances, the data is unrepresentative for the system. If these results are then omitted, the average and the spread of values is significantly different. The average of the C_i ratios becomes 1.29 with a standard error of 0.04 over the six values. This is further away from the theoretical value than before, but is believed to be more representative of this interface. The result is high compared with the theoretical value for this system. However, this result is close to the overall result from the HB5 for this system. This indicates that there is consistency between data from the HB5 and the Tecnai. In addition, there is some correlation between the results for the line spectrum image and the spectrum image from the Tecnai. It is not clear why the C_i ratio is consistently high. Some possible reasons have been given in section 6.1.6 to explain sources of error. However, it is possible that these results are accurate for the interfaces examined and that the deviation results from the interface itself. As discussed previously, the theoretical model deals with atomically sharp interfaces. The high-resolution micrograph showed that the interface examined was not perfect. Though the exact nature of the problem at the interface could not be determined, it is likely that it will have an effect on the EELS spectrum.

6.2 Summary

In this chapter, the results obtained from the Al/Mg_2Si system were presented. Once the experimental technique had been refined, the experimental results were found to be consistent, even between different microscopes. However, the results for the decay of the interface plasmon, as measured by the C_i ratio, were found to be high compared with the theoretical value. Some reasons to explain this discrepancy have been proposed, though this will be discussed further in Chapter 8.

A further comparison of experimental results with the theoretical equations is given in the next chapter. There, the results from the Al/Si system with be presented with conclusions pertaining to that data.

CHAPTER 7

RESULTS: AL/SI SYSTEM

The results from the Al/Si system will be presented in this chapter. The chapter will take a similar form to the latter part of chapter 6. Initially, the results from a single HB5 experiment will be compared with expected values. Following this, a theoretical fit will be discussed, before the overall results from the HB5 are given and conclusions drawn. Data acquired on the Tecnai microscope will then be presented together with relevant conclusions. Finally, all the experimental results for the system will be compared and comparisons made with the expected and theoretical values.

7.1 Results from a Single Dataset

In this section, the results from a single dataset acquired from an Al/Si interface is presented. This data will be related to the overall results for the entire system in section 7.3. All experimental data presented was acquired using the techniques outlined in chapter 5.

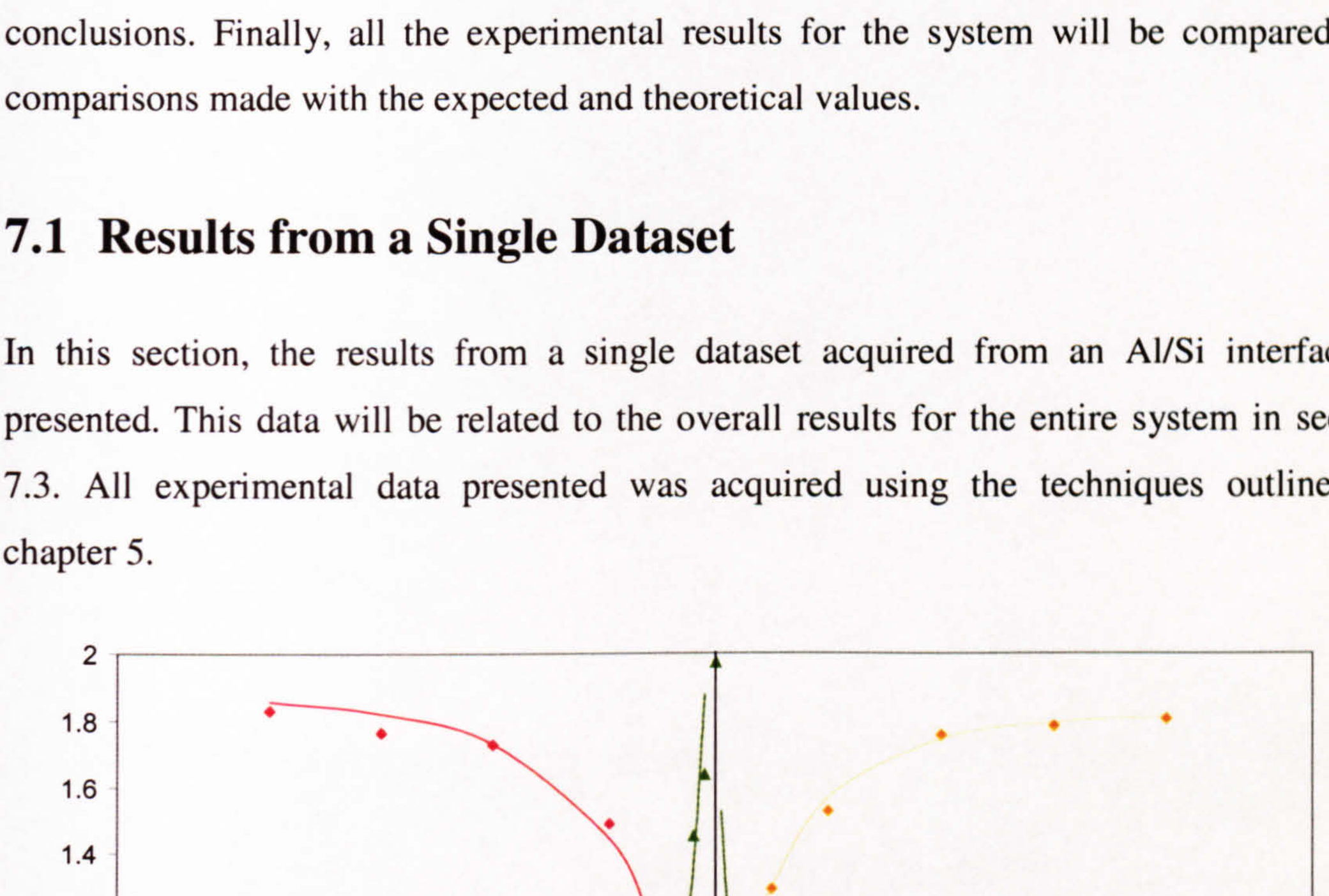

Figure 7.1: Plot of t/λ vs distance for and Al/Si interface. The graph indicates the relative proportions of aluminium (*red*), silicon (*orange*) and interface (green) components with distance from the interface. Also shown is the best-fit Bessel function to each component.

Fig 7.1 gives the t/λ vs distance plot for data taken from an Al/Si interface. Using the same approximations given in section 5.4 to aid analysis, it was expected that the interface plasmon would decay more quickly on the silicon side than on the aluminium side. This results from the silicon having a higher plasmon energy than aluminium. This expected result was observed within the data.

As with the Al/Mg_2Si system, Bessel functions were fitted to the bulk and interface components. Best-fit lines using eqns 5.1a and 5.1b were fitted to the data. The scaling value, A_i, and the decay constants B_i and C_i were varied as before. For the Al/Si system, the expected values for the ratios of the interface plasmon decay, C_i, and the bulk plateau values, P_i, are given below (section 5.4 and eqn 2.11).

$$\frac{C_{Al}}{C_{Si}} = \frac{E_p(Al)}{E_p(Si)} = \frac{15}{16.7} = 0.90$$

$$\frac{P_{Al}}{P_{Si}} = \frac{t/\lambda(Al)}{t/\lambda(Si)} = \frac{\lambda(Si)}{\lambda(Al)} = \frac{85.48}{87.31} = 0.98$$

The results determined from the data given in Fig. 7.1 were as follows.

$$\frac{P_{Al}}{P_{Si}} = 1.02 \qquad \frac{A_{Al}}{A_{Si}} = 1.03 \qquad \frac{C_{Al}}{C_{Si}} = 0.67$$

The fit was observed to be very good with an excellent result for the ratio of the A_i values compared with the expected value of 1. This indicated that the interface position had been well chosen. The ratio of the plateaus was also found to be close to the expected value. However, the data on the aluminium side of the interface did not appear to have reached a plateau, indicating that there may be a variation in thickness in the sample. Thickness effects could account for the slightly low value of P_{Al}/P_{Si}. For this dataset, the ratio of C_i values was observed to be very low. It was not clear why this was the case, particularly as the other ratios were close to the expected values. However, this result was indicative of experimental results for the system as a whole (section 7.3).

Unusually for experimental data, the amount of interface plasmon component peaked sharply at the interface. Associated with this, the tailing of each of the bulk plasmons did not extend noticeably into the opposite side of the interface. This dataset appeared to have exceptional spatial resolution, which was better than any other dataset. However, as the

probe size was not altered between datasets, the spatial resolution was unlikely to have changed. If this interface had been more accurately aligned to the electron beam or was free from defects and hence sharper than the other interfaces, better data would result. However, it would still be expected that the size of the probe would cause a contribution from the bulk plasmons on either side of the interface. The reason for the absence of these contributions is unclear.

An analysis was performed on a theoretical system to determine alternative reference values for the ratios of interest. This is presented in the next section.

7.2 Fitting to Theoretical Data

The procedure followed was identical to that given in section 6.1.4. In summary, theoretical spectra were generated for points at different distances from the interface. These spectra were generated using eqn 2.33 with dielectric functions calculated using experimental data from the bulk materials. These spectra were then processed as experimental spectra to create a plot of effective proportion vs distance from the interface. This plot is given in figure 7.2.

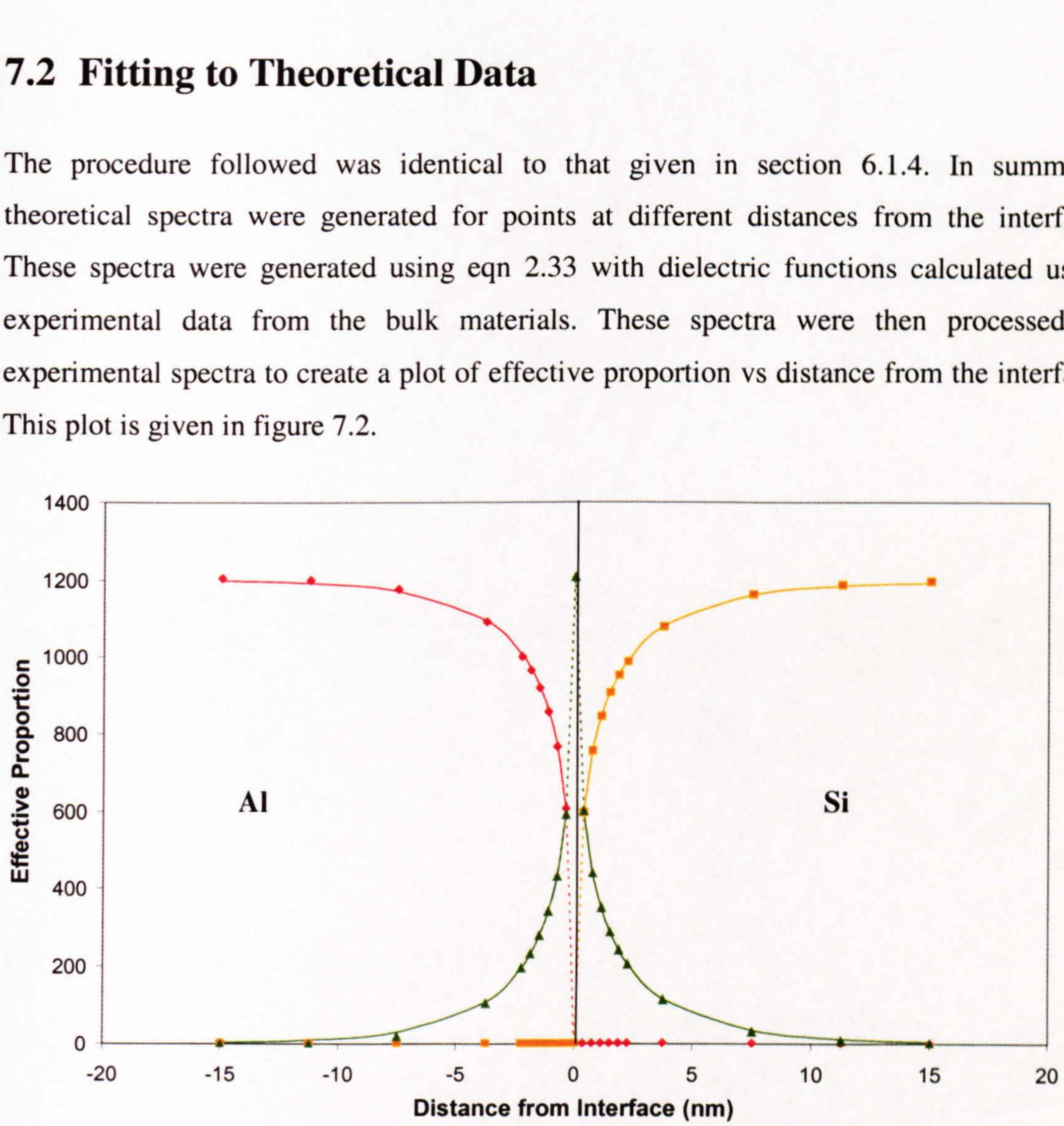

Figure 7.2: Theoretical plot of proportion of each component with distance from the interface. Plot shows Al (*red*), Si (*orange*) and interface (*green*) components with their respective fits (*solid lines*). In addition, fits are extrapolated to the data point at 0nm (*broken lines*).

As for the Al/Mg_2Si system, the Bessel function provided an excellent fit to the theoretical data. However, several unexpected results were noted. Firstly, the plateau values of the two bulk materials appeared to be almost identical. Whilst the difference between the mean free paths for Al and Si is smaller than that for Al and Mg_2Si it is still about 10%, considerably greater than that displayed in Fig. 7.2. Secondly, the decay of the interface plasmon on each side of the interface also appeared to be very similar. Further examination suggested that the theoretical data displayed a more rapid decay with distance on the aluminium side than on the Si side, opposite to that predicted by the expected values.

The ratios for this theoretical system were calculated and are given below.

$$\frac{P_{Al}}{P_{Si}} = 1.01 \qquad \frac{A_{Al}}{A_{Si}} = 1.02 \qquad \frac{C_{Al}}{C_{Si}} = 1.07$$

These results confirmed the observations given above. The plateau values were effectively equal and the C_i decay values were similar. The asymmetry in decay lengths was opposite to that expected for the system. Compared with the Al/Mg_2Si system the deviation between the expected value for the C_i ratio of 0.90 and theoretical result was quite large for this system. Whereas the difference between expected and theoretical values was less than 6% in Al/Mg_2Si, for Al/Si this increased to 15%. This may be a result of the different peak widths. Mg_2Si has a FWHM of 3eV compared with 4.4eV for Si. Therefore, selecting a single energy to define the plasmon peak was a worse approximation for Si than for Mg_2Si. As this approximation was used in the calculation of the expected C_i ratios, it was probable that the expected value was also less accurate for the Al/Si system. This is discussed in more detail in section 8.2. As the expected values use a number of approximations, the theoretical values are a more accurate indicator of the behaviour of the non-relativistic eqaution.

7.3 Overall Results for the System

Table 7.1 gives the ratios of interest for six representative datasets from the Al/Si system. The plateau value for the aluminium is also included as an indicator of sample thickness. All the datasets were acquired from different interfaces.

Dataset	Al Plateau	P_{Al}/P_{Si}	A_{Al}/A_{Si}	C_{Al}/C_{Si}
Set 1	0.44	0.97	0.92	0.61
Set 2	0.52	0.87	0.81	0.51
Set 3	1.85	1.02	1.03	0.67
Set 4	0.90	1.04	1.00	0.58
Set 5	0.47	0.81	0.99	1.06
Set 6	0.63	1.08	0.94	0.66
Average		0.97	0.95	0.68
Standard Error		0.04	0.03	0.08
Theoretical Value		1.01	1.02	1.07
Expected Value		0.98	1.00	0.90

Table 7.1: Table of results for Al/Si system

The experimental data from the Al/Si system showed good agreement with both the theoretical and the expected values for the ratio of the plateau values. As with the Mg_2Si, the optimum position for the interface has been selected for all the datasets examined. However, as was observed in the Mg_2Si system, the ratio of experimental C_i values was noticeably different from both the theoretical and the expected values. In the Al/Mg_2Si system the C_i ratio was high compared with theory; for this system the experimental values were consistently low, with the exception of set 5. It is not clear why the ratio for this set is so different. There was nothing apparent within the data to suggest a reason.

Variations in thickness appeared to be more prevalent in this system. A number of datasets exhibited obvious signs of thickness variation. One such set, showing clear evidence of increasing thickness on both sides of the interface, is shown in Fig. 7.3 (see also section 7.4). This figure corresponds to the data from set 2 in table 7.1. It would be expected that such thickness variations would have a notable effect not only on the plateau values but also on the ratio of C_i. As a result, this was likely to be the major source of error for this system.

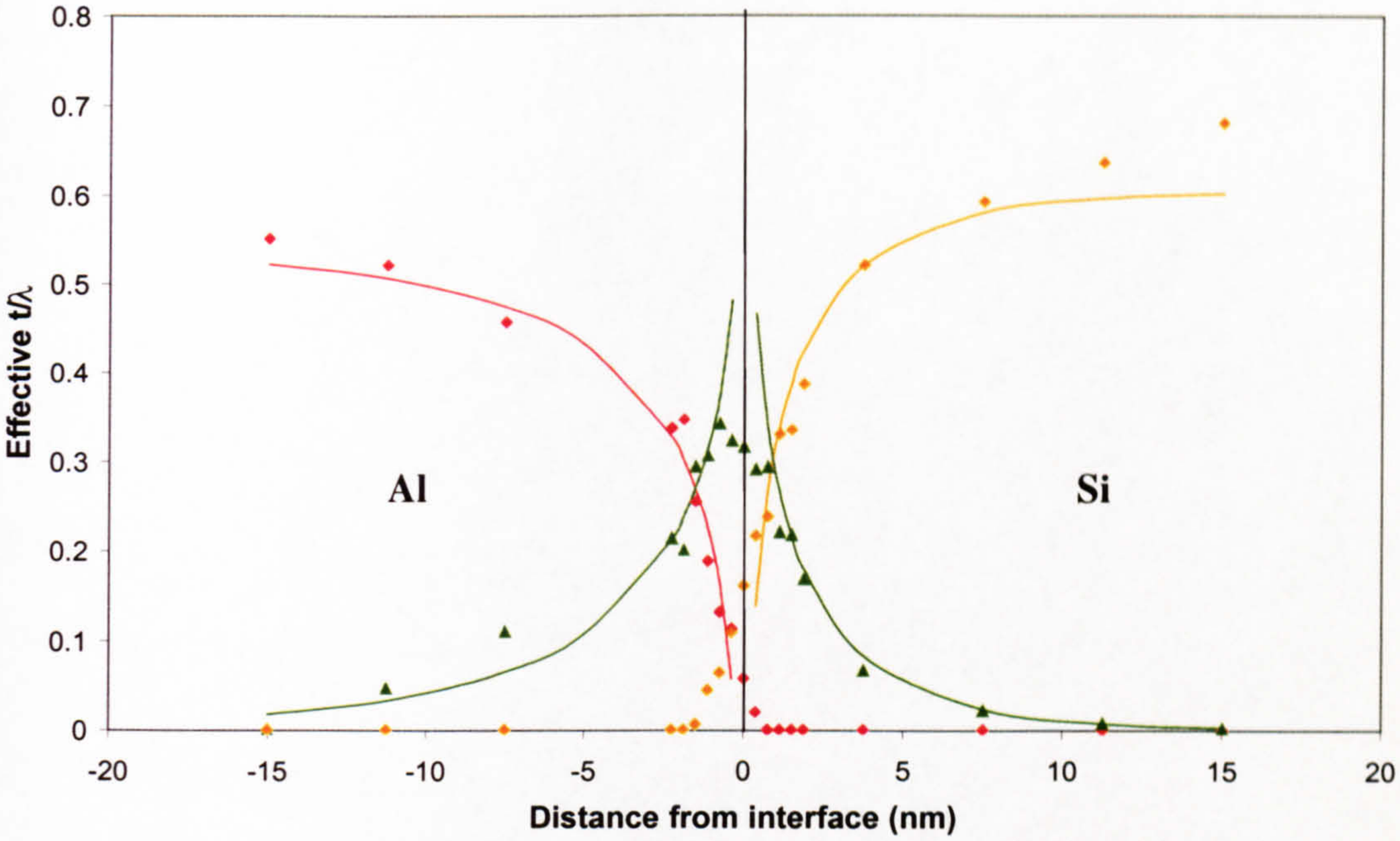

Figure 7.3: Plot indicating thickness variations in the bulk. Relative proportions of aluminium (*red*), silicon (*orange*) and interface (*green*) components are shown.

7.4 Tecnai Results

The FEI Tecnai microscope was used to supplement the data obtained from the HB5. As with the Al/Mg_2Si system, high-resolution images were taken of prospective interfaces. Interfaces which appeared suitable were used for the acquisition of line spectrum images and spectrum images.

7.4.1 High-Resolution Imaging

High-resolution imaging was used to determine the quality of interfaces. Many possible problems with the interface such as tilting of the interface, dislocations or steps will be evident using high-resolution electron microscopy. Fig 7.4 shows an image obtained from the Tecnai, with the aluminium tilted to a [110] pole.

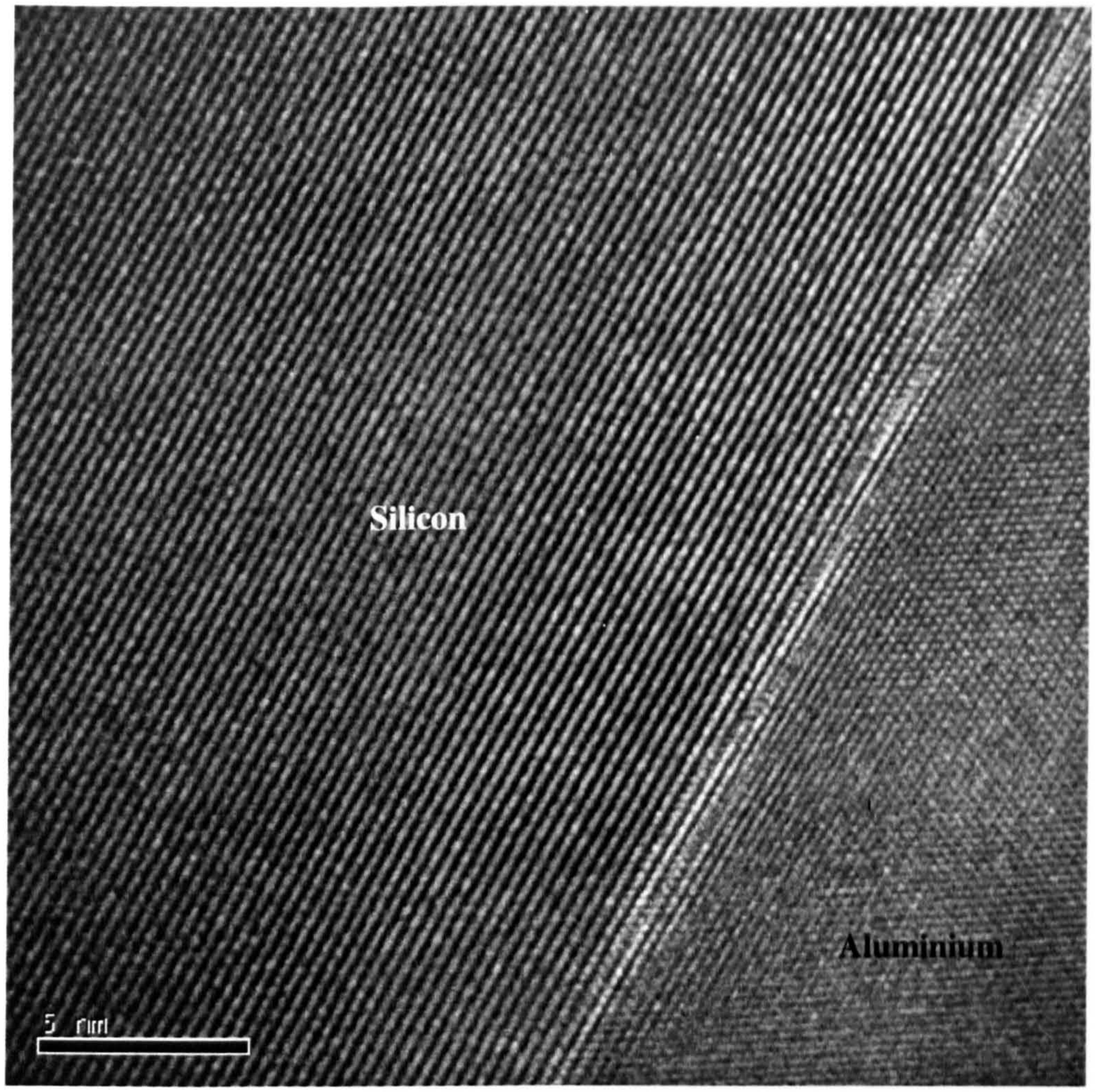

Figure 7.4: High-resolution image of an aluminium/silicon interface. Aluminium was aligned to a [110] pole.

This image demonstrated that the Al/Si interfaces were sharp. However, steps were apparent along the interface. The lattice planes of the aluminium and the silicon within this image are not parallel to each other. In addition, neither of the sets of lattice planes are parallel to the interface. As a result of this, steps are necessary to accommodate the mismatch between the lattice planes of the two materials. It was not clear what effect, if any, the steps along the interface would have on the data.

If the lattice mismatch requires the formation of steps along the interface in one plane, then they may be present along the interface in the perpendicular plane. It is expected that steps in the direction of the electron beam will have a greater effect than those perpendicular to it. However, there appears to be no discussion in the literature of the effect of steps on EELS of an interface. A simplistic analysis is given in section 8.3 of the possible results from a stepped interface. As an approximation, EELS from a stepped interface is thought

to be similar to EELS from a tilted interface. The sample was aligned to the [110] direction of the aluminium. If the interface were not parallel to this crystallographic direction, as would be the case if steps were present, then the interface would be tilted with respect to the electron beam.

7.4.2 Line Spectrum Imaging

The Tecnai was used to acquire line spectrum images from an Al/Si interface. Chronologically, this work was done prior to the acquisition of the Tecnai data from the Al/Mg_2Si interface. As the EELS set-up was optimised after the Al/Si data was acquired, the acquisition times and number of acquisitions are very different for the two systems. Despite this, the basic procedure for obtaining the data remained the same.

Data were acquired from a single interface using an acquisition time of 5ms per acquisition. The number of acquisitions per point was varied between 30 and 120. In addition, spectrum images were taken with 0.2, 0.3 and 0.4nm between points. The data were processed and analysed using the techniques outlined in section 5.6.

Fig 7.5 gives a plot showing processed energy loss spectra at different distances across an interface. The *y* dimension corresponds to the distance across the interface and the *x* dimension represents the energy loss in eV. The magnitude of the intensity is represented by the brightness of the point. The horizontal black lines represent missing spectra caused by problems in the deconvolution routine.

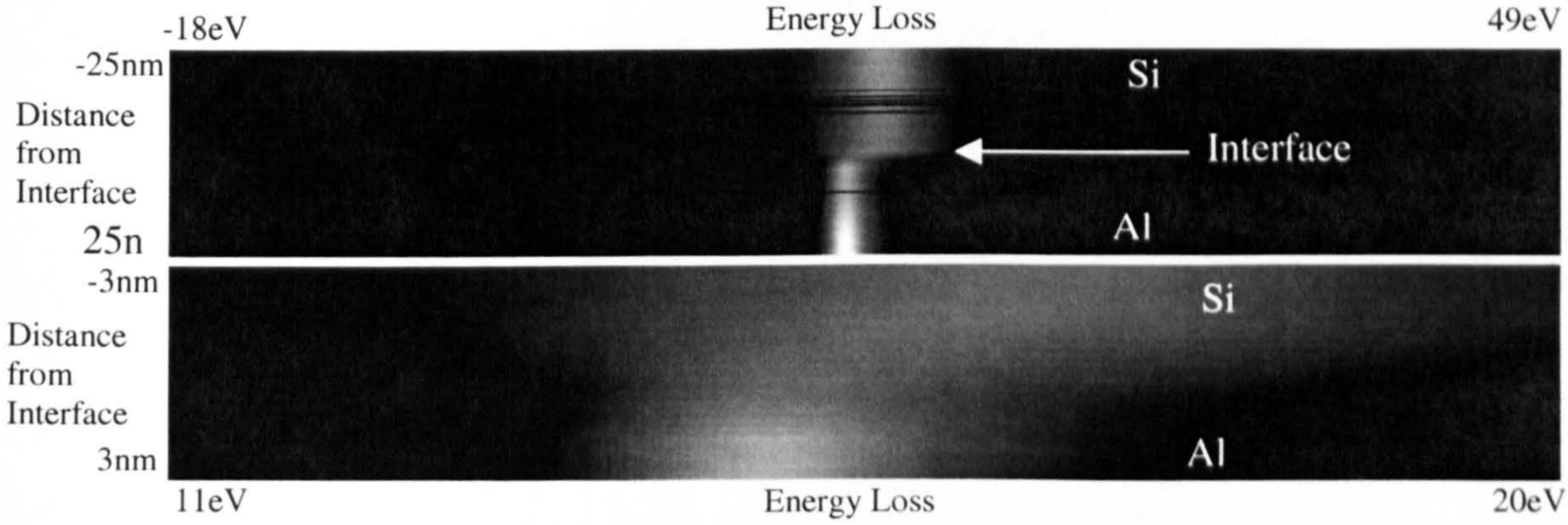

Figure 7.5: Line spectrum image with horizontal dimension corresponding to energy and the vertical dimension corresponding to distance across the interface. The intensity of each pixel indicates the intensity of that channel in the EELS spectrum. *Bottom* shows magnified region of *top* image.

The transition from Al to Si is difficult to see in this figure, even in the magnified section (Fig. 7.5 *bottom*). The silicon plasmon is very broad and so the interface plasmon is difficult to resolve. As with the Al/Mg_2Si interface, the transition between plasmons occurs over a very short distance.

All fitting performed on data from the HB5 had the constraint that none of the components could have a negative contribution. It was not possible to apply this constraint to the fitting procedure for data from the Tecnai. This introduced some serious problems. It was often the case that a better fit would be achieved by having a negative amount of one of the components. Clearly, this is not physical. In addition, as the amount of each component in a fit was related, the subtraction of one component was compensated with an excess of another to maintain a good fit. Fig 7.6 shows a t/λ vs distance plot for a dataset indicating the problems associated with allowing negative components.

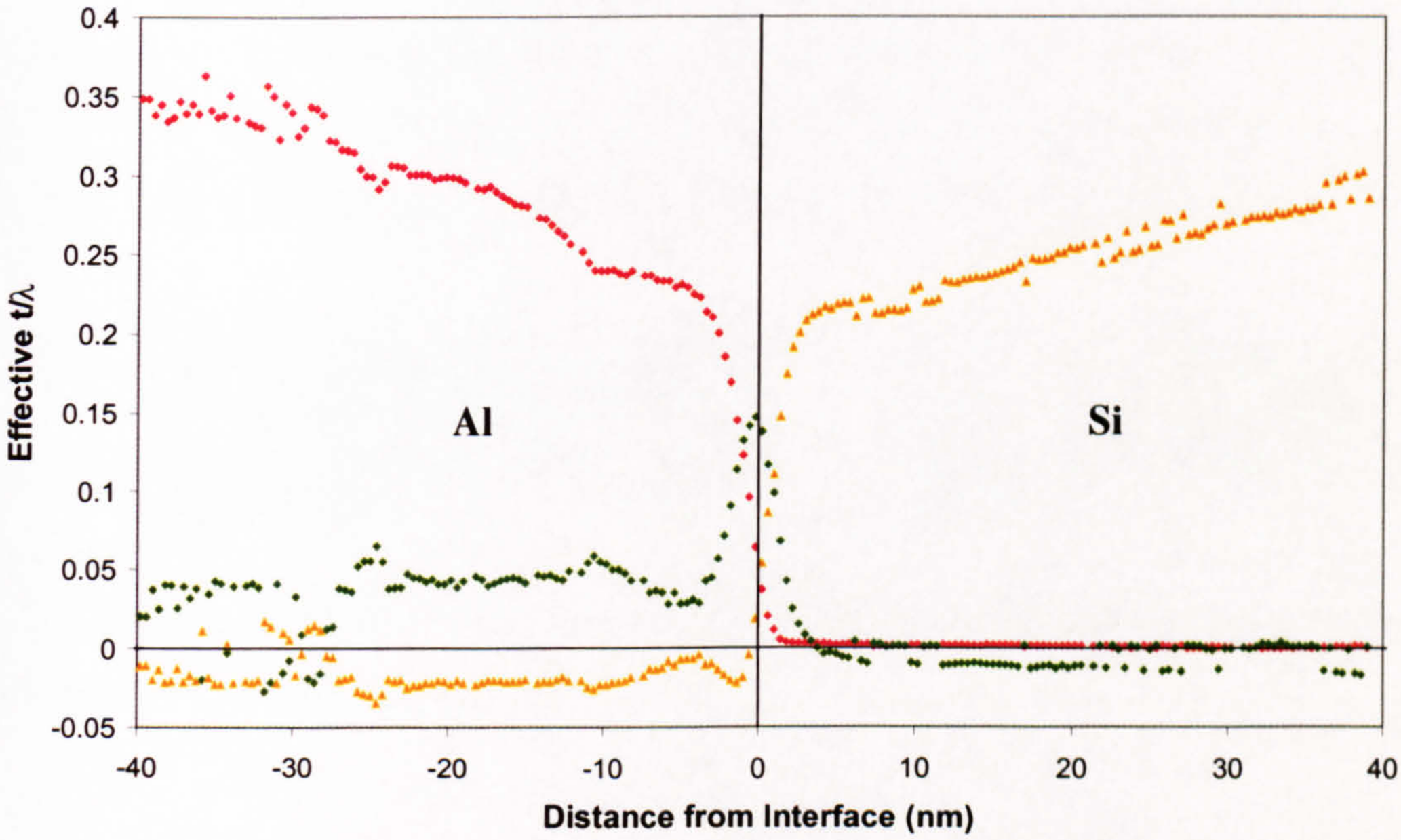

Figure 7.6: Plot of Effective t/λ vs distance for data acquired using FEI Tecnai. Plot indicates problems caused by allowing negative components (see text). Aluminium (*red*), interface (*green*) and silicon (*orange*) components are shown

On the aluminium side of the interface, the interface component did not decay to zero. This was directly related to the negative amount of silicon component in the fit. Peaks and troughs in the silicon component were echoed in the interface component. For example, the

peak in the silicon component at –28nm corresponded exactly to a trough in the interface component. Further to this, a peak was also observed in the aluminium component at the same distance, though of a lesser magnitude. It was notable also, that when the silicon component increased to become zero, the interface component also became zero. This indicated that if the silicon component were prevented from becoming negative, that the interface component would fall to zero as expected. The combination of the interface component and the negative silicon component results in a slight increase in counts on the higher energy side of the aluminium peak. This could have, for example, been to compensate for a small amount of carbon contamination. However, the correction is so small that its effect is negligible.

A secondary problem, related to the first, is apparent on the silicon side of the interface. Slight variations in the spectra from point to point, possibly arising from noise in the spectra, resulted in the fitting of a negative component to some spectra but not others. This caused the bulk and interface components to split. This is seen most clearly in the Si component on the right of Fig. 7.6. At distances greater than 5nm, the trend of the silicon t/λ appeared to have split into two parallel lines. This was nonsensical in terms of a physical system and was purely an artefact resulting from the fitting procedure.

These problems made it difficult to obtain meaningful fits to the data. However, the artefacts only became predominant at >3nm from the interface. It was therefore possible to fit over a range that excluded the region that contained spurious results. Fig 7.7 gives a t/λ vs distance plot for the same interface as figs 7.5 and 7.6. In the acquisition of this spectrum image, the spatial range observed in Fig. 7.5 was sacrificed in favour of a smaller distance between the points (0.2nm).

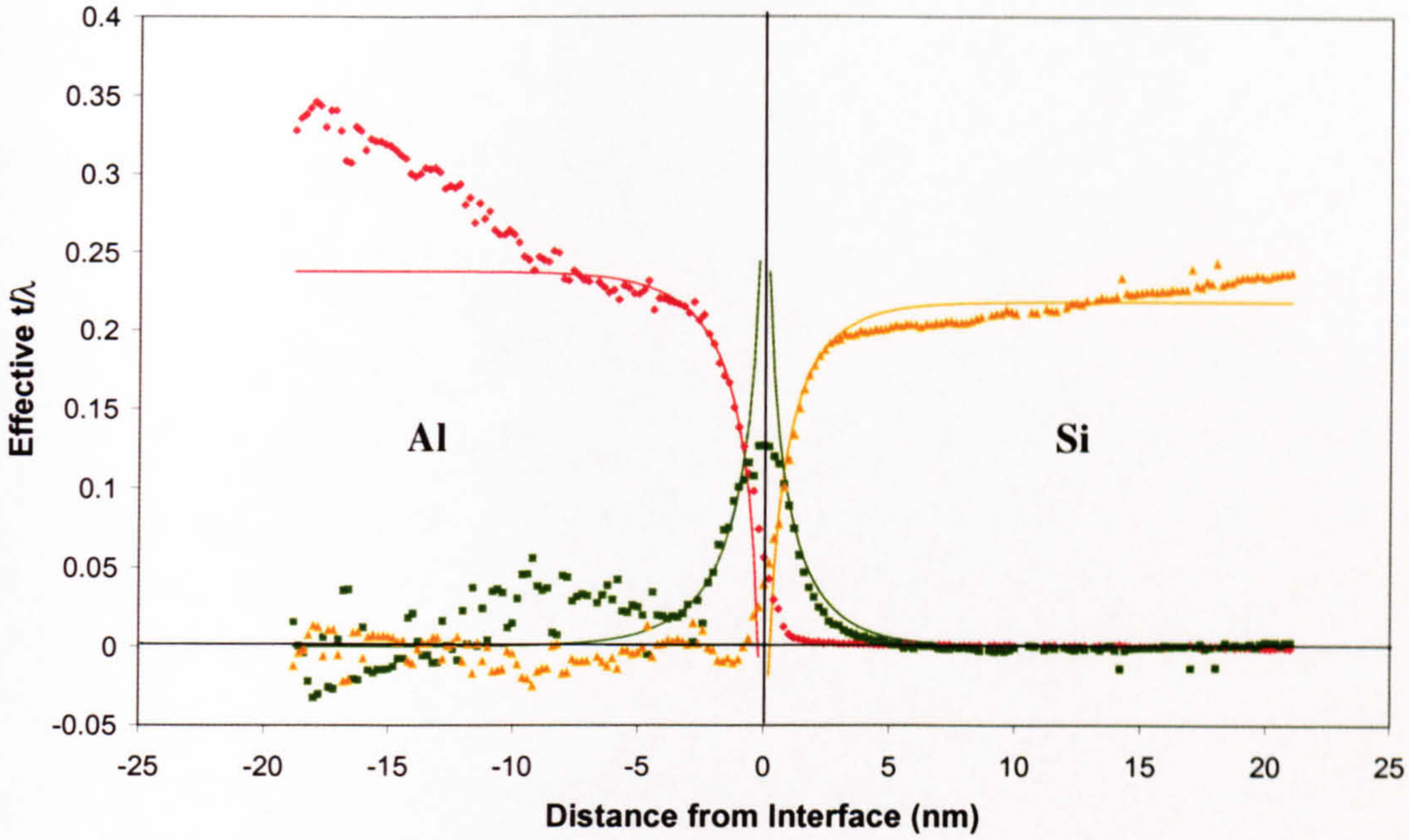

Figure 7.7: t/λ vs distance plot calculated from a line spectrum image. Plot shows aluminium (*red*), silicon (*orange*) and interface (*green*) components. Also shown are the fits to the data (*solid lines*).

This data had significant variation in the effective t/λ from point to point in the interfacial component beyond 3nm. This problem was believed to result from the least-squares fitting procedure to the data. As the large variation in results would significantly effect the fitting of the Bessel function, the fit on the aluminium side was restricted. Fits using eqn 5.1a and 5.1b were performed over the range 0.8 → 21nm on the silicon side of the interface and 0.8 → 2.6nm on the aluminium side of the interface. It was not believed to be necessary to restrict the fit on the silicon side, other than close to the interface (section 5.33).

It was observed that a good fit was achieved on both sides of the interface up to about 5nm. Despite the restricted fit range and the accompanying limited number of points, the fit on the aluminium side was extremely good. The fit continued to reflect the data at distances of up to 2nm outside the fit range. This data proved that there was a notable change in thickness with distance from the interface in both bulk components, though particularly on the aluminium side. However, the aluminium fit range was restricted and so the thickness variation may not have had a significant effect on the fit for this side of the interface. As the silicon fit-range continued to large distance, the silicon fit was affected by the thickness

variation. This was indicated by the angle between the trend of the bulk silicon data and the best-fit line.

The results corresponding to this fit are given below.

$$\frac{P_{Al}}{P_{Si}} = 1.09 \qquad \frac{A_{Al}}{A_{Si}} = 0.98 \qquad \frac{C_{Al}}{C_{Si}} = 0.89$$

It would be expected that the data from the Tecnai system would be a more accurate representation of the experimental system. Not only did the Tecnai offer a considerably larger data set, resulting in a more representative fit, but also the distances were more accurately determined and drift was reduced. From this point of view it was unsurprising that the results for this system were extremely good and consistent with both expected and theoretical values. The problem with a very low C_i ratio, noted in section 7.3, was not apparent in this dataset, though the result was still slightly low in comparison with the theoretical value. In practice, the thickness variations were so significant that the correlation between experimental and theoretical results was unexpected. However, a thickness increase on both sides of the interface will have a cancelling effect (section 8.1). In addition, the problems resulting from allowing negative components are apparent even within the restricted fit-range on the aluminium side. This would certainly have had an effect on the results.

7.4.3 Spectrum Imaging

The Al/Si system was further investigated using spectrum imaging. In this way the variation of results along the interface was examined. Fig 7.8 gives a zero loss image of the interface examined in figs 7.7 and 7.5. The brightness indicates the magnitude of the zero loss peak in the corresponding EELS spectrum.

The drift observed with the Al/Mg_2Si system (section 6.2.3) was also observed here. The spatial extent of the drift was not as significant as the total acquisition time was shorter. The method of analysis (section 5.6.2) is believed to eliminate the effect of drift for this data.

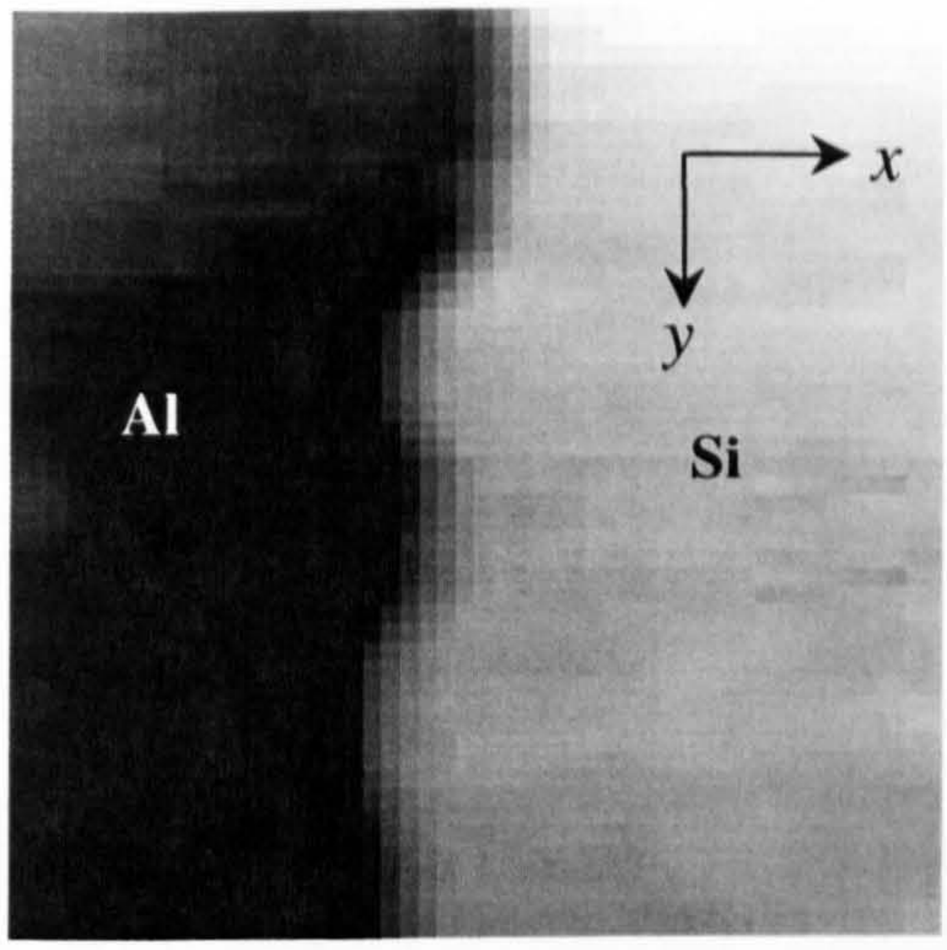

Figure 7.8: 0eV slice of a spectrum image from an Al/Si interface. Intensity in each pixel is calculated using the number of counts in the corresponding zero loss peak for that pixel. This spectrum image covers an area of dimensions 15nm x 15nm

Fig 7.9 gives a 3D surface plot of the effective t/λ of the bulk and interface components vs position for this interface. The interface component is presented as a 3D plan view. In each case, a darker colour indicates a larger value of t/λ. As with the Al/Mg_2Si data, there was not a significant variation in the shape of the interface plasmon decay. However, there was a notable variation in thickness within the area analysed. This data covered a total x distance of 15nm, half that examined in the HB5 datasets. However, it has been observed in earlier data (see Fig. 7.7) that both Al and Si reaches a plateau well within this range. Thickness variations were observed in the plateau both perpendicular (x direction) and parallel (y direction) to the interface. The silicon plot within Fig. 7.9 shows a t/λ variation of about 0.05 over a y distance of 15nm. A similar variation was observed within the aluminium. It was expected that the thickness changes parallel to the interface would affect the consistency of the results from this interface.

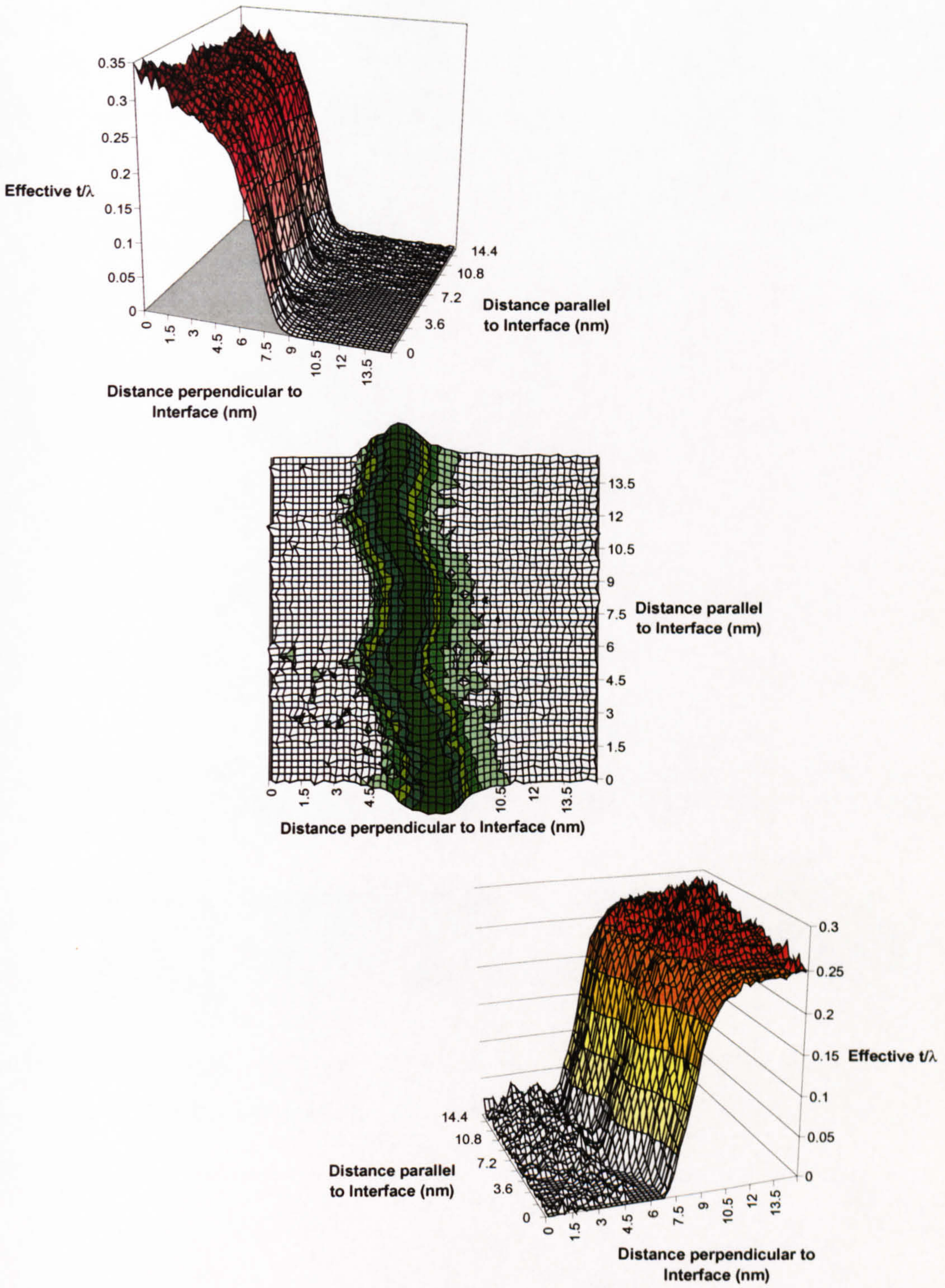

Figure 7.9: 3D surface plots indicating effective t/λ for aluminium (*top*), interface (*centre*) and silicon (*bottom*) components with respect to distance parallel and perpendicular to the interface. Each contour indicates a variation of 0.05 in t/λ.

The 3D data consisted of a number of 2D lines (50 in the case of Fig. 7.9) combined. Each line was a plot of t/λ vs distance from the interface. It was impractical using the techniques available to fit Bessel functions to all of the slices. Instead, 12 slices were selected to give roughly equally spaced sets and processed as t/λ plots. One such plot is given in Fig. 7.10

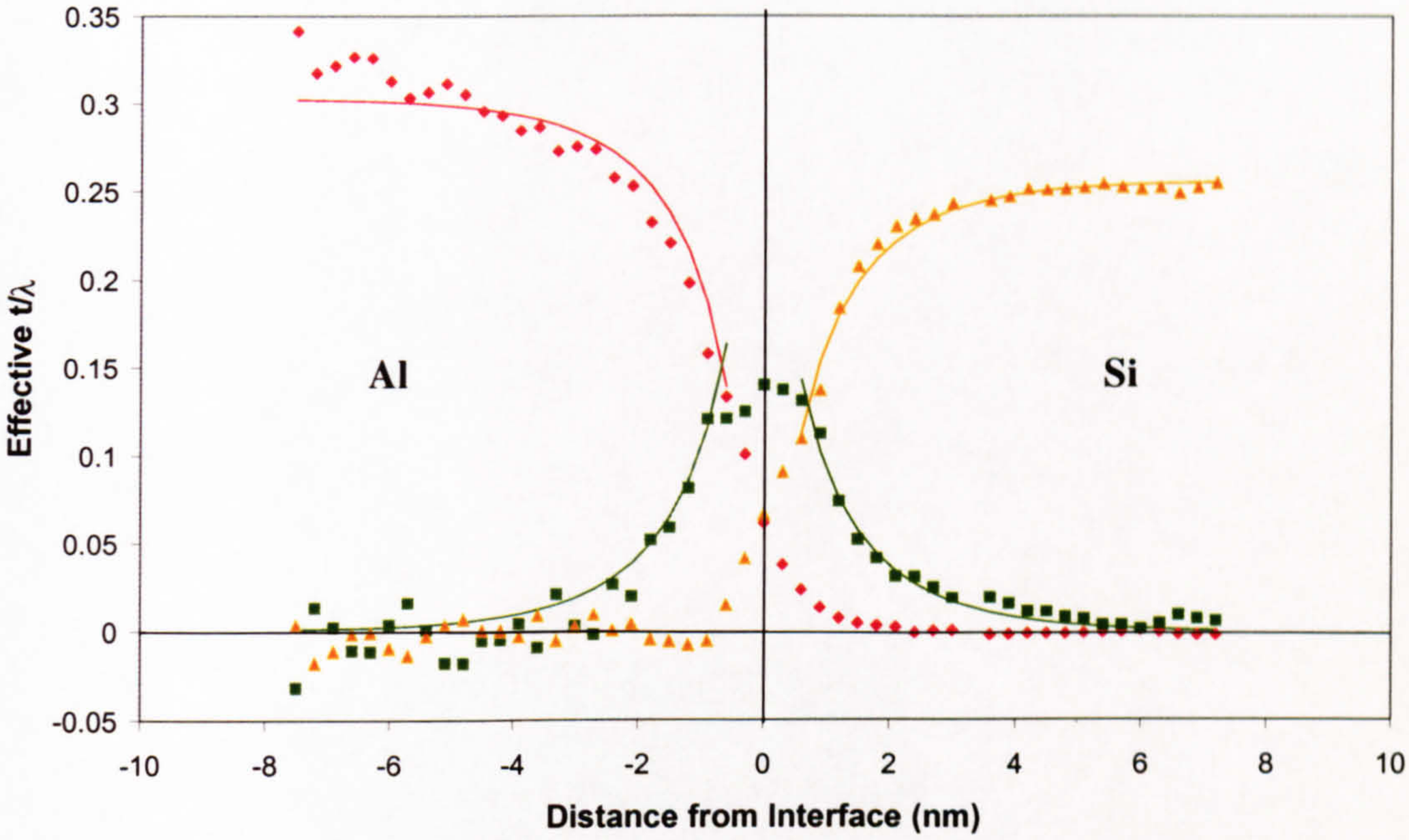

Figure 7.10: Slice of 3D t/λ plot. Proportion of aluminium (*red*), interface (*green*) and silicon (*orange*) components are shown with best-fit lines calculated using eqns 5.1a and 5.1b. Each point is 0.3nm apart.

The results from this plot are given in table 7.2 along with the other results from this interface. The data given in Fig. 7.10 was taken from a *y* distance of 1.8nm. The problems caused by negative component amounts, discussed in the previous section, were not as significant for this data, largely due to the smaller spatial range. As a result, the Bessel function fit was performed over the full range, starting at a distance of 0.6nm from the interface.

y Distance (nm)	Al Plateau	Si Plateau	P_{Al}/P_{Si}	A_{Al}/A_{Si}	C_{Al}/C_{Si}
0	0.31	0.25	1.24	1.26	1.04
0.9	0.30	0.25	1.20	1.16	0.98
1.8	0.30	0.25	1.20	1.15	1.02
3.0	0.30	0.26	1.15	1.11	1.02
4.5	0.29	0.26	1.13	1.34	1.07
6	0.29	0.27	1.06	1.10	1.43
7.5	0.30	0.27	1.09	1.37	1.18
9	0.30	0.27	1.09	1.07	1.41
10.5	0.29	0.27	1.07	1.33	1.24
12	0.29	0.28	1.05	1.20	1.30
13.5	0.29	0.28	1.04	1.28	1.20
14.7	0.30	0.28	1.07	1.06	1.85
Average			1.12	1.20	1.22
Standard Error			0.02	0.03	0.07
Theoretical value			1.01	1.02	1.07
Expected value			0.98	1.00	0.90

Table 7.2: Table of results from a single Tecnai dataset

These results showed a clear trend in the value of the Si plateau. As expected, the t/λ of the plateau increased with *y* distance. No obvious trend was observed in the plateau values for aluminium. However, the plateau values given in table 7.2 are those from the Bessel function fit. Examination of the actual component values at large distance from the interface indicated that the aluminium t/λ value decreased from 0.34 at a *y* distance of 0nm, to 0.30 approaching the other extreme. This was opposite to the increasing t/λ values observed in Si. As the plateau values are very dependent on the thickness, a trend was also seen in the plateau ratio values. As the *y* distance increased, the P_{Al}/P_{Si} value decreased. There may also have been a trend in the C_i ratios, though this was less clear. As the *y* distance was increased, the C_i ratio also increased. Unfortunately, the spread of values was such that it was difficult to determine whether this was a genuine result, or merely random fluctuations.

Overall, the average A_i and C_i ratios were not very close to the expected or theoretical values. The spectra and fits corresponding to the values that deviated most strongly were examined. These spectra were affected by the problems associated with negative fit components. This suggested that the poor values were not directly caused by the experiment.

Perhaps the most interesting result from this dataset was that the C_i ratios were, in general, too high. This was opposite to the result from HB5 data for the Al/Si system. However, the interface examined in the Tecnai was a different interface from all those examined in the HB5. It is therefore possible that this discrepancy was caused by the interface itself. One other interface was examined using the Tecnai. The data presented in Set 1 of the HB5 data was acquired from this interface. A comparison of the data sets from this interface would therefore give a better indication of consistency between the HB5 and Tecnai data.

7.4.4 Comparison of HB5 and Tecnai Data from the Same Interface

A spectrum image was acquired using the technique outlined in section 5.6.1 with the setup described in section 7.4.2. An image of the interface and the area over which the spectrum image was acquired is shown in Fig. 7.11.

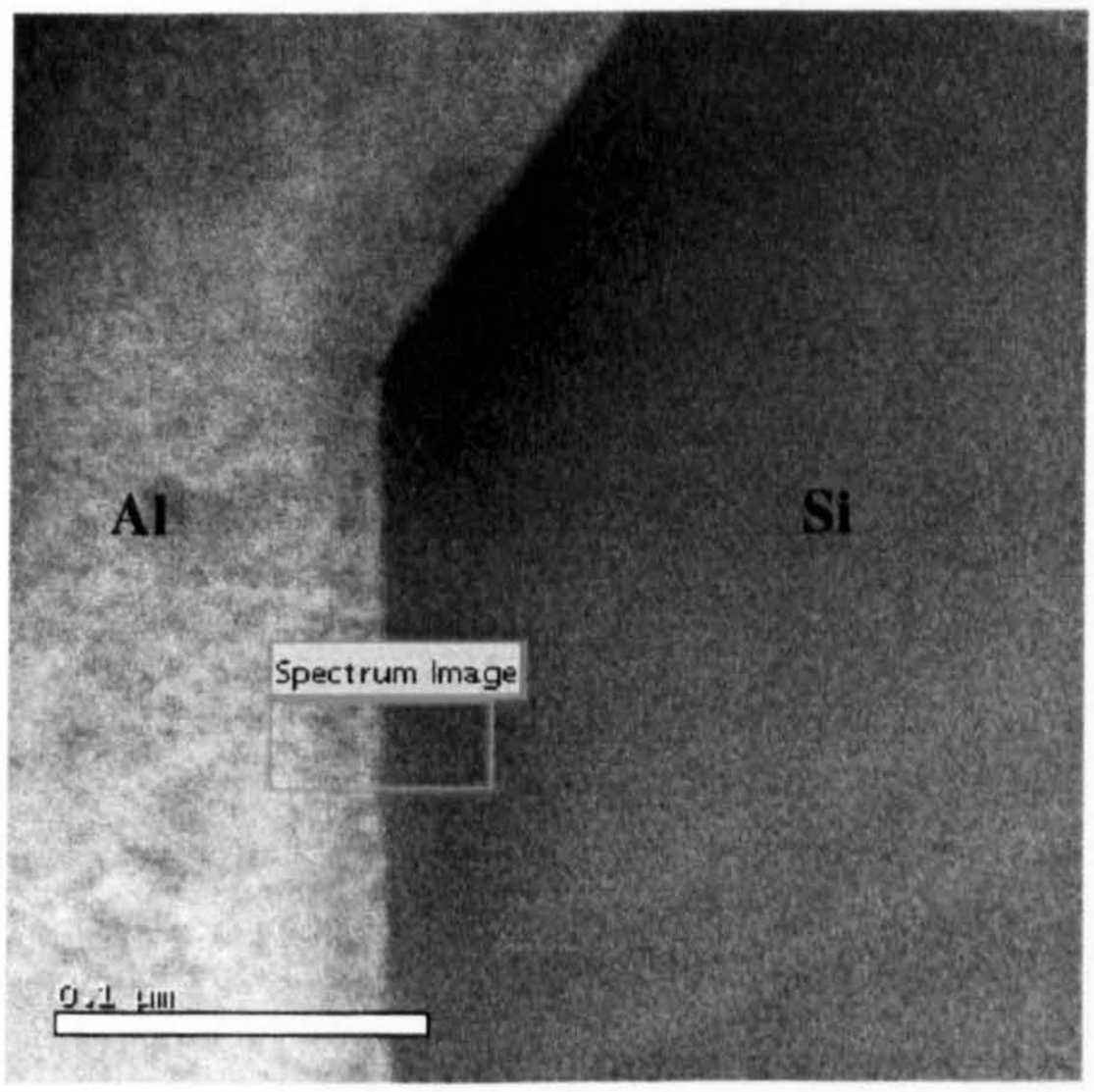

Figure 7.11: Tecnai bright-field STEM image of an Al/Si interface. Green box shows the area over which a spectrum image was acquired. Scale marker reads 0.1µm

The spectrum image was acquired and processed in the same way as discussed in sections 7.4.3 and 5.6.2. Fig 7.12 gives the t/λ plot of a line from the spectrum image. This line was taken from a y distance of 6nm.

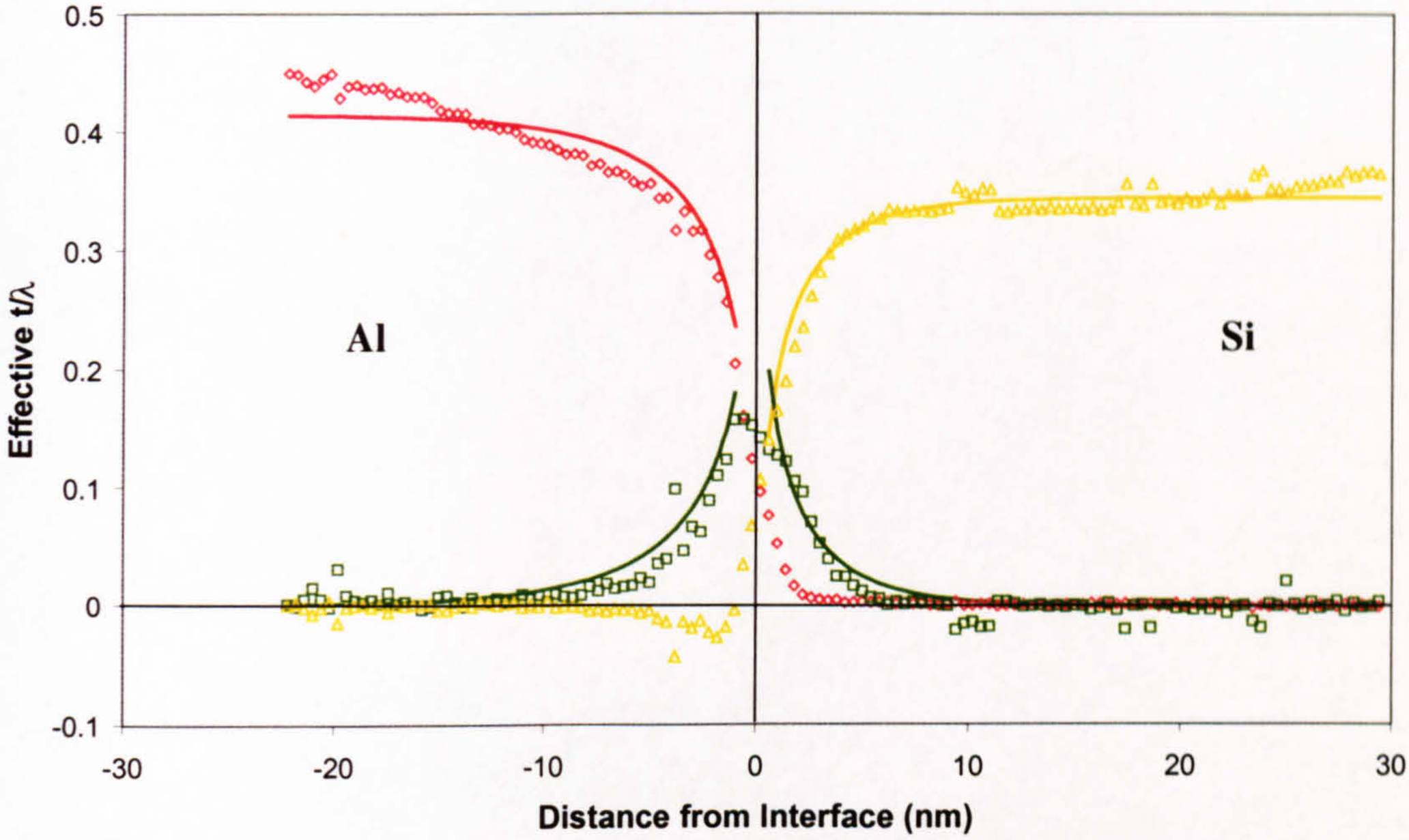

Figure 7.12: t/λ vs distance plot taken from a y distance of 6nm. Proportion of aluminium (*red*), interface (*green*) and silicon (*orange*) components are shown with best-fit lines. Each point is 0.4nm apart.

Table 7.3 gives the overall results for this spectrum image with the results from the corresponding HB5 dataset.

y distance (nm)	Al Plateau	Si Plateau	P_{Al}/P_{Si}	A_{Al}/A_{Si}	C_{Al}/C_{Si}
0	0.40	0.34	1.19	0.86	0.82
1.2	0.41	0.34	1.21	0.96	0.85
2.4	0.41	0.34	1.20	0.83	0.63
3.6	0.41	0.34	1.19	1.00	0.67
4.8	0.41	0.34	1.20	0.92	0.70
6.0	0.41	0.34	1.20	0.96	0.67
7.2	0.41	0.35	1.20	0.93	0.63
8.4	0.42	0.35	1.20	0.80	0.56
9.6	0.42	0.35	1.21	1.11	0.77
10.8	0.43	0.35	1.21	0.96	0.72
12	0.43	0.36	1.21	1.04	0.71
13.2	0.43	0.36	1.21	1.07	0.59
Tecnai Average			1.20	0.96	0.69
Standard Error			0.002	0.03	0.03
HB5 Set 1	0.44	0.46	0.97	0.92	0.61
HB5 Average			0.97	0.95	0.68
Theoretical Value			1.01	1.02	1.07
Expected value			0.98	1.00	0.90

Table 7.3: Comparison of HB5 and Tecnai results.

These results showed considerable similarity between the Tecnai and HB5 results. The ratio of C_i values was found to be very close to the HB5 result from the same interface and the overall results from the HB5. This indicated that the difference in values from the HB5 and Tecnai noted in the previous section, was caused by the interface.

The plateau value for bulk silicon in the Tecnai data was found to be lower than the HB5 data. However, a small increase in silicon thickness was observed over 13nm within the Tecnai data. As the length of this interface is greater than 0.2μm it is likely that the overall thickness increase along the interface is much greater. Data taken from different positions along the interface could therefore display noticeably different plateau values.

It is not clear why there is such a significant difference in the results from the two interfaces examined in the Tecnai. Some possible causes are discussed in the next chapter.

7.5 Summary

In this chapter the results obtained from a number of Al/Si interfaces were discussed. These results were obtained using the HB5 and Tecnai microscopes. The data was initially not found to be consistent between the two microscopes. However, when data acquired from the same interface were compared, the HB5 and Tecnai results showed strong similarity. In general, the results were not close to the expected or theoretical values. This was partially attributed to problems with the analysis, though the main cause is believed to be the interface itself. A discussion of possible physical factors affecting EELS from an interface is given in the next chapter.

The data from the Tecnai showed conclusively that, for some interfaces, the thickness varied with distance from the interface. In addition, the high-resolution images indicated that, for silicon, the interfaces were sharp, but not necessarily perfectly planar. Whilst it is not known exactly what effect this will have on the data, this is one of the factors considered in the next chapter.

The results presented in this chapter will be further discussed in Chapter 8. There, comparisons will be made between the data from this system and that from the Al/Mg_2Si system and overall conclusions reached. In addition, some methods to analyse further the results will be examined. Finally, suggestions for extending the work in this thesis will be made.

CHAPTER 8

DISCUSSION, CONCLUSIONS AND FURTHER WORK

This chapter will initially discuss some of the factors that are believed to affect the data obtained from an interface using EELS. Following this, the experimental data will be compared and conclusions drawn with reference to these factors. Finally, suggestions for experiments and analyses to extend the work in this thesis will be presented.

8.1 Effect of Thickness on Theoretical Results

Thickness variations have been noted at a number of the interfaces examined in this thesis. The effect of these thickness variations is not clear. Therefore it is of interest to consider the effects of different thickness profiles on the experimental data.

A variety of different thickness profiles were simulated for the Al/Si system. The effect of these thickness profiles on the Bessel function fit and the resulting ratios of interest was investigated. In addition, the effect of correcting thickness variations in experimental data was examined. Unfortunately, the theoretical equations (eqns 2.32 & 2.33) do not directly allow for variations in sample thickness. However, just as the experimental data was scaled using the number of counts in the zero loss peak it was possible to scale the experimental data in a similar manner. As the theoretical spectra do not contain zero loss peaks, the data was scaled using an arbitrary scaling value. By altering the scaling value used, changes in local thickness within the sample were simulated.

Recalling eqn 2.16b for a deconvoluted spectrum,

$$\frac{t}{\lambda} = \frac{I_1}{I_0},$$

where I_0 corresponds to the total intensity in the zero loss peak and I_1 corresponds to the intensity in the rest of the spectrum. By artificially altering the I_1/I_0 ratio, the t/λ value will also change. Since λ is constant for a material, such changes represent a variation in thickness. If I_1 is normalised for all the different spectra, then the relative thickness will depend solely on the value of I_0. The theoretical spectra are calculated using normalised

dielectric data, hence the spectra must also be normalised. Therefore, by tailoring the values of I_0 used to scale the components from a fit (section 5.3.3), it is possible to simulate different thickness profiles. The calculated sample thickness is inversely proportional to the number of counts in the zero loss peak *i.e.* a larger I_0 value corresponds to a thinner sample and *vice-versa*.

However, the analysis is not quite that simple and certain assumptions must be made. The first of these assumptions is best explained by a thought experiment. If a beam is passing through a standard two-layer system, parallel to and a small distance from the interface (Fig. 8.1 *left*) then the resulting EELS spectrum will contain a certain amount of bulk component and a certain amount of interface component. If the thickness on one side of the interface is then increased whilst keeping the other constant, the length of the interface remains the same (Fig. 8.1 *right*). The EELS spectrum from the same point will then have an increased bulk component (and will have some component from the material/vacuum interface) but it would not be expected that the material/material interface component would increase. As a result, for the method being used here to simulate varying thickness, it is necessary to keep the scaling factor for the interface component constant irrespective of the intended sample thickness at the electron probe. In addition, for this method to be consistent, the scaling factor for the bulk component close to (or at) the interface must be equal to the scaling factor for the interface component.

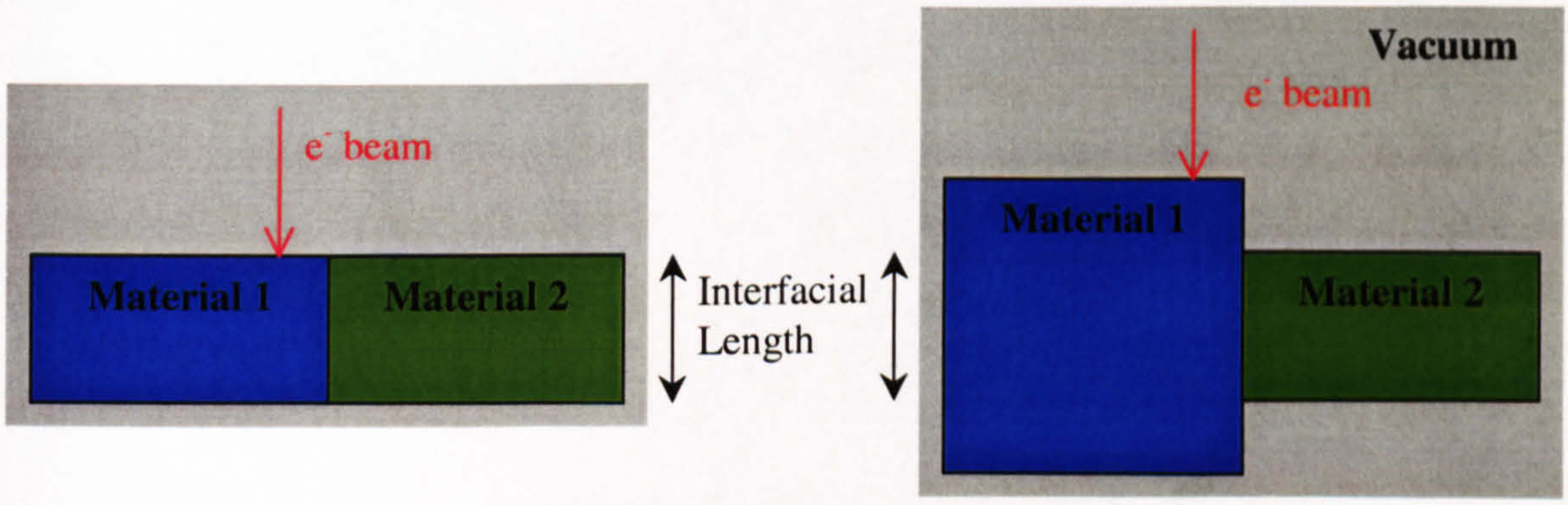

Figure 8.1: Sample thickness profiles for the thought experiment.

The processed theoretical Al/Si data was taken and each data point scaled using a simulated value. The magnitudes of the values were chosen for convenience, the resultant t/λ were physically quite high. However, it is the variation in values that is important. A

25% change in the scaling value results in an approximately 25% change in the t/λ value. Following scaling, Bessel function fits were applied to each component.

8.1.1 Altered Thickness Profile – Symmetric Bow-tie

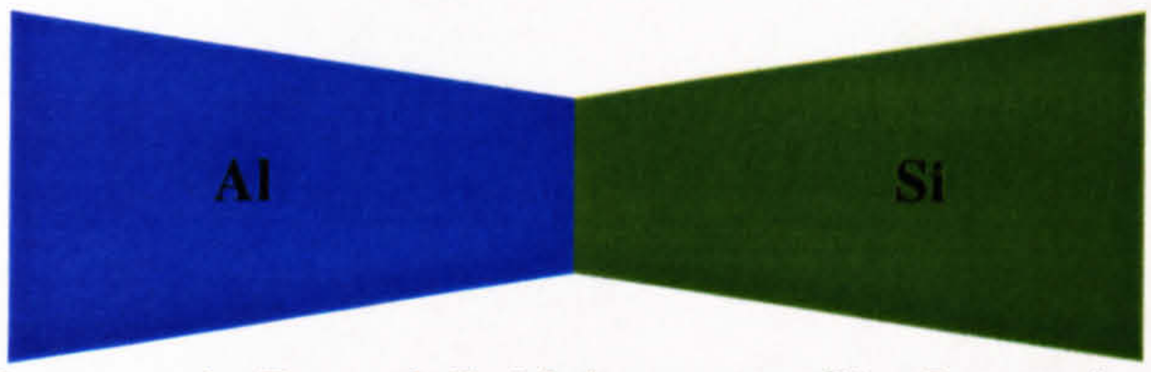

Figure 8.2: "Symmetric Bow-tie" thickness profile. Image is not to scale.

Using the technique outlined above specific thickness profiles will be considered. The first of these is designated the "symmetric bow-tie" profile and deals with the case where the sample has been preferentially thinned in the vicinity of the interface. As a result, the thickness of both bulk materials increases with distance from the interface (Fig. 8.2). Specifically, scaling values were chosen to give a 25% increase in thickness over 15nm on each side of the interface.

Strictly, for this thickness profile, the two-layer equation may not be entirely appropriate. The EELS spectrum from this thickness profile will have a small contribution from the material/vacuum interface. In addition, there may be a material/vacuum/material contribution (*i.e.* a three-layer system). Neither of these contributions are considered in this treatment. However, if it is assumed that the contribution is small compared with that from the bulk and interface components, then these effects can be neglected.

Fig 8.3 shows the t/λ vs distance plot for this profile with the Bessel function fits included in the plot.

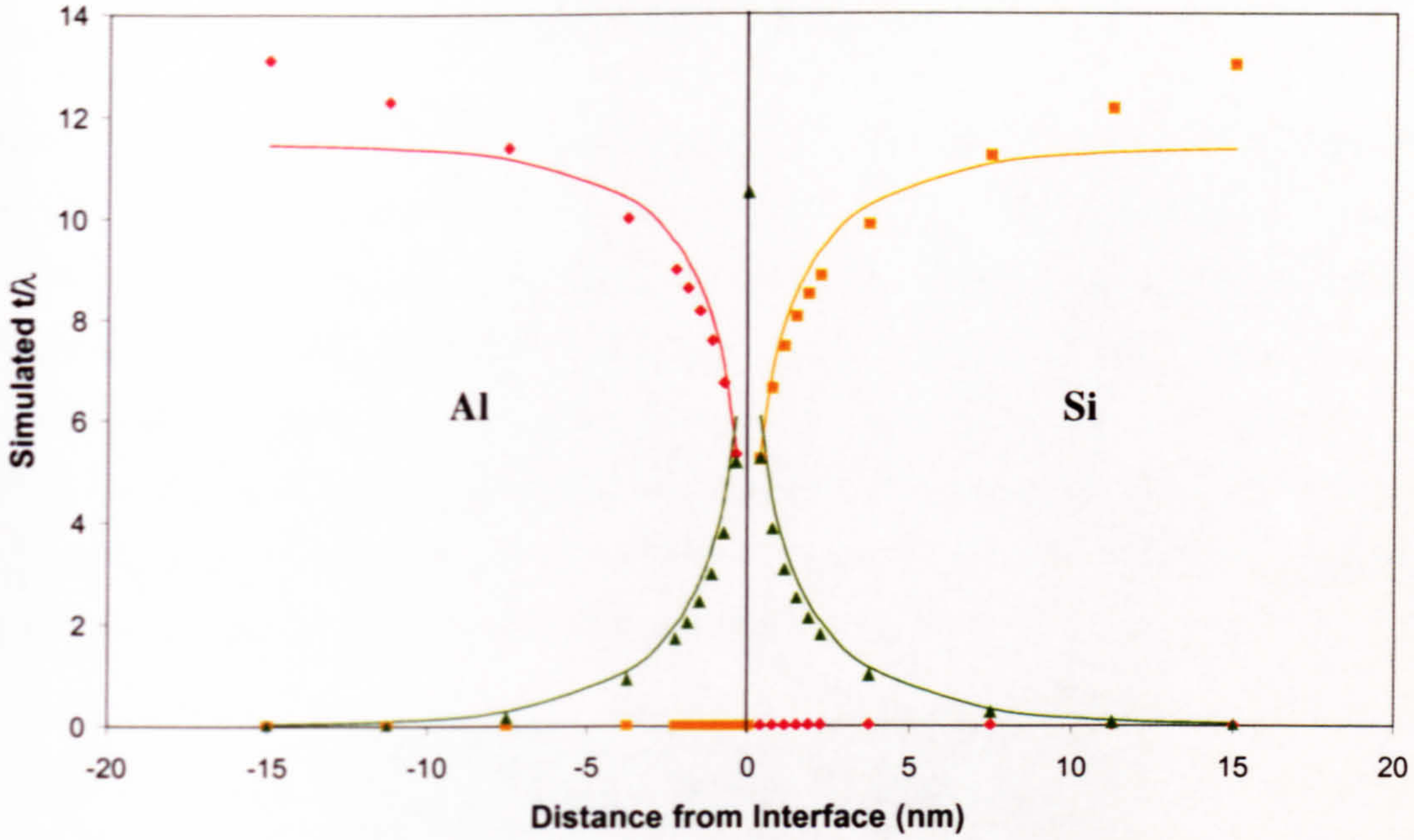

Figure 8.3: t/λ vs distance plot for the "symmetric bow-tie" thickness profile. Aluminium (*red*), silicon (*orange*) and interface (*green*) components are shown.

Unlike the excellent fit displayed for the standard theoretical data, the Bessel functions fit poorly to this data. This is unsurprising as the Bessel function reaches a plateau value, whereas, due to the thickness variations, this data does not. As a result, the fit is in general too high for the interface component and also for the bulk components close to the interface. Further away from the interface, the bulk components become increasingly larger than the Bessel fit.

For this system with constant thickness the results for the fits were as follows

$$\frac{P_{Al}^{Fit}}{P_{Si}^{Fit}} = 1.01 \qquad \frac{P_{Al}^{Data}}{P_{Si}^{Data}} = 1.01 \qquad \frac{A_{Al}}{A_{Si}} = 1.02 \qquad \frac{C_{Al}}{C_{Si}} = 1.07$$

Using the "symmetric bow-tie" thickness profile the results were not significantly altered

$$\frac{P_{Al}^{Fit}}{P_{Si}^{Fit}} = 1.01 \qquad \frac{P_{Al}^{Data}}{P_{Si}^{Data}} = 1.01 \qquad \frac{A_{Al}}{A_{Si}} = 1.01 \qquad \frac{C_{Al}}{C_{Si}} = 1.05$$

This was unsurprising for the plateau values. As the thickness increase was symmetric about the interface, the ratio of plateau values should remain unchanged. Similarly, any changes to the decay constants, C_i, will be balanced due to the symmetry.

8.1.2 Altered Thickness Profile – Asymmetric Bow-tie

The "asymmetric bow-tie" profile is a more physically realistic version of the "symmetric bow-tie" profile. This profile allows for the likelihood that the aluminium and silicon would be thinned at different rates, whilst still having preferential thinning at the interface. It is possible that interfaces showing thickness variations had a profile similar to this. A cross-section indicating the profile is shown in Fig. 8.4. In this case, the aluminium was chosen to have a 10% increase in thickness and the silicon a 20% increase in thickness compared with the thickness at the interface. In both cases the thickness increase is measured over 15nm on either side of the interface.

Figure 8.4: "Asymmetric bow-tie" thickness profile. Image is not to scale.

Fig 8.5 shows the t/λ vs distance plot for this profile with the Bessel function fits included in the plot.

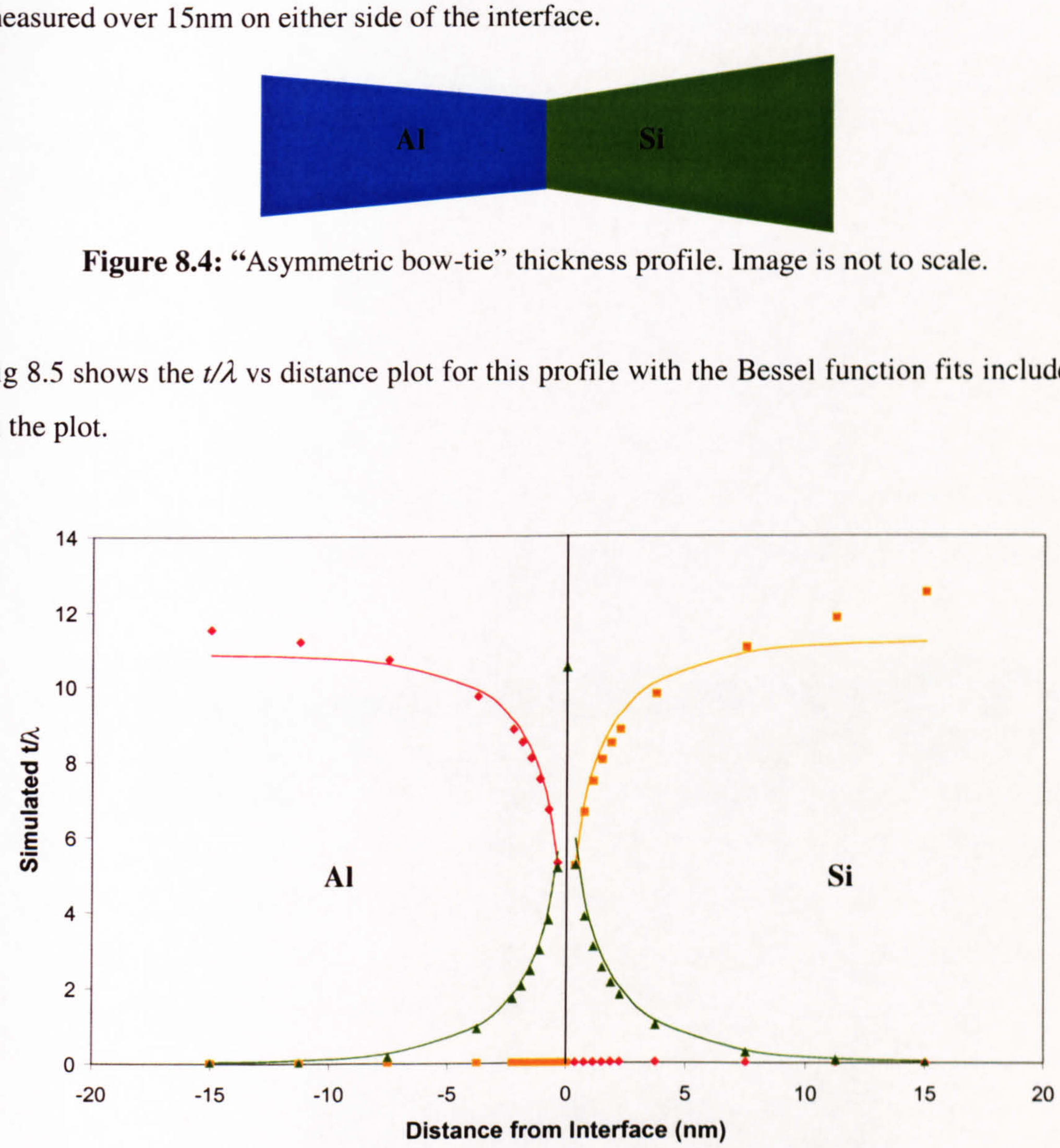

Figure 8.5: t/λ vs distance plot for the "asymmetric bow-tie" thickness profile. Aluminium (*red*), silicon (*orange*) and interface (*green*) components are shown.

Naturally, the plot has similar features to the "symmetric bow-tie" profile. The deviation between fit and data on the aluminium side is not as significant as previously, due to the smaller thickness increase. Other than this, the plot is largely the same. However, as the profile is asymmetric, it would be expected that the results from the fit would be quite different to those from the "symmetric bow-tie" profile.

$$\frac{P_{Al}^{Fit}}{P_{Si}^{Fit}} = 0.97 \quad \frac{P_{Al}^{Data}}{P_{Si}^{Data}} = 0.92 \quad \frac{A_{Al}}{A_{Si}} = 0.97 \quad \frac{C_{Al}}{C_{Si}} = 1.06 .$$

The ratio of plateau values from the data is lower than for the theoretical data of constant thickness. This was expected as the silicon thickness was greater than that of the aluminium. However, the ratio of plateau values from the fit is closer to the standard theoretical value. This results from the fit having an averaging effect on the thickness increase and so 'buffering' the thickness change.

It was expected that the decay values would be affected by the asymmetric thickness variation. In fact, they were not. The ratio was closer to the theoretical value for this profile than for the "symmetric bow-tie" profile. This was an unexpected result, but indicates that some of the concerns relating to thickness variations for the experimental data were unfounded. For an interface with a thickness profile similar to this, even with relatively substantial thickness variations, no significant change should be expected in the ratio of C_i values.

8.1.3 Altered Thickness Profile – Flat Bow-tie

The "flat bow-tie" profile is another adaptation of the bow-tie profile. In this case, preferential thinning not only of the interface but also of the vicinity of the interface is considered. A cross-section indicating the profile is shown in Fig. 8.6. In this case, the thickness is constant to 5nm on each side of the interface. The thickness then increases symmetrically to give a 20% increase in thickness at 15nm.

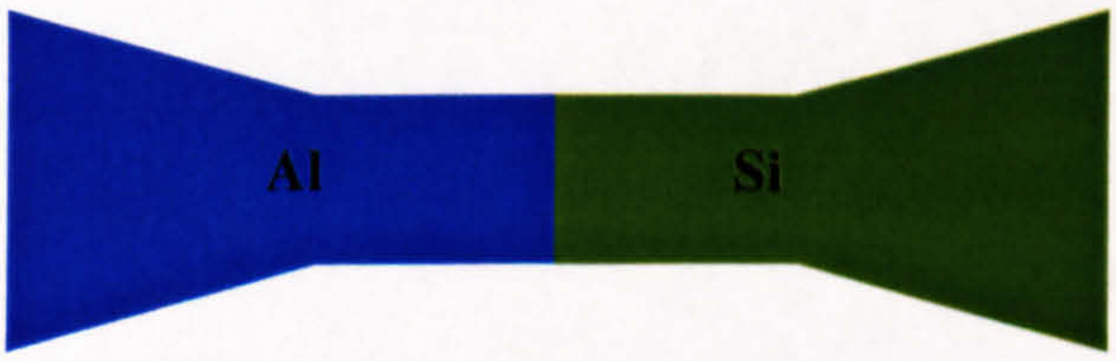

Figure 8.6: "Flat bow-tie" thickness profile. Image is not to scale.

Fig 8.7 shows the t/λ vs distance plot for this profile with the Bessel function fits included in the plot.

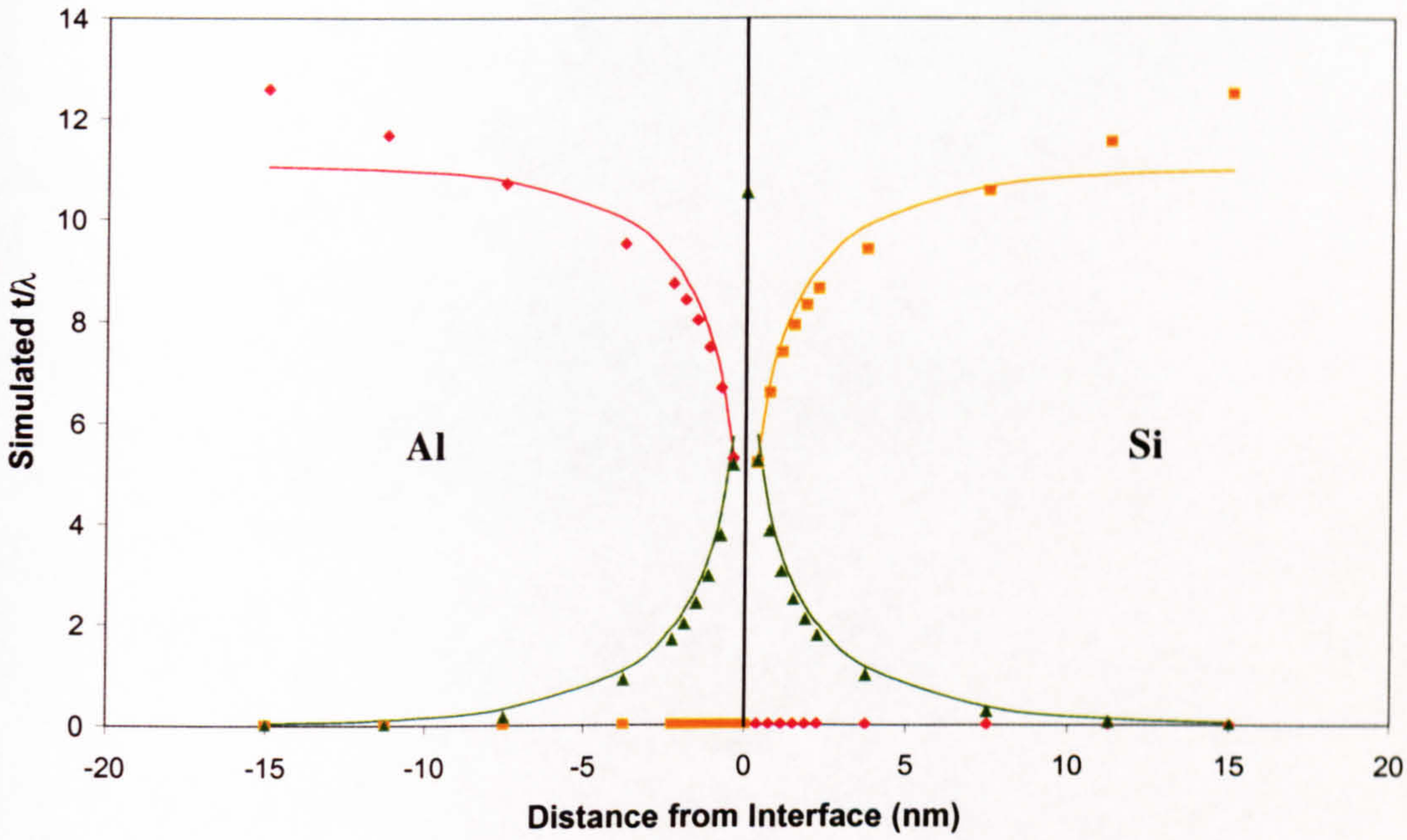

Figure 8.7: t/λ vs distance plot for the "flat bow-tie" thickness profile. Aluminium (*red*), silicon (*orange*) and interface (*green*) components are shown.

The plot from this profile was largely identical to that from the "symmetric bow-tie" profile. As there was a change in thickness gradient at 5nm it was expected that the decay of the interface plasmon would also show a change. However, no such change was apparent. As the profile is symmetric, it would once again be expected that the values would balance on each side of the interface and hence the ratios would be largely unchanged.

$$\frac{P_{Al}^{Fit}}{P_{Si}^{Fit}} = 1.01 \qquad \frac{P_{Al}^{Data}}{P_{Si}^{Data}} = 1.01 \qquad \frac{A_{Al}}{A_{Si}} = 1.01 \qquad \frac{C_{Al}}{C_{Si}} = 1.06 .$$

This assumption was validated by the data. The results from this profile were the same as for the "symmetric bow-tie" profile except for a slight difference in C_i ratio. These results suggested that any thickness profile based on the bow-tie profile would not show noticeably different results.

8.1.4 Altered Thickness Profile – Turbine

The final thickness profile examined was designated the "turbine" profile. This profile simulates the preferential thinning of one of the bulk materials (in this case silicon). The masking from the other material during the thinning results in a thickness gradient over the interface (Fig. 8.8). For this profile the silicon is 25% thinner than the aluminium and the thickness variation occurs over a distance of 10nm (*i.e.* extends 5nm on either side of the interface).

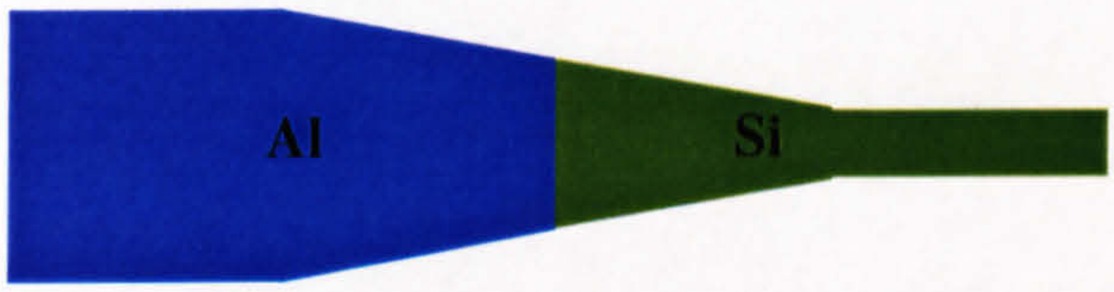

Figure 8.8: "Turbine" thickness profile. Image is not to scale.

Fig 8.9 shows the t/λ vs distance plot for this profile with the Bessel function fits included in the plot.

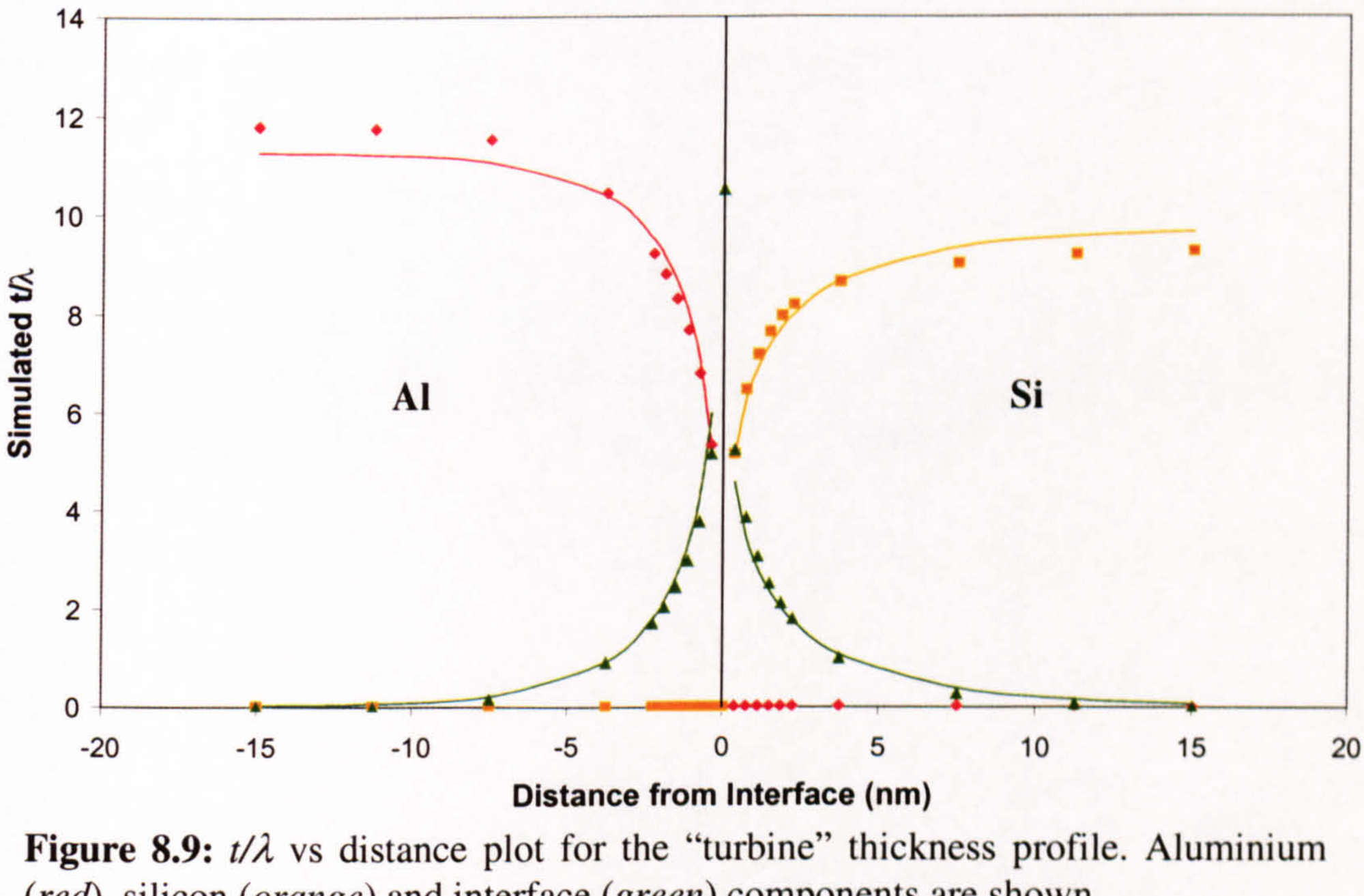

Figure 8.9: t/λ vs distance plot for the "turbine" thickness profile. Aluminium (*red*), silicon (*orange*) and interface (*green*) components are shown.

The fit to the data for this profile was not particularly bad, except at larger distances from the interface. Unusually, the fit on the silicon side beyond 5nm was higher than the data

itself. This corresponds to the thickness decrease in the silicon close to the interface. The results for this profile were difficult to predict and proved interesting.

$$\frac{P_{Al}^{Fit}}{P_{Si}^{Fit}} = 1.17 \qquad \frac{P_{Al}^{Data}}{P_{Si}^{Data}} = 1.27 \qquad \frac{A_{Al}}{A_{Si}} = 1.55 \qquad \frac{C_{Al}}{C_{Si}} = 1.55 .$$

A notable difference was seen in all the ratios for this profile compared with the constant thickness case. The ratios of the plateau values were large, as would be expected given the smaller silicon thickness. However, the ratio of C_i values was significantly different from the theoretical value. The increasing thickness on the aluminium side caused the aluminium component to grow more quickly in the t/λ plot. Similarly, the decreasing thickness on the silicon side resulted in slower growth of the silicon component. These two effects combined, caused an increase in the C_i ratio.

8.1.5 Correcting Thickness Variations

In addition to modelling thickness variations, it is also of interest to correct their effects. The techniques applied above in simulation can also be applied to experimental data to remove some of the effects caused by non-constant thickness.

The data shown in Fig. 7.12 displayed a thickness variation within the aluminium. This data is given again in Fig. 8.10 to provide easy reference.

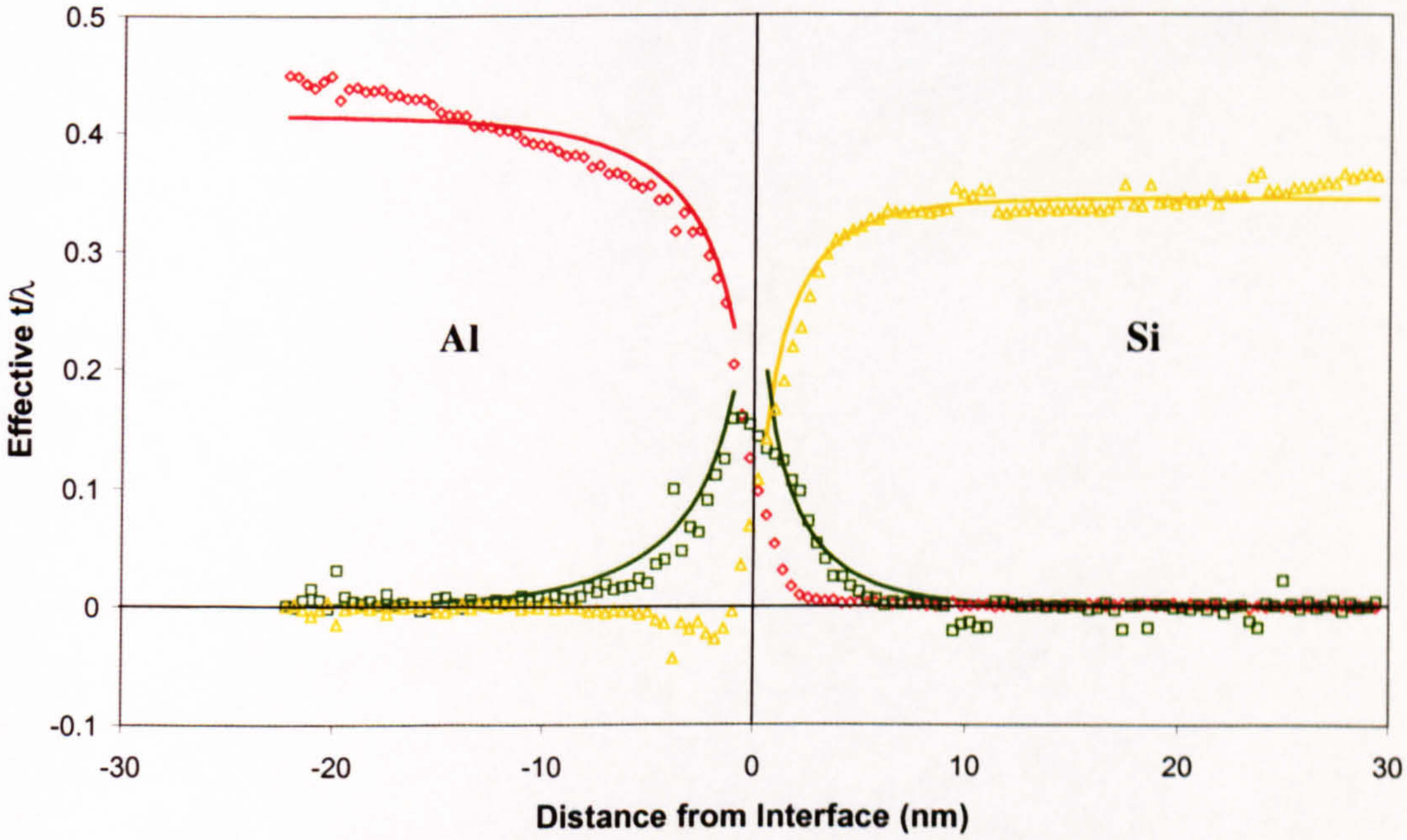

Figure 8.10: t/λ plot of data given in fig 7.12

In order to correct this data, it is assumed that the aluminium thickness varies in a linear manner and the silicon thickness remains constant. Furthermore, the assumption is made that the thinnest point is located at the interface (*i.e.* a one-sided "bow-tie" profile). For this profile, the aluminium thickness varies as $y=mx_0+c$ where y is the recorded t/λ value, m is the gradient of the thickness change, x_0 is the distance from the interface and c is the flattened thickness (also the thickness at the interface). Therefore, the flattened thickness can be determined from $c=y-mx_0$. Knowledge of the gradient of the thickness change thus allowed the thickness to be corrected. Using the same argument given at the beginning of section 8.1, no adjustment was necessary to the interface component.

A linear best-fit line was fitted to the aluminium component between –8 and –22nm. In this region the component was believed to be varying solely due to differences in thickness. A gradient was then determined from this best-fit line. This gradient was equal to the gradient of the thickness change.

Using the gradient of the thickness change, corrected t/λ values were calculated for each point. In addition, following the correction, the interfacial position was re-selected. Fig 8.11 shows the plot of the corrected data.

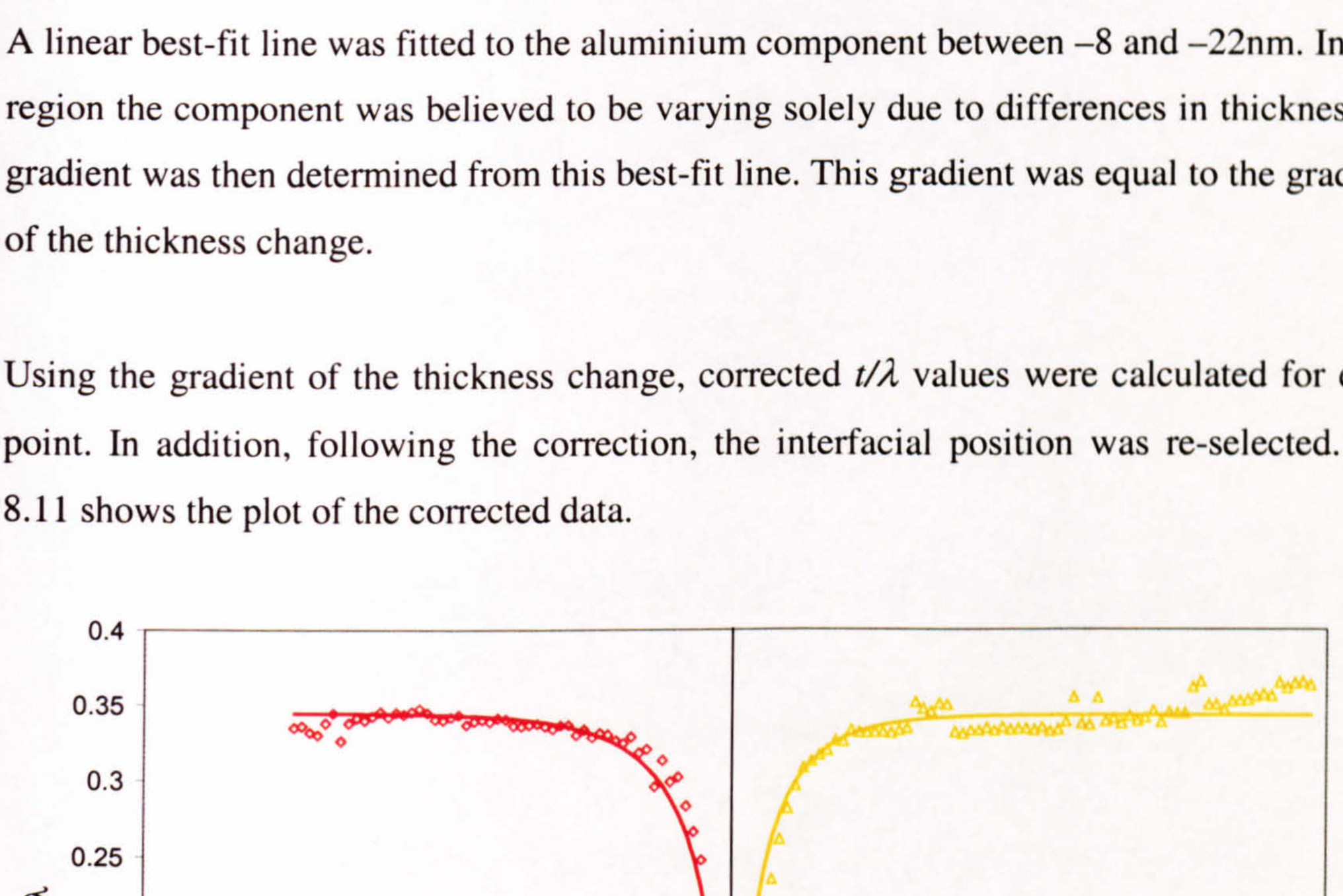

Figure 8.11: Data from fig 7.12 corrected to give constant thickness across the interface. Proportion of aluminium (*red*), silicon (*orange*) and interface components (*green*) are shown.

This technique was clearly very successful. The significant variation in thickness within the aluminium is no longer apparent. Both bulk materials do show a slight thickness variation at large distance from the interface; this is discussed below. The Bessel function fit on the aluminium side is considerably closer to the data than for the uncorrected case. With the exception of the slight variation at large distance from the interface, the plateau value of the fit is equivalent to that of the data. The results from the uncorrected data were

$$\frac{P_{Al}^{Fit}}{P_{Si}^{Fit}} = 1.20 \quad \frac{P_{Al}^{Data}}{P_{Si}^{Data}} = 1.29 \quad \frac{A_{Al}}{A_{Si}} = 0.96 \quad \frac{C_{Al}}{C_{Si}} = 0.67,$$

compared with the results from the corrected data

$$\frac{P_{Al}^{Fit}}{P_{Si}^{Fit}} = 1.00 \quad \frac{P_{Al}^{Data}}{P_{Si}^{Data}} = 1.03 \quad \frac{A_{Al}}{A_{Si}} = 0.93 \quad \frac{C_{Al}}{C_{Si}} = 0.80.$$

As expected, the plateau values changed significantly. The plateau ratios for the corrected data showed greater similarity between the fit and data. In addition, both corrected plateau ratios were close to the theoretical value of 1.01. The C_i ratio for the corrected data was closer to the theoretical value of 1.07. The change in the ratio of decay constants was surprising. In the simulations above, variations in thickness moving out from the interface (*i.e.* the "bow-tie" profiles) did not result in any change in the ratio of decay constants. Here, the change is quite significant. However, it is not clear why such a change was apparent in this case, but not in the simulated data. The optimal interface position was re-selected following the thickness correction. This required an offset of 0.2nm. Such an offset does not result in a significant change in the C_i ratio. As noted above, there is a slight thickness variation apparent at the extremity of the plot. Initially, this region was excluded from the fitting of the best-fit line (the fit was performed over –8nm → -18nm). This resulted in a C_i ratio of 0.92, closer again to the theoretical value. However, the thickness variation appeared over-corrected. This indicated that the C_i ratio was very sensitive to the thickness corrections, an opposite conclusion to the theoretical investigation.

One possibility is that the fit for the theoretical data is effectively perfect and becomes only slightly worse when the thickness profile is altered. The experimental data on the other hand shows a poor fit. This fit improves when the thickness is corrected. As a result, the fit

and corresponding values are more representative of the data following thickness correction. It is apparent that the fit before (Fig. 8.10) and after (Fig. 8.11) the thickness correction is quite different. The fit to the corrected data is considerably better, resulting from a sharper decay in the Bessel function. In addition, it was noted that the data presented in Fig. 7.10 had a similar thickness profile to that in Fig. 7.12 and yet the C_i ratios were significantly different. The data was taken from different interfaces but also the x distance examined in each case varied. If the Bessel function fit range for the data in Fig. 8.10 is limited to 9nm on each side of the interface, the resultant C_i ratio is quite different. Instead of the original 0.67 observed, the value becomes 0.85. This difference in values still results from the thickness variation. The Bessel function fit is unable to fit properly to a constantly increasing thickness at distance from the interface, just as a line with zero gradient does not fit well to a line with non-zero gradient. At best it will attempt to average out the difference between fit and data, increasing the plateau value of the fit. If the experimental data extends out to large distance, a lot of the data will correspond to the plateau region. Therefore, the fit for such a case will be worse. This could also be an explanation as to why no significant difference was noted in the theoretical data. The theoretical data neither covers the same spatial distance nor has the same density of points as the corrected experimental data. As a result, the fit to the experimental data will be considerably more sensitive to the general trend of the data.

The correction of the data resulted in a significantly better fit both at large and small x. As the technique is believed to be valid the resultant C_i ratio should be closer to the theoretical value. The C_i ratio for the corrected data of 0.80 was close to the theoretical value of 1.05. This showed that variations in thickness do have an effect and that this effect can be corrected, at least in part.

8.2 Effect of Plasmon Width on Theoretical Results

It was proposed in section 7.2 that the difference in plasmon widths between silicon and magnesium silicide may have an effect on the results. For these two systems the effect is difficult to quantify as a number of factors are different, most noticeably plasmon energy. In order to examine the effect of plasmon peak width on the theoretical values, data was generated for a system with a wide bulk plasmon peak and one with a narrow bulk plasmon

peak. The wide and narrow plasmons had the same plasmon energy. These systems were then processed as for the standard theoretical data to obtain the ratios of interest.

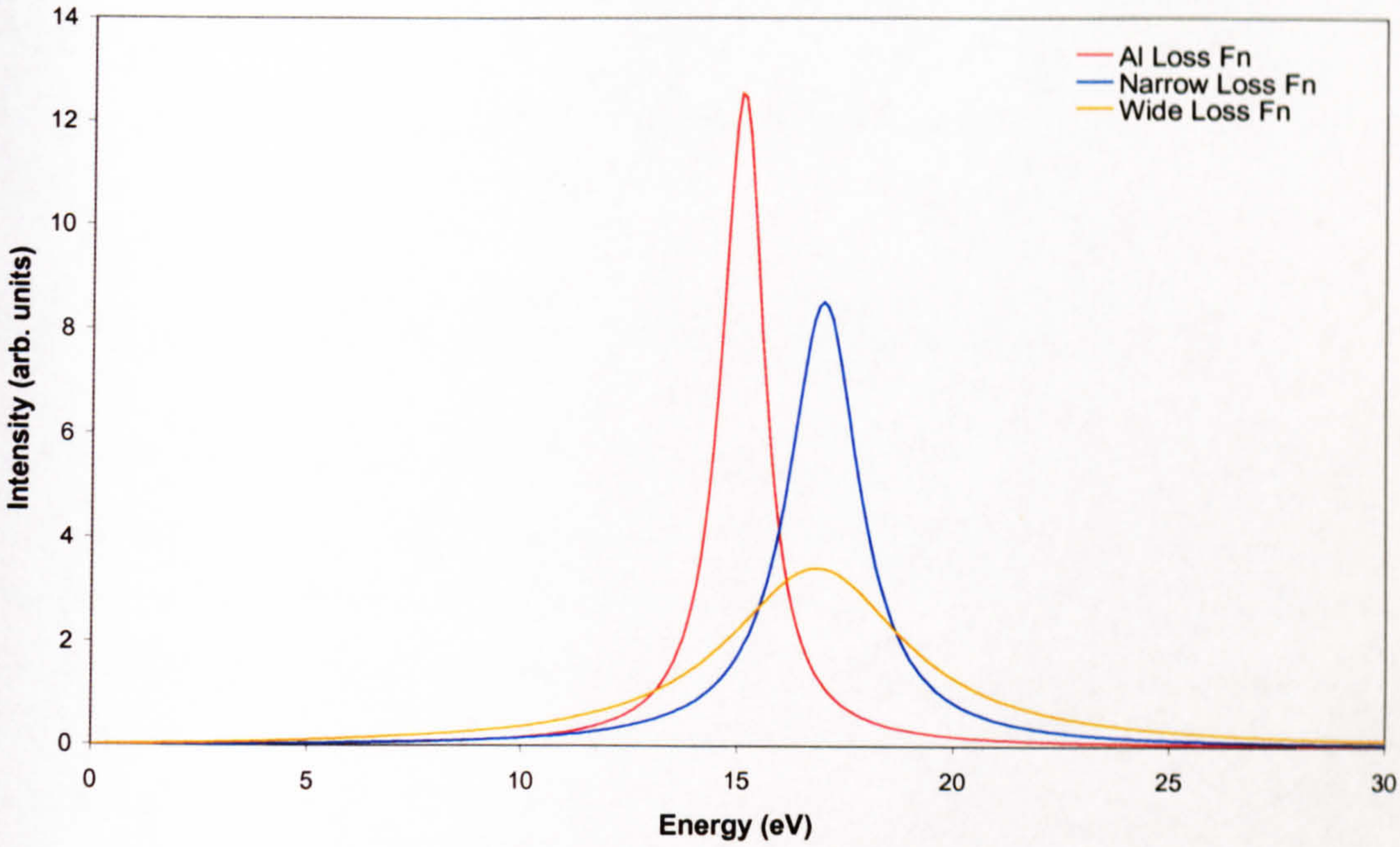

Figure 8.12: Loss functions generated from Drude dielectric data for aluminium, narrow and wide plasmons.

Drude dielectric functions were calculated using eqn 2.5 with $\Gamma=\Delta E_p/\hbar$ to calculate the damping constant. ΔE_p, the FWHM of the plasmon peak, was chosen as 2eV and 5eV for the narrow and wide plasmons respectively. In addition, a Drude aluminium dielectric function was calculated using values of 15.1eV for E_p and 1.2eV for ΔE_p. Fig 8.12 shows the loss functions corresponding to this dielectric data.

These dielectric functions were used to generate a theoretical dataset for Al/narrow and Al/wide systems. These datasets were processed as before to determine the fit values.

Using the approximations discussed in section 5.4, the expected values for both systems would be identical as the plasmon energies are the same. The actual values determined from the fit were

Narrow: $\frac{P_{Al}^{Fit}}{P_{Si}^{Fit}}=0.93$ $\frac{P_{Al}^{Data}}{P_{Si}^{Data}}=0.92$ $\frac{A_{Al}}{A_{Si}}=0.94$ $\frac{C_{Al}}{C_{Si}}=0.89$

Wide: $\frac{P_{Al}^{Fit}}{P_{Si}^{Fit}}=0.97$ $\frac{P_{Al}^{Data}}{P_{Si}^{Data}}=0.97$ $\frac{A_{Al}}{A_{Si}}=0.97$ $\frac{C_{Al}}{C_{Si}}=0.92$

These results showed that the plasmon width does make a difference to the results obtained. However, the change in results is quite small and since the difference between the plasmon widths of silicon and magnesium silicide is only ~0.8eV compared with 3eV in this analysis it would be expected that the effect of plasmon widths for the experimental data would be negligible.

8.3 Effect of Finite Probe Size on Theoretical Results

It has been observed that in the t/λ vs distance graphs, the bulk components appear to extend to the opposite side of the interface. This tailing was not apparent in the theoretical predictions. In previous discussions within this thesis the effect has been attributed to the finite spatial extent of the electron probe. In order to investigate the validity of this assumption the effect of a finite probe was simulated within the theoretical data. The method chosen to perform this analysis was to convolute a function simulating the probe with theoretical data. As this could be performed within *Matlab* where the original theoretical data had been produced, it was decided that this would be the most suitable option.

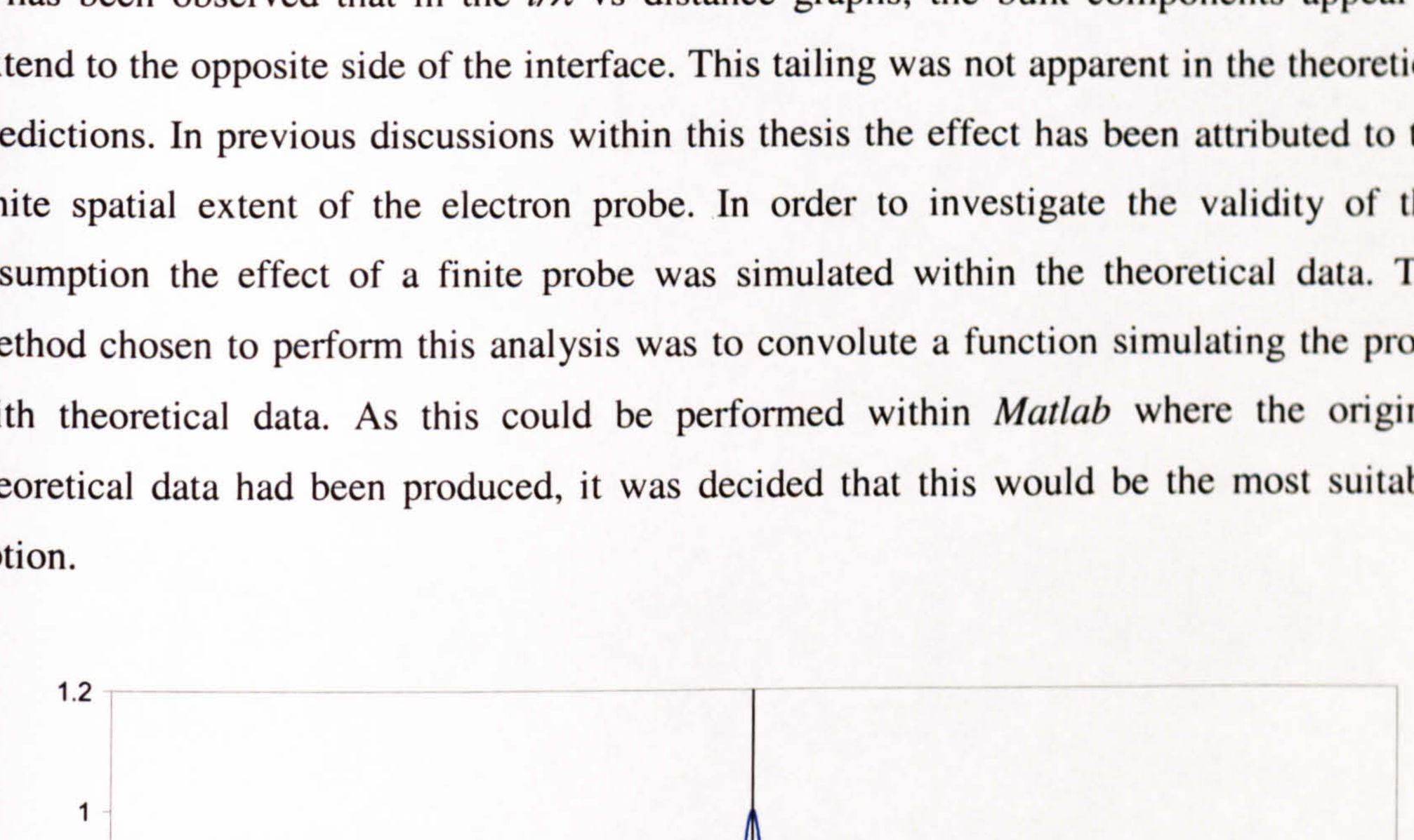

Figure 8.13: Graph of function used to simulate the electron probe.

The intensity distribution of the electron probe was simulated using a Gaussian function. Values were chosen to provide a FWHM of 1.5nm with the function centred on x=0nm. A graph of the function is given in Fig. 8.13. To provide sufficient data to represent accurately the Gaussian function, a spacing of 0.1nm was chosen between data points, with 41 points in total (*i.e.* covering 2nm either side of the central point). However, in order to perform a convolution within *Matlab*, the two sets of data (theoretical data and simulated probe) were required to have the same scale. Therefore for the convolution to be performed correctly the theoretical data also needed a 0.1nm spacing. By altering the *Matlab* program theoretical data was generated with this spacing.

The convolution function within *Matlab* was then used to convolute the simulated electron probe with the theoretical data. The effect of convolution here was to simulate placing the finite electron probe at each point of interest. This meant that each convoluted spectrum had a contribution from 41 different theoretical spectra from adjacent data points (*i.e.* the same number as in the probe function) in varying proportions dependent on the probe function.

To provide the spatial range in the theoretical data as in previous graphs it was necessary to have over 400 theoretical energy loss spectra. It was not practical to perform the standard analysis on this number of points. Therefore, following the convolution procedure, spectra were selected from distances equivalent to those used in previous theoretical treatments within this thesis. These spectra were then processed using the standard method for theoretical spectra and a t/λ vs distance plot calculated (Fig. 8.14)

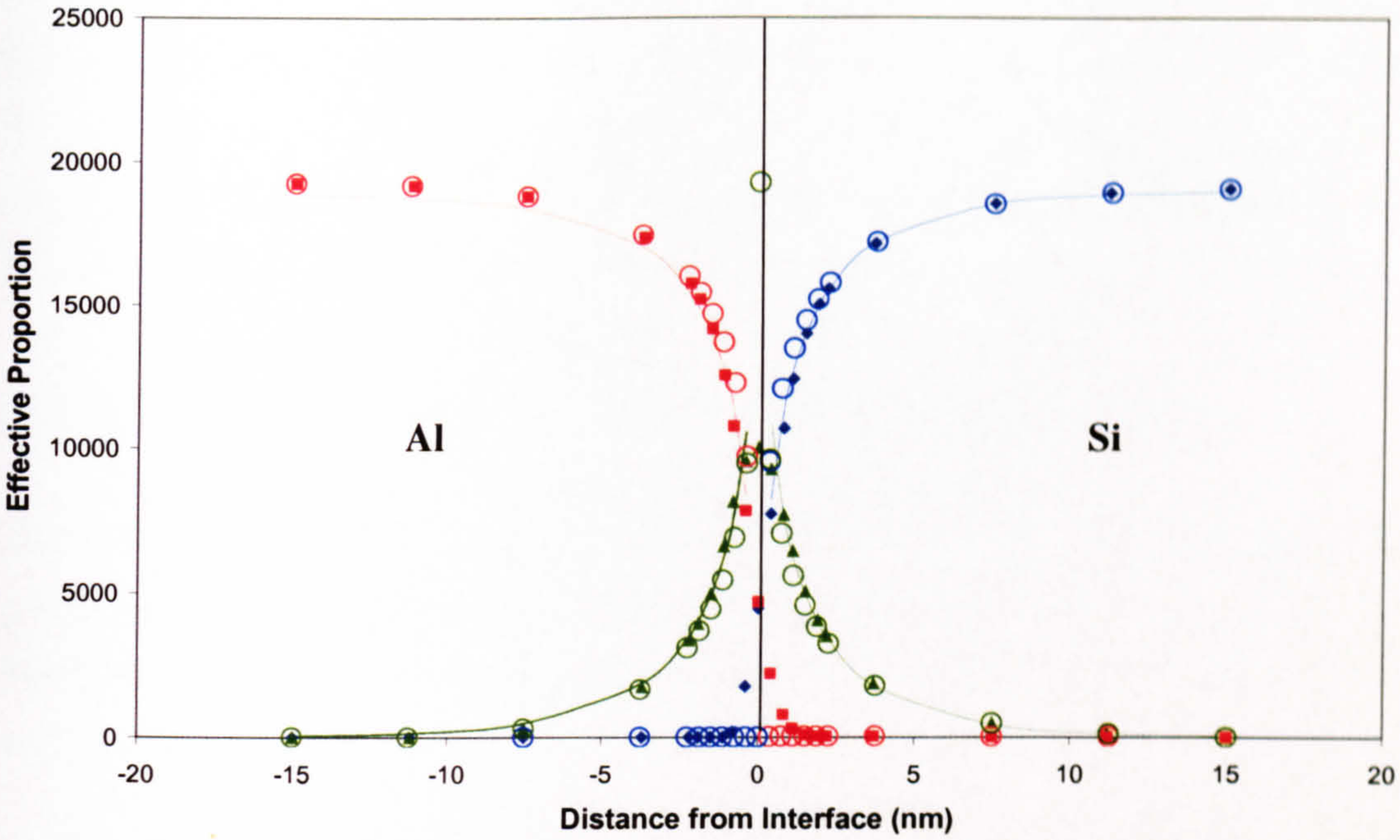

Figure 8.14: Theoretical t/λ plot for a system with finite probe size (*filled symbols*). Aluminium (*red*), silicon (*orange*) and interface (*green*) components are shown. Also shown are the standard theoretical results for the Al/Si system (*hollow circles*) for comparison.

As was expected the bulk components did extend to the opposite side of the interface. Associated with this, the interface component had a rounded peak compared with the sharp peak observed in previous theoretical data. This was an indication that the probe may be the cause of the tailing within the experimental data.

The results from this data were:

$$\frac{P_{Al}}{P_{Si}} = 1.01 \qquad \frac{A_{Al}}{A_{Si}} = 1.05 \qquad \frac{C_{Al}}{C_{Si}} = 1.06$$

As would be expected the plateau ratio was not altered as this should be independent of the probe size. It is shown in Fig. 8.14 that the theoretical and convoluted theoretical data vary only close to the interface. The ratio of A values was increased slightly from the standard theoretical Al/Si system, though the reason for this is not clear. The ratio of C values was not significantly different from the standard theoretical value. This was not a surprising result as the simulated probe was symmetric and so would effect both sides of the interface equally. As a result if the decay values were altered, they would be altered by an equivalent amount, leaving the ratio unchanged.

The probe size chosen for this analysis was 1.5nm, this is slightly larger than the 1nm probe size present in the HB5. A larger probe size was chosen to accentuate any effect on the data. It would be anticipated that any effect of the probe would be smaller than that shown here. Therefore, despite the effect of finite probe size on the t/λ plot itself, it is not believed to have a notable effect on the values of interest.

8.4 Effect of Interfacial Steps on Theoretical Results

Steps were observed at the interface in the high-resolution image shown in Fig. 7.4. It was postulated that the interface may additionally be stepped in the direction of the electron beam. It was therefore of interest to determine what effect steps would have on EELS data from an interface.

No discussion is given in literature of EELS from stepped interfaces. However, it might be expected that the effect would be similar to that from a tilted interface. The approximation was made that a stepped interface was equivalent to a number of identical interfaces stacked. These interfaces are then progressively displaced in the x direction with respect to each other (Fig. 8.15 right). The resulting loss function from a point x_0 would then be equal to

$$I_f^{total} = I_f\left[x_0 + \frac{n}{2}x_s\right] + I_f\left[x_0 + \left(\frac{n}{2}-1\right)x_s\right] + \ldots + I_f[x_0] + \ldots + I_f\left[x_0 - \left(\frac{n}{2}-1\right)x_s\right] + I_f\left[x_0 - \frac{n}{2}x_s\right]$$

Where I_f is the loss function observed at a distance x from a planar interface, x_0 is the distance from the central line of the stepped interface, x_s is the height of a step (in the x direction) and n is the number of steps. This is a very approximate way of handling steps. The expression for a planar interface is intended to deal with semi-infinite media and neglects any effect from the outer surfaces of the material. Clearly, stacking a series of semi-infinite media is physically nonsensical. In addition, such surface effects can be significant. Aizpurua *et al* (1999) investigated coupling between the edge modes in theoretical EELS spectra from a truncated slab. Further problems arise if the dimensions of the steps are considered. Plasmons are a bulk excitation and as such interact over ~5-10nm. If the steps are smaller than 5nm in height, then theoretically they are unable to support a plasmon excitation. Attempting to rectify all these limitations is likely to require a complex computational solution. The purpose of this section is not to provide a fully accurate theoretical model, but instead to offer an indication of the effect of steps on EELS from an

interface. For this, the assumption is made that the major effect is from the displacement of the interface with respect to the electron beam and other effects can be discarded.

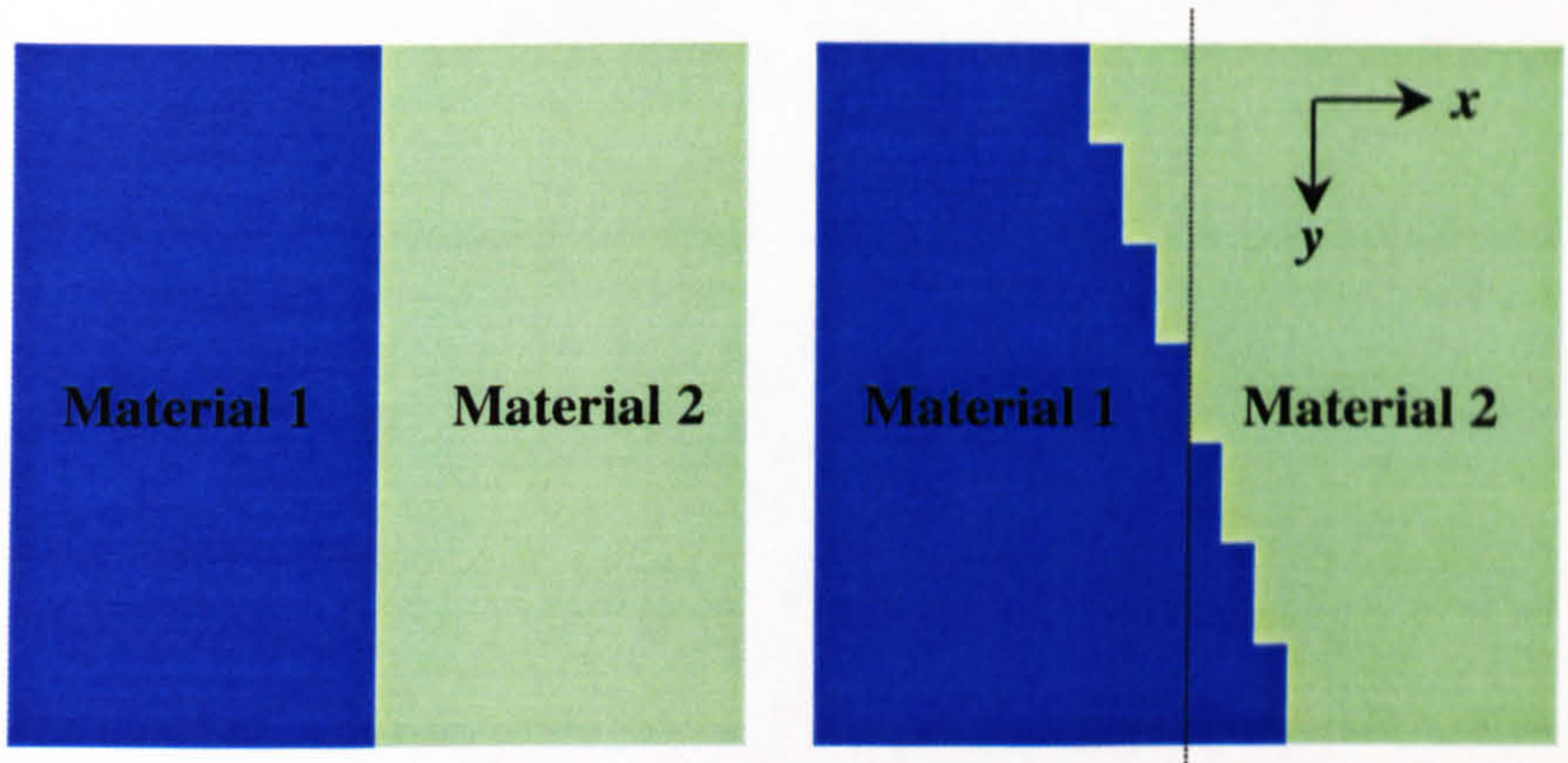

Figure 8.15: Diagram of a planar (*left*) and a stepped (*right*) interface. The *dotted line* marks the central line of the interface.

The method of simulation used will also give an approximation to a tilted planar interface and EELS from a planar interface using an electron probe of finite size. In these cases, the steps should be considerably smaller as strictly an integral over the horizontal interface extent or probe width respectively is required. Even if this analysis did perform the relevant integral it involves further approximations. For the tilted interface case it is assumed that the energy lost is associated with the component of velocity of the electron beam parallel to the interface. This assumption has been made by others for a beam at glancing incidence (Echenique and Pendry, 1975) and also here, in the application of this treatment to a stepped interface. For simulating a probe of finite size, this approximation is not required. It is, however, assumed that all the incident electrons are parallel to the electron beam and, for this treatment, that at the sample the probe has a square profile of uniform electron intensity. This simulation is not intended to model correctly these two cases. However, it does offer a first approximation to their behaviour.

A theoretical t/λ plot was calculated for an Al/Si system with a stepped interface. For this interface the number of steps, n=6 and the height of a step, x_s=0.5nm. The t/λ results from this system are shown in Fig. 8.16.

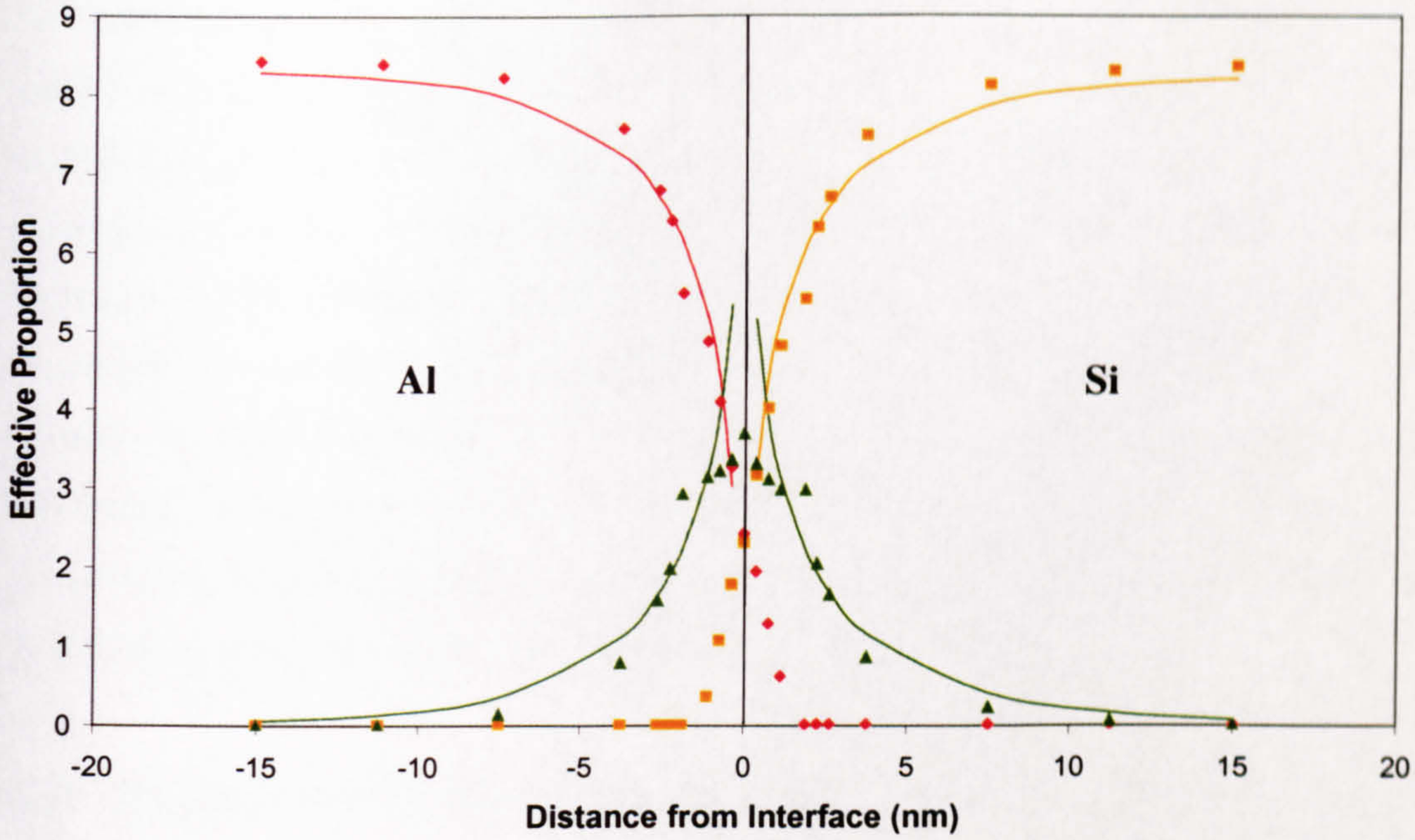

Figure 8.16: Theoretical t/λ plot for a stepped system. Aluminium (*red*), silicon (*orange*) and interface (*green*) components are shown.

As with the finite probe analysis, the bulk components were observed to have a tail on the opposite side of the interface. For this system, the interface extends 1.5nm either side of the central point. This agrees with the tails of the bulk component, which have fallen to zero by 1.9nm. The chosen spatial resolution does not allow more accurate determination of the point at which they become zero. Also observed on this plot is that the interfacial component is flattened in the vicinity of the centre of the interface. Both of these features have been observed in the majority of the experimental data.

The ratios of interest from the Bessel function fits were calculated and found to be

$$\frac{P_{Al}^{Fit}}{P_{Si}^{Fit}} = 1.01 \qquad \frac{P_{Al}^{Data}}{P_{Si}^{Data}} = 1.01 \qquad \frac{A_{Al}}{A_{Si}} = 1.08 \qquad \frac{C_{Al}}{C_{Si}} = 1.10.$$

For a planar interface the results were

$$\frac{P_{Al}^{Fit}}{P_{Si}^{Fit}} = 1.01 \qquad \frac{P_{Al}^{Data}}{P_{Si}^{Data}} = 1.01 \qquad \frac{A_{Al}}{A_{Si}} = 1.02 \qquad \frac{C_{Al}}{C_{Si}} = 1.07.$$

As would be expected, the plateau values of the bulk material remained unaffected. The plateau values are indicative of the behaviour at large distance from the interface and so should not be affected by the interface at all. The ratio of C_i values was slightly changed from the planar case. As this interface is broadened it would be expected that the decay of

the interface plasmon would be shallower. However, it would be anticipated that this would be symmetrical about the interface and so the C_i ratio would remain unaltered. Examination of the bulk tails shows that the silicon decays slightly more sharply than the aluminium. It is not clear whether this is an effect from the fitting of reference spectra or is indicative of the data itself. The experimental stepped interface (section 7.4) did show an increased C_i ratio as did this theoretical data. However, for the stepped interface, the average C_i ratio was found to be 1.22. Clearly this is still high compared with the theoretical result from a stepped interface. However, the experimental data was significantly affected by thickness variations not accounted for here and so steps at the interface may explain, in part, for the high value of the C_i ratio.

8.5 Detection of a Thin Interfacial Layer Using EELS

The analysis in this section has a different intent compared with the preceding sections. Instead of examining the effect of an interfacial layer on the results, this section intends to determine whether a thin layer of a third material would be detected using EELS. In analysing and presenting the data, it has always been assumed that the interfaces were two-layer interfaces. It was therefore of interest to investigate whether, if a thin layer of a third material were present at the interface, would it be detected? Fig 8.17 shows the geometry of the interface. The analysis in this section is not intended to be physical; it is understood that a 0.1nm layer of a material is not experimentally realisable. Equally, the layers of the materials chosen are not necessarily able or likely to form at the Al/Mg_2Si interface under investigation. The materials were chosen to be difficult to detect in an EELS spectrum due to their wide bulk plasmons. In addition, the materials were readily available, simplifying the process of obtaining experimental dielectric data. Four materials (X) were investigated. These were MgO, Si, SiO_2 and Al_2O_3.

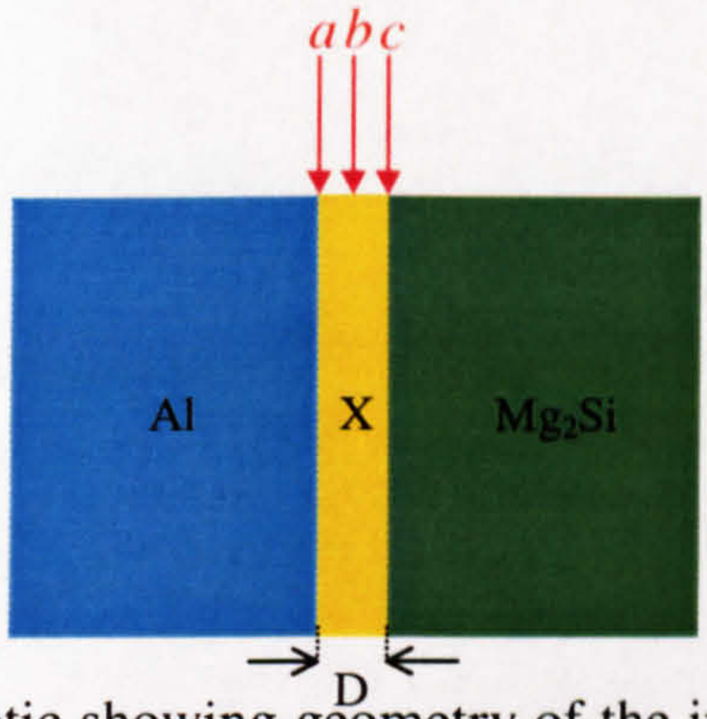

Figure 8.17: Schematic showing geometry of the interfaces modelled. *X* indicates the material forming the interfacial layer and *D* is the width of the layer. *a, b* and *c* indicate the three beam positions investigated.

8.5.1 Interfacial MgO Layer

The result obtained for the case where *X*=MgO for a width *D*=0.5nm is shown in Fig. 8.18 with the beam travelling down at *b*. The results for the three different beam positions were almost identical. The theoretical data indicated that it would be very easy to detect if there was a 0.5nm layer of MgO at the Al/Mg_2Si interface. Although there is only a slight shift in the Al/Mg_2Si interface plasmon to higher energy, the additional detail between 18 and 28 eV arising from the MgO plasmon would make such a layer easily identifiable. In addition, the FWHM of the main plasmon peak almost doubled from 2.7eV up to 5eV. When *D* was reduced to 0.1nm, the intensity in the 18-28eV region was greatly decreased. However, the overall shape in that region remained largely unchanged. The FWHM of the main plasmon peak was observed to have increased to 3.5eV, though there was no notable shift in energy. For the 0.1nm case it was possible that an interfacial MgO layer would not be detected, with the extra peak in the 18-28eV region attributed to carbon on the sample. However, further examination of the spectrum would identify that this peak did not result from carbon. The shape of the peak is very distinct and could be discerned from carbon, which has a simple plasmon shape.

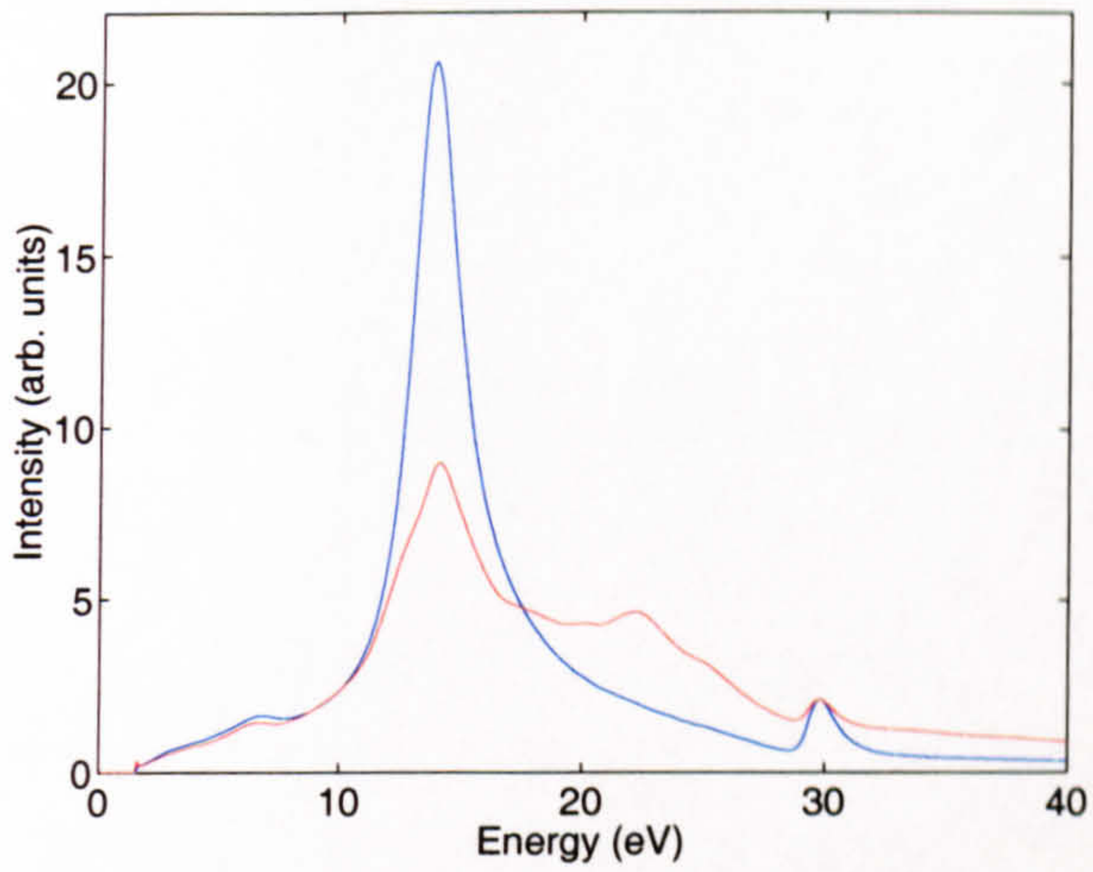

Figure 8.18: Theoretical spectrum for an Al/Mg_2Si system with D=0.5nm and X=MgO (*red*). Beam is positioned at *b*. Theoretical spectrum for a two-layer interface is included for comparison (*blue*).

8.5.2 Interfacial SiO_2 Layer

Fig 8.19 gives the results from the case where X=SiO_2. Initially, D=0.1nm was investigated. For this case, the spectra from the three different beam positions were effectively identical. The plasmon energy was observed to shift slightly to lower energy and the FWHM of the main peak increased to 3.3eV. Once again, the number of counts on the higher energy side of the main plasmon peak was increased. Unlike the MgO case, the shape in this region is quite uniform. As a result it would be extremely difficult to differentiate this spectrum from a two-layer interfacial spectrum with a small amount of carbon present.

The width of the interfacial layer was then increased to 0.5nm, the results for which are also given in Fig 8.19. Here the deviation from the two-layer case was much more noticeable. Though the shift in plasmon energy was not significantly greater than the D=0.1nm case, the FWHM was observed to have increased to 4.9eV. As with the MgO, the counts in the 18-28eV region were increased again from the 0.1nm case. However, this could still be mistaken for carbon due to the shape of the extra peak. The data for the beam positioned at *a* also indicated an increase in counts in the 5-11eV region. Whilst the experimental data often has a small peak present around 7eV, it is never observed to have a secondary peak at 9eV. The shape in this region would act as an indicator of the presence of a thin layer of SiO_2.

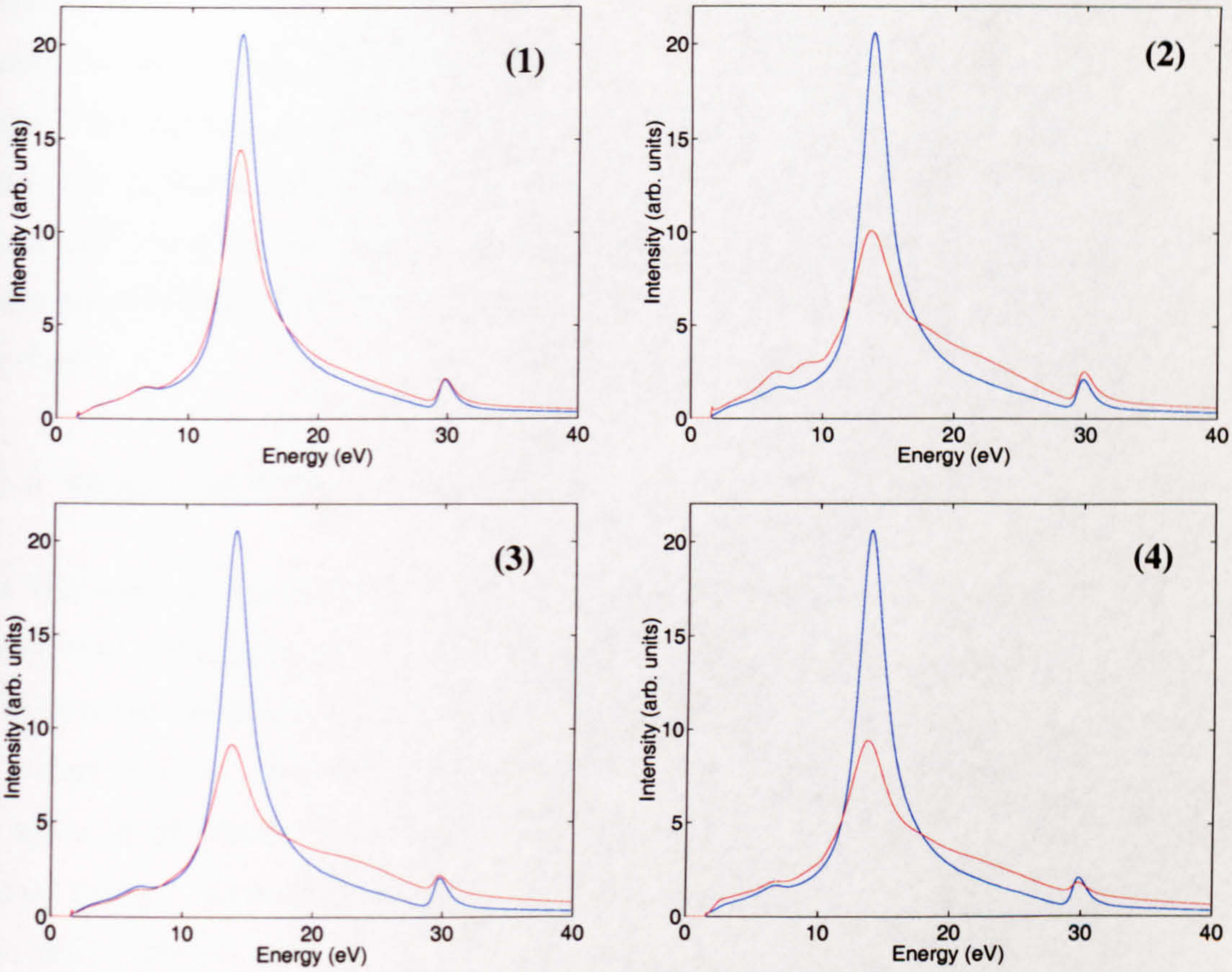

Figure 8.19: Theoretical results for three-layer Al/*X*/Mg_2Si system (*red*). *X*=SiO_2 in each case. (1) *D*=0.1nm, beam positioned at *b*. (2)-(4) *D*=0.5nm beam positioned at *a*, *b* and *c* respectively. Two-layer interface plasmon is included for comparison (*blue*).

8.5.3 Interfacial Al_2O_3 Layer

The results from *X*=Al_2O_3 were found to be similar to the SiO_2 case. Fig 8.20 gives the results for the Al/Al_2O_3/Mg_2Si system. For *D*=0.1nm the FWHM of the main plasmon peak was increased to 3.8eV with a shift in peak energy of the order of 0.3eV to lower energy. As with SiO_2, increased counts were observed on the higher energy side of the plasmon and once again these could be mistakenly attributed to the presence of carbon. The effect of having a 0.5nm interfacial layer was also investigated for this system. The results were once again similar to the equivalent situation for the Al/SiO_2/Mg_2Si system. The main plasmon peak was shifted by 0.5eV to lower energy and the FWHM was increased to 4.3eV compared to the two-layer system. The behaviour in the 18-28eV region was extremely similar to the SiO_2 results, both in shape and intensity. This leads, once again, to the conclusion that these results could easily be mistaken for data taken a small distance away from an Al/Mg_2Si interface with a reasonable amount of carbon

contamination. However, as with the SiO_2 results, the theoretical data corresponding to position *a* shows characteristic behaviour at lower energy. This behaviour in the 5-11eV range is not reproduced in any simulated or experimental two-layer Al/Mg_2Si data. As a result, this region would serve to identify the presence of a relatively thin layer of Al_2O_3. Indeed, the shape is such that theoretically speaking it would be possible, with sufficient thickness, to differentiate between a layer of Al_2O_3 and a layer of SiO_2 at an Al/Mg_2Si interface.

8.5.4 Interfacial Si Layer

The final system examined was Al/Si/Mg_2Si, for which the data is given in Fig. 8.21. This system was of particular interest as *X* was a semiconductor. The results were quite different to those observed for the other systems, as would be expected. For both the *D*=0.1nm and the 0.5nm case, an increase in counts was only observed in the 15-25eV range. This had the effect of increasing the FWHM of the interface plasmon peak and causing a shift to higher energy. Unusually, all six situations investigated for this system produced noticeably different data. The 0.1nm case with the beam directed down at *c* showed very little alteration in the Al/Mg_2Si interface plasmon peak. The FWHM of the plasmon peak remained unchanged at 2.7eV and the plasmon energy was shifted by only 0.1eV. When the beam position was changed to *b* a larger difference was noted. The plasmon FWHM was increased to 3.6eV, though the plasmon energy was still only shifted by 0.1eV compared with the two-layer case. With the beam situated at *a* the effect was increased again with a FWHM of 3.7eV and a energy shift of 0.2eV. The broadening and shifting of the plasmon would all be observed within a two-layer Al/Mg_2Si system. A very small movement of the electron beam from the interface towards the bulk aluminium in the two-layer system would generate spectra that would be effectively indistinguishable from those resulting from *D*=0.1nm.

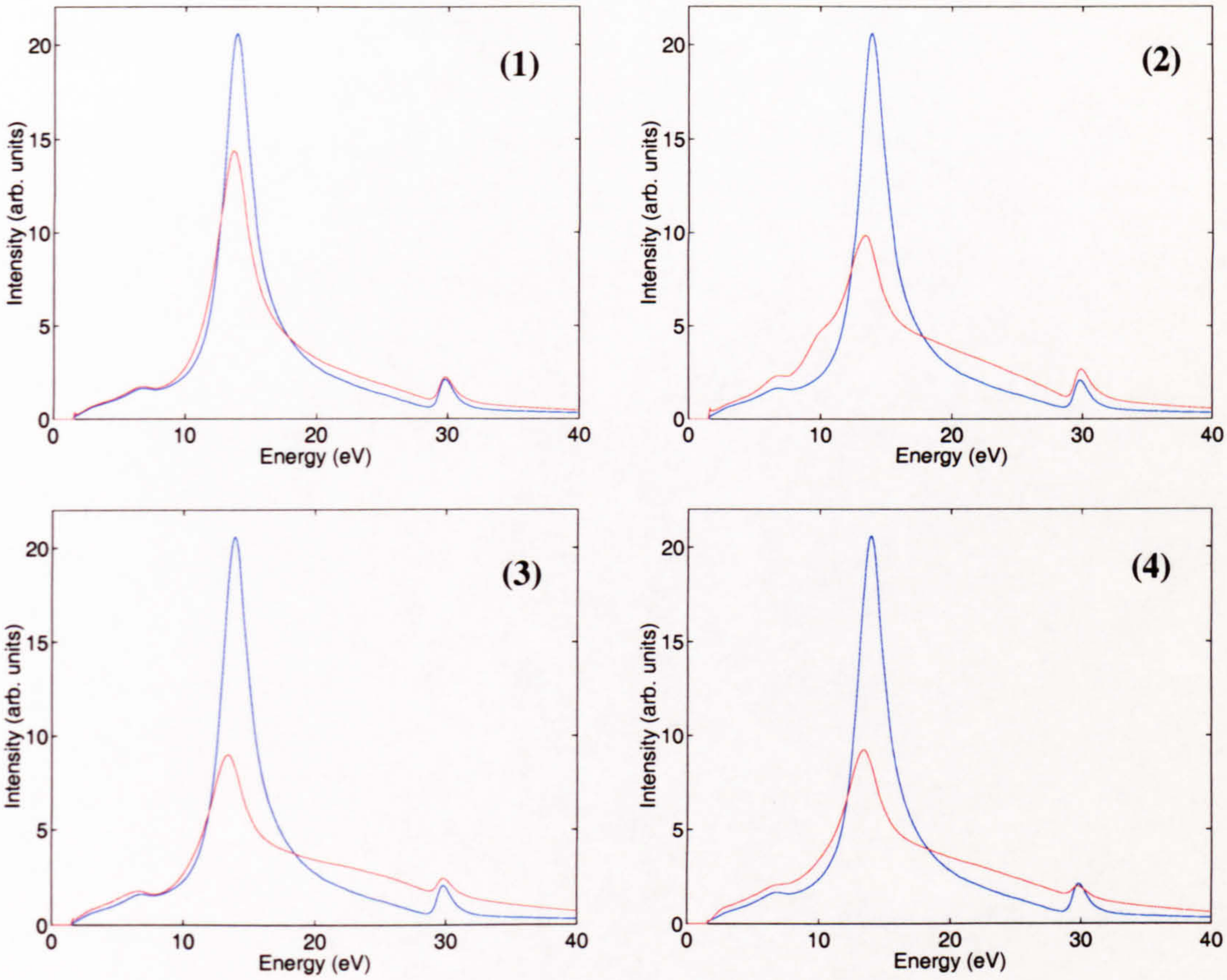

Figure 8.20: Theoretical results for three-layer Al/*X*/Mg_2Si system (*red*). *X*=Al_2O_3 in each case. (1) *D*=0.1nm, beam positioned at *b*. (2)-(4) *D*=0.5nm beam positioned at *a*, *b* and *c* respectively. Two-layer interface plasmon is included for comparison (*blue*).

The situation was not significantly improved by increasing *D* to 0.5nm. It was initially observed that the three-layer results were easily discernible from the two-layer interface spectrum. At *a*, a significant shift of 0.7eV was observed, along with a FWHM of 4.8eV. Modelling the beam at *b* gave a shift of only 0.3eV but a very large FWHM of 5.5eV. Having the beam at *c* gave the spectrum that was most similar to the two-layer system. This scenario resulted in a 0.2eV shift coupled with a FWHM of 4.3eV. Despite these differences, it would once again be possible to generate very similar spectra to all of these from a two-layer system merely by moving the electron probe a short distance from the interface. However, in this project, spectra were not examined in isolation. If a trace over the interface were performed, as is described in chapter 5, it is likely that the results would indicate that the interface was not ideal. The presence of a thin Si layer at the interface would be sufficient to vary the data enough that it would not be mistaken for a good Al/Mg_2Si two-layer interface.

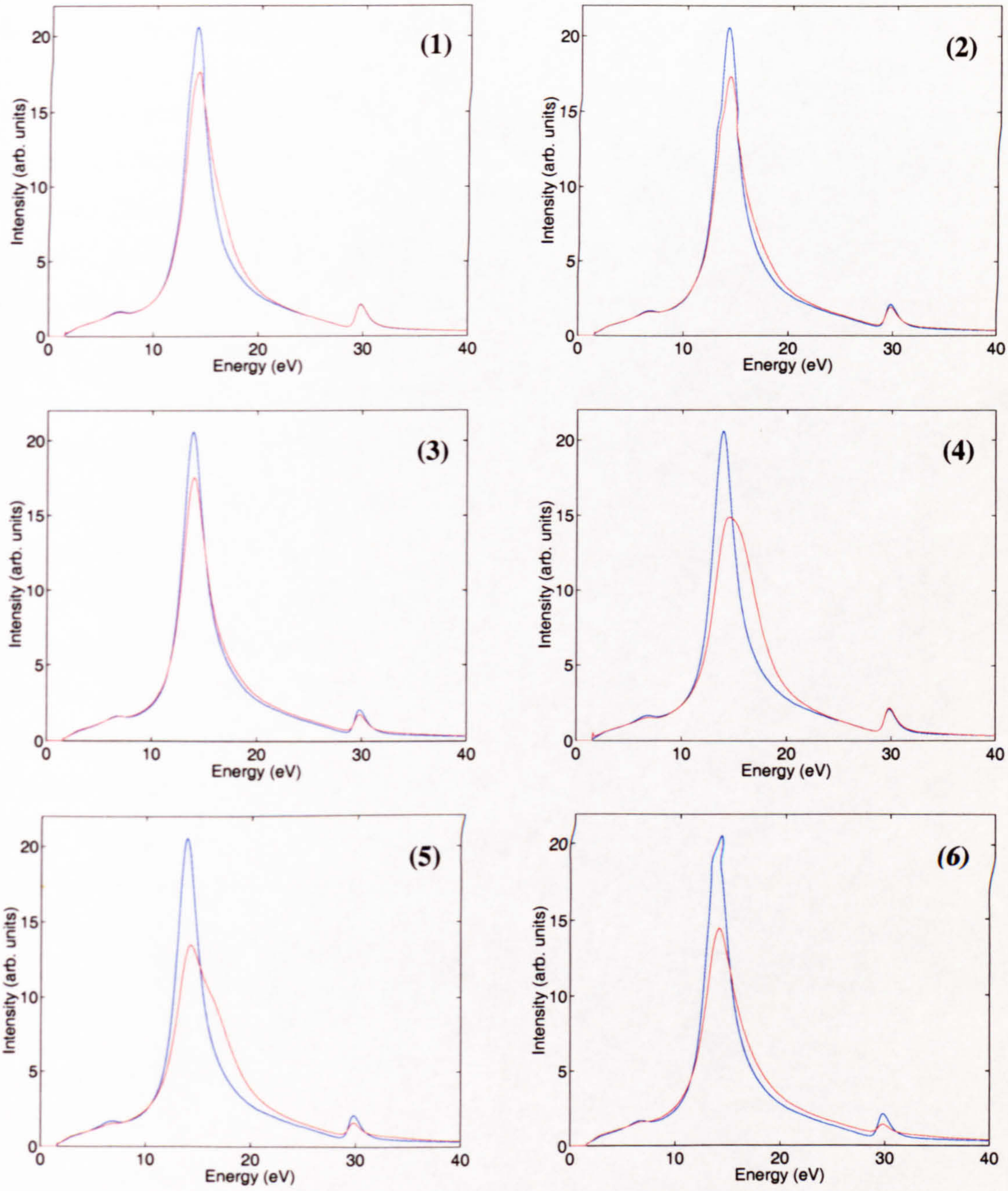

Figure 8.21: Theoretical results for a three-layer Al/*X*/Mg_2Si system (*red*). *X*=Si in each case. (1)-(3) *D*=0.1nm, beam positioned at *a*, *b* and *c* respectively. (4)-(6) *D*=0.5nm, beam positioned at *a*, *b* and *c* respectively. A two-layer interface plasmon is included for comparison (*blue*).

8.5.5 Conclusions on the Detection of an Interfacial Layer

The results for the various three-layer systems indicate that this technique is not sensitive to very thin layers of either SiO_2 or Al_2O_3. In both cases the resulting shape could easily be mistaken for the presence of carbon contamination with the slightly thicker layer, these materials would be identified due to characteristic behaviour in the 5-11eV region. The sensitivity would be increased in a sample known to have low contamination. In such a sample, a carbon plasmon would not be expected and hence the three-layer interface plasmon would not be mistakenly identified. The technique displayed least sensitivity to the presence of an interfacial layer of Si. *The shapes of the* plasmons were not sufficiently different from those obtainable from the two-layer system that the Si would be instantly noticed. Only on further analysis would the interface be flagged as non-ideal, though this may not be recognised as being caused by a layer of Si. It is likely that with different bulk materials, a layer of Si would be instantly noticeable. The most promising results came from the MgO system. A thicker layer of MgO would be instantly identified due to its characteristic shape. A thinner layer would be identified once the spectrum was examined in greater detail. In general, this technique is largely insensitive to a 0.1nm interfacial layer of any material. However, the sensitivity is increased with increased width of the layer. With a thickness of 0.5nm all the materials examined had an observable effect on the EELS spectrum. This once again indicated the excellent spatial resolution available using EELS.

A significant assumption is made within this section. It is assumed that the dielectric function from a thin layer of a material is identical to that from the bulk material. This is very unlikely to be the case, particularly for very thin layers (< 1nm). However, this assumption has been made by other workers (French, 2000). The assumption is made as it simplifies the process of calculating Hamaker constants for three-layer systems. EELS may offer the opportunity to dispense with this assumption. Spectra can be obtained from an interfacial layer with high spatial resolution. Once corrected for interface contributions, these spectra can be used to determine the dielectric function of the interfacial layer. This would then provide considerably more accurate values for the Hamaker constant.

8.6 Overall Discussion and Conclusions

In this thesis, data recorded from Al/Mg_2Si and Al/Si interfaces has been presented. By examination of the non-relativistic theoretical equation, expected values of key results were estimated. The results examined were the ratio of plateau values of the bulk component, P_i, which gave a measure of the thickness variation across the interface; the ratio of A_i values, which gave an indication of how well the interfacial position had been determined and finally the ratio of C_i values, which measured the comparative decay of the interface component and the corresponding growth of the bulk components on each side of the interface. Due to the approximations involved in the determination of expected values, theoretical data was *generated and processed*. This data provided more accurate values to describe the theoretical behaviour of the systems. Experimental data was *acquired from the* HB5 and Tecnai microscopes from a number of interfaces. The data from the different microscopes was compared with each other and with the theoretical values to determine how well experimental data holds to the theoretical equation.

8.6.1 Al/Mg_2Si System

	P_{Al}/P_{Mg2Si}	A_{Al}/A_{Mg2Si}	C_{Al}/C_{Mg2Si}
Average of HB5 Data	1.23 ± 0.04	1.10 ± 0.03	1.25 ± 0.05
Tecnai Line Spectrum Image	1.17	1.16	1.44
Tecnai Spectrum Image	1.19 ± 0.003	1.05 ± 0.03	1.14 ± 0.09 1.29 ± 0.04
Theoretical Value	1.18	1.10	1.09

Table 8.1: *Table of* results for the Al/Mg_2Si system with standard errors

Table 8.1 gives the results obtained from the Al/Mg_2Si system. The errors quoted are the standard errors for that set of results (chapter 6). As the line spectrum image provided only a single result for each value, it does not have a standard error. As discussed in section 6.1.6, the actual errors are likely to be much larger, but are difficult to quantify.

The results were all quite consistent for the plateau values and close to the theoretical value. This indicated that the areas examined were all of fairly constant thickness. The results for the A_i ratios indicated that the technique used for selecting the optimum

interface position was valid and worked effectively. Unfortunately, the C_i values did not compare as well. Two values are included for the spectrum image, these respectively correspond to the 'as recorded' average and the average after the non-representative results were removed (section 6.2.3). The two results for the Tecnai spectrum image indicates the variety of values obtained, though the difference in this case is caused by problems in the analysis rather than differences in the data. As already discussed (section 6.2.3), the spectrum image and line spectrum image were acquired from the same interface. The trend in the results from the spectrum image and the positions of the spectrum images were compared. Using this information, the data were compared and found to agree, though it indicated the variation in results that can be obtained from an interface. The 'corrected' Tecnai spectrum image value was close to the HB5 result. This indicated that there was good agreement amongst all the experimental results. Compared with the theoretical value, the results were consistently high. It is not clear why this is the case but a number of possible sources of error are discussed in section 6.1.6 and section 8.5.4.

8.6.2 Al/Si System

	P_{Al}/P_{Si}	A_{Al}/A_{Si}	C_{Al}/C_{Si}
Average of HB5 data	0.97 ± 0.04	0.95 ± 0.03	0.68 ± 0.08
Tecnai Line Spectrum Image	1.09	0.98	0.89
Tecnai Spectrum Image	1.12 ± 0.02	1.20 ± 0.03	1.22 ± 0.07
Tecnai Spectrum Image 2	1.20 ± 0.002	0.96 ± 0.03	0.69 ± 0.03
Theoretical Value	1.01	1.02	1.07

Table 8.2: Table of results for the Al/Si system with standard errors

Table 8.2 gives the results from the Al/Si system. Difficulties with the analysis routines made the line spectrum image result questionable (section 7.4.2). The first result from spectrum imaging did not correlate with the result from the HB5. However, this was believed to be caused by differences in the interfaces. Analysis of Tecnai data acquired from one of the interfaces examined in the HB5, produced results very similar to that from the HB5. The ratio of plateau values from the second spectrum image is significantly larger than that from the HB5. Despite this, the Al t/λ is found to be ~0.46 in both cases. The thickness was observed to vary significantly along an interface. Therefore the difference in

plateau values is unsurprising. Though the C_i ratios from the HB5 and the Tecnai for the same interface were found to agree, they were lower than the theoretical value. However, Tecnai data that was corrected for thickness variations displayed a C_i ratio of 0.80, considerably closer to the theoretical value.

8.6.3 Factors Affecting the Experimental Results

It was clear both from the difference between experimental and theoretical values and from the variation in the experimental values that the results were highly dependent on the area and interface under examination. To investigate this, a number of different thickness profiles were theoretically modelled. In addition, other possible factors affecting the experimental results were simulated. The results from these analyses are given in table 8.3.

	P_{Al}/P_{Si} (fit)	A_{Al}/A_{Si}	C_{Al}/C_{Si}
Flat	1.01	1.02	1.07
Bow-tie	1.01	1.01	1.05
Asymmetric Bow-tie	0.97	0.97	1.06
Flat Bow-tie	1.01	1.01	1.06
Turbine	1.17	1.55	1.55
Finite Probe	1.01	1.05	1.06
Stepped Interface	1.01	1.08	1.10

Table 8.3: Table of results from factors affecting experimental results

The only thickness profile that was observed to make a significant difference to the decay ratio was the turbine profile. Variations in thickness are easy to identify experimentally only when there is a change in thickness at large distance from the interface. At such distances the thickness is indicated solely by the bulk plasmon. As a result, the turbine profile would be difficult to identify in experimental data as the thickness variation occurs close to the interface. Unexpectedly, correcting for variations in thickness in experimental data did cause a change in the decay ratios. This was attributed to the different qualities of fit between the theory and experiment and to the fit range. Finally, the theoretical effect of a finite probe and steps at an interface were examined and found to be significant for the

t/λ plots, but not so for the ratios of interest. A slight increase was observed in the decay ratio.

8.6.4 Overall

The techniques used in this project were shown to be well suited to obtaining energy loss information from interfaces in materials. EELS has been shown to be a sensitive technique which is able to detect small misalignments between the interface and the beam. However, it is best used in conjunction with HRTEM, which offers greater sensitivity in the examination of the interface structure. For this reason, along with the more accurate beam positioning, the FEI Tecnai TF20 microscope was found to be a very powerful tool in this work.

The Bessel functions fitted well to the experimental data, indicating that the form of the decay agreed with the theory. Different series acquired from the same interface were found to have consistent C_i ratios. This was a very positive result as it demonstrated that the results were characteristic for the interface. It also showed that the results for different interfaces and from different regions of the same interface can vary significantly. However, the C_i ratio values showed poor agreement with the values obtained from the theoretical fits.

The C_i ratio was considered to be the most important value for characterising a two-layer system. If the decay lengths for an interface could be accurately predicted, it would demonstrate a strong understanding of the EELS response from the interface. With such an understanding comes the evolution of new techniques. In particular, the correction of the interface plasmon contribution, enabling isolation of the bulk plasmon.

The results for the Al/Si system deviated significantly from the theoretical value. However, this was largely attributed to the thickness variations, which were significant for this system. It has been shown that correction of thickness variations in experimental data resulted in substantial changes in the C_i ratio, resulting in values that were closer to the theory. The Mg_2Si results were in closer agreement with the theory, though still had some deviation. Comparison of the Al/Mg_2Si and corrected Al/Si values with theory, yields a +15-20% and a -25% discrepancy, respectively. The cause of this difference is not clear,

nor is the reason for the differing signs. Perhaps the difference in signs can be explained by Mg_2Si lying at lower energy than aluminium whilst silicon has a higher plasmon energy. In both systems the HRTEM images showed non-perfect interfaces. The effect of steps in the Si case and the unidentified band in the Mg_2Si is not clear. However, these may go partly to explain the discrepancy in values.

The theoretical treatment required a number of assumptions. The main assumptions are those of constant thickness, that the electron probe was infinitely small and that the interfaces were planar and parallel to the electron beam. When the difference between the theoretical and experimental systems are taken into account, the experimental results hold well to the theory.

Using EELS, the presence of a thin layer of a third material at the interface can be detected for thicknesses of less than a nanometre. Techniques such as Fresnel contrast imaging (Ness *et al*, 1986) have been shown to be able to measure the thickness of interfacial layers to accuracies of 0.1nm down to widths of ~0.5nm. Similarly, high-resolution imaging is able to detect sub-nanometre layers at an interface. These techniques are superior for the detection of thin interfacial layers. However, the way in which EELS excels is in obtaining information from such layers, most noticeably the dielectric function. Many of the techniques and analyses presented in this thesis will be useful in determining the dielectric function from thin interfacial layers. The three-layer equation has been used to generate theoretical spectra. Equally, it could be used as a basis to separate out the components of an experimental spectrum acquired from a three-layer system. By isolating the bulk component from the interfacial phase, accurate dielectric data can be calculated through a Kramers-Kronig transformation.

Finally, the problems described in this and previous chapters help to identify extensions to this work which are necessary to gain a fuller understanding of EELS from an interface.

8.7 Possibilities for Further Work

It has been necessary to make a number of assumptions on the effect of various factors on EELS from an interface. The effect of a finite probe was investigated and not found to have a significant effect on the ratios of interest. However, this investigation could be

extended. An experimental treatment of different probe sizes may enable greater understanding of some of the results presented.

In a similar manner, the investigation of interfacial 'imperfections' such as dislocations and steps would be beneficial in the application of the theory to physical systems. It has been discussed that the theoretical interfaces are perfect. Interfaces in actual materials are often not. By understanding the effect of dislocations and steps, experimental results can be better understood and perhaps, if necessary, corrected to remove such effects.

Due to the sample preparation methods available, many of the interfaces displayed significant thickness variations. The preparation and investigation of interfaces with constant thickness would serve to identify how significant thickness variations are in affecting the data.

Naturally, the ultimate extension of this work is the investigation of three-layer systems. As mentioned, many of the techniques applied in this thesis would be applicable to examination of a three-layer system. With an understanding of EELS from a three-layer system it will be possible to isolate the data from an interfacial layer and hence determine its dielectric function. With this, the Hamaker constant can be determined and the interfacial forces examined.

APPENDIX 1

MODIFIED BESSEL FUNCTIONS

There are two functions known as modified or hyperbolic Bessel functions. These are $I_p(x)$ and $K_p(x)$. They are two independent solutions of the differential equation

$$x^2y''+xy'-\left(x^2+p^2\right)y=0.$$

The solution of interest for this thesis is $K_p(x)$ which takes the following form

$$K_p(x)=\tfrac{\pi}{2}i^{p+1}H_p^{(1)}(ix).$$

Where

$$H_p^{(1)}(x)=J_p(x)+iN_p(x)$$

$$N_p(x)=\frac{\cos(\pi p)J_p(x)-J_{-p}(x)}{\sin(\pi p)}$$

$$J_p(x)=\sum_{n=0}^{\infty}\frac{(-1)^n}{\Gamma(n+1)\Gamma(n+p+1)}\left(\frac{x}{2}\right)^{2n+p}$$

$$J_{-p}(x)=(-1)^pJ_p(x)$$

Fortunately, it is only $K_0(x)$ which is required for this thesis. This can be expressed in terms of the integral For integral p

$$K_0(x)=\int_0^{\infty}\frac{\cos(xt)}{\sqrt{t^2+1}}dt$$

Where x is a real number greater than zero.

In addition, there are expressions to give the limiting values of the function, these are:

$$\lim_{x\to 0}K_0(x)=-\ln(x) \qquad \textbf{Equation A1.1a}$$

$$\lim_{x\to\infty}K_0(x)=\sqrt{\frac{\pi}{2x}}e^{-x}\left\{1-\frac{1}{8x}+\frac{9}{2!(8x)^2}-\frac{9\times25}{3!(8x)^3}+\ldots\right\} \qquad \textbf{Equation A1.1b}$$

At the values of x used in this thesis it is reasonable to ignore the all the terms after the first in eqn A1.1b. The effect of the higher order terms is negligible.

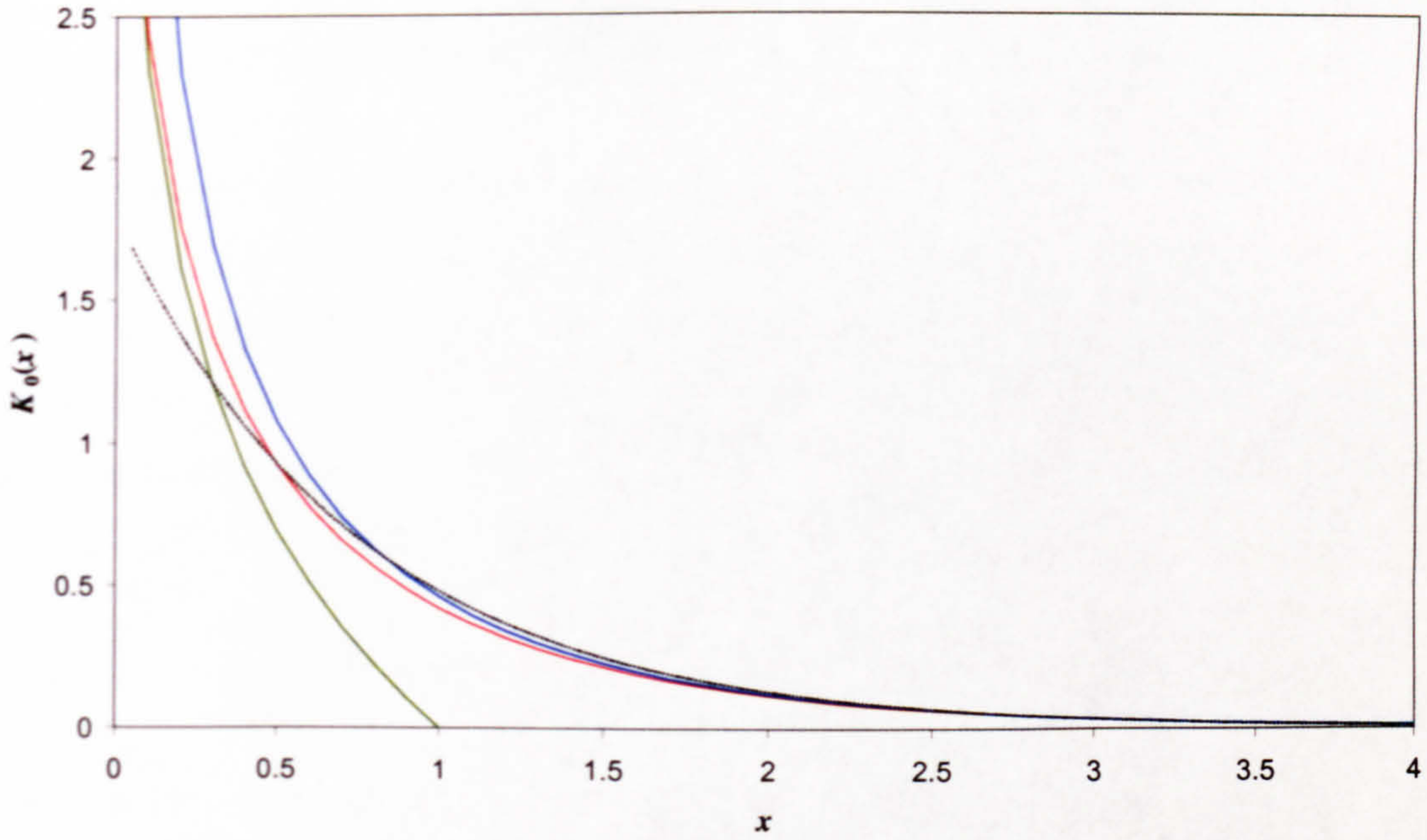

Figure A1.1: Plot comparing K_0 Bessel Function (*red*) with $-ln(x)$ (*green*) and $\sqrt{\frac{\pi}{2x}}e^{-x}$ (*blue*). Also shown is the best-fit exponential (*black dashed line*).

Fig A1.1 compares the K_0 Bessel function with its small x and large x approximations. In addition, the best-fit exponential function is included. As expected the small x approximation compares favourably at small x but deviates strongly above x=0.4. Equivalently, the large x approximation shows strong similarity to the Bessel function above x=0.7 but deviates at values below that. The best-fit exponential does not approximate the Bessel function as well as either of the two other functions over their respective ranges. However, the exponential demonstrates a reasonable fit over a greater range than either of the two other functions.

APPENDIX 2

CONVERTING FROM EL/P

The vast majority of the data processing was performed in Gatan EL/P v3.0. This software package runs in a Macintosh environment. Data can be output from EL/P in a variety of formats. The output format used was the EMSA/MAS format, which offers the greatest flexibility for conversion due to the information it contains. The EMSA format is text-based and an example file is given in Fig. A2.1.

```
#FORMAT     : EMSA/MAS Spectral Data File
#VERSION    : 1.000000
#TITLE      : Admgo
#DATE       : 14-AUG-2002
#TIME       : 16:02
#OWNER      : EM
#NPOINTS    : 821.0000
#NCOLUMNS   : 5.000000
#XUNITS     : eV
#YUNITS     :
#DATATYPE   : Y
#XPERCHAN   : 0.1014022
#OFFSET     : 1.460314E-06
#SIGNALTYPE : ELS
#XLABEL     : Energy Loss
#COMMENT    : Specimen: MgO specimen
#BEAMKV     : 100.0000
#CONVANGLE  : 11.00000
#OPERMODE   : IMAGE
#COLLANGLE  : 12.50000
#ELSDET     : PARALL
##GPROCSTATUS: 4392
##GTICKTIME  : 1319049
#SPECTRUM   :
1.717872E+07, -146.5767, -145.5979, -144.6303, -143.6826,
-142.7013, -141.7621, -140.8063, 0.000000, 0.000000,
...
... 160 lines of data omitted
...
594.4294, 590.4698, 586.0258, 577.3279, 533.7500,
1499.424,
#ENDOFDATA  :
#CHECKSUM   : 456441
```

Figure A2.1: Example EL/P output file in EMSA format.

The EMSA file contains only the y data, in a comma-delimited list. In addition to this, the energy of the first channel (*#OFFSET*) and the energy width of each channel (*#XPERCHAN*) are included to calculate the corresponding x values. Other information of note within the file is the accelerating voltage used in the collection of the data (*#BEAMKV*) and the number of data points in the file (*#NUMPOINTS*).

The program used for generating the dielectric data, DK, allowed input of spectra in only one format. This format had a very specific layout that required being exactly correct for the file to load correctly. The first line contains the name of the file with the second line used for comments or often left blank. Once again only the y-data is given directly. The data is presented in 10 columns each with exactly 9 characters in it, one of which is a decimal point. The data in each column is separated by a comma, there is no comma following the data in the last column. The very first value gives the number of data points in the file, including itself as a data point *i.e.* A file containing 704 y values will have 705 as the first value in the file. The very last row contains additional information, including (in order) the energy corresponding to the first y-value, the energy per channel and the accelerating voltage used in the acquisition of the data. Fig A2.2 gives an example input *file for DK.*

admgo.txt

```
 832.,    0.,    0.,    0.,    0.,    0.,    0.,    0.,    0.,    0.
   0., 20000., -146., -145., -144., -143., -142., -141., -140.,    0.
   0.,    0.,    0.,    0.,    0.,    0.,    0.,    0.,    0.,    0.
   0.,    0.,    0.,    0.,    0.,    0.,    0.,    0.,    0.,    0.
   0.,    0.,    0.,    0.,    0.,    0.,    0.,    0.,    0.,    0.
   0.,    0.,    0.,    0.,    0.,    0.,    0.,    0.,    0.,    0.
   0.,    0.,    0.,    0.,    0.,    0.,    0.,    0.,    0.,    0.
   6.,   87.,  122.,  122.,  242.,  508.,  676.,  850., 1013., 1148.
1254., 1335., 1399., 1453., 1507., 1560., 1614., 1673., 1733., 1793.
1855., 1916., 1976., 2029., 2085., 2145., 2207., 2270., 2336., 2405.
2480., 2560., 2644., 2737., 2841., 2953., 3071., 3202., 3343., 3497.
3665., 3845., 4032., 4221., 4391., 4522., 4609., 4646., 4642., 4607.
...
... 69 lines of data omitted
...
  620.,  615.,  613.,  610.,  605.,  598.,  594.,  590.,  586.,  577.
  533., 1499.,
-1.010, 0.101, 100.000, 0.100, 0.000, 0.300, 0.000, 0.000, 0.000, 0.000
```

Figure A2.2: Example DK input file.

In order to easily convert the output from EL/P into a format suitable for inputting to DK, it was necessary to write a program in C. This program read the header of the EMSA file to determine the number of points, the energy of the first channel, the accelerating voltage used in acquiring the data and the energy per channel. With this information and the data from the spectrum it was able to generate an input file for DK. In addition to its file requirements DK had further requirements on the spectrum itself. It would not process spectra in which the first data point corresponded to 0eV or which had more than 1020 data points. Fortunately, the majority of spectra exported from EL/P already had less than 1020 channels. However, all of the single-scattered spectra exported from EL/P have 0eV as the first point. It was therefore necessary to add additional channels to displace the first data point from 0eV. This was performed by the C conversion program. In addition to this, the program marked the 0eV point by placing 20000 counts into the first channel prior to inserting the additional channels. Fig A2.3 gives the code of the DK conversion program.

```
#include <stdio.h>
#include <stdlib.h>
#include <string.h>
#include <conio.h>

void main()
{
 char inname[40], outname[40], temp[20], outtext[12], test[3];
 int numpoints, check, length, loop, speccount, specread;
 float evchan, initen, accel;
 /* numpoints= Number of points
    initen=energy of first channel
    accel=accelerating voltage
    evchan=ev per channel */

/*Take input filename and set output file*/
 do{
    printf("Please enter the name of the file to convert.\n");
    scanf("%s",&inname);
    printf("\nPlease enter the name of the file to save as.\n");
    scanf ("%s",&outname);
    FILE *infile, *outfile;
    infile=fopen(inname,"r");
    outfile=fopen(outname,"w");

do{
      fscanf(infile,"%s",&temp); //Look for Npoints line
      check=strncmp(temp, "#NPOINTS",8);
    }while(check!=0);
    printf("Check");      // Feedback to user
```

Figure A2.3: Code of EL/P to DK file conversion program. Comments are given in blue.

```
fscanf(infile,"%s",&temp); //Read colon
fscanf(infile,"%d",&numpoints); //Read the # points
numpoints=numpoints+10;       // Adding in pre-0 points

do{
  fscanf(infile,"%s",&temp); //Look for XPERCHAN line
  check=strncmp(temp, "#XPERCHAN",9);
}while(check!=0);
fscanf(infile,"%s",&temp); //Read colon
fscanf(infile,"%f",&evchan); //Read eV per channel

do{
  fscanf(infile,"%s",&temp); //Look for OFFSET line
  check=strncmp(temp, "#OFFSET",7);
}while(check!=0);
fscanf(infile,"%s",&temp); //Read colon
fscanf(infile,"%f",&initen); //Read initial energy

do{
  fscanf(infile,"%s",&temp); //Look for spectrum
  check=strncmp(temp, "#SPECTRUM",9);
}while(check!=0);
fscanf(infile,"%s",&temp); //read colon

fprintf(outfile,"%s\n\n",outname); //Print filename
for (loop=0;loop<8;loop++){
   outtext[loop]=' '; // Clear out array
   }
   _itoa(numpoints+1,outtext,10); //num→string (base 10)
   length=strlen(outtext);
   for (loop=0;loop<8-length;loop++){
      fprintf(outfile,"%c",' ');     // add in whitespace
   }
   fprintf(outfile,"%s.,",outtext);    //number of points

   for (loop=0;loop<8;loop++){
      fprintf(outfile,"      0.,"); //Pre zero data
   }
/*Mark 0eV with 20000 counts and remove original data */
   fprintf(outfile,"      0.\n      0.,   20000.,"); // Mark 0ev
   fscanf(infile,"%d",&specread);     //Remove original 0ev data
   fscanf(infile, "%s", &temp);

 /* The actual spectrum bit */

  for (speccount=12;speccount<numpoints+1;speccount++){
     fscanf(infile,"%d",&specread); //Read pt from spectrum
     for (loop=0;loop<8;loop++){
        outtext[loop]=' ';        //clear string
     }
     _itoa(specread,outtext,10); //num→string (base 10)
     length=strlen(outtext);   //check length
```

Figure A2.3 (cont): Code of EL/P to DK file conversion program.

```
    for (loop=0;loop<8-length;loop++){
       fprintf(outfile,"%c",' ');     // add in whitespace
    }

    fprintf(outfile,"%s.",outtext); //output data to file
    fscanf(infile,"%s",&temp); //read comma
    if (!((speccount-9)%10)){
      fprintf(outfile,"\n"); //Only 10 columns
    }
    else{
       fprintf(outfile,","); //print a comma
    }
}
fprintf(outfile,"\n");

/* Last Row */

  length=sprintf(outtext,"%.3f",initen); //initial energy

  for (loop=0;loop<9-length;loop++){
     fprintf(outfile,"%c",' ');     // add in whitespace
  }
  fprintf(outfile,"%s,",outtext);  // Output initial energy to file

  length=sprintf(outtext,"%.3f",evchan); //ev/channel

  for (loop=0;loop<9-length;loop++){
     fprintf(outfile,"%c",' ');     // add in whitespace
     }
     fprintf(outfile,"%s,",outtext); // Output eV per channel to file

length=sprintf(outtext,"%.3f",accel); //Accelerating voltage

     for (loop=0;loop<9-length;loop++){
        fprintf(outfile,"%c",' ');     // add in whitespace
     }
fprintf(outfile,"%s,",outtext);

fprintf(outfile,"   0.100,");
     fprintf(outfile,"   0.000,");
     fprintf(outfile,"   0.300,");
     fprintf(outfile,"   0.000,");
     fprintf(outfile,"   0.000,");
     fprintf(outfile,"   0.000,");
     fprintf(outfile,"   0.000");

     fclose(infile);
     fclose(outfile);
     printf("\nProgram complete.\n");
/* Ask user for more files, go back to top if yes, quit if no*/
     printf("Would you like to convert another file? \n");
     scanf("%s",&test);
     check=strncmp(test,"y",1);
```

Figure A2.3 (cont): Code of EL/P to DK file conversion program.

```
  }while(check==0);
  printf("\nGoodbye\n");
  system("PAUSE");
  return 0;
}
```

Figure A2.3 (cont): Code of EL/P to DK file conversion program.

The vast majority of spectra, however, were never imported into DK. Most of them were imported straight into Excel. As the import requirements are considerably less stringent for Excel than for DK, it was considerably easier to convert files for import. However the volume of files to convert was such that it was felt that writing another conversion program would save a considerable amount of time. To this end, another program was written in C for conversion between EL/P EMSA format and a comma-delimited x,y format suitable for Excel. As the program used the same form of input file, it was possible to use the same program as previously with some alterations to the second section. The code for this second conversion program is given in Fig. A2.4.

```
#include <stdio.h>
#include <stdlib.h>
#include <string.h>
#include <conio.h>

void main()
{
 char inname[40], outname[40], temp[20], outtext[12], test[3];
 int numpoints, check, length, loop, speccount, specread;
 float evchan, initen, accel, energy;
 /* numpoints=Number of points
 initen= energy of first channel
 accel=accelerating voltage
 evchan =ev per channel */
 do{
   printf("Please enter the name of the file to convert.\n");
   scanf("%s",&inname);
   sprintf(outname,"%sb.txt",&inname);
   FILE *infile, *outfile;
   infile=fopen(inname,"r");
   outfile=fopen(outname,"w");
   do{
     fscanf(infile,"%s",&temp); //Look for Npoints line
     check=strncmp(temp, "#NPOINTS",8);
   }while(check!=0);
   printf("Check");
   fscanf(infile,"%s",&temp); //the colon
   fscanf(infile,"%d",&numpoints);
```

Figure A2.4: Code of EL/P to Excel file conversion program. Comments are given in blue.

```
numpoints=numpoints+10;       // Adding in pre-0 points

do{
  fscanf(infile,"%s",&temp); //Look for XPERCHAN line
  check=strncmp(temp, "#XPERCHAN",9);
}while(check!=0);
fscanf(infile,"%s",&temp); //the colon
fscanf(infile,"%f",&evchan);

do{
  fscanf(infile,"%s",&temp); //Look for OFFSET line
  check=strncmp(temp, "#OFFSET",7);
}while(check!=0);
fscanf(infile,"%s",&temp); //the colon
fscanf(infile,"%f",&initen);

do{
  fscanf(infile,"%s",&temp); //Look for spectrum
  check=strncmp(temp, "#SPECTRUM",9);
}while(check!=0);
fscanf(infile,"%s",&temp); //the colon

for (loop=0;loop<8;loop++){
   outtext[loop]=' '; // Clear out array
}
_itoa(numpoints+1,outtext,10); //convert dec to integer (base 10)
fprintf(outfile,"%s.\n",outtext);    //number of points

/* The actual spectrum bit */
 for (speccount=0;speccount<numpoints+1;speccount++){
    fscanf(infile,"%d",&specread);
    for (loop=0;loop<8;loop++){
       outtext[loop]=' ';
    }
    _itoa(specread,outtext,10); //convert dec to integer (base 10)
    energy=initen+speccount*evchan;
    fprintf(outfile,"%.3f, ",energy);
    fprintf(outfile,"%s\n",outtext); //output data
    fscanf(infile,"%s",&temp); //the comma
 fprintf(outfile,"\n");

 fclose(infile);
 fclose(outfile);
 printf("\nProgram complete.\n");
 printf("Would you like to convert another file? \n");
 scanf("%s",&test);
 check=strncmp(test,"y",1);
}while(check==0);
printf("\nGoodbye\n");
system("PAUSE");
return 0;
}
```

Figure A2.4: Code of EL/P to Excel file conversion program. Comments are given in blue.

APPENDIX 3

MATLAB PROGRAMS

The theoretical spectra using the relativistic equation and the three-layer equation were all generated using programs written in Matlab. Matlab was chosen as it is extremely good at handling matrices. By treating the *energy* and *intensity* values from a spectrum as being two separate vectors, Matlab was able to manipulate them easily.

Both the relativistic two-layer equation (eqn 2.32) and he three-layer equation (eqn 2.34) contain integrals. Simpson's Rule was used for numerically evaluating these integrals. Simpson's Rule works by splitting the function being integrated into a number of small, equal ranges. The assumption is that the function can be approximated to a quadratic over these ranges. By summing the area under these ranges the integral is calculated. The expression for Simpson's rule is given in eqn A3.1.

$$\frac{h}{3}f(x_0)+\frac{4h}{3}f(x_1)+\frac{2h}{3}f(x_2)+\frac{4h}{3}f(x_3)+\ldots+\frac{2h}{3}f(x_{N-2})+\frac{4h}{3}f(x_{N-1})+\frac{h}{3}f(x_N)$$

Equation A3.1

Here h is the width of the range and N is the (even) number of ranges.

The Matlab programs used, occupy two files. One of these files is as a function and contains the integrand being evaluated. The other controls the input data and the integration procedure. The listing for this latter part is given in Fig. A3.1. In this program, the dielectric functions of the two materials are read in from a text file, along with the corresponding energy. To ensure that the vectors are the same size, only 470 data points are inputted, this gives a range up to ~47.5 eV. The user then inputs the x value (in metres), the k_y^m value (normally set to $1\text{x}10^{10}\text{m}^{-1}$) and the number of steps (normally set to 200). The program then uses Simpson's rule to calculate the integral over the range of k_y=0 → k_y^m. For each step the function file is called by the line "[rel, nonrel]=lossfn(kayy,eps1,eps2,x,energy);". This line passes the values of k_y, ε_1, ε_2, x and the energy loss to the secondary file which calculates the function for a specific k_y. The relativistic result is held in the variable 'relsum' and this is updated after each part of the Simpson's formula is calculated.

```
FID1=fopen('ialf.txt'); % Aluminium imaginary
alim=fscanf(FID1,'%f',470);
FID2=fopen('ralf.txt'); % aluminium real
alre=fscanf(FID2,'%f',470);
FID3=fopen('isif.txt');  %Mg2Si imaginary
mgim=fscanf(FID3,'%f',470);
FID4=fopen('rsif.txt');  % Mg2Si real
mgre=fscanf(FID4,'%f',470);
FID3=fopen('energyf.txt'); % Energy
energy=fscanf(FID3,'%f',470);

eps1=alre+I*alim; % Define epsilon 1
eps2=mgre+I*mgim; % Define epsilon 2

x=input('Enter the x value:')
kayym=input('Enter the ky value:')
N=input('Enter number of steps:')
kayy=0
[rel, nonrel]=lossfn(kayy,eps1,eps2,x,energy);
h=kayym/(2*N)
relsum=h/3*rel;
counter=0;
for looper = 1:2*N-1,
      kayy=h*looper;
      [rel, nonrel]=lossfn(kayy,eps1,eps2,x,energy);
      relsum=relsum+h/3*(3-(-1)^looper)*rel;
end

kayy=kayym;
[rel, nonrel]=lossfn(kayy,eps1,eps2,x,energy);
relsum=relsum+h/3*rel;

fclose('all')
```

Figure A3.1: Listing of main Matlab file used for calculating relativistic and non-relativistic equations.

The function itself was calculated by a function file. This file is shown in Fig. A3.2. This file is considerably more straightforward in terms of operation as it merely defines the constants and then calculates the function. This file calculates both the relativistic and non-relativistic equations. However, calculation of the Bessel function is time consuming and so the non-relativistic equation was calculated only when $k_y=k_y^m$. This is the last time the function is called for a particular integrand and so the overall calculation time was reduced.

```
Function [rel, nonrel] = lossfn(kayy,eps1,eps2,x0,en)
% Relativistic equation for x0

c=3e8;
hbar=1.055e-34;
e=1.6e-19;
gamma=1.1957; % 1.1957 for 100kV, 1.3914 for 200Kv, 2.9567 for 1000Kv
m0=9.11e-31;
v=sqrt(0.3005*c^2); % sq(v)/sq©=0.3005 for 100kv, 0.4835 for 200kv, 0.8856 for 1000Kv
K0=1697e9; %1697e9 for 100kv, 2505e9 for 200kv, 7205e9 for 1000Kv
energy=en*e;

omega=energy/(hbar);
thetae=14*1.6e-19/(gamma*m0*v^2);
kz=omega/v;
K=kayy.^2+kz.^2;
alpha1=sqrt(K-eps1.*(omega.^2)/c^2);
alpha2=sqrt(K-eps2.*(omega.^2)/c^2);

PA=(2*alpha2.^2.*(eps1-eps2))./(eps2.*alpha1+eps1.*alpha2)+(alpha1-alpha2).*(1-
eps2*(v/c)^2);
PB=exp(-2*alpha2*x0)./(eps2.*alpha2.*(alpha2+alpha1));

if kayy==1e10
      bf=besselk(0,2*omega*x0/v);
      first=imag(-2./(eps1+eps2)).*bf;
      second=imag(-1./eps2).*(log(theta*v./omega)-bf);
      nonrel=first+second;
end

G=PA.*PB;

rel = imag(G-(1-eps2*(v/c)^2)./(alpha2.*eps2));
```

Figure A3.2: Matlab function file for calculation of relativistic and non-relativistic two-layer equations.

Calculation of the three-layer equation for section 8.4 required modification of both the main and function Matlab files. As the thickness of the interfacial phase, the distance from the centre of the phase, the number of steps and the value of k_y^m were kept largely constant, the user was no longer required to enter them. Dielectric functions of all the materials of interest were loaded in from text files. The specific material for the interfacial phase was then selected with the 'data' variable. Otherwise, the working of the function file was largely the same as previously. The main program file is given in Fig. A3.3.

```
FID1=fopen('3lalim.txt'); % Aluminium imag
alim=fscanf(FID1,'%f',400);
FID2=fopen('3lalre.txt'); % aluminium real
alre=fscanf(FID2,'%f',400);

FID3=fopen('3lmgsiim.txt');  %Mg2Si imaginary
mgsiim=fscanf(FID3,'%f',400);
FID4=fopen('3lmgsire.txt');  % Mg2Si real
mgsire=fscanf(FID4,'%f',400);

FID5=fopen('3lenergy.txt');
energy=fscanf(FID5,'%f',400); % energy

FID6=fopen('3lsiim.txt'); % Si imag
siim=fscanf(FID6,'%f',400);
FID7=fopen('3lsire.txt'); % Si real
sire=fscanf(FID7,'%f',400);

FID8=fopen('3lmgoim.txt');  %MgO imaginary
mgoim=fscanf(FID8,'%f',400);
FID9=fopen('3lmgore.txt');  % MgO real
mgore=fscanf(FID9,'%f',400);

FID10=fopen('3laloim.txt'); % Alumina imag
aloim=fscanf(FID10,'%f',400);
FID11=fopen('3lalore.txt'); % alumina real
alore=fscanf(FID11,'%f',400);

FID12=fopen('3lsioim.txt');  %Sio2 imaginary
sioim=fscanf(FID12,'%f',400);
FID13=fopen('3lsiore.txt');  % Sio2 real
siore=fscanf(FID13,'%f',400);

al=alre+i*alim;
mgsi=mgsire+i*mgsiim;
mgo=mgore+i*mgoim;
si=sire+i*siim;
sio=siore+i*sioim;
alo=alore+i*aloim;

% Beam travelling external to interfacial phase
% d is width of interfacial phase
% x is distance from centre of interfacial phase
d=0.5e-9;
x=-0.25e-9;
K=1e10;
N=200;

data=mgo;
ky=0;
[answer]=three(d,x,ky,energy,al,mgsi,data);
```

Figure A3.3: Listing of main Matlab file used for calculating three-layer equation.

```
h=K/(2*N);
relsum=h/3*answer;
for looper = 1:2*N-1,
      ky=h*looper;
      [answer]=three(d,x,ky,energy,al,mgsi,data);
      relsum=relsum+h/3*(3-(-1)^looper)*answer;
end

ky=K;
[answer]=three(d,x,ky,energy,al,mgsi,data);
relsum=relsum+h/3*answer;

fclose('all')
```

Figure A3.3 (cont.): Listing of main Matlab file used for calculating the three-layer equation.

The function file for the three-layer equation is very similar in layout to the two-layer case. The result for the function is passed back to the main Matlab program in the variable 'answer'. The listing for the function file is given in Fig. A3.4.

```
function [answer] = three(d,x,kwee,en,eps1,eps3,eps2) % Relativistic equation for x

c=3e8;
hbar=1.055e-34;
e=1.6e-19;
gamma=1.1957; % 1.1957 for 100kV, 1.3914 for 200Kv, 2.9567 for 1000Kv
m0=9.11e-31;
v=sqrt(0.3005*c^2); % sq(v)/sq(c)=0.3005 for 100kv, 0.4835 for 200kv, 0.8856 for 1000Kv
energy=en*e;
omega=energy/(hbar);
thetae=14*1.6e-19/(gamma*m0*v^2);
kz=omega/v;
K=sqrt(kwee.^2+kz.^2);

xi1p=eps2+eps1;
xi1m=eps2-eps1;
xi3p=eps2+eps3;
xi3m=eps2-eps3;

fnum=xi1p.*xi3p.*exp(K*d)+xi3m.*xi1m.*exp(-
K*d)+xi1p.*xi3m.*exp(2*K*x)+xi1m.*xi3p.*exp(-2*K*x);
fdenom=xi1p.*xi3p.*exp(K*d)-xi3m.*xi1m.*exp(-K*d);

answer=1./K.*imag(-1./eps2.*fnum./fdenom);
```

Figure A3.4: Listing of Matlab function file used for calculating the three-layer equation

LIST OF REFERENCES

Abramowitz, M. and Stegun, I. A., 1964, *Handbook of Mathematical Functions* (Washington; NBS)

Aizpurua, J., Howie, A. and García de Abajo, 1999, *Phys. Rev. B*, **60**, 11149

Batson, P. E., 1999, *Physica B*, **273**, 593

Batson, P. E., Kavanagh, K. L., Wong, C. Y. and Woodall, J. M., 1987, *Ultramicroscopy*, **22**, 89

Batson, P. E., Kavanagh, K. L., Woodall, J. M. and Mayer, J. W., 1986, *Phys. Rev. Lett*, **57**, 2729

Becher, P. F., Painter, G. S., Sun, E. Y., Hsueh, C. H. and Lance, M. J., 2000, *Acta. Mater.*, **48**, 4493

Bergström, L.,1997, *Adv. Colloid Interface Sci.*, **70**, 125

Bolton, J. P. R. and Chen, M., 1995, *Ultramicroscopy*, **60**, 247

Brockt, G. and Lakner, H., 2000, *Micron*, **31**, 435

Clarke, D. R., 1987, *J. Am. Ceram. Soc.*, **70**, 15

Craven, A. J., 1977, *Int. Phys. Conf. Ser.*, **36**, 311

Craven, A. J. and Buggy, T. W., 1981, *Ultramicroscopy*, **7**, 27

Crozier, P. A., 1990, *Phil. Mag. B*, **61**, 311

de Gennes, P. G., 1981, *J. Phys. Lett.*, **42**, L-377

Dagastine, R. R., Prieve, D. C. and White, L. R., *J. Colloid Interface Sci.*, **231**, 351

Daniels, J., Festenberg, C. V., Raether, H. and Zeppenfield, K., 1970, *Springer Tracts Mod. Phys.*, **54**, 78

Delby, N. and Krivanek, O. L., 2002, *Private Communication*

Derjaguin, B. V. and Churaev, N. V., 1974, *J. Colloid Interface Sci.*, **49**, 249

Donnadieu, P., 1999, *Phil. Mag. A*, **79**, 1347

Dzyaloshinskii, I. E., Lifshitz, E. M. and Pitaevskii, L. P., 1961, *Adv. Phys.*, **10**, 165

Echenique, P. M. and Pendry, J. B, 1975, *J. Phys. C*, **8**, 2936

Egerton, R. F., 1982, *Phil. Trans. R. Soc. Lond. A*, **305**, 521

Egerton, R. F., 1996, *Electron Energy-Loss Spectroscopy in the Electron Microscope – Second Edition* (New York: Plenum Press)

Egerton, R. F. and Cheng, S. C., 1987, *Ultramicroscopy*, **21**, 231

Edwards, G. A., Stiller, K., Dunlop, G. L. and Couper, M. J., 1998, *Acta. Mater.*, **46**, 3893

Eskin, D. G., Massardier, V. and Merle, P., 1999, *J. Mat. Sci.*, **34** 811

Fernández-Varea, J. M. and Garcia-Molina, R., 2000, *J. Colloid Interface Sci.*, **231**, 394

French, R. H., 2000, *J. Am. Ceram. Soc.*, 83, 2117

French, R. H., Cannon, R. M., DeNoyer, L. K. and Chiang, Y.-M., 1995, *Solid State Ionics*, 75, 13

Garcia-Molina, R., Gras-Marti, A., Howie, A. and Ritchie, R. H., 1985, *J. Phys. C.: Solid State Phys.*, 18, 5335

Garvie, L. A., Craven, A. J. and Brydson, R., 1994, *American Minerologist*, 79, 411

Hainfeld, J. and Isaacson, M., 1978, *Ultramicroscopy*, 3, 87

Hamaker, H. C., 1937, *Physica*, 4 1058

Hamilton, D., 2002, *Digital Micrograph plug-in modules*

Hirsch, P. B, Howie, A., Nicholson, P. B., Pashley, D. W and Whelan, M. J., 1965, *Electron Microscopy of Thin Crystals* (London, UK: Butterworth & Co. Ltd.)

Hough, D. B. and White, L. R., 1980, *Adv. Colloid Interface Sci.*, 14, 3

Howie, A., Aizpurua, J., Garcia de Abajo, F. J., and Rafferty, B. K., 1999, *J. Elec. Microsc.*, 48, 673

Howie, A. and Milne, R. H., 1984, *J. Microsc.*, 136, 279

Howie, A. and Milne, R. H., 1985, *Ultramicroscopy*, 18, 427

Howie, A. and Walsh, C., 1991, *Microsc. Microanal. Microstruct.*, 2, 171

Isabell, T. C., Fischione, P. E., O' Keefe, C., Guruz, M. U. and Vinayak, D. P., 1999, *Microsc. Microanal. Microstruct.*, 5, 126

Jacobs, M. H., 1972, *Phil. Mag.*, 26, 1

Jain, M., 1992, *J. Mater. Sci.*, 27, 399

Keast, V. J., Scott, A. J., Brysdson, R., Williams, D. B. and Bruleys, J., 2001, *J. Microsc.*, 203, 135

Keyse, R. J., Garratt-Reid, A. J., Goodhew, P. J. and Lorrimer, G. W., 1998, *Introduction to Scanning Transmission Electron Microscopy* (London, UK: BIOS Scientific Publishers)

Knowles, K. M. and Turan, S., 2000, *Ultramicroscopy*, 83, 245

Kobayashi, K., Shingu, P. H. and Ozaki, R., 1976, *J. Mater. Sci.*, 11, 399

Koike, J., Mabuchi, M., and Higashi, K., 1995, *Acta. Metall. Mater.*, 43, 199

Kolodzie, A. T., Murfitt, M. and Bleloch, A. L., 2001, *Inst. Phys. Conf. Ser.*, 168, 247

London, F., 1937, *Trans. Faraday Soc.*, 33, 8

Lyons, L., 1991, *Data Analysis for Physical Science Students*, (Cambridge, UK: Cambridge University Press)

Mahan, J. E., Vantomme, A. and Langouche, G., 1996, *Phys. Rev. B*, 54, 16965

Matsuda, K., Naoi, T., Uetani, Y., Sato, T., Kamio, A. and Ikeno, S, 1999, *Scripta Materialia*, 41, 379

McComb, D. W., Ning, X-G., Weatherly, G., Pan, J. and Lloyd, D. J., 2000, *Phil. Mag. A*, 80, 2509

Moreau, P., Brun, N., Walsh, C. A., Colliex, C. and Howie, A., 1997, *Phys. Rev. B*, **56**, 6774

Ness, J. N., Stobbs, W. M and Page, T. F., 1986, *Phil. Mag. A*, **54**, 679

Oleshko, V. P., Murayama, M. and Howe, J. M., 2002, *Micros. Microanal.*, **8**, 350

Parsegian, V. A., and Ninham B. W., 1969, *Nature*, **224**, 1197

Palik, E. D., (editor), 1985, *Handbook of Optical Constants of Solids* (Orlando, Florida: Academic Press)

Ritchie, R. H., 1957, *Phys. Rev.*, **106**, 874

Roessler, D. M. and Walker, W. C., 1967, *Phys. Rev.*, **159**,733

Schamm, S. and Zanchi, G., 2001, *Ultramicroscopy*, **88**, 211

Scheinfein, M., Muray, A. and Isaacson, M., 1985, *Ultramicroscopy*, **16**, 233

Thomas, G., 1961, *J. Inst. Metals*, **90**, 57

Thomas, P., 2002, *Digital Micrograph plug-in modules*

Walls, M. G., 1987, *PhD Thesis*

Walls, M. G. and Howie, A., 1989, *Ultramicroscopy*, **28**, 40

Walsh, C. A., 1991, *Phil. Mag. B*, **63**, 1063

Wang, Z. L., 1996, *Micron*, **27**, 265

Widom, B., 1978, *J. Chem. Phys.*, **68**, 3878

Williams, D. B. and Carter, C. B., 1996, *Transmission Electron Microscopy* (New York: Plenum Press)

Williams, D. B. and Edington, J. W., 1976, *J. Microsc.*, **108**, 113

Zavattieri, P. D. and Espinosa, H. D., 2001, *Acta. Mater.*, **49**, 4291

Zhen, L., Fei, W. D., Kang, S. B. and Kim, H. W., 1997, *J. Mat. Sci.*, **32**, 1895